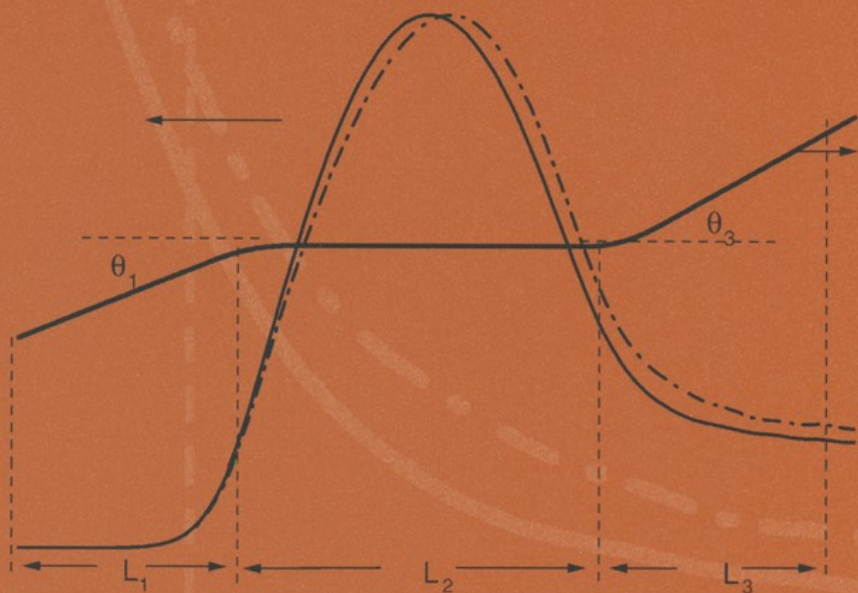# M. V. Kartikeyan
E. Borie
M. K. A. Thumm

Gyrotrons

High-Power Microwave and Millimeter Wave Technology
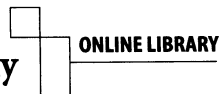

Springer

Gyrotrons

Advanced Texts in Physics

This program of advanced texts covers a broad spectrum of topics which are of current and emerging interest in physics. Each book provides a comprehensive and yet accessible introduction to a field at the forefront of modern research. As such, these texts are intended for senior undergraduate and graduate students at the MS and PhD level; however, research scientists seeking an introduction to particular areas of physics will also benefit from the titles in this collection.

Physics and Astronomy

ONLINE LIBRARY

springeronline.com

M.V. Kartikeyan
E. Borie
M.K.A. Thumm

Gyrotrons

High Power Microwave
and Millimeter Wave Technology

With 101 Figures

Springer

Dr. M.V. Kartikeyan
Associate Professor
Department of Electronics and Computer Engineering
Indian Institute of Technology-Roorkee (IITR)
Roorkee – 247 667 (UA), India
E-mail: kartkfec@iitr.ernet.in

Professor Dr. E. Borie
Professor Dr. M.K.A. Thumm
Institute for Pulsed Power and Microwave Technology (IHM)
Bau 421, Forschungszentrum Karlsruhe (FZK)
Postfach 3640, 76021 Karlsruhe, Germany
E-mail:
borie@ihm.fzk.de
manfred.thumm@ihm.fzk.de

Professor Dr. M.K.A. Thumm is also with the
Institute of High Frequency Techniques
and Electronics (IHE)
University of Karlsruhe
Kaiserstrasse 12, 76128 Karlsruhe, Germany

Preface

Gyrotron oscillators (gyrotrons) are capable of providing hundreds of kilo-
watts of power at microwave and millimetric wavelengths. From their con-
ception in the late fifties until their successful development for various ap-
plications, gyrotrons have come a long way technologically and made an ir-
reversible impact on both users and developers. The possible applications
of high power millimeter and sub-millimeter waves from gyrotrons and their
variants (gyro-devices) span a wide range of technologies. The plasma physics
community has already taken advantage of the recent advances of gyrotrons
in the areas of RF plasma production, heating, non-inductive current drive,
plasma stabilization and active plasma diagnostics for magnetic confinement
thermonuclear fusion research, such as lower hybrid current drive (LHCD)
(8 GHz), electron cyclotron resonance heating (ECRH) (28–170 GHz), elec-
tron cyclotron current drive (ECCD), collective Thomson scattering (CTS)
and heat-wave propagation experiments. Other important applications of gy-
rotrons are electron cyclotron resonance (ECR) discharges for the generation
of multi-charged ions and soft X-rays, as well as industrial materials process-
ing and plasma chemistry. Submillimeter wave gyrotrons are employed in high
frequency, broadband electron paramagnetic resonance (EPR) spectroscopy.
Additional future applications await the development of novel high power
gyro-amplifiers and devices for high resolution radar ranging and imaging
in atmospheric and planetary science as well as deep space and specialized
satellite communications and RF drivers for next generation high gradient
linear accelerators (supercolliders). The subject has thus stimulated us to
bring this book in its present form, as a supplement to the efforts of earlier
researchers and authors and as an assistance to future work in this field.

   The basic motivation for this book on "Gyrotrons" comes from the needs
of the gyrotron community in general and our own practical experiences and
the problems we are facing in our design and development projects and the
application to specific gyrotrons. This book is to some extent a compendium
of our previous work, which we would like to share with the community of
high power microwave engineers/scientists. Efforts are made to give a brief
review of gyro-devices followed by theory, design of individual components,
some specific design examples, and applications of gyrotrons. We have tried

to present the contents to help beginners, as well as researchers, designers and end users.

During the course of the preparation of this book, our colleagues at the Institut für Hochleistungsimpuls- und Mikrowellentechnik (IHM), Forschungszentrum Karlsruhe (FZK), helped us immensely. We sincerely thank Ms. Ursula Feisst, Ms. Christine Kastner, Ms. Martina Klenk, Dr. Manju Paulson, Ms. Manuela Wettstein, Dr. Günter Dammertz, Dr. Bernhard Piosczyk, Dr. Michael Kuntze, Dr. Lambert Feher, Dr. Guido Link, Dr. Stefan Illy, Dr. Oliver Drumm, Dr. Xiao Yang, Mr. Kai Koppenburg, Mr. Andreas Arnold, Mr. Joachim Anderer, Mr. Jianbo Jin, Mr. Sebastijan Stanculovic, Mr. Roland Vincon, Mr. Herbert Budig, Mr. Hans Richard Kunkel and Mr. Josef Szczesny. Special thanks are due to the Alexander von Humboldt Foundation for their generous support.

Special Acknowledgements

We sincerely thank the following publishers for reprint permission to use the cited figures. Publication details are given in the respective references; the corresponding citations are given in the figure captions:

- American Institute of Physics, USA

- Artech House Inc., USA

- Elsevier Science B.V., Ireland

- Institute of Applied Physics, Russian Academy of Sciences, Nizhny Novgorod, Russia

- Institute of Electrical and Electronic Engineers (IEEE), USA

- Institute of Physics Publishing, UK

- International Journal of Electronics, UK

- International Society for Optical Engineering (SPIE), USA

- IOS Press, The Netherlands.

- Plenum Publishing Corporation, USA

- Taylor & Francis Ltd., UK.

In addition, special thanks are due to all the authors of the original sources of the figures for the use of their work in the book.

Contents

1 Introduction

1.1 General Introduction

Although this is the era of solid state semiconductor devices, microwave tubes are still extensively employed in certain areas for applications where their solid state counterparts are not able to compete as far as delivering the required power at microwave to millimetric wavelengths. These applications vary from electron cyclotron resonance heating of plasmas in fusion reactors to the sintering of industrial ceramics. This unique ability to produce hundreds of kilowatts of pulsed to continuous waves (CW) at frequencies greater than 1 GHz has made microwave tubes an indispensable source for high power and high frequency applications. Microwaves are electromagnetic waves whose frequencies fall approximately in the range 1–300 GHz. Microwaves are used for a great variety of applications. Some of these are: all types of communications applications (from mobile to deep space), strategic applications (from radar to missile guidance), scientific applications (from particle accelerators to thermonuclear plasma fusion devices and plasma diagnostics), and industrial applications (from simple domestic ovens to various heating, drying and sintering purposes). As already mentioned, low power applications employ solid state microwave devices extensively as they are small in size and cost effective (long lifetime, no high voltage), whereas for high power applications, the only choice is microwave tubes.
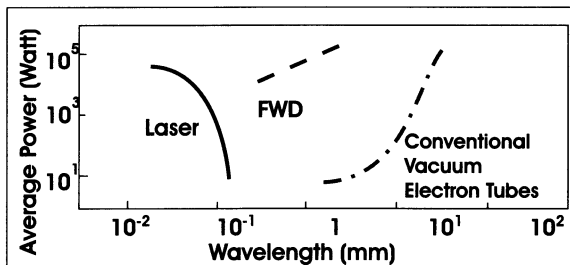
Fig. 1.1. Chart showing the the limitation of conventional microwave tubes for the generation of higher power levels at elevated frequencies. Here, FWDs are fast wave devices such as gyrotrons and its variants

The actual story of microwaves in the electromagnetic spectrum began at the Polytechnical University of Karlsruhe, Germany, with the experimental verification of Maxwell's equations by Heinrich Hertz in 1887. In 1906, Lee de Forest invented the triode, the only device available in those days for the radio-frequency community. It is a transit time based device in which the finite transit time of the electron is comparable to the period of the alternating voltage between the electrodes. Its improved variants and developed versions such as tetrodes are still used in systems for certain applications, such as radio and TV broadcasting and induction heating applications in industry. This new invention of electron tubes paved the way for further developments in radio and wireless transmission in the first two decades of the 1900s. Radar and antenna technology also started to bloom with the advent of various electron tubes. But these electron tubes had some inherent limitations. Although they are capable of delivering very high powers at low frequencies, their power levels decrease rapidly at higher frequencies. Moreover, the onset of two world wars pushed the strategic needs to higher frequencies and higher power levels as the lower frequency regions of the electromagnetic spectrum were slowly becoming congested. This motivated the quest for still higher powers and frequencies. In 1921, Hull invented the magnetron, one of the oldest members of the family of microwave tubes. It is a crossed field device in which the potential energy of the electrons is transferred to the waves. It is called an M-type device since the electric and magnetic fields are perpendicular to each other. Especially during and after world war II, the importance of high power and high frequency microwave sources was immensely felt by the need of specific users for military applications which led to further investigations in the field of microwave tubes. Meanwhile, in 1937, the Varian brothers developed their earlier version of the klystron amplifier and in 1944 Kompfner developed the helix travelling wave tube. Both these microwave tubes are O−type devices in which the electric and magnetic fields are parallel to each other. In the travelling wave type of tubes, the kinetic energy of the electrons is transferred to the waves by amplifying them further. Travelling wave tubes and klystrons widely dominated the microwave tube industry in the 1950s and 1960s. A variety of these conventional microwave tubes and their variants were successfully developed and employed in systems during this period. In later years, solid state devices started to show great promise both in size and cost. They offer a variety of cost-effective devices for a wide range of microwave applications. But the main problem remains for this otherwise very useful technology. They cannot offer higher powers at frequencies above a certain limit for use in some of the applications mentioned earlier [1, 2].

The search moved slowly towards higher frequencies with the successful use of microwaves for plasma, spectroscopy, medical, industrial heating and other applications. Conventional microwave tubes, although promising for delivering a few hundreds of kilowatts of CW power at frequencies below 1 GHz showed little sign of hope to work at frequencies above this while giving higher
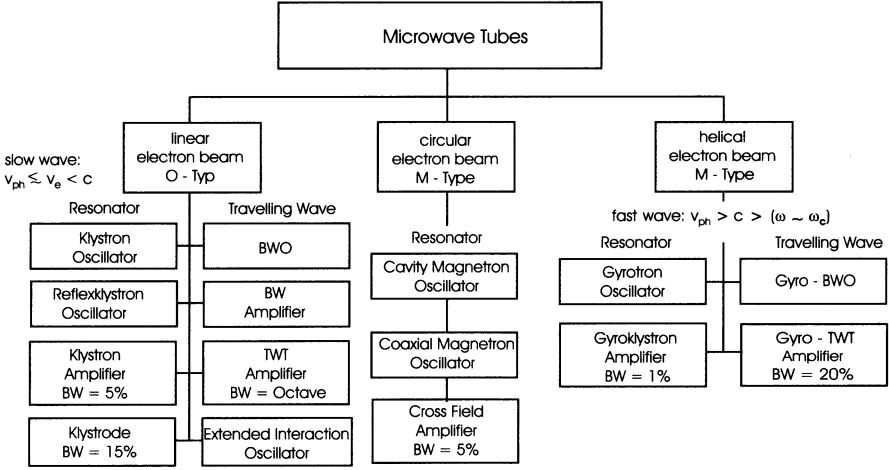
Fig. 1.2. General classification chart of microwave tubes

powers. The inherent limitation with these conventional microwave tubes is the tremendous decrease in the dimensions of the interaction structure with increasing frequency (that is decreasing wavelength, see Fig. 1.1). Therefore, the possibility of extracting higher power to as needed for ECRH type applications from conventional microwave tubes has been ruled out. This required newer ideas in the development of novel devices by suitably exploring and exploiting the first principles of physics. The sixties and seventies of the last century saw the field of superconductivity making great strides both in terms of materials and technology. Superconducting magnets capable of providing a few tens of Teslas of magnetic field have been built for various scientific applications. These new circumstances, requirements, and efforts of the earlier researchers on basics gave birth to a new fast wave device, *the gyrotron* in the mid sixties; the possibility of such a device was conceived in the late fifties. A general classification of the different types of microwave tubes is given in Fig. 1.2. Some of these will be discussed in more detail in the next chapter.

1.2 Outline and Scope

As has already been mentioned, the first cavity based linear and crossed–field microwave sources of the 1930s have come a long way in the production of very high powers, both pulsed and CW. Crossed–field amplifiers were also developed successfully in the 1960s. In addition, tremendous technological changes and advancements took place in the production of relativistic electron beams and in the field of modulators and pulsed power technology. Experimental tokamaks and stellarators started functioning for plasma researchers, and experimental fusion reactors were discussed and planned; these require very

high powers in various regions of the microwave spectrum. The concepts of
the generation of microwaves by making use of electron cyclotron resonance
maser instabilities explored in the late 1950's led to the development of the
earliest version of the gyrotron in Russia in the mid sixties [3]. From then
on, the gyrotron technology has gained momentum and matured to today's
version of the device which could meet the requirements of specific users.
The following Table 1.1 shows the major events leading to the development
of modern gyrotrons.

Table 1.1. The major events leading to the development of today's gyrotrons [1, 2]

Year	Event
1870	Theoretical Maxwell's equations
1876	Telephone by Alexander Graham Bell
1887	Experimental demonstration of Maxwell's equations by H. Hertz
1897	Discovery of the electron by J.J. Thomson
1901	Transatlantic wireless transmission
1904	First rudimentary radar by C. Hülsmeyer
1906	Triode type electron tube by L. de Forest
1909	G. Marconi and K.F. Braun share the physics Nobel Prize for contributions to the physics of electric oscillations and radio-telegraphy
1911	Discovery of superconductivity by H. Kammerling Onnes
1920	First transit time microwave tube (retarding field tube) by H. Barkhausen
1921	Magnetron by A.W. Hull
1935	First publication on the theory of linear beam microwave tubes by Oskar and Agnesa Heil
1937	Klystron by Varian brothers
1943	Traveling wave tube by R. Kompfner
1950	Note on microwave generation by using the rotational energy of helical electron beam by H. Kleinwächter
1954	Discovery of maser by Gordon
1958, 1959	Theoretical investigations on the generation of microwaves by ECM interaction by R. Twiss, J. Schneider, and A. Gaponov
1965	Earliest version of gyrotrons developed in Russia
1980s	Plans and proposals on JET and ITER
1990s to present	Successful development of modern gyrotron technology at IAP (Nizhny Novgorod), Russia, FZK (Karlsruhe), Germany, JAERI (Naka), Japan, CPI (formerly Varian, Palo Alto), USA, and elsewhere in the world
2002	European 140 GHz gyrotron produces 0.9, 0.55, 0.26 MW for 180, 940, 1300 s respectively (FZK, CRPP, CEA, TED)

The basic objective of this book is to provide a detailed monograph on the theory and design of gyrotrons (mainly of conventional type), that provides a ready reference for practicing researchers, scientists and engineers in microwave technology. In Chap. 2, a brief review of gyro-devices is given. Chapters 3 and 4 cover the theory of gyrotrons. The basic principle of gyrotrons, physical model for the high frequency behaviour of tapered open resonators, equation of motion and self-consistent calculations, and mode competition are presented. In addition to the conventional hollow cavity structures, coaxial and complex cavity resonators are also treated and various versions of dimensionless variables are discussed. Chapter 5 provides practical considerations for gyrotron design, keeping in mind the design constraints, including technological and physical limitations. Estimation of wall losses, voltage depression, and limiting current is given. The choice of beam radius and the Fresnel parameter are discussed. Based on linearized theory, the starting current is derived; this is useful for understanding the sequential startup of the various possibly competing modes in the interaction structure. Rieke diagrams for gyrotron oscillators to assess the effect of reflections are also presented. Chapter 6 deals with the design of magnetron injection guns, magnetic guiding system, and beam dump (collecting system). The design of the output taper and quasi-optical launcher is given in Chap. 7. RF windows for gyrotrons are dealt with in Chap. 8. As an example, the design of various specific gyrotrons is described in Chap. 9. Finally, various scientific and technological applications of gyrotrons are presented in chap. 10. An extensive list of references, both early and currently relevant for the latest developments on gyrotrons and other fast wave microwave sources is provided to benefit contemporary researchers and readers.

2 Review of Gyro-Devices

2.1 Introduction

The possible applications of gyrotron oscillators and other cyclotron–resonance maser (CRM) fast wave devices span a wide range of technologies [4–6]. Most work on CRM devices has investigated the conventional gyrotron oscillator (gyromonotron) [7–17] in which the wave vector of the radiation in an open-ended, irregular cylindrical waveguide cavity is transverse to the direction of the applied magnetic field, resulting in radiation near the electron cyclotron frequency or one of its harmonics. Long pulse and CW gyrotron oscillators delivering output powers of 100–960 kW at frequencies between 28 and 170 GHz have been used very successfully in thermonuclear fusion research for plasma ionization and start-up, electron cyclotron resonance heating (ECRH) and local current density profile control by noninductive electron cyclotron current drive (ECCD) at system power levels up to 4 MW.

ECRH has become a well established heating method for both tokamaks [18–23] and stellarators [24–29]. The confining magnetic fields in present day fusion devices are in the range of $B_0 = 1.0–3.6$ Tesla. As fusion machines become larger and operate at higher magnetic fields ($B \cong 5–6$ T) and higher plasma densities in steady state, it is necessary to develop CW gyrotrons that operate at both higher frequencies and higher mm-wave output powers. The requirements of the projected tokamak experiment ITER (International Thermonuclear Experimental Reactor) and of the future new stellarator (W7–X) at the Division of the Max–Planck–Institut für Plasmaphysik in Greifswald are between 10 and 40 MW at frequencies between 140 GHz and 170 GHz [19, 27, 30–33]. This suggests that mm-wave gyrotrons that generate output power of at least 1 MW, CW per unit are required. Since efficient ECRH needs axisymmetric, narrow, pencil-like mm-wave beams with well defined polarization (linear or elliptical), single–mode gyrotron emission is necessary in order to generate a TEM$_{00}$ Gaussian beam mode. Single-mode 110–170 GHz gyromonotrons with conventional cylindrical cavities, capable of 1 MW per tube, CW, and 2 MW coaxial cavity gyrotrons are currently under development. There has been considerable progress towards higher frequency and power but the main issues are still long pulse or CW operation and the appropriate mm-wave vacuum window. The availability of sources with fast frequency tunability would permit the use of a simple, non-steerable mirror

antenna at the plasma torus for local current drive experiments [34, 35]. Frequency tuning has been shown to be possible in quasi-optical Fabry–Perot cavity gyrotrons [36, 37] as well as in cylindrical cavity gyrotrons with step tuning (different operating cavity modes) [38–46].

The state-of-the-art status and future prospects of the development of gyrotron oscillators is annually brought out by Thumm [2] for ECRH as well as for ECR plasma sources for the generation of multi-charged ions and soft X-rays [47, 48], the development of very high frequency gyromonotrons for active plasma diagnostics [49–54], high-frequency step tunable gyrotrons, technological gyrotrons, relativistic gyrotrons and quasi-optical gyrotrons.

Gyrotron oscillators have also been successfully utilized in materials processing (e.g. advanced ceramic sintering, surface hardening or dielectric coating of metals and alloys) as well as in plasma chemistry [4–6, 55–58]. The use of gyrotrons for such technological applications appears to be of interest if one can realize a relatively simple, low cost device which is as easy to use as, for example, a magnetron. Gyrotrons with low magnetic field (operated at the second harmonic of the electron cyclotron frequency), low anode voltage, high efficiency and long lifetime are under development. Mitsubishi in Japan and Gycom in Russia are employing permanent magnet systems [59–63].

The next generation of high energy physics accelerators and the next frontier in understanding of elementary particles is based on the supercollider. For normal conducting linear electron positron colliders that will reach center of mass energies of ($> 1\,\mathrm{TeV}$ it is thought that sources at 17 to 35 GHz with $P_{\mathrm{out}} = 300\,\mathrm{MW}$, $\tau = 0.2\,\mu\mathrm{s}$ and characteristics that will allow approximately 1000 pulses per second will be necessary as drivers [64–66]. These must be phase-coherent devices, which can be either amplifiers or phase locked oscillators. Such generators are also required for super-range high resolution radar and atmospheric sensing [67–70].

2.2 Classification of Fast Wave Microwave Sources

Fast wave devices in which the phase velocity v_{ph} of the electromagnetic wave is greater than the speed of light c, generate or amplify coherent electromagnetic radiation by stimulated emission of bremsstrahlung from a beam of relativistic electrons. The electrons radiate because they undergo oscillations transverse to the direction of beam motion by the action of an external force (field). For such waves the electric field is mainly transverse to the propagation direction.

The condition for coherent radiation is that the contribution from the electrons reinforces the original emitted radiation in the oscillator or the incident electromagnetic wave in the amplifier. This condition is satisfied if a bunching mechanism exists to create electron density variations of a size comparable to the wavelength of the imposed electromagnetic wave. To achieve such a mechanism, a resonance condition must be satisfied between

the periodic motion of the electrons and the electromagnetic wave in the interaction region [16, 71, 72]

$$\omega - k_z v_z \cong s\Omega\,, \quad s = 1, 2 \cdots (k_z v_z = \text{Doppler term})\,. \tag{2.1}$$

Here ω and k_z are the wave angular frequency and characteristic axial wavenumber, respectively, v_z is the translational electron drift velocity, ω is an effective frequency, which is associated with macroscopic oscillatory motion of the electrons, and s is the harmonic number.

In the electron cyclotron maser (ECM), electromagnetic energy is radiated by relativistic electrons gyrating in an external longitudinal magnetic field. In this case, the effective frequency ω corresponds to the relativistic electron cyclotron frequency:

$$\omega_c = \frac{\Omega_0}{\gamma} \quad \text{with} \quad \Omega_0 = \frac{eB_0}{m_e} \quad \text{and} \quad \gamma = \frac{1}{\sqrt{1 - (v/c)^2}}\,, \tag{2.2}$$

where $-e$ and m_e are the charge and rest mass of an electron, γ is the relativistic factor, and B_0 is the magnitude of the guide magnetic field. A group of relativistic electrons gyrating in a strong magnetic field will radiate coherently due to bunching caused by the relativistic mass dependence of their gyration frequency. Bunching is achieved because, as an electron loses energy, its relativistic mass decreases and it thus gyrates faster. The consequence is that the electric field of a small amplitude wave, while extracting energy from the particles, causes them to become bunched in gyration phase and reinforces the existing wave electric field. The strength of the magnetic field determines the radiation frequency.

In the case of a spatially periodic magnetic or electric field (undulator/wiggler), the transverse oscillation frequency Ω_b (bounce frequency) of the moving charges is proportional to the ratio of the electron beam velocity v_z to the wiggler field spatial period λ_w. Thus,

$$\Omega_b = k_w v_z\,, \quad k_w = 2\pi/\lambda_w\,. \tag{2.3}$$

The operating frequency of such devices, an example of which is the free electron maser (FEM) [73–77], is determined by the condition that an electron in its rest frame "observes" both the radiation and the periodic external force at the same frequency. If the electron beam is highly relativistic, $(v_{\text{ph}} \cong v_z \cong c)$ the radiation will have a much shorter wavelength than the external force in the laboratory frame $(\lambda \cong \lambda_w/2\gamma^2$ so that $\omega \cong 2\gamma^2\Omega_b)$. Therefore, FEMs are capable of generating electromagnetic waves of very short wavelength determined by the relativistic Doppler effect. The bunching of the electrons in FEMs is due to the perturbation of the beam electrons by the ponderomotive potential well which is caused by "beating" of the electromagnetic wave with the spatially periodic wiggler field. It is this bunching that enforces the coherence of the emitted radiation.

In the case of ECMs and FEMs, unlike most conventional microwave sources and lasers, the radiation wavelength is not determined by the characteristic size of the interaction region. Such fast-wave devices require no periodically rippled walls or dielectric loading and can instead use a simple hollow-pipe oversized waveguide as a circuit. These devices are capable of producing very high power radiation at cm-, mm-, and submillimeter wavelengths since the use of large waveguide or cavity cross sections reduces wall losses and breakdown restrictions, as well as permitting the passage of larger, higher power electron beams. It also relaxes the constraint that the electron beam in a single cavity can only remain in a favourable RF phase for half of a RF period (as in klystrons and other devices employing transition radiation). In contrast with klystrons, the reference phase for the waves in fast wave devices is the phase of the electron oscillations. Therefore, the departure from the synchronous condition, which is given by the transit angle $\theta = (\omega - k_z v_z - s\Omega)L/v_z$, can now be of order 2π or less, even in cavities or waveguides that are many wavelengths long.

The origin of ECMs traces back to the late 1950s, when three investigators began to examine theoretically the generation of microwaves by the ECM interaction [7, 78]: R. Twiss in Australia [79], J. Schneider of Germany in the US [80] and A. Gaponov in Russia [81]. A short note on the possibility of using the rotational energy of a helical electron beam for microwave generation was published by the German H. Kleinwächter in 1950 [82]. In early experiments with devices of this type, there was some debate about the generation mechanism and the relative roles of fast-wave interactions mainly producing azimuthal electron bunching and slow-wave interactions mainly producing axial bunching [7, 78]. The predominance of the fast wave ECM resonance with its azimuthal bunching in producing microwaves was experimentally verified in the mid-1960s in the US [83] (where the term "electron cyclotron maser" was apparently coined) and in Russia [3].

Many configurations can be used to produce coherent radiation based on the electron cyclotron maser instability. The departure point for designs based on a particular concept is the wave-particle interaction. Dispersion diagrams, also called $\omega - k_z$ plots or Brillouin diagrams [4, 72, 84–86], show the region of cyclotron interaction (maximum gain of the instability) between an electromagnetic mode and a fast electron cyclotron mode (fundamental or harmonic) as an intersection of the waveguide mode dispersion curve (hyperbola):

$$\omega^2 = k_z^2 c^2 + k_\perp^2 c^2 \tag{2.4}$$

with the beam-wave resonance (straight) line given by (2.1). In the case of a device with a cylindrical resonator the perpendicular wavenumber is given by $k_\perp = x_{mn}/R_0$ where x_{mn} is the nth root of the corresponding Bessel function (TM$_{mn}$ modes) or its derivative (TE$_{mn}$ modes) and R_0 is the waveguide radius. Phase velocity synchronism of the two waves is present in the intersection region. The interaction can result in a device that is either an oscillator

or an amplifier. In the following subsections, the different ECM devices are classified according to their dispersion diagrams.

2.2.1 Gyrotron Oscillator and Gyroklystron Amplifier

Gyrotron oscillators were the first ECMs to undergo major development. Increases in device power were the result of Russian developments starting from the early 1970s, of magnetron injection guns, which produce electron beams with the necessary transverse energy (while reducing the spread in transverse energies to acceptable levels) and in tapered, open-ended waveguide cavities that maximize efficiency by tailoring the electric field distribution in the resonator [7–15].

Gyrotron oscillators and gyroklystrons are devices which usually utilize only weakly relativistic electron beams ($E < 100\,\mathrm{keV}$, $\gamma < 1.2$) with high transverse momentum (velocity ratio $\alpha = v_\perp/v_z > 1$) [72]. The wavevector of the radiation in the cavity is transverse to the direction of the external magnetic field ($k_\perp \gg k_z$, and the Doppler shift is small) resulting, according to equations (2.1) and (2.2), in radiation near the electron cyclotron frequency or one of its harmonics:

$$\omega \cong s\omega_c, \quad s = 1, 2, \cdots.$$

(2.5)

In the case of cylindrical cavity tubes (see Figs. 2.1 and 2.2) the operating mode is close to cutoff ($v_{\mathrm{ph}} = \omega/k_z \gg c$) and the frequency mismatch $\omega - s\omega_c$ is small but positive in order to achieve correct phasing, i.e. keeping the electron bunches in the retarding phase [72, 84–86]. The Doppler term $k_z v_z$ is of the order of the gain width and is small compared with the radiation frequency. The dispersion diagrams of fundamental and harmonic gyrotrons are illustrated in Figs. 2.3 and 2.4, respectively. The velocity of light line is determined by $\omega = ck_z$. For given values of γ and R_0, a mode represented by x_{mn} and oscillating at frequency ω is only excited over a narrow range of B_0. By variation of the magnetic field, a sequence of discrete modes can be excited. The frequency scaling is determined by the value of B_0/γ. Modern high power, high order volume mode gyrotron oscillators for fusion plasma applications employ an internal quasi-optical mode converter with lateral microwave output [72] and a single–stage depressed collector (SDC) for energy recovery (see Fig. 2.5). Operation at higher cyclotron harmonics reduces the required magnetic field for a given frequency by the factor s. The predicted efficiencies for gyrotrons operating at higher harmonics ($s = 2$ and 3) are comparable with those operating at the fundamental frequency [7–15, 72, 84–86]. At low voltages, the number of electron orbits required for efficient bunching and deceleration of electrons can be large, which means that the resonant interaction has a narrow bandwidth, and that the RF field may have moderate amplitudes. In contrast with this, at high voltages, electrons should execute only about one orbit. This requires correspondingly strong RF
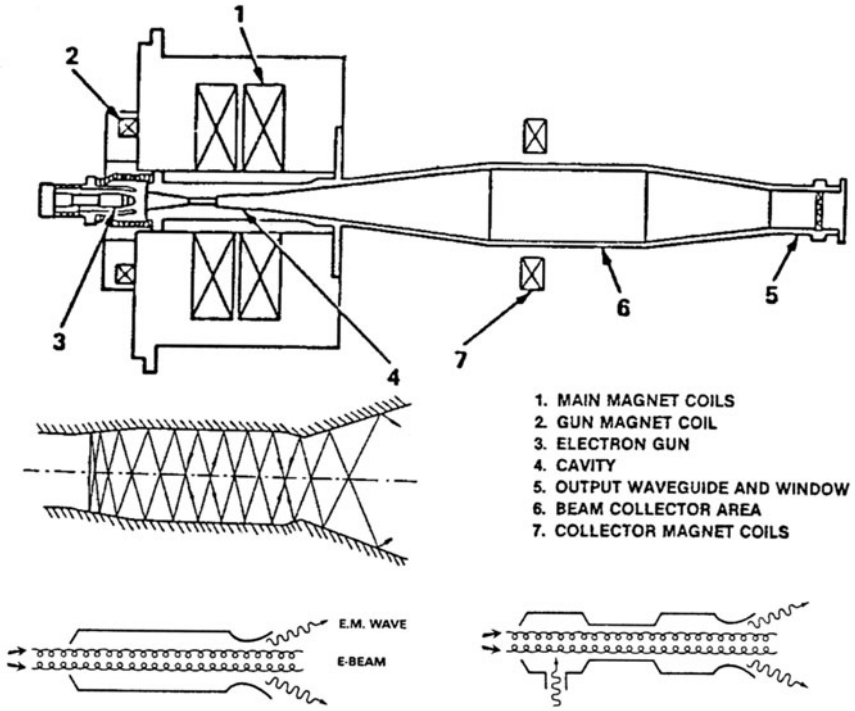
Fig. 2.1. Schematics of a gyrotron oscillator and of the irregular waveguide of a gyromonotron oscillator [12, 17] (left) and gyro-klystron amplifier [84] (right)

fields, possibly leading to RF breakdown, and greatly broadens the cyclotron resonance band, thus making possible an interaction with many parasitic modes.

2.2.2 Cyclotron Autoresonance Maser (CARM)

In a gyrotron with a more relativistic beam ($\geq 1\,\mathrm{MeV}$), an efficient interaction will lead to an average energy loss comparable to the initial electron energy. As a result, the change in the gyrofrequency is much greater than in the weakly relativistic case. It is therefore desirable to identify the condition under which such a highly relativistic electron beam remains synchronous with the RF field. A possibility for achieving synchronism is to utilize the interaction of electrons with electromagnetic waves propagating with a phase velocity close to the speed of light in the direction of the magnetic field. In this case, the Doppler shift term $k_z v_z$ is large, and the appropriate resonance condition is

$$\omega \simeq k_z v_z + s\omega_c. \tag{2.6}$$
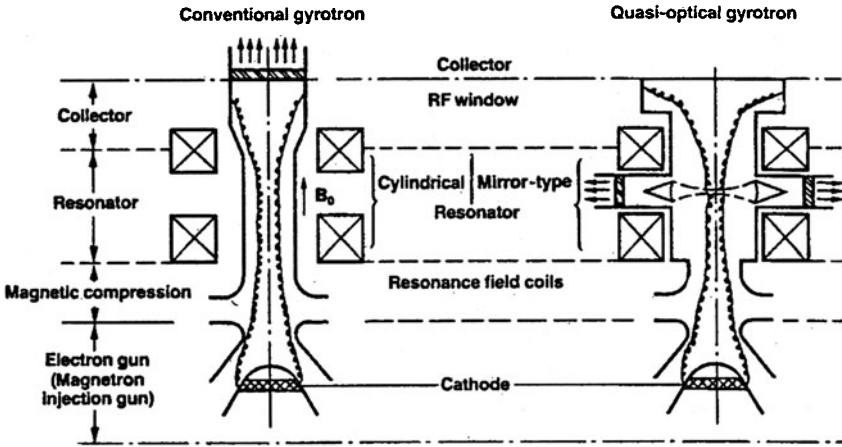
Fig. 2.2. Principle of a conventional gyrotron with cylindrical cavity resonator and of a quasi-optical gyrotron with mirror resonator [36, 37]
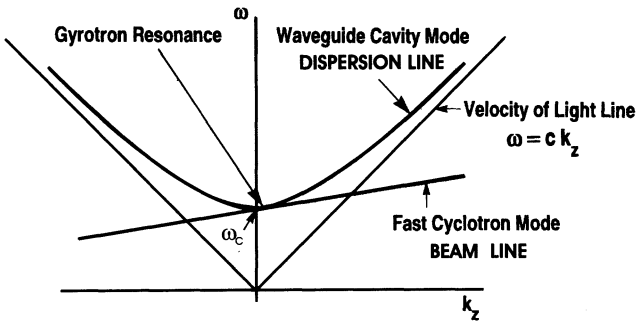
Fig. 2.3. Dispersion diagram of a gyrotron oscillator (fundamental resonance)
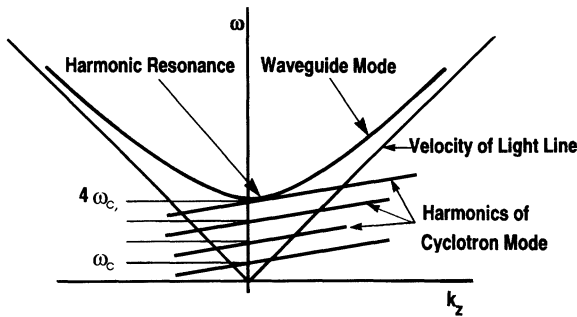
Fig. 2.4. Dispersion diagram of a harmonic frequency gyrotron oscillator

depressed
collector

insulator

rf-window

rf-output
(Gaussian beam)

quasi-optical
converter

resonator

beam tunnel

electron gun

cryostat with
sc-magnet

high voltage
supply

400mm
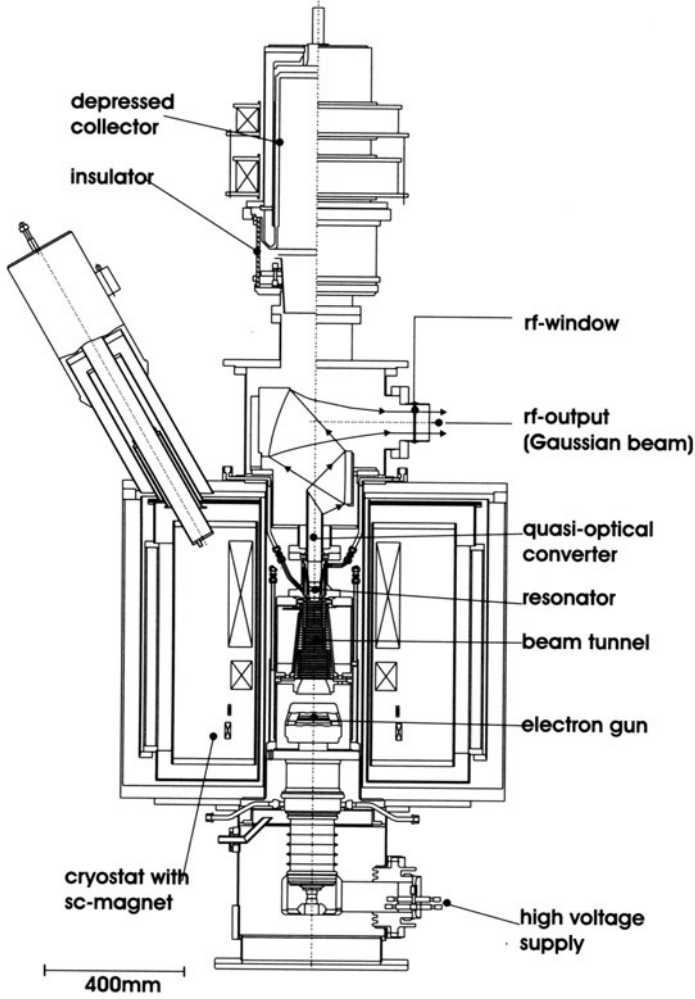
Fig. 2.5. Schematic layout of a modern high order volume mode gyrotron with quasi-optical mode converter and single stage depressed collector [2]

If $v_{\mathrm{ph}} \simeq c$, the increase in cyclotron frequency due to extraction of beam energy (decrease of γ) nearly compensates the decrease in the Doppler shifted term. Therefore, if the resonance condition is initially fulfilled, it will continue to be satisfied during the interaction. This phenomenon is called autoresonance, and the cyclotron maser devices operating in the relativistic Doppler-shifted regime are called cyclotron autoresonance masers or CARMs [16, 71]. Figure 2.6 shows how the Brillouin diagram of the fast cyclotron wave changes during the autoresonance interaction such that the working frequency ω remains constant even though both ω_c and v_z are changing.
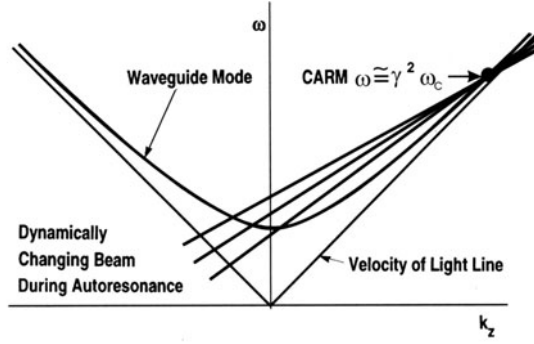
Fig. 2.6. Dispersion diagram of the cyclotron autoresonance maser (CARM)
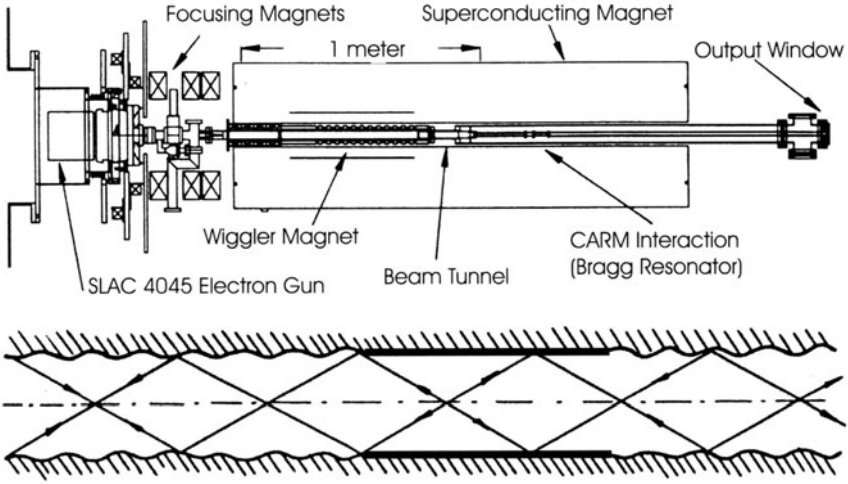
Fig. 2.7. Schematic of a long pulse CARM oscillator [87] with Bragg resonator [71]

The CARM interaction corresponds to the upper intersection and is based on the same instability mechanism as that of the gyrotron but operated far above cutoff. The instability is convective, so feedback, for instance, by a Bragg resonator (see Fig. 2.7) [71] is required for an oscillator and it is necessary to carefully discriminate against other interactions corresponding to the lower frequency intersection in the dispersion diagram Fig. 2.6. The problem can be alleviated by employing the fundamental TE_{11} or (HE_{11} hybrid) mode and properly choosing the system parameters to be within the stability limit. Compared to a gyrotron, there is a large Doppler frequency upshift of the output ($\omega \simeq \gamma^2 \omega_c$) permitting a considerably reduced magnetic field B_0 for a given frequency. Since the axial bunching mechanism can substantially

offset the azimuthal bunching, the total energy of the beam and not only the transverse component is available for RF conversion.

In contrast to a gyrotron, a CARM has an electron beam with low to moderate velocity ratio ($\alpha < 0.7$). The efficiency of a CARM is extremely sensitive to a spread in the parallel beam velocity. The velocity spread $\Delta v_z/v_z$ must be lower than 1% to achieve the full theoretically expected efficiency of 40% [71, 87].

It has been suggested that an ECM operating in the Cherenkov regime ($v_{ph} < c$) may be an attractive alternative high power microwave source. This slow-wave CARM utilizes the coupling between the slow cyclotron wave on the electron beam and the slow electromagnetic waves of the cavity at the anomalous Doppler cyclotron resonance equation (2.6) with $s = -1$ or any other negative integer. Such a slow-wave ECM can be driven by an electron beam with predominantly axial velocity as in conventional Cherenkov devices. Experimental demonstrations were reported in [88–91], in which dielectric loaded and corrugated waveguide slow-wave structures were used. Since the transverse wavenumber of slow waves is imaginary, their fields are localized near the structure wall, and therefore the electron beam should also propagate close to the wall to couple to these waves.

2.2.3 Gyro-TWT (Travelling Wave Tube) and Gyrotwystron Amplifier

From the theoretical point of view, the gyro-TWT differs from the CARM only in the regimes of operation. The gyro-TWT utilizes a moderately relativistic electron beam to interact with a fast waveguide mode near the grazing intersection of the frequency versus wavenumber plot (see Fig. 2.8) where the resonance line is tangent to the electromagnetic mode.

This produces high gain and efficiency because the phase velocities of the two modes are nearly matched and the group velocity of the waveguide mode is nearly equal to v_z. In the gyro-TWT regime ($\omega/k_z \gg c$), the axial bunching mechanism is too weak to be of any significance. To benefit from autoresonance, the cutoff frequency should be reduced relative to the cyclotron frequency. The circuit employed in a gyro-TWT consists simply of an unloaded waveguide. Since no resonant structures are present, the gyro-TWT is potentially capable of much larger bandwidth than a gyroklystron and thus can be used as the output amplifier in mm-wave radar communication systems. Recent devices employ tapered magnetic fields and interaction circuits as well as two stages in order to optimize the beam-wave interaction along the waveguide [92, 93].

The sensitivity to velocity spread can be greatly reduced by coupling between the second harmonic cyclotron mode of a gyrating electron beam and the radiation field in the region of nearly infinite phase velocity over a broad bandwidth by using a cylindrical waveguide with a helical corrugation on its inner surface [94].
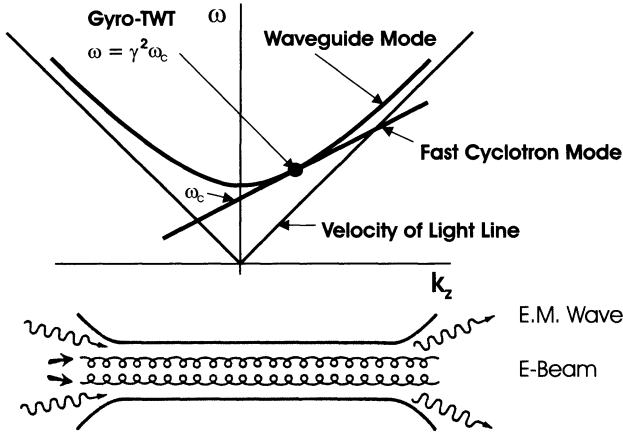
Fig. 2.8. Dispersion diagram and scheme of the interaction circuit of a Gyro-TWT amplifier

The gyrotwystron [7], a hybrid device, is derived from the gyroklystron by extending the length of the drift section and replacing the output cavity with a slightly tapered waveguide section as in a gyro-TWT. The output waveguide section is excited by the beam of electrons that are bunched because of modulation in the input cavity. The gyrotwystron configuration can mitigate the problem of microwave breakdown at high power levels, since the microwave energy density in the output waveguide can be much smaller than in an output cavity. The inverted gyrotwystron is a device consisting of the input waveguide, drift section, and output cavity [95]. The travelling signal wave in the input waveguide may induce a high harmonic content in the electron current density. Then the prebunched electron beam can excite phase-locked oscillations in the cavity at a harmonic of the signal frequency.

2.2.4 Gyro-BWO (Backward Wave Oscillator)

If the electron beam and/or magnetic field is adjusted so that the straight fast wave beam line crosses the negative k_z-branch of the waveguide mode hyperbola (see Fig. 2.9) then an absolute instability (internal feedback) with a "backward wave" occurs.

In the gyro-BWO the frequency of operation is now governed by the slope of the line, which is a function of v_z, and thus of the beam acceleration voltage U_{beam}. Consequently, just as in the case of conventional BWOs (e.g. carcinotron), the frequency of oscillation can be continuously changed very fast over a broad range, using U_{beam} in place of B_0. However, there is a Doppler down shift in frequency ($\omega_c/2 < \omega < \omega_c$), so that very high magnetic fields are required for high frequency operation.
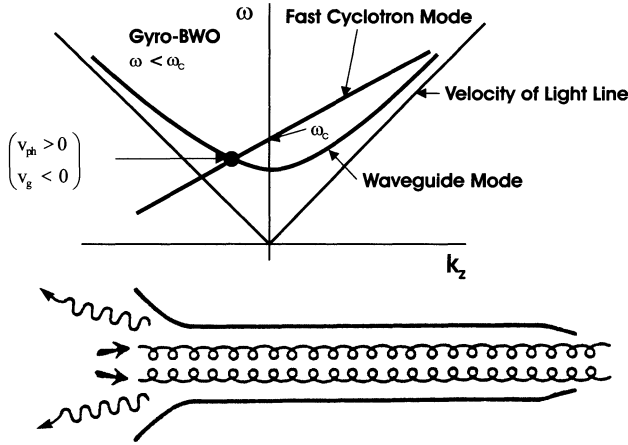
Fig. 2.9. Dispersion diagram and scheme of interaction circuit of Gyro-BWO

2.2.5 Overview of Gyro-Devices

The bunching of electrons in the gyrotron oscillator discussed in Sect. 2.2.1 has much in common with that in conventional linear electron beam devices, namely, monotron, klystron, TWT, BWO and twystron [7]. In both cases the primary energy modulation of the electrons gives rise to bunching (azimuthal or longitudinal) which is inertial. The bunching continues even after the primary modulation field is switched off (at the drift section of a klystron-type devices). This analogy suggests a correspondence between linear-beam (O–type) devices and various types of gyro-devices. Figure 2.10 presents schematic drawings of devices of both classes and the orbital efficiencies calculated using a simplified uniform approximation for the longitudinal structure of the RF field in the gyromonotron $(s = 1)$ [7]. For the gyroklystron, the calculation was made in the narrow-gap approximation of the RF field in the input and output cavities. The electrodynamic systems of the gyro-TWT and gyro-BWO, as well as the output section of the gyrotwystron, were assumed to have the form of a uniform waveguide. In all these cases the magnetic field is assumed to be homogeneous.

In addition, relativistic gyrotrons, large-orbit harmonic and pulsed gyrotrons, peniotrons, and gyro-peniotrons are source types similar to, but also quite different in one way or another from, the ECMs. The large orbit gyrotron employs an axis-encircling electron beam in which the trajectory of each electron takes it around the axis of the cylindrical interaction region. Peniotrons and gyropeniotrons are driven by an interaction that is phased quite differently from the ECM interaction; in practice, the peniotron and ECM mechanisms compete [72, 84–86, 96].
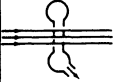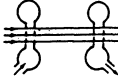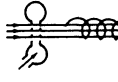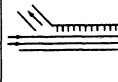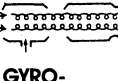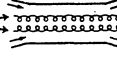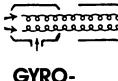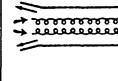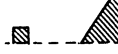
"0" TYP DEVICES					
	MONOTRON	KLYSTRON	TWT	TWYSTRON	BWO
TYPE OF GYROTRON					
	GYRO-MONOTRON	GYRO-KLYSTRON	GYRO-TWT	GYRO-TWYSTRON	GYRO BWO
MODEL RF-FIELD STRUCTURE					
ORBITAL EFFICIENCY	0.42	0.34	0.7	0.6	0.2

Fig. 2.10. Overview of gyro-devices and comparison with their conventional counterparts [7]

2.2.6 Magnicons and Gyroharmonic Converters

The magnicon is a member of the class of scanning–beam amplifier tubes [14, 97]. It is a magnetized device that uses a fast-wave output cavity. Therefore, it can also be grouped with gyro-devices in which electrons gyrating in an external magnetic field emit bremsstrahlung radiation near the cyclotron resonance. In the earliest version of the magnicon, an electron beam is deflected in the unmagnetized input cavity, using a rotating TM_{110} mode and after passing through an also unmagnetized drift space, the deflected beam is spun up to high transverse momentum by entry into a strong magnetic field at the entrance of the output cavity.

As a result of the phase-synchronous transverse deflection of the electron beam as a whole, the beam electrons entering the output cavity execute Larmor motion whose entry point and guiding center rotate in space around the cavity axis at the drive frequency. In the output cavity, the beam is used to drive a cyclotron-resonant fast-wave interaction with a synchronously rotating TM_{110} mode that extracts mainly the transverse beam energy. This interaction can be highly efficient, because the magnicon beam is fully bunched in space and in gyrophase, so that the phase bunching produced by the cyclotron maser instability is not required. With all the electrons decelerated identically, very high efficiencies can be achieved.

Recently, higher perveance versions of the magnicon have been developed [97], in which a fully magnetized electron beam is spun up to a high transverse

momentum in a sequence of deflection cavities containing synchronously rotating TM_{110} modes, the first driven by an external RF source (see Fig. 2.11). In addition, the output cavity can operate in the mth harmonic of the drive frequency by using TM_{m10} modes with $m > 1$, permitting extension of magnicon operation to higher operating frequencies. Again the point of injection of the beam into the output cavity, as well as the entry gyrophase, rotate synchronously with a rotating RF mode of the output cavity. This makes possible much higher efficiencies than in most other gyro-devices. The key to the efficiency of these new magnicon designs is to spin the beam up to high transverse momentum ($\alpha > 1$) without producing large spreads in energy and gyrophase, so that the output cavity interaction will remain coherent over the entire ensemble of electrons, and not just synchronous in time. This requires great care in the design of the deflection cavities, in particular of the penultimate deflection cavity that produces more than half of the beam spin up. Since these spreads are generated by the fringing fields of the beam tunnel apertures in the deflection cavities and the output cavity, it also requires the use of a very small initial beam radius.

A similar "scanning–beam" device is the gyroharmonic converter in which so-called "co-generation" arises from a near match in group and phase velocities between the input cavity TE_{11} mode at frequency ω and the TE_{72} mode at frequency 7ω in a cylindrical waveguide [98]. This match allows efficient power transfer into the 7th harmonic from a fundamental frequency wave that energizes an electron beam via cyclotron autoresonance acceleration (CARA). Theory indicates that high conversion efficiency can be obtained for a high quality beam injected into CARA, provided that mode competition can be controlled. Generation of 0.5 MW power (3 μs pulse duration, 5% efficiency) at 8.57 GHz (third harmonic of 2.856 GHz) in the TE_{31} mode has been observed in experiments using a 350 kV, 30 A electron beam [98, 99].

2.2.7 Free Electron Lasers

Free electron lasers (FELs) differ from the other high-power microwave sources considered in this report in that they have demonstrated output over a range of frequencies extending far beyond the microwave spectrum, well into the visible and ultraviolet range [73–77, 84, 85]. To achieve this spectral versatility, FELs exploit relativistic beam technology to upshift the electron "wiggle" frequency by an amount roughly proportional to γ^2 (see Fig. 2.12). In this respect, perhaps a more descriptive name is that coined by R.M. Phillips [100]: UBITRON, for an "undulated beam interaction electron" tube. A magnetostatic wiggler is the most common, but not the only means, for providing electron undulation. An electrostatic wiggler or the oscillatory field of a strong electromagnetic wave can also play this role. Devices with such electromagnetic wigglers are sometimes called scattrons [7, 16, 71]. The distinction between long wavelength free electron masers (FEM) ($\lambda \geq 0.5$ mm)
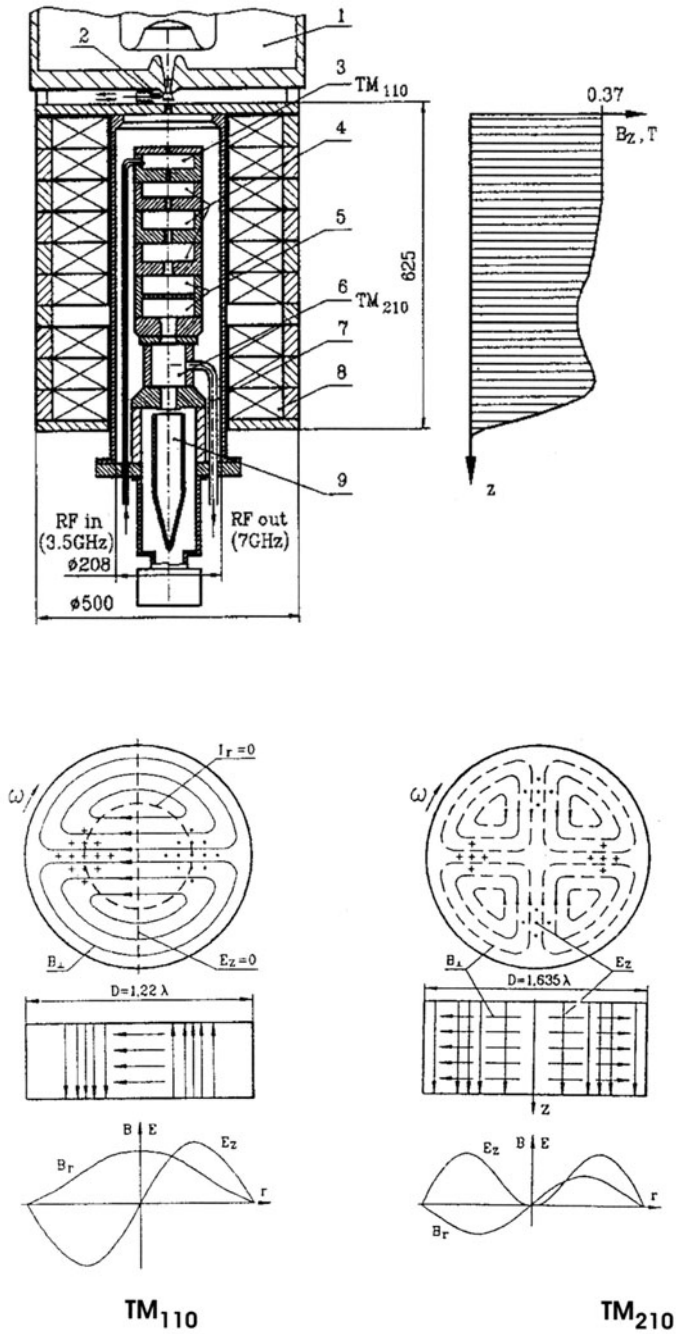
Fig. 2.11. Schematic layout of a Magnicon [97]
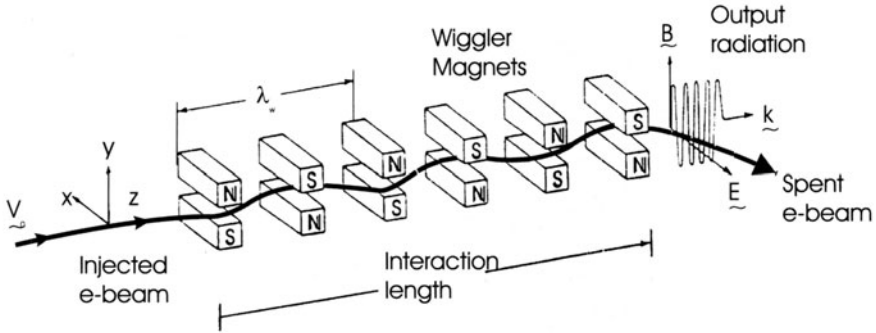
Fig. 2.12. The basic FEM configuration in which the electron beam undulates in the periodic magnetic field of the wiggler [2]

and short wavelength FELs is natural because higher current and lower energy beams are typically employed for long wavelength devices and space-charge effects are more important. In particular, the dominant interaction mechanism is often coherent Raman scattering. Also, while short wavelength FELs excite optical modes, dispersion due to the beam dielectric effects and finite transverse dimensions in the drift tubes and cavities are important at longer wavelengths. A low power (3 W, 2 ms pulses) FEL operating at radio frequencies (FER) employing a 420 V, 0.2 A electron beam holds the world record for long wavelength ($f = 266\,\mathrm{MHz}$, $\lambda = 1.1\,\mathrm{m}$, $\lambda_w = 0.04\,\mathrm{m}$, $B_w = 0.04\,\mathrm{T}$) [101].

The FEM appears to be potentially capable of fulfilling all the requirements for a frequency tunable high-power mm-wave source. Coverage of the entire frequency range of 130–260 GHz presents no severe problems, and even higher frequencies are feasible [102–111]. Rapid tunability over more than $\pm 5\%$ can be obtained by variation of the beam energy. The interaction occurs in a cavity operating in low-order modes, which have very good coupling to a Gaussian beam output. The relatively low RF wall loading and the use of high electron beam energy ($> 0.5\,\mathrm{MeV}$) and a multi–stage depressed collector are compatible with a high unit power at efficiencies around 50% if the electron beam interception can be maintained at an acceptable level. The highest CW power generated by an FEM is 36 W (15 GHz) [112] whereas the IR (3.1 μm)-FEL at the Thomas Jefferson National Accelerator Facility obtained a record average power of 2.13 kW at 3.5% efficiency [113].

Table 2.1 gives a comparison of the main performance parameters and features of gyrotron oscillators and FEMs for ECRH of plasmas in nuclear fusion research. The important advantage of the FEM is its continuous frequency tunability and the possibility of high unit power, but the gyromonotron is a much simpler device. Up to now, the cylindrical cavity gyrotron is the only millimeter wave source which has had an extensive *on-the-field* experience

Table 2.1. Comparison of parameters and features of gyrotron oscillators and FEMs for ECRH [2]

	Gyrotron Oscillator (Cyclotron Res. Maser, – Axial Magnetic Field)	Free Electron Maser Oscillator – Periodic Transverse Magnetic Field
Beam voltage	low (70–95 kV)	high (0.2–2 MV)
Magnetic field (140 GHz)	high (5.5, 1 st harmonic)	low (0.2 T, wiggler)
Frequencies	8–650 GHz	270 MHz – visible
Frequency tunability	$\Delta U_{\mathrm{beam}} + \Delta U_{\mathrm{mod}}$: fast step tuning (5%) ΔB: slow step tuning (35%)	ΔU_{beam} : fast continuous tuning (10%) slow mechanical tuning (50%)
Electron beam	magnetron injection gun	Pierce elctron gun, acceleration and deceleration tubes, beam optics
Ohmic losses in cavity	cutoff cavity 2 kW/cm^2	oversized circuit far away from cutoff
Power density in cavity	high	low
Longitudinal mode competition in cavity	single mode operation	nonlinear temporal dynamics can result in a broad frequency spectrum
Linearly polarized output mode	generated by internal quai-optical mode converter	linearly polarized,low–order resonator mode
Number of internal quasi-optical mirrors	2–4 at ground potential 0.9% ohmic losses	15–25 phase coherence required mostly on 2 MW potential 6% ohmic losses
Absorbed power on first mirror (1 MW, 140 GHz)	3 kW	12 kW
Internal microwave diagnostics	not required	required
Output power (140 GHz) present status	high average power 1 MW/12 s 0.9 MW/180 s (coax. 2.2 MW/17 ms)	2 GW/20 ns very low duty cycle (LLNL amplifier)
Exp. system efficiency without energy recovery	high 35%	low 5–10%
Collector loading	relatively low	high
Theor. system efficiency with depressed collector	60% (exp. 50%)	60%
Physical size	3 m × 3 m × 3 m	12 m × 3 m × 3 m
Power per unit (at 140 GHz)	1 MW (coax. 4 MW)	5 MW

during fusion plasma heating experiments over a wide range of frequencies and power levels (8–170 GHz, 0.1–1.0 MW).

2.3 Remarks

Gyrotron oscillators (gyromonotrons) are mainly used as high power millimeter wave sources for electron cyclotron resonance heating (ECRH), electron cyclotron current drive (ECCD), stability control and diagnostics of magnetically confined plasmas for generation of energy by controlled thermonuclear fusion. The maximum pulse length of commercially available 1 MW gyrotrons employing synthetic diamond output windows is 5 s at 110 GHz (CPI and JAERI–TOSHIBA), 12 s at 140 GHz (FZK–CRPP–CEA–TED) and 9 s at 170 GHz (JAERI–TOSHIBA), with efficiencies slightly above 30%. Total efficiencies of 45–50% have been obtained using single-stage depressed collectors (for energy recovery). The energy world record of 160 MJ (0.89 MW at 180 s pulse length and 140 GHz) at power levels higher than 0.8 MW has been achieved by the European FZK–CRPP–CEA–TED collaboration at FZK where the pulse length restriction to 180 s is due to the high voltage (HV) power supply at $I_b = 40$ A. At lower beam current ($I_b = 26$ A) it was even possible to obtain 506 MJ (0.54 MW for 937 s). The longest shot lasted for 1300 s at 0.26 MW output power. These very long pulses were limited by a pressure increase in the tube. A maximum output power of 1.2 MW in 4.1 s pulses was generated with the JAERI–TOSHIBA 110 GHz gyrotron. The Russian and the Japan 170 GHz ITER gyrotrons achieved 0.5 MW at 80 s pulse duration and 0.3 MW at 60 s, respectively. Diagnostic gyrotrons deliver $P_{out} = 40$ kW with $\tau = 40$ µs at frequencies up to 650 GHz ($\eta \geq 4\%$). Gyrotron oscillators have also been successfully used in materials processing. Such technological applications require gyrotrons with the following parameters: $f \geq 24$ GHz, $P_{out} = 10$–50 kW, CW, $\eta > 30\%$. The highest CW powers produced by gyrotron oscillators, gyroklystrons and FEMs are, respectively, 340 kW (28 GHz), 10 kW (94 GHz) and 36 W (15 GHz). The IR (3.1 µs) FEL at the Thomas Jefferson National Accelerator Facility obtained a record average power of 2.13 kW with an efficiency of 3.5% (with energy recovery).

This chapter gives a brief review of the gyrotron oscillators and their invariants related to the development of high power microwave sources with adequate references. An extensive collection of references on the recent developmental status of fast- and slow-wave cyclotron autoresonance masers (CARM), gyroklystrons, gyrotron travelling wave tube amplifiers (Gyro-TWT), gyrotwystrons, gyropeniotrons, and magnicons for such purposes as well as of free electron masers (FEM) and broadband gyrotron backward wave oscillators (Gyro-BWO) for use as drivers for FEM amplifiers is given in [2].

3 Basic Principles and Gyrotron Cavities

3.1 Basic Principle of Gyrotrons

The gyrotron is a microwave power tube that emits coherent radiation at approximately the electron cyclotron frequency or its harmonics. Typical conventional gyrotron oscillators are built as shown schematically in Fig. 3.1. A gyrotron oscillator can be described as follows: the magnetron injection gun produces an annular electron beam with the desired beam parameters. The beam is transported to the interaction region, where the interaction cavity converts a fraction of the beam power to RF power. In case of axial output coupling, the spent beam will be collected on the uniform output waveguide section after the uptaper and the RF power in the TE_{mn} mode is coupled through the axial output vacuum window.

In the case of radial output coupling, a quasi-optical mode converter is connected to the output waveguide and it transforms the rotating TE_{mn} mode with axial power flow to a Gaussian mode with a radial power flow. The power is then transmitted through a radially located vacuum window and the spent beam is dissipated on the collector. A strong externally applied magnetic field supports the cyclotron motion of the electrons in the beam. The magnetic field in the interaction region is chosen such that the cyclotron frequency or one of its harmonics is close to the frequency of the RF field in the beam frame of reference. The interaction region consists of an open ended waveguide cavity, usually with a circular transverse cross-section. The transverse components of the RF fields in this region interact with the electrons in the annular beam and convert a large part of the orbital kinetic energy into the RF output. The electrons in the beam must therefore have a substantial transverse velocity $v_\perp$ as well as the usual longitudinal velocity v_z. Most of this transverse velocity comes as a result of the adiabatic compression resulting from the increasing magnetic field leading to the interaction region. The final ratio of transverse to longitudinal velocity $\alpha = v_\perp/v_z$ in the interaction region is typically between 1 and 2 for gyrotrons that use magnetron injection guns with thermionic cathodes. The electrons follow helical paths around the lines of force of the external field. In order for a net flow of energy from the transverse electron motion to the electromagnetic wave to take place, the electrons must become bunched in phase within their cyclotron orbits. Such bunching can occur due to the fact that the electron
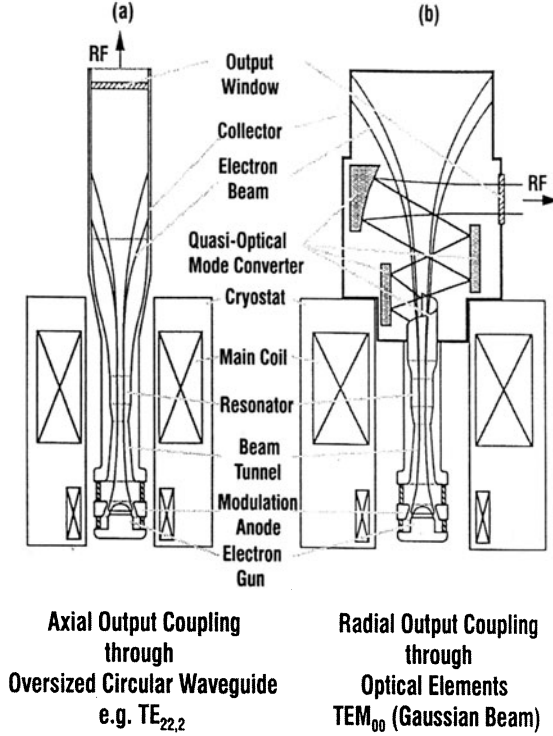
Fig. 3.1. Schematic of gyrotron with solenoids, magnetron injection gun, interaction cavity, output waveguide and RF window. Here (**a**) is with axial output collection and (**b**) is with radial output coupling [256]

cyclotron frequency

$$\omega_c = \frac{eB_0}{m_e\gamma} = \frac{\Omega_0}{\gamma} \tag{3.1}$$

is a function of electron energy. Here $-e$ and m_e are the charge and rest mass of the electron, B_0 is the magnetic field in the resonator and $\gamma = E/m_e c^2$ is the usual relativistic factor. E is the total energy of the electron.

   The phase bunching process can be most easily understood in a reference frame in which the axial velocity vanishes. In Fig. 3.2 an annular electron beam with radius R_e is depicted in this frame. The electrons arranged around this annulus execute circular orbits with radius $r_L = v_\perp \gamma/\Omega_0$. Typically $r_L \ll R_e$. Initially the phase of the electrons in their cyclotron orbits is random as shown in Fig. 3.2.

   In the presence of a transverse RF electric field characteristic of a microwave cavity TE_{mn} mode, the electrons will be accelerated or decelerated. As a specific example, Fig. 3.2 depicts an electric field with only an azimuthal component, as is characteristic of TE_{0n} modes in circular waveguide. With
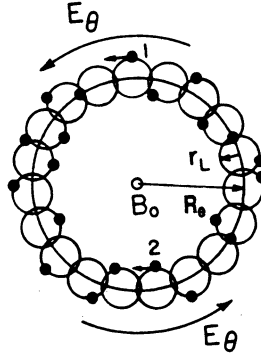
Fig. 3.2. Annular electron beam with initial random phasing of electrons in their cyclotron orbits
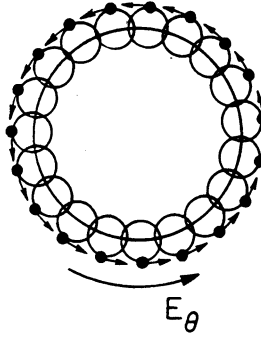
Fig. 3.3. Annular electron beam with electrons bunched in phase in their cyclotron orbits

random phasing, there is no net energy exchange. Electron 1 will be decelerated by the azimuthal electric field and thus lose energy, while electron 2 will be accelerated and hence gain an equal amount of energy.

Phase bunching and net energy transfer can occur if the wave frequency is slightly larger than the initial value of the cyclotron frequency; that is if

$$\omega' - \frac{eB_0}{m_e\gamma_0'} = (\delta\omega)' > 0 \qquad (3.2)$$

where the subscript 0 denotes the initial value and the prime denotes the reference frame in which the electron axial velocity vanishes. Then, as electron 2 gains energy, its cyclotron frequency decreases; this electron falls farther from resonance, gaining less energy on each successive cycle. On the other hand, electron 1, which initially loses energy, experiences an increasing value of ω_c' and moves closer to exact resonance with the electric field, thereby
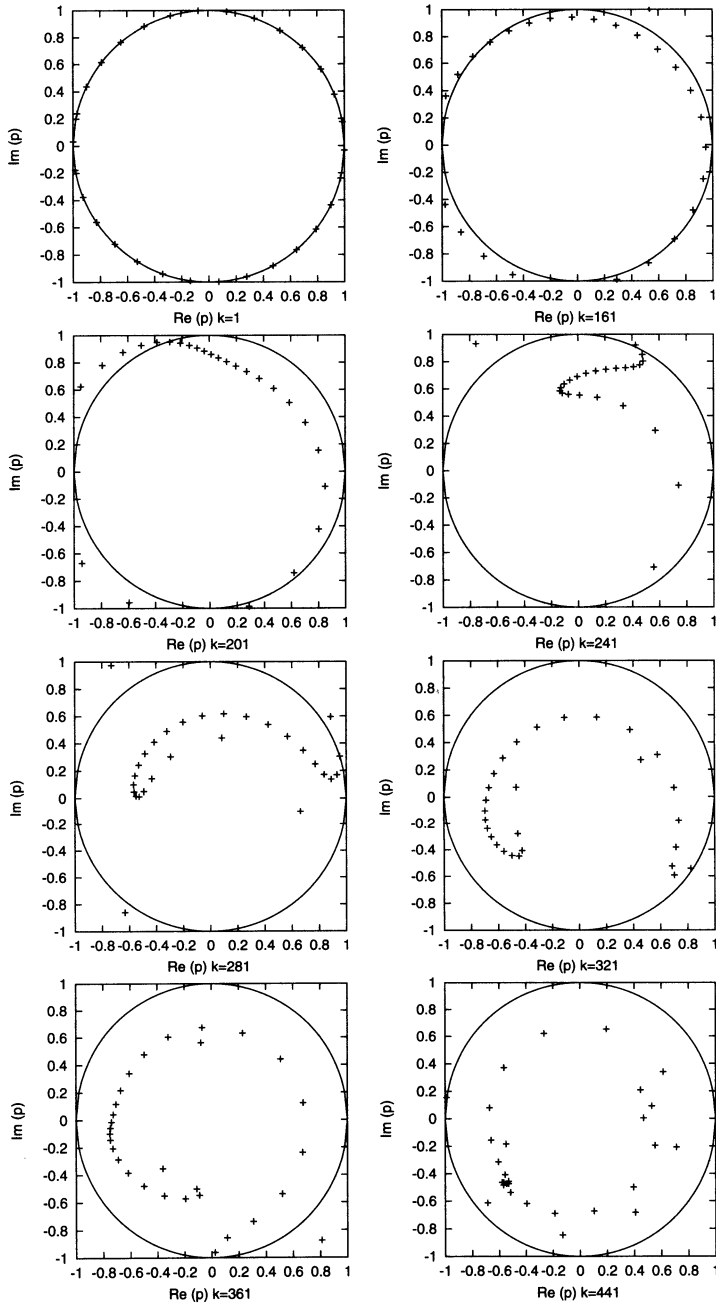
Fig. 3.4. Phase bunching for the $TE_{22,8}$ mode with beam energy $75.7\,keV$, beam current $I_b = 39.5\,A$, magnetic field $B = 5.56\,T$, beam radius $8.1\,mm$, and average velocity ratio $\alpha = 1.35$. Output power $= 900\,kW$. The index k denotes the distance along the resonator ($z = 0.1*k\,mm$)

losing an increasing amount of energy on each successive cycle. An insta-
bility develops in which the wave energy grows in time and the electrons
bunch in phase within their cyclotron orbits as shown in Fig. 3.3. A more
complete example of the azimuthal bunching of the electrons in the phase
space for a $TE_{22,8}$ mode gyrotron at 140 GHz is shown in Fig. 3.4. From this
figure it is quite clear that the randomly distributed electrons in frame 1 are
bunched azimuthally in frame 8 as they drift along the interaction region.
Once the electrons are bunched, they may give up energy to an electric field
which reverses its direction in each half cycle of the cyclotron frequency in
synchronism with the Larmor gyration of the electrons. This makes possible
amplification of an electromagnetic wave at the electron cyclotron frequency.
Other energy transfer mechanisms also play a role, as has been pointed out
by Lindsay et al. [114], and actual gyrotron performance is governed by a
subtle interplay of these factors. Briefly, these are:

- RF phase shift bunching due to the relativistic variation of the electron
  mass.
- Axial bunching due to the relativistic variation of the electron mass (if
  the RF magnetic field can be ignored and the external magnetic field
  is uniform, then γv_z and not v_z is constant. This shifts the gyrophase
  relative to a circularly polarized RF field).
- Antibunching counteracting both of these, due to the RF magnetic field.
  The effects are proportional to $1 - c^2 k_z{}^2/\omega^2$ and are thus small for TE
  modes near cutoff ($k_z \simeq 0$), as is usual for a gyrotron oscillator. They will
  be important in other devices, such as CARMs (cyclotron autoresonance
  masers), for which $k_z \neq 0$.

In terms of quantum theory, an electron in a magnetic field has a dis-
crete energy spectrum for motion transverse to the magnetic field. According
to Akhiezer and Berestetskii [115], the energy levels (Landau levels) of an
electron in a homogeneous magnetic field are given by

$$\frac{E_n{}^2}{c^2} = m_e{}^2 c^2 + p_z{}^2 + e\hbar B_0(n - \mu + 1/2) \quad \text{with} \quad \mu = \pm 1 \,. \qquad (3.3)$$

The energy levels are unequally spaced, with $E_n - E_{n-1} > E_{n+1} - E_n$,
and thus stimulated emission and absorption occur at slightly different fre-
quencies. The condition $\omega' > \Omega\gamma'$ defines tuning the frequency of the RF
field to correspond to stimulated emission of the transition $n \to n - 1$. It
has been pointed out by Flyagin et al. [7] that the bandwidth determined
by the lifetime in a classical system is considerably larger than the frequency
difference between the transitions $n \to n+1$ and $n \to n-1$, and this classical
broadening completely dominates the interaction.

Two points should be mentioned briefly. Only the transverse energy of
electron motion can be transferred to the RF field. This limits the efficiency.
If we define $\alpha = v_\perp/v_z$, then the maximum efficiency which can be attained is

TE$_{0,3}$ TE$_{15,2}$ TE$_{10,4}$
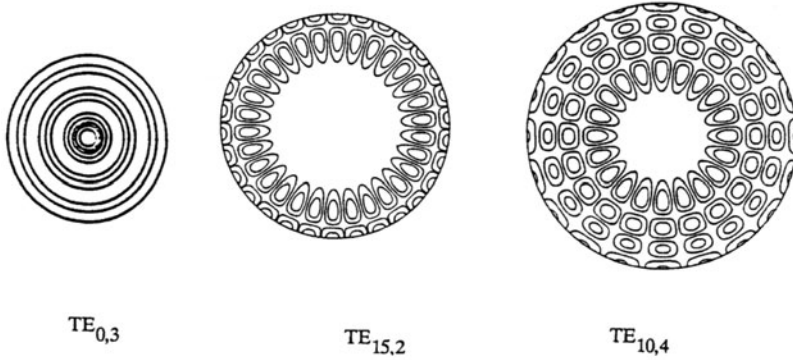
Fig. 3.5. Common classes of cavity modes used in gyrotrons. Contours of the axial component of the Poynting vector are shown

$$\eta_{max} \simeq \frac{\alpha^2}{1 + \alpha^2} \, . \tag{3.4}$$

It is thus desirable to work with a beam having as high a transverse energy as possible, consistent with limitations arising from reduced beam quality at higher values of α. Also from the preceding, it is clear that $\omega > \omega_c$ is desired, and that it is also desirable to have the electrons give up their energy near the end of the interaction region. Otherwise, they may regain some of their energy from the RF field again. This is known as *over bunching.*

In a microwave cavity, the operating frequency is determined by both the resonant frequency of the cavity mode and by the electron cyclotron frequency. Thus, the gyrotron can operate with improved stability in a higher order cavity mode as compared with other microwave tubes. Therefore, gyrotron cavities are relatively large for a given operating frequency and they can handle high power. A disadvantage of working with a large cavity is that the spectral density of cavity eigenmodes becomes large (the cavity is said to be *overmoded*) and mode competition can become a severe problem. This is discussed in Sect. 4.4.

The electric field patterns for three major mode classes that have been used in gyrotrons are sketched in Fig. 3.5. The TE$_{0n}$ modes with purely azimuthal electric fields have been employed in many gyrotrons [116–120]. However, gyrotrons designed to operate in simple azimuthally symmetric modes (or *axisymmetric modes* – TE$_{0n}$) suffered from mode competition especially with TE$_{2n}$ modes when $n \geq 3$ [117–119]. The *whispering gallery* TE$_{mn}$ modes with $m \gg n$ and $n = 1, 2$ have higher wall losses than the TE$_{0n}$ modes, but suffer less from mode competition, provided the beam radius R_e is suitably chosen (typically on the first radial maximum of the transverse field). But for high power operation (long pulse to CW gyrotrons), one should have the wall losses less than a technically feasible limit ($< 2\,\text{kW/cm}^2$) and the whispering gallery modes can pose problems in terms of wall losses. Therefore, as

a trade-off between these two type of modes, a third type of mode, known as *asymmetric volume modes*, with $m \gg 1$ and $p > 2$ are frequently used in present day gyrotrons. They suffer less from high wall losses than whispering gallery modes and less from mode competition than axisymmetric modes.

3.2 Eigenmodes of Tapered, Open Resonator Cavities

The design of resonators for gyrotron oscillators requires the knowledge of the RF field profile, resonator eigenfrequencies, and quality factor Q. In conventional gyrotrons, the resonator is usually a three section smooth walled cylindrical cavity structure as shown in Fig. 3.6. The input taper is a cut-off section which prevents the back propagation of RF power to the gun. The beam-wave interaction takes place mainly in the uniform middle section where the RF-fields reach peak values. The uptaper connects the cavity with the output waveguide and the q.o. launcher. The junctions between the sections are smoothed in order to minimize unwanted mode conversion at sharp edges. Reflections at tapers lead to resonant behaviour of the apparatus; Q is a measure of the efficiency with which a wave is transmitted out of the resonator. The resonance frequency ω and the quality factor Q are determined by radiation boundary conditions at the resonator output section. There are several schemes to determine the eigenmodes in an open-ended cavity resonator [121–128]. The basic procedure is to solve the wave equation in the cavity geometry by applying radiation boundary conditions for minimum reflections to obtain resonant frequencies of the eigenmodes. Here we give a method [72, 123] that is equivalent to the above approaches.
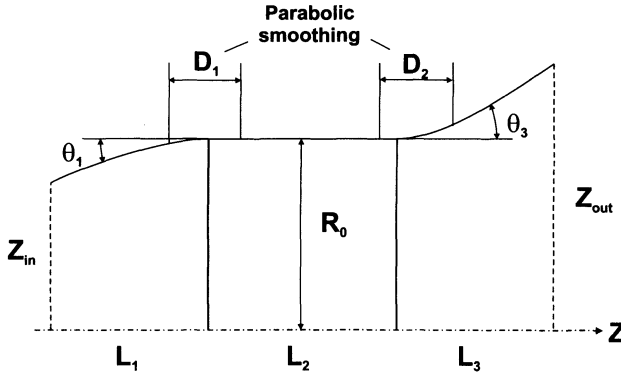
Fig. 3.6. Resonator geometry

3.2.1 Physical Model for the High Frequency Fields in a Resonator

We are interested in the eigenmodes of a weakly irregular waveguide, considered as an open ended resonator. The azimuthal dependency is taken as $e^{-im\theta}$ ($m = 0, 1, 2, \cdots$) and the fields are assumed to vary as $e^{i\omega t}$ where the complex parameter $\omega = \omega_0(1 + i/2Q)$ corresponds to the resonance frequency ω_0 and quality factor Q respectively. The cavity geometry is shown in Fig. 3.6. Maxwell's equations can be written in the form

$$\nabla \times \boldsymbol{E} = -i\omega \boldsymbol{B} = -i\omega\mu\boldsymbol{H}\,, \tag{3.5a}$$

$$\nabla \times \boldsymbol{H} = \boldsymbol{J} + i\omega\epsilon\boldsymbol{E}\,, \tag{3.5b}$$

$$\nabla \cdot (\epsilon\boldsymbol{E}) = \rho\,, \tag{3.5c}$$

$$\nabla \cdot \boldsymbol{B} = 0\,, \tag{3.5d}$$

where ρ and $\boldsymbol{J}$ are the charge and current densities respectively. From Maxwell's equations one can obtain the wave equation for an axially symmetric situation in the form [129]

$$(\nabla_t^2 + k_z{}^2)h = 0 \tag{3.6}$$

where h is an auxiliary function that satisfies the field equation for TE/TM modes. In cylindrical coordinates (r, θ, z), the Laplacian operator ∇^2 is

$$\nabla^2 = \nabla_t^2 + \frac{\partial^2}{\partial z^2} = \frac{\partial^2}{\partial r^2} + \frac{1}{r}\frac{\partial}{\partial r} + \frac{1}{r^2}\frac{\partial^2}{\partial\theta^2} + \frac{\partial^2}{\partial z^2}$$

and k_z is the wave propagation number given by

$$k_z^2 = k_0^2 - k_{mp}^2 = \frac{\omega^2}{c^2} - \frac{x_{mp}^2}{R^2} \tag{3.7}$$

where χ_{mp} is the pth Bessel zero for TE$_{mp}$ modes defined by $J_m'(x_{mp}) = 0$ and for TM$_{mp}$ modes by $J_m(x_{mp}) = 0$.

Let $\hat{n}$ be the unit vector normal to the cavity wall such that

$$n_\theta = 0\,, \tag{3.8a}$$

$$n_r = -\cos\theta_w\,, \tag{3.8b}$$

$$n_z = \sin\theta_w \quad \text{with} \tag{3.8c}$$

$$\tan\theta_w = \frac{dR(z)}{dz}\,. \tag{3.8d}$$

θ_w is the taper angle. Now, the boundary conditions at the cavity wall (assumed to be a perfectly conducting surface) can be written as

$$\hat{n} \cdot \boldsymbol{B} = 0 \quad \Longrightarrow \quad B_r = B_z \tan\theta_w \,, \tag{3.9a}$$

$$\hat{n} \times \boldsymbol{E} = 0 \quad \Longrightarrow \quad E_\theta = 0, E_z = -E_r \tan\theta_w \tag{3.9b}$$

at $r = R(z)$.

Since we are interested in minimizing the reflections at the output, the following boundary conditions at z_{out} are imposed

$$\frac{\partial \boldsymbol{E}}{\partial z} = -ik_z \boldsymbol{E} \,, \quad \frac{\partial \boldsymbol{H}}{\partial z} = -ik_z \boldsymbol{H} \,. \tag{3.10}$$

This condition should hold for all $z > z_{\text{out}}$. In the absence of sources, the appropriate boundary condition at the input is that of an evanescent wave given by

$$\frac{\partial \boldsymbol{E}}{\partial z} = |k_z| \boldsymbol{E} \,, \quad \frac{\partial \boldsymbol{H}}{\partial z} = |k_z| \boldsymbol{H} \,. \tag{3.11}$$

Now let us write the $\boldsymbol{E}$ and $\boldsymbol{H}$ fields in the form

$$\boldsymbol{E} = \boldsymbol{E_t} + \hat{z} E_z \,, \quad \boldsymbol{H} = \boldsymbol{H_t} + \hat{z} H_z \,. \tag{3.12}$$

Let us, now, expand the transverse fields $\boldsymbol{E_t}$ in terms of orthonormal basis functions as follows:

$$\boldsymbol{E_t} = \sum_{mp} V_{mp}(z) \boldsymbol{e}_{mp}(r, z, \theta) + \sum_{mp} U_{mp}(z) \widetilde{\boldsymbol{e}}'_{mp}(r, z, \theta) \,, \tag{3.13}$$

where

$$\int_0^{2\pi} d\theta \int_0^{R(z)} r \, dr \boldsymbol{e}^*_{mp} \cdot \boldsymbol{e}_{m'q} = \delta_{pq} \delta_{mm'}$$

and similarly for $\widetilde{\boldsymbol{e}}_{mp}$.

Let us now introduce the scalar functions (also called membrane functions)

$$\psi_{mp} = C_{mp} J_m(k_{mp} r) e^{-im\theta} \,, \tag{3.14a}$$

$$\widetilde{\psi}_{mp} = B_{mp} J_m(\gamma_{mp} r) e^{-im\theta} \,, \tag{3.14b}$$

which satisfy

$$(\nabla_t^2 + k_{mp}^2) \psi_{mp} = 0 \,, \tag{3.15a}$$

$$(\nabla_t^2 + \gamma_{mp}^2) \widetilde{\psi}_{mp} = 0 \,. \tag{3.15b}$$

This results in [129]

$$\boldsymbol{e}_{mp} = \hat{z} \times \nabla \psi_{mp} \,, \quad \widetilde{\boldsymbol{e}}_{mp} = -\nabla_t \widetilde{\psi}_{mp} \,. \tag{3.16}$$

Requiring $E_\theta = 0$ at $r = R(z)$ gives

$$k_{mp} = \frac{x_{mp}}{R(z)}, \qquad (3.17a)$$

$$\gamma_{mp} = \frac{y_{mp}}{R(z)}, \qquad (3.17b)$$

where x_{mp} is the pth root of $J_m'(x)$ and y_{mp} is the pth root of $J_m(x)$ respectively, and

$$C_{mp}^{-1} = \sqrt{\pi(x_{mp}^2 - m^2)}J_m(x_{mp}), \qquad (3.18a)$$

$$B_{mp}^{-1} = \sqrt{\pi}y_{mp}J_{mp}'(y_{mp}). \qquad (3.18b)$$

From $-\partial \boldsymbol{B}/\partial t = \nabla \times \boldsymbol{E}$, we obtain

$$-i\omega B_z = -\sum_{mp} V_{mp}(z)k_{mp}^2\psi_{mp}, \qquad (3.19a)$$

$$-i\omega B_r = -\frac{\partial E_\theta}{\partial z} - \frac{imE_z}{r}, \qquad (3.19b)$$

$$-i\omega B_\theta = \frac{\partial E_r}{\partial z} - \frac{\partial E_z}{\partial r}, \qquad (3.19c)$$

when $m \neq 0$, E_z no longer vanishes. Instead one finds that E_z satisfies the inhomogeneous Bessel equation

$$\nabla_t^2 E_z + \frac{\omega^2}{c^2}E_z - i\omega\mu J_z = \sum_p \gamma_{mp}^2 \left[\tilde{\psi}_{mp}\frac{dU_{mp}}{dz} - \frac{R'}{R}U_{mp}\frac{1}{r}\frac{\partial(r^2\tilde{\psi}_{mp})}{\partial r} \right] \quad (3.20)$$

and the boundary condition at $r = R(z)$

$$E_z(R) = -\tan\theta_w E_r(R)$$

$$= -\frac{dR/dz}{R\sqrt{\pi}}\exp^{-im\theta}\sum_p \left[\frac{imV_{mp}(z)}{\sqrt{x_{mp}^2 - m^2}} + U_{mp} \right]. \qquad (3.21)$$

U_{mp} and V_{mp} satisfy second order equations which are derived from

$$-i\omega\epsilon E_r - J_r = \frac{\partial H_\theta}{\partial z} - \frac{im}{r}H_z, \qquad (3.22a)$$

$$-i\omega\epsilon E_\theta - J_\theta = \frac{\partial H_z}{\partial r} - \frac{\partial H_r}{\partial z}. \qquad (3.22b)$$

Multiplying (3.22a) by $(e_{mq}^*)_r$ and (3.22b) by $(e_{mq}^*)_\theta$, adding and integrating over the transverse surface gives the following expression:

$$\frac{d^2 V_{mq}}{dz^2} + \left(\frac{\omega^2}{c^2} - k_{mq}^2 \right) V_{mq} + \sum_p \left(2T_{qp}^m \frac{dV_{mp}}{dz} + V_{mp} \frac{dT_{qp}^m}{dz} \right)$$

$$- 2 \left(\frac{R'}{R} \right) \sum_p V_{mp} T_{pq}^m + \left(\frac{R'}{R} \right)^2 V_{qm} \frac{[4m^2 - (x_{mq}^2 - m^2)^2]}{3(x_{mq}^2 - m^2)}$$

$$- 2 \left(\frac{R'}{R} \right)^2 \sum_{p \neq q} \frac{x_{mp}^2 V_{mp}}{[(x_{mp}^2 - m^2)(x_{mq}^2 - m^2)]^{1/2}}$$

$$\times \left\{ \frac{4x_{mp}^2 x_{mq}^2 - 2m^2(x_{mp}^2 + x_{mq}^2)}{(x_{mp}^2 - x_{mq}^2)^2} \right.$$

$$\left. + m \left[1 - \frac{4(x_{mq}^2 + x_{mp}^2)}{(x_{mq}^2 - x_{mp}^2)^2} \right] \left[1 - \frac{1 + m(m+1)/x_{mp}x_{mq}}{x_{mq} - x_{mp}} \right] \right\}$$

$$+ 2 \frac{2im}{\sqrt{x_{mq}^2 - m^2}} \sum_p \left[2 \left(\frac{R'}{R} \right) \frac{dU_{mp}}{dz} \left(\frac{R'}{R} \right)' U_{mp} \right]$$

$$= + i\omega\mu J_{mq} . \tag{3.23}$$

Similarly, multiplying (3.22a) by $(\widetilde{e}_{mq}^*)_r$ and (3.22b) by $(\widetilde{e}_{mq}^*)_\theta$, adding and integrating gives:

$$\frac{d^2 U_{mq}}{dz^2} + \left(\frac{\omega^2}{c^2} - \gamma_{mq}^2 \right) U_{mq} + \sum_p \left(2\widetilde{T}_{qp}^m \frac{dU_{mp}}{dz} + U_{mp} \frac{d\widetilde{T}_{qp}^m}{dz} \right)$$

$$- 2 \left(\frac{R'}{R} \right) \sum_p U_{mp} \widetilde{T}_{pq}^m + \left(\frac{R'}{R} \right)^2 U_{mq} (4 + y_{mq}^2 - m^2)/3$$

$$- 2 \left(\frac{R'}{R} \right)^2 \sum_{p \neq q} \frac{y_{mp}^2 U_{mp}}{[y_{mq}^2 - y_{mp}^2]^2} \left\{ 2(y_{mq}^2 + y_{mp}^2) \right.$$

$$\left. - \frac{(m+1)(y_{mq} - y_{mp})}{y_{mq} y_{mp}} \left[y_{mq}^2 - y_{mp}^2 - \frac{4(y_{mq}^2 + y_{mp}^2)}{y_{mq}^2 - y_{mp}^2} \right] \right\}$$

$$= + i\omega\mu \widetilde{J}_{mq} . \tag{3.24}$$

The mode coupling coefficients are defined by

$$T_{pq}^m = 2\pi \int_0^R r e_{mq}^* \cdot \frac{\partial e_{mp}}{\partial z} \, dr , \tag{3.25a}$$

$$\widetilde{T}_{pq}^m = 2\pi \int_0^R r \widetilde{e}_{mq}^* \cdot \frac{\partial \widetilde{e}_{mp}}{\partial z} \, dr , \tag{3.25b}$$

and

$$J_{mq} = \int d\theta \int_0^R r e_{mq}^* \cdot \boldsymbol{J} \, dr \,, \tag{3.26a}$$

$$\widetilde{J}_{mq} = \int d\theta \int_0^R r \widetilde{e}_{mq}^* \cdot \boldsymbol{J} \, dr \,. \tag{3.26b}$$

Straightforward integration gives

$$T_{pq}^m = -2\frac{R'}{R}\sqrt{\frac{x_{mp}^2 - m^2}{x_{mq}^2 - m^2}} \left[\frac{x_{mq}^2}{(x_{mp}^2 - x_{mq}^2)}\right], \quad p \neq q \tag{3.27a}$$

$$T_{qq}^m = -\frac{R'}{R}\frac{m^2}{(x_{mq}^2 - m^2)} \quad \text{for TE modes and} \tag{3.27b}$$

$$\widetilde{T}_{pq}^m = +2\frac{R'}{R}\frac{y_{mp}^2}{(y_{mq}^2 - y_{mp}^2)}, \quad p \neq q \tag{3.27c}$$

$$\widetilde{T}_{qq}^m = -\frac{R'}{R} \quad \text{for TM modes}. \tag{3.27d}$$

J. Luginsland [122] obtained the same set of equations for the special case $m = 0$ using a Galerkin method similar to that used by Bernstein et al. [121], but a slightly different Ansatz for the basis functions. For small taper angles when $R' \longrightarrow 0$, the TE and TM modes decouple and the system reduces to the Vlasov approximation, in which all the coupling coefficients vanish. In this case, the cavity eigenmodes are given by a single function of the form (3.12)–(3.16), and the complex eigenfrequencies are determined by the boundary conditions (3.10) and (3.21).

The functions V_{mq} and U_{mq} must satisfy radiation boundary conditions as given above for $\boldsymbol{E}$ and $\boldsymbol{B}$. For the V_{mq} this means [72, 123, 124]

$$\frac{dV_{mq}}{dz} = -ik_z V_{mq}$$

at $z = z_{\text{out}}$ (i.e. at the resonator output end).

When a source is present, the eigenfrequency of a steady-state solution is real. But in case of empty open-ended cavity resonators, the eigenfrequencies are complex with positive imaginary part to account for damping due to the radiation out of the cavity. In that case, the normalization of the field profile is arbitrary. When a source is present, normalization is determined by the source term.

The cold cavity fields can be normalized to the desired output power as follows. From Poynting's theorem, we have

$$P_{\text{out}} = \pi \int_0^R r \, dr \, \text{Re}(\boldsymbol{E} \times \boldsymbol{H}^*)_z \Bigg|_{z=z_{\text{out}}} \tag{3.28}$$

Since

$$(\boldsymbol{E} \times \boldsymbol{H}^*)_z = E_r H_\theta^* - E_\theta H_r^* \, , \tag{3.29}$$

substituting appropriate field expressions in (3.28) and making use of (3.29), gives

$$
\begin{aligned}
P_{\text{out}} = Re \left(\frac{-i}{2\omega\mu} \right) &\left[\sum_p \left(V_{mp} \frac{dV_{mp}^*}{dz} + U_{mp} \frac{dU_{mp}^*}{dz} \right) \right. \\
&+ \sum_{pqm} \left(V_{mq}^* T_{qp}^m V_{mp} + U_{mq}^* T_{qp}^m U_{mp} \right) \\
&+ \sum_{pqm} \frac{2imR'}{R\sqrt{x_{mp}^2 - m^2}} V_{pm} U_{qm}^* + 2\pi R' R |E_r(R)|^2 \\
&\left. + 2\pi \sum_{mp} \gamma_{mp}^2 U_{mp} \int_0^R r\widetilde{\psi}_{mp} E_z^* dr \right]_{\text{out}}
\end{aligned} \tag{3.30}
$$

and by making use of (3.10) in (3.30), finally we get the following expression for P_{out} as

$$
\begin{aligned}
P_{\text{out}} = Re \left(\frac{1}{2\omega\mu} \right) &\left[\sum_{mp} \left(k_{z(mp)}^* |V_{mp}|^2 + \gamma_{z(mp)}^* |U_{mp}|^2 \right) \right. \\
&- i \sum_{pqm} \left(V_{mq}^* T_{qp}^m V_{mp} + U_{mq}^* T_{qp}^m U_{mp} \right) \\
&+ \sum_{pqm} \frac{2imR'}{R\sqrt{x_{mp}^2 - m^2}} V_{mp} U_{mq}^* \\
&\left. - 2\pi \sum_{pm} \gamma_{mp}^2 U_{mp} \int_0^R r\widetilde{\psi}_{mp} E_z^* \, dr \right]_{\text{out}} .
\end{aligned} \tag{3.31}
$$

The formalism given here is valid when $R(z)$ is continuous and differentiable. If $R(z)$ has discontinuities, then the equations must be solved piecewise and the fields and their derivatives have to be matched at the discontinuities of $R(z)$.

For numerical calculations, the boundary condition at z_{in} is used to determine the starting value of $\partial V/\partial z$ for the integration of (3.23)–(3.24). The boundary condition at z_{out} is reformulated in the form

$$|R| = \left| \frac{\frac{dV}{dz} + ik_z V}{\frac{dV}{dz} - ik_z V} \right| = \text{minimum} \tag{3.32}$$

one could also specify a non-zero reflection coefficient R_{load} such that the condition $|R - R_{\text{load}}| = \text{minimum}$ is imposed.

As an example [123], we present the cold cavity analysis for a 147 GHz gyrotron that might operate in the TE_{23} mode. The geometry of the cavity
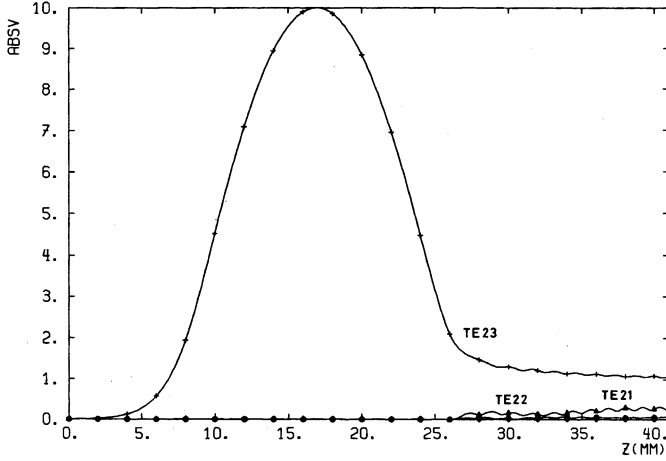
Fig. 3.7. Cold cavity field profile (normalized to 10) with full-wave analysis for a TE$_{23}$ mode gyrotron at 147 GHz. Here, the effects of the admixing of TM$_{21}$ and TM$_{22}$ modes is not visible. $f = 147.01$ GHz and $Q = 3185$ [123]

is: $\theta_1 = 1°$, $\theta_2 = 0°$, $\theta_3 = 10°$, $L_1 = 10$ mm, $L_2 = 16$ mm, $L_3 = 15$ mm and $R_0 = 3.24$ mm. The nominal mode is TE$_{23}$ and TE$_{21}$, TE$_{22}$, TM$_{21}$ and TM$_{22}$ modes can also propagate. The field profile $V_{mp}(z)$ is computed by solving (3.23)–(3.24) and is shown in Fig. 3.7.

From Fig. 3.7, it is evident that the coupling to the TE$_{22}$ mode is only noticeable in the output taper, while the coupling to the TE$_{21}$ mode is small and the admixture of the TM modes is negligible. In fact, the field amplitudes of TM modes are smaller than that of the TE$_{22}$ mode by a factor of about 1000. The Q value is 3185. The field profile for the same geometry under single mode Vlasov approximation is nearly identical to the corresponding field profile shown in Fig. 3.7. The only observable change is a slight decrease in the Q value (from 3185 to 3064). When the taper angles are smaller than about 10°, there is practically no difference between the fields calculated from more exact equations and those calculated in the Vlasov approximation [123, 128]. Hence, when the taper angles are small, it is legitimate to use the single mode Vlasov approximation in which only a single TE$_{mp}$ mode is retained in the expansion of (3.13) and coupling to the other modes due to cavity tapers is neglected.

Thus, in single mode approximation, (3.23) reduces to

$$\frac{d^2 V_{mq}}{dz^2} + \left(\frac{\omega^2}{c^2} - k_{mq}^2\right) V_{mq} \simeq +i\omega J_{mq}, \qquad (3.33)$$

where J_{mq} is given by (3.26).

The solution of the above simplified equation (3.33) is best carried out with the Numerov algorithm [130] when $J_{mq} = 0$. Further, the dependence of
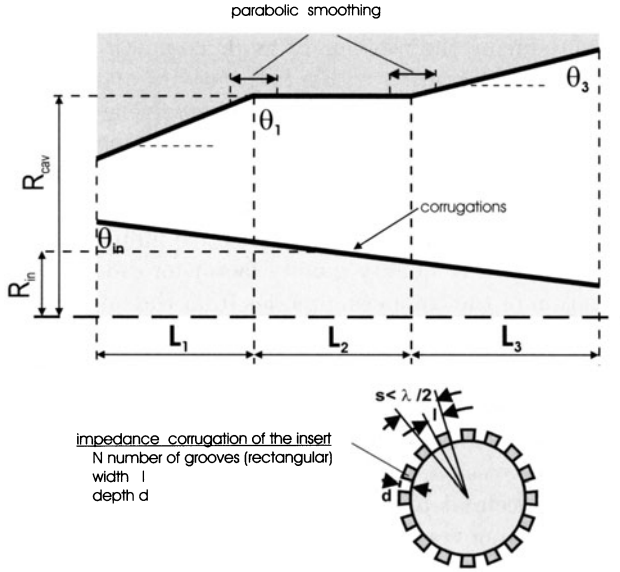
Fig. 3.8. Coaxial cavity geometry

the frequency and quality factors on resonator geometry have been studied in [128]. The frequency is also sensitive to the manufacturing tolerances of the cavity radius. The quality factor increases with increasing cavity length. For proper bunching and energy extraction at nearly optimal efficiency, one has to design the cavity resonator appropriately. This requires computation of the interaction of an electron beam with the electromagnetic fields of the cavity modes. This will be described in the next chapter.

It is convenient to work with a normalized field profile. This will be done by defining

$$V_{mp}(z) = V_{max}\hat{f}_{mp}(z).$$

(3.34)

Here, $\hat{f}_{mp}(z)$ is the field profile normalized to a maximum absolute value 1. In the cold cavity approximation, $V_{\max}$ and the output power are related by:

$$QP_{\text{out}} = \omega W = \left(\frac{\omega\epsilon_0}{2}\right) V_{\max}^2 \int_{z_{\text{in}}}^{z_{\text{out}}} \left|\hat{f}_{mp}(z)\right|^2 dz.$$

(3.35)

3.2.2 Coaxial Cavity Structures

The cylindrical cavity structure with a coaxial insert is another potential interaction structure employed in very high power gyrotrons [13, 131–133]. The schematic of a practical coaxial structure with longitudinal slots on the inner conductor is shown in Fig. 3.8.

Important features (and advantages) of the coaxial insertion [134, 135] are:

1. The coaxial insertion tends to rarefy the mode spectrum (near the desired mode), thus reducing the problem of mode competition, and permitting stable single mode operation with a larger cavity diameter.
2. In the case of coaxial cavity structures, the mode eigenvalue (that is, the roots of the characteristic dispersion relation of the coaxial structure) χ_{mp} is a function of the ratio of the inner to the outer radii of the coaxial conductors $(= R_o(z)/R_i(z))$. Therefore, if the inner conductor is tapered, then χ_{mp} varies as R_o/R_i resulting a selective influence on the start up scenario and diffractive quality quality factor for different modes.
3. The segregation of the competing modes from the operating mode could further be addressed with the introduction of longitudinal slots on the inner conductor with suitable slot width and depth. In the case that the corrugation period is much smaller than $\lambda/2$, an impedance model can be used for describing the influence of the corrugations.
4. Less voltage depression.
5. Possibility of special depressed collectors and ultra fast frequency tuning by biasing the inner conductor.

A disadvantage is, of course, the increased technical complexity. The advantages may justify this, although the jury is still out.

For weakly tapered, smooth walled cylindrical cavity resonators, the eigenvalues of the cylindrical cavity are used to determine the eigenmodes. In the case of coaxial cavity structures, first the characteristic equation has to be deduced from the geometry of the interaction structure through field analysis. The roots of this characteristic equation give the mode eigenvalues (χ_{mp}'s). This mode eigenvalue is used in the one dimensional wave equation for the cold cavity analysis as discussed in previous section and the interaction models are essentially identical.

The characteristic equation of the coaxial cavity structure can be obtained from standard field analytical procedures in which the field expressions are written in different regions of the problem domain and regular boundary conditions for $\boldsymbol{E}$ and $\boldsymbol{H}$ fields are taken and the field expressions are substituted in the boundary conditions. This gives a set of transcendental equations up on solving which gives the characteristic dispersion relation. The characteristic equation for a simple coaxial structure is given as [131, 133]:

$$J'_m(\chi)N'_m\left(\frac{\chi}{C}\right) = N'_m(\chi)J'_m\left(\frac{\chi}{C}\right),\tag{3.36}$$

where $C = R_o/R_i$, and J'_m and N'_m are the derivatives of the Bessel and Neumann functions respectively of order m.

In case of a coaxial cavity with slotted inner conductor, the characteristic equation is [134, 135]

$$\begin{aligned} J'_m(\chi_{mp})\left[Y'_m\left(\frac{\chi_{mp}}{C}\right) + \omega Y_m\left(\frac{\chi_{mp}}{C}\right)\right] \\ -Y'_m(\chi_{mp})\left[J'_m\left(\frac{\chi_{mp}}{C}\right) + \omega J_m\left(\frac{\chi_{mp}}{C}\right)\right] = 0,\end{aligned}\tag{3.37}$$

where $\omega = (l/s)\tan(\chi_{mp}d/R_o)$. The slot dimensions l, s, and d are described in Fig. 3.8.

By making use of (3.36) or (3.37) depending on the geometry of the structure, (3.33) and (3.35) are solved considering the radiation boundary conditions (3.32) for the analysis of coaxial cavity resonators. The behavior of the solutions of the characteristic equation are discussed in the dissertation of S. Kern [136] and in [134, 135].

3.2.3 Complex Cavities

Complex cavities [72, 128] are another, no longer popular, type of interaction structures for gyrotrons. They were proposed in 1979 [137] and first practical studies were reported in 1981 [138, 139]. The geometry of the complex cavity structure is shown in Fig. 3.9 It consists of two resonators I and II and a transition region III.

The basic idea behind a complex cavity structure is that a pair of modes having same azimuthal index and different radial indices can be coupled to produce a mode with high Q. The resonators I and II are coupled due to mode conversion in the transition region III. The two resonator sections I and II are designed such that the local waveguide modes of the desired pair have the same frequency and are simultaneously near cut-off in the two sections. These two sections are detuned for other mode pairs. It is designed in such a way that the eigenfrequency of a lower order mode in the first resonator section matches that of a higher order mode in the second resonator section. It can be viewed in another way that the first section serves to prebunch the beam which in turn will preferentially excite the mode with the same frequency in the second section. Thus, the first cavity provides mode control and the second cavity provides the working space needed for power generation. In this scheme, the beam should be placed on the same radial peak of the field in both the resonator sections. The use of a higher order mode in the second cavity reduces wall losses, and mode control by the first cavity reduces mode competition in highly overmoded gyrotrons. The complex cavity concept was
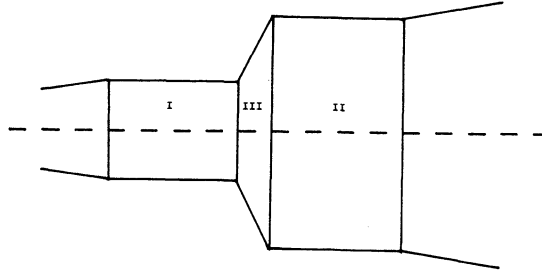
Fig. 3.9. Geometry of a complex cavity resonator

further demonstrated experimentally [138] in a TE_{01}/TE_{04} configuration, and has been incorporated in TE_{01}/TE_{02} devices at 60 and 70 GHz and in a 140 GHz TE_{02}/TE_{03} device developed at Varian. Operation of step cavity devices at higher harmonics has also been demonstrated by Zapevalov et al. and by Malygin [128]. On the other hand, Thomson CSF experienced difficulties with a TE_{02}/TE_{04} complex cavity at 100 GHz [140] and decided to work instead with volume modes in simple cavities. Theoretical treatments of complex cavities have been given by Dumbrajs and Borie [141], Fliflet [142], Pavelyev et al. [143], and Nielson et al. [144].

In the analysis of complex cavities [128], one must consider the field matching at the cavity step (at $z = 0$). The field is expanded in terms of the eigenfields of the normal modes of the two connecting waveguides:

In *Region I*

$$\boldsymbol{E}_t = \sum (a_{ip} + a_{rp}) \bar{e}^a_{mp} , \tag{3.38a}$$

$$\boldsymbol{H}_t = \sum (a_{ip} - a_{rp})/Z^a_{mp} \bar{h}^a_{mp} \quad \text{with} \tag{3.38b}$$

$$\bar{h}^a_{mp} = \hat{z} \times \bar{e}^a_{mp} \quad \text{and} \tag{3.38c}$$

$$Z^a_{mp} = \mu_0 \omega / \sqrt{(\omega^2/c^2) - (x^2_{mp}/a^2)} \quad \text{for TE modes}, \tag{3.38d}$$

$$= \sqrt{(\omega^2/c^2) - (y^2_{mp}/a^2)}/\epsilon_0 \omega \quad \text{for TM modes}. \tag{3.38e}$$

Similarly, in *Region II*

$$\boldsymbol{E}_t = \sum (b_{ip} + b_{rp}) \bar{e}^b_{mp} , \tag{3.39a}$$

$$\boldsymbol{H}_t = \sum (b_{ip} - b_{rp})/Z^b_{mp} \bar{h}^b_{mp} \quad \text{with} \tag{3.39b}$$

$$\bar{h}^b_{mp} = \hat{z} \times \bar{e}^b_{mp} \quad \text{and} \tag{3.39c}$$

$$Z^b_{mp} = \mu_0 \omega / \sqrt{(\omega^2/c^2) - (x^2_{mp}/b^2)} \quad \text{for TE modes}, \tag{3.39d}$$

$$= \sqrt{(\omega^2/c^2) - (y^2_{mp}/b^2)}/\epsilon_0 \omega \quad \text{for TM modes}. \tag{3.39e}$$

The subscripts i and r refer to incoming and reflected waves respectively (or waves propagating forward and backward). The basis functions (including normalization) are the same as in Sect. 3.2.1. Matching the fields at $z = 0$ gives

$$\sum (a_{ip} + a_{rp}) \bar{e}^a_{mp} = \sum (b_{ip} + b_{rp}) \bar{e}^b_{mp} , \tag{3.40}$$

$$\sum (a_{ip} - a_{rp})/Z^a_{mp} \bar{h}^a_{mp} = \sum (b_{ip} - b_{rp})/Z^b_{mp} \bar{h}^b_{mp} . \tag{3.41}$$

Taking the scalar product of (3.40) with $\bar{e}^{a*}_{mp}$ and of (3.41) with $\bar{h}^{a*}_{mp}$ and integrating over surface gives

$$a_{ip} + a_{rp} = \sum (b_{is} + b_{rs}) C_{ps} , \tag{3.42a}$$

$$a_{ip} - a_{rp} = \sum (b_{is} - b_{rs}) Z^a_{mp}/Z^b_{mp} C_{ps} . \tag{3.42b}$$

Here, $C_{ps} = \int \bar{e}_{mp}^{*a} \bar{e}_{ms}^{b} dA$ are coupling coefficients. They have been given explicitly (for the normalization given here) by Nielson et al. [144] for general m and by Dumbrajs and Borie [141] for $m = 0$.

For TE(I) $\longrightarrow$ TE(II):

$$C_{ps} = \frac{2ax_{ms}}{2} \frac{J'_m(x_{ms}a/b)}{J_m(x_{ms})} \frac{1}{\sqrt{(x_{mp}^2 - m^2)(x_{ms}^2 - m^2)}}$$
$$\times [1 - (x_{ms}a/x_{mp}b)^2] \qquad (3.43a)$$

For TE(I) $\longrightarrow$ TM(II):

$$C_{ps} = \frac{2m}{y_{ms}} \frac{J_m(y_{ms}a/b)}{J_{m+1}(y_{ms})} \frac{1}{\sqrt{x_{mp}^2 - m^2}} \qquad (3.43b)$$

For TM(I) $\longrightarrow$ TE(II):

$$C_{ps} = 0 \qquad (3.43c)$$

For TM(I) $\longrightarrow$ TM(II):

$$C_{ps} = -\frac{2}{y_{ms}} \frac{J_m(y_{ms}a/b)}{J_{m+1}(y_{ms})} \frac{1}{[1 - (y_{mp}b/y_{ms}a)^2]} \qquad (3.43d)$$

Although these complex cavity structures were once thought to be advantageous, successful use of them depends on several factors, including mode density, fabrication tolerances and mode conversion at the cavity step. At sufficiently high mode densities, more than one mode can become simultaneously resonant. Conversion to unwanted modes at the step can degrade the mode purity of the device. Step cavity devices are much more sensitive to machining tolerances than conventional gyromonotrons because of the bimodal resonance conditions. These factors limited the use of such complex structures at high frequencies in most practical situations.

3.3 Remarks

A gyrotron is a mildly relativistic device in which the helical electron beam interacts with the fields in the interaction region and energy transfer occurs. Though there are several schemes to explain the electron bunching and energy extraction, we tried to explain this non-trivial phenomenon in simple terms with appropriate phase bunching plots. As far as the interaction structures are concerned, one prefers either weakly tapered conventional hollow cylindrical cavity resonators or coaxial cavity resonators, both open ended. The conventional type of resonator is mostly preferred in moderate to low power gyrotrons whereas coaxial structures are very promising at very high powers

($> 1\,\mathrm{MW}$, CW) at elevated frequencies ($> 140\,\mathrm{GHz}$). Owing to step induced effects and machining tolerance limitations, complex cavity resonators do not seem to have much practical utility.

In the numerical evaluation of the cavity analysis, the minimization of $|R|^2$ as a function of frequency ω and Q (in cold cavity approximation) can be done with a number of methods. One of these makes use of the CERN routine MINUIT [145]. For other equivalent methods, see [146]. To solve the coupled equations (3.23)–(3.24), standard Runga–Kutta algorithms [146] work well. To ensure the oscillatory behavior of the RF field in the region of the output to be reproduced accurately, a stepwidth of $\Delta z \approx \lambda/20$ is sufficient. Whatever numerical method is used to integrate the equations, accuracy will be poor if $\Delta z > \lambda/10$. Furthermore, it is usually adequate to use the Vlasov approximation, if the tapering angles are small enough ($< 6°$), in which case the coupling to other modes is negligible, thereby reducing the problem to the solution of a one dimensional wave equation with appropriate radiation boundary conditions at the resonator input and output. In this case, the Numerov algorithm [130] or the leapfrog method [147] work very well with significantly less computational effort than the Runga–Kutta algorithms.

4 Calculation of RF Behaviour

To calculate the efficiency and output power, one must solve the equation of motion for a single electron traversing the resonator in the given electric and magnetic fields numerically and compute the energy loss or gain. The efficiency is then computed by averaging over an ensemble of electrons uniformly distributed in their initial gyration phase angle. The numerical solution of the equation of motion is facilitated by taking into account the fact that the electrons gyrate rapidly around the guiding center. This leads either to the slow variables transformation [148, 149] or, with the further approximation of neglecting the RF magnetic fields and guiding center drift, and taking advantage of the fact that maximum energy transfer occurs when the electron gyration is approximately synchronous with a rotating field component, to an approximate, one dimensional equation known as the *adiabatic approximation* [7, 150, 151]. The accuracy of the adiabatic approximation has been checked for several cases [152] by integrating the equation of motion for the so-called slow variables introduced by Rapoport et al. [148] and used by Ganguly and Ahn [149]. In most cases the efficiency calculated with the two approaches is the same within one or two per cent. This adiabatic approximation has been used for extensive parameter studies at FZK [153], and elsewhere [150]. It is also used in the extensive Russian literature, with a few additional [10, 50, 132, 139, 154, 155] approximations.

In this chapter, the adiabatic approximation to equation of electron motion is derived and this equation of motion is solved in the fixed field approximation to compute the efficiency. Later, in self-consistent calculations, the equations of motion for the electrons are solved simultaneously with the field equations, taking into account the effect of the beam on the cavity field profile and quality factor, as well as frequency pulling.

4.1 Equation of Motion

Figure 4.1 illustrates the gyrotron oscillator model considered. An annular electron beam is injected into an open ended cavity from the left hand side and propagates to the right, guided by a constant (in time) magnetic field B_0.
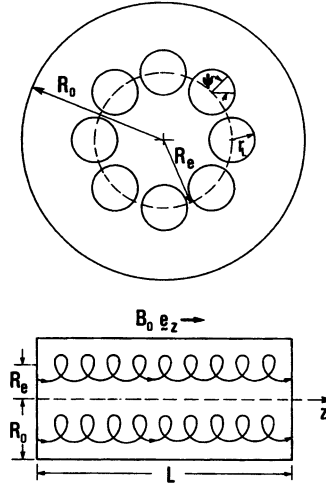
Fig. 4.1. Beam geometry in a gyrotron resonator

The electrons, moving along helical trajectories, have a substantial part of their kinetic energy in the form of transverse motion. Inside the cavity, the electron beam loses a portion of its energy through interaction with the electromagnetic fields. It is assumed that the beam is sufficiently tenuous that its space charge field can be neglected and that it will not modify the normal mode electromagnetic field structure of the resonator. This is a reasonable approximation for beam powers below a few hundred kilowatts. The cyclotron interaction takes place between the electron beam and TE modes. If the average power lost by the beam is equal to the wave power diffracted out of the cavity, a steady state is established. One wishes to optimize the beam energy loss in this steady state. The electron beam shown in Fig. 4.1 is typical of those generated from a magnetron injection gun. The beam parameters are obtained from gun simulations (see Chap. 6). Among the most important of these are

$$E/m_e c^2 = \gamma_0 = 1 + U_b/511\,\text{kV}$$

where eU_b is the beam kinetic energy and the guiding center radius R_e. One wishes to choose R_e such that the beam-field coupling is maximum. In other words, the guiding center radius should coincide with a radial maximum of the RF field. For a TE_{mpq} mode this means that

$$J_{m\pm s}^2(x_{mp}R_e/R_0)$$

should be maximized (s is the harmonic number, assumed equal to 1 in the following, x_{mp} is the pth root of $J_m'(x) = 0$ and R_0 is the cavity radius). The reason for this will become apparent in the subsequent discussion.

For the purpose of gyrotron modelling, we assume that the electrons are initially monoenergetic with guiding centers all at $r = R_e$ and uniformly distributed in phase Ψ_0 (see Fig. 4.1).

The equation of motion for an arbitrary charged particle in given electric and magnetic fields is

$$\frac{d\boldsymbol{p}}{dt} = -e(\boldsymbol{E} + \boldsymbol{v} \times \boldsymbol{B}), \tag{4.1a}$$

$$\frac{d\varepsilon}{dt} = -e\boldsymbol{E} \cdot \boldsymbol{v}, \tag{4.1b}$$

where $\boldsymbol{p} = \gamma m_e \boldsymbol{v} = m_e c \boldsymbol{u}$, $\varepsilon = \gamma m_e c^2$, and $\gamma = 1/\sqrt{1 - v^2/c^2} = \sqrt{1 + u^2}$ is the usual relativistic factor. It is convenient to define the dimensionless variable

$$\boldsymbol{u} = \gamma \boldsymbol{v}/c = \gamma \boldsymbol{\beta} = \boldsymbol{p}/m_e c.$$

Then the equation of motion becomes

$$\frac{d\gamma}{dt} = -\frac{e}{m_e c}\left(\boldsymbol{E} \cdot \frac{\boldsymbol{u}}{\gamma}\right), \tag{4.2a}$$

$$\frac{d\boldsymbol{u}}{dt} = -\frac{e}{m_e c}\left(\boldsymbol{E} + \boldsymbol{u} \times \frac{\boldsymbol{B}}{\gamma}\right). \tag{4.2b}$$

In the absence of an RF field, but in the presence of a nearly uniform magnetic field B_0 in the axial direction, the electrons gyrate about the guiding center at the cyclotron frequency

$$\omega_c = eB_0/m_e\gamma = \Omega_0/\gamma.$$

The gyration radius is given by

$$r_L = \frac{cu_t}{\Omega_0}$$

where u_t is the component of $\boldsymbol{u}$ perpendicular to the external magnetic field.

Now, let us introduce slow-time variables [148, 149]: If

$$\Psi = \int_{t_0}^t \frac{\Omega_0}{\gamma}dt + \phi - \phi_0 \tag{4.3}$$

we make the *Ansatz*

$$u_x + iu_y = iu_t e^{i\Psi} \tag{4.4}$$

and thus
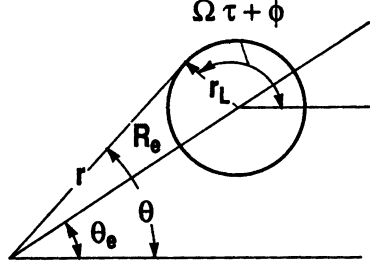
Fig. 4.2. Projection of electron orbit in the transverse plane, showing various orbital parameters [128]

$$x = X_0 + r_L \cos \Psi, \tag{4.5a}$$

$$y = Y_0 + r_L \sin \Psi, \tag{4.5b}$$

$$\frac{dx}{dt} = -\frac{cu_t}{\gamma} \sin \Psi, \tag{4.5c}$$

$$\frac{dy}{dt} = +\frac{cu_t}{\gamma} \cos \Psi, \tag{4.5d}$$

$$\frac{dz}{dt} = \frac{cu_z}{\gamma}. \tag{4.5e}$$

Here $X_0 = R_e \cos \theta_e$ and $Y_0 = R_e \sin \theta_e$ define the position of the electron's guiding center (see Fig. 4.2). In the absence of an RF field, this provides an exact solution of the equations of motion, with the electrons gyrating around the fixed guiding center (X_0, Y_0) for uniform magnetic fields. From (4.5) we readily derive

$$\frac{\Omega_0}{c} \dot{X}_0 + \dot{u}_t \cos \Psi + u_t \left(\frac{\Omega_0}{\gamma} - \dot{\Psi} \right) \sin \Psi = 0, \tag{4.6a}$$

$$\frac{\Omega_0}{c} \dot{Y}_0 + \dot{u}_t \sin \Psi - u_t \left(\frac{\Omega_0}{\gamma} - \dot{\Psi} \right) \cos \Psi = 0. \tag{4.6b}$$

Now, let us define

$$\boldsymbol{a} = -\frac{e}{m_e c} (\boldsymbol{E}_{RF} + \boldsymbol{v} \times \boldsymbol{B}_{RF}).$$

The equation of motion becomes

$$\frac{d\boldsymbol{u}}{dt} = \boldsymbol{a} - \frac{e}{m_e c} (\boldsymbol{v} \times \boldsymbol{B}_0). \tag{4.7}$$

After working out the components of (4.7), taking appropriate linear combination for the transverse variables and transforming to cylindrical polar

coordinates, we obtain the following system of slow variable equations (here $\tilde{\eta} = e/m_e c$):

$$\frac{du_t}{dt} = a_r \sin(\theta - \Psi) + a_\theta \cos(\theta - \Psi) \tag{4.8a}$$

$$+ \frac{\tilde{\eta} c u_z}{2\gamma} \left[r_L + R_e \cos(\Psi - \theta_e) \right] \frac{dB_0}{dz},$$

$$u_t \frac{d\theta}{dt} = a_\theta \sin(\theta - \Psi) - a_r \cos(\theta - \Psi) \tag{4.8b}$$

$$- \frac{\tilde{\eta} c u_z}{2\gamma} R_e \sin(\Psi - \theta_e) \frac{dB_0}{dz},$$

$$\frac{dz}{dt} = \frac{c u_z}{\gamma}, \tag{4.8c}$$

$$\frac{du_z}{dt} = a_z - \frac{\tilde{\eta} c u_t}{2\gamma} \left[r_L + R_e \cos(\Psi - \theta_e) \right] \frac{dB_0}{dz}, \tag{4.8d}$$

$$\frac{\Omega_0}{c} \frac{dR_e}{dt} = -a_\theta \cos(\theta - \theta_e) - a_r \sin(\theta - \theta_e) - \frac{\tilde{\eta} c u_z}{2\gamma} R_e \frac{dB_0}{dz}, \tag{4.8e}$$

$$\frac{\Omega_0}{c} R_e \frac{d\theta_e}{dt} = -a_\phi \sin(\theta - \theta_e) + a_r \cos(\theta - \theta_e). \tag{4.8f}$$

The calculations performed with these slow-time variables (4.8) yield nearly identical results when compared with the ordinary variables. But the basic limitation and the approximation inherent in slow-time variables is that the system is not defined when $u_t \longrightarrow 0 \Longrightarrow \partial\theta/\partial t \longrightarrow \infty$ and $r_L \longrightarrow 0$. This can happen when the entire transverse energy of the electrons is transferred to the RF field, the electrons stop gyrating (the angle ϕ becomes undefined), and merely move in the z-direction. It is obvious that in this situation the slow-time variables (4.8) are not valid when the RF fields are very strong. In practice this means that in solving (4.8) numerical instabilities may occur when u_t becomes small. One necessary condition for the system of (4.8) to be well defined is:

$$eA_0/mc^2\gamma_0 \ll 1, \tag{4.9}$$

where A_0 is the amplitude of the RF field (for an estimate, we take it to be the maximum of $|V(z)|$). Numerically $mc^2/e \simeq 511\,\text{kV}$.

For powers below a few hundred kilowatts, $|V(z)| < 90\,\text{kV}$, and (4.9) is satisfied, so that the slow-time variable system of equations (4.8) can be safely used. However, for modelling higher power gyrotrons ($P_{\text{out}} \geq 1.5\,\text{MW}$), it might be necessary to use the complete unapproximated system of equations (4.2) (written out in components).

The integration of this system is straightforward and presents no numerical problems when $u_t \longrightarrow 0$. However, in order to achieve the same accuracy as in case of slow-variable system (4.8), the time step must be ~ 20 times smaller, and the computational time will increase by the same factor. Therefore, the system described in (4.2) is not useful for parameter studies or for

an extension to a self consistent formulation. It is only useful to verify the results using slow-time variables or the adiabatic equation of motion in case of distrust in results. Further approximations result in the so-called adiabatic equation of motion which is used in many computations and modelling since they are well tested against the other methods and have proven to be adequate for most purposes. These additional approximations involve neglecting the RF magnetic fields, which are very small for TE modes near cutoff, and neglecting also the transverse motion of the guiding center, which is small for nearly uniform magnetic fields. Since the interaction is strongest under the condition of synchronous operation, the equation of motion reduces to a one dimensional one.

Following Fliflet et al. [150], the equation of motion for the transverse motion of the electrons in complex phasor form can be written as

$$
\begin{aligned}
i\frac{du_t}{dt} - \left(\frac{d\Psi}{dt} - \frac{\Omega_0}{\gamma}\right) u_t &= (a_r + ia_\theta)\, e^{i(\theta - \Psi)} + \frac{i\tilde{\eta}cu_z}{2\gamma}\frac{dB_0}{dz}\left(R_e e^{i(\theta_e - \Psi)} + r_L\right) \\
&\simeq -\tilde{\eta}\left(E_r + iE_\theta\right)e^{i\theta}e^{-i\Psi} \\
&\quad + \frac{i\tilde{\eta}cu_z}{2\gamma}\frac{dB_0}{dz}\left(R_e e^{i(\theta_e - \Psi)} + r_L\right).
\end{aligned}
\tag{4.10}
$$

Now, let us recall from the previous chapter, the expressions for the decoupled transverse fields E_t and the normalized orthonormal basis functions from (3.13) and (3.34):

$$
\boldsymbol{E_t} = \sum_{mp} V_{mp}(z)\boldsymbol{e}_{mp}(r, z, \theta)
$$

with

$$
V_{mp}(z) = V_{\max}\hat{f}_{mp}(z).
$$

Substituting these expressions into (4.10) gives

$$
\begin{aligned}
i\frac{du_t}{dt} - \left(\frac{d\Psi}{dt} - \frac{\Omega_0}{\gamma}\right) &= \frac{i\tilde{\eta}cu_z}{2\gamma}\frac{dB_0}{dz}\left(R_e e^{i(\theta_e - \Psi)} + r_L\right) \\
&\quad - \frac{i\tilde{\eta}}{2}e^{-i\Psi}\sum_{mp}C_{mp}k_{mp}e^{i\omega_{mp}t}
\end{aligned}
$$
$$
\times V_{\max}\hat{f}_{mp}(z)J_{m-1}(k_{mp}r)e^{-i(m-1)\theta} \tag{4.11a}
$$
$$
\frac{du_z}{dt} = -\frac{\tilde{\eta}cu_t}{2\gamma}\left(r_L + R_e\cos(\Psi - \theta_e)\right)\frac{dB_0}{dz}. \tag{4.11b}
$$

Now, let us introduce a slowly varying part of the gyrophase Λ defined by

$$
\Lambda = \omega_a t - \Psi
$$

where ω_a is an averaging frequency, approximately equal to the cyclotron frequency; it was first introduced by Nusinovich [156, 157] in connection with

mode competition. Neglecting all contributions except those corresponding to stationary phases $\omega_{mp} \simeq s\omega_a$ and by applying Graf's addition theorem [158], (4.11) reduces to

$$\frac{du_t}{dt} + i\left(\omega_a - \frac{d\Lambda}{dt} - \frac{\Omega_0}{\gamma}\right)u_t = +\left(\frac{\tilde{\eta}cu_z r_L}{2\gamma}\right)\frac{dB_0}{dz}$$

$$-\frac{\tilde{\eta}}{2}\sum_{mp}C_{mp}k_{mp}V_{\max}\hat{f}_{mp}(z)J_{s-1}(k_{mp}r_L)$$

$$\times e^{i(\omega_{mp}-s\omega_a)t+is(\Lambda+\theta_e)}J_{m-s}(k_{mp}R_e)e^{-im\theta_e},$$

$$\text{(4.12a)}$$

$$\frac{du_z}{dt} = -\left(\frac{\tilde{\eta}cu_t}{2\gamma r_L}\right)\frac{dB_0}{dz}. \tag{4.12b}$$

In the fixed guiding center approximation, the initial azimuth θ_e (see Fig. 4.2) is approximately constant. For counter-rotating modes, $J_{m-s}(k_{mp}R_e)$ $\times \exp(-im\theta_e)$ should be replaced by $(-1)^s J_{m+s}(k_{mp}R_e)\exp(-im\theta_e)$. To compute the efficiency, one must average over both θ_e and initial gyrophase Λ_0.

For small values of the Larmor radius, one may take

$$J_{s-1}(k_{mp}r_L) \simeq \left(\frac{k_{mp}cu_t}{2\Omega_0}\right)^{s-1}\frac{1}{(s-1)}. \tag{4.13}$$

Assuming that $k_{mp}c/\Omega_0 \simeq 1$, this approximation (4.13) is valid if $(u_t/2)^2 < 0.1$ or $\gamma\beta_\perp < 0.6$. For $\beta_{\perp_0} \simeq 0.4$, this means $\gamma_0 < 1.5$ or $U_b < 250$ kV. Thus, this approximation is not valid for high voltage gyrotrons (where beam energies exceed 250 keV) or CARMs. Assuming that the approximation (4.13) is valid, and defining $P = iu_t e^{-i(\Lambda+\theta_e)}$, we have

$$\frac{dP}{dt} + i\left(\omega_a - \frac{\Omega_0}{\gamma}\right)P = \frac{i\tilde{\eta}cu_z}{2\gamma}\frac{dB_0}{dz}\frac{P}{\Omega_0} - \frac{i\tilde{\eta}}{2}\sum_{mp}C_{mp}k_{mp}V_{\max}\hat{f}_{mp}(z)$$

$$\times\frac{1}{(s-1)}J_{m-s}(k_{mp}R_e)e^{im\theta_e}$$

$$\times\left[\exp\left(\omega_{mp} - s\omega_a\right)t\right]\left(\frac{ck_{mp}P^*}{2\Omega_0}\right)^{s-1} \tag{4.14}$$

with $\gamma = \sqrt{1 + u_z^2 + |P|^2}$. We now change the independent variable from t to

$$z = \int_{t_0}^t \frac{cu_z}{\gamma}dt.$$

For a single mode calculation, it suffices to average over the initial phase

$$\Lambda_0 + \left(1 - \frac{m}{s}\right)\theta_e$$

and take $\omega_a = \omega_{mp}/s$. The average over θ_e then becomes trivial and one may ignore the explicit dependence on it. The result is

$$\frac{dP}{dz} + \frac{i\omega}{cu_z}\left(\gamma - \frac{\Omega_0}{\omega}\right)P = +\frac{i\tilde{\eta}}{2}\frac{dB_0}{dz}\frac{P}{\Omega_0}$$

$$+\frac{i\tilde{\eta}}{2}\frac{\gamma}{u_{z0}}C_{mp}k_{mp}V_{\max}\left(\frac{\hat{f}_{mp}(z)}{(s-1)!}\right)$$

$$\times J_{m-s}(k_{mp}R_e)\left(\frac{ck_{mp}P^*}{2\Omega_0}\right)^{s-1}, \quad (4.15a)$$

$$\frac{du_z}{dz} = -\left(\frac{\tilde{\eta}cu_t r_L}{u_z}\right)\frac{dB_0}{dz}. \quad (4.15b)$$

For counter-rotating modes the factor $J_{m-s}(k_{mp}R_e)$ is replaced by $(-1)^s J_{m+s}(k_{mp}R_e)$. In the following treatment, this factor will usually be denoted by G_{mp}.

The terms explicitly involving the magnetic field tapering are frequently neglected in the literature. In fact, it has already been shown in several cases of interest that their contribution to the efficiency is small for very high frequency gyrotrons [159] and that the dominant contribution to the effect of magnetic field tapering is in the fact that the detuning depends on z. When these terms are neglected, the adiabatic equation of motion becomes a single complex differential equation of the form:

$$u_z \simeq \text{constant}, \quad (4.16a)$$

$$\frac{dP}{dz} + \left(\frac{i\omega}{c\beta_{z0}}\right)\left(\frac{\gamma}{\gamma_0} - \frac{\Omega_0}{\omega\gamma_0}\right)P = \frac{i\tilde{\eta}}{2}\frac{\gamma}{u_{z0}}C_{mp}G_{mp}k_{mp}V_{\max}$$

$$\times\left(\frac{\hat{f}_{mp}(z)}{(s-1)!}\right)\left(\frac{ck_{mp}P^*}{2\Omega_0}\right)^{s-1}.$$

$$(4.16b)$$

The effect of space charge on the beam field interaction has been neglected in the entire derivation. For most cases of interest, this is justified. Modifications to include the space charge effects has been given in the literature [128, 154, 160, 161]. The electromagnetic radiation in a gyrotron is generated by the azimuthal bunching of electrons in their gyro-orbits. This bunching is also a source of electrostatic fields, which then could affect the electron motion.

The effects of space charge can be included by considering the electrostatic potential produced in the distributed beam model [161]

$$\left\langle \frac{q\phi}{m_e} \right\rangle = -\left(\frac{2q^2}{4\pi\epsilon_0 m_e} \right) \int \left(\frac{d^3u'f}{2} \right) \int dt_0 \left(\frac{\Omega_0}{2\pi\gamma} \right) \left(\frac{\pi\Delta^2}{2} \right)$$

$$= -\left(\frac{e^2}{4\epsilon_0 m_e} \right) \int d^3u' \left[\frac{f\left(u_t^2 + u_t'^2 - 2u_t'u_t \cos(\varphi - \varphi') \right)}{\Omega_0^2} \right].$$

(4.17)

Here f is the distribution function of guiding centers. The electrostatic field which contributes to the equation of motion is the gradient of ϕ. After considerable manipulation, one finds, with $n_0 = \int f d^3u'$ and assuming that $\Psi - \Psi' = \varphi - \varphi'$, $\Omega/\Omega_0 \simeq 1$,

$$(a_x)_{sc} \simeq -\frac{\partial \langle q\phi/m_e \rangle}{\partial x}$$

$$= \left(\frac{e^2}{4\epsilon_0 m_e} \right) \left[\Omega \cos\Psi \frac{\partial \langle q\phi/m_e \rangle}{\partial u_t} - \frac{\Omega}{u_t} \frac{\partial \langle q\phi/m_e \rangle}{\partial \varphi} \right]$$

$$= \left(\frac{e^2}{2\epsilon_0 m_e \Omega_0} \right) \left[\cos\Psi \left\{ u_t n_0 - \int d^3u' f u_t' \cos(\varphi - \varphi') \right\} \right.$$

$$\left. - \sin\Psi \int d^3u' f u_t' \sin(\varphi - \varphi') \right]$$

$$= \left(\frac{e^2}{2\epsilon_0 m_e \Omega_0} \right) \left[u_y n_0 - \int d^3u' f u_t' \sin\Psi' \right], \qquad (4.18a)$$

similarly

$$(a_y)_{sc} \simeq -\left(\frac{e^2}{2\epsilon_0 m_e \Omega_0} \right) \left[u_x n_0 - \int d^3u' f u_t' \sin\Psi' \right], \qquad (4.18b)$$

where $(a_x)_{sc}$ and $(a_y)_{sc}$ are the components of the acceleration a appearing in the equation of motion (4.7) with a subscript to denote the space charge contribution.

Hence the space charge contributions to the right hand side of the expression for the adiabatic equation of motion (4.16) are

$$\left(\frac{i\omega_p^2}{2\Omega_0} \right) \left[u_\perp - \frac{1}{n_0} \int d^3u' f u_t' \left\{ \cos(\Psi - \Psi') - i\sin(\Psi - \Psi') \right\} \right], \qquad (4.19)$$

where ω_p is the plasma frequency. For an annular beam of thickness r_L it is given by:

$$\omega_p^2 = \left(\frac{e^2 n_0}{\epsilon_0 m_e} \right) \simeq \frac{2\pi I_0}{8500A} \frac{\Omega_0 c}{4\pi R_e \beta_\perp \beta_z}. \qquad (4.20)$$

By ignoring the dependence on θ_e as is appropriate for a single mode calculation, the additional contributions to the right hand side of (4.16) then becomes

$$\left(\frac{i\omega_p^2}{2\Omega_0}\right)\left[P + \frac{i}{n_0}\int d^3u'\, fu'_t \exp(i(\Psi' - \omega t))\right]$$

$$= \left(\frac{i\omega_p^2}{2\Omega_0}\right)\left[P - \frac{1}{n_0}\int d^3u'\, fP'\right]. \tag{4.21}$$

We now replace $(1/n_0)\int d^3u'\, fP'$ by $(1/N)\sum P_i = \langle P\rangle$, where the average is over initial gyrophases, as before. The equation of motion then becomes

$$\frac{dP}{dz} + \left(\frac{i\omega}{c\beta_{z0}}\right)\left(\frac{\gamma}{\gamma_0} - \frac{\Omega_0}{\omega\gamma_0}\right)P$$

$$= \left(\frac{\eta}{2}\cdot\frac{\gamma}{u_{z0}}\right)C_{mp}G_{mp}k_{mp}\hat{f}_{mp}(z)V_{\max}$$

$$+ \left(\frac{i\omega_p^2}{2\Omega_0}\right)\left(\frac{\gamma}{cu_{z0}}\right)[\langle P\rangle - P]. \tag{4.22}$$

This form is computationally much easier to work with than the formulas given by Bratman and Petelin [154], although the latter use a more realistic model for the beam. A similar term was found by Latham [162] for gyroklystron amplifiers. For that case, space charge results in some efficiency enhancement at very high power levels and a moderate reduction in efficiency at lower power levels when ω_p^2/Ω_0^2 is larger than ≈ 0.005. This is equivalent to the criterion given by Bratman et al [155], namely $(4/\pi\beta_\perp^2)\omega_p^2/\Omega_0^2 \ll 1$. Now

$$\frac{\omega_p^2}{\Omega_0^2} = \frac{2\pi I_0}{8500A}\frac{c}{4\pi R_e\beta_\perp\beta_z\Omega_0} \simeq 9.4\times 10^{-6}A^{-1}\frac{I_0\lambda}{R_e\beta_\perp\beta_z}. \tag{4.23}$$

The results of some earlier experiments at FZK with a $TE_{10,4}$ gyrotron with $\lambda = 2.14$ mm, $R_e = 3.64$ mm, and $\beta_z\beta_\perp \approx 0.1 - 0.15$ indicated that the effect of space charge on the interaction is negligible for currents less than several hundred amperes. This is also true for the TE_{03} gyrotron experiments [153]. For a more powerful gyrotron, the current I_0 increases, but a more highly overmoded gyrotron with a smaller value of λ/R_e is used, and the effect of space charge on the beam-wave interaction in the resonator is probably not larger. A more important effect of space charge for gyrotron operation is the degradation of the beam quality due to voltage depression which will be discussed in detail in a subsequent chapter.

Interaction Efficiency

The electronic or interaction efficiency η can be calculated from the electron energy loss as follows. It has been observed that since $\gamma = \sqrt{1 + u_z^2 + |P|^2}$,

$$\frac{d\eta}{dz} = \left(\frac{1}{1-\gamma_0}\right) \frac{d\langle\gamma\rangle}{dz} ,$$

$$\gamma\frac{d\gamma}{dz} = \frac{1}{2} \frac{d|P|^2}{dz} .$$

Thus, the electronic efficiency is given by

$$\eta_{el} = \left(\frac{\gamma_0 - \langle\gamma(z_{out})\rangle}{\gamma_0 - 1}\right) . \tag{4.24}$$

The average $\langle\cdots\rangle$ is to be taken over initial gyrophase Λ_0 (as mentioned before, in single mode approximation, averaging over θ_e is trivial). The electronic efficiency is also given by an integral over the beam-field interaction:

$$\eta_{el} = \left(\frac{e}{2m_ec^2}\right) C_{mp}G_{mp}k_{mp}V_{max(mp)} \left(\frac{Im\left\langle\int_{z_{in}}^{z_{out}} P(z)\hat{f}^*_{mp}(z)\,dz\right\rangle}{u_{z0}(\gamma_0-1)}\right) . \tag{4.25}$$

Numerical checks show that the efficiency calculated with (4.24) and (4.25) is the same to within a fraction of a per cent, for the same parameters. As an example, the equation of motion is solved for a typical set of parameters [163] and the beam current and efficiency as a function of power for an experimental gyrotron of FZK is shown in Fig. 4.3.
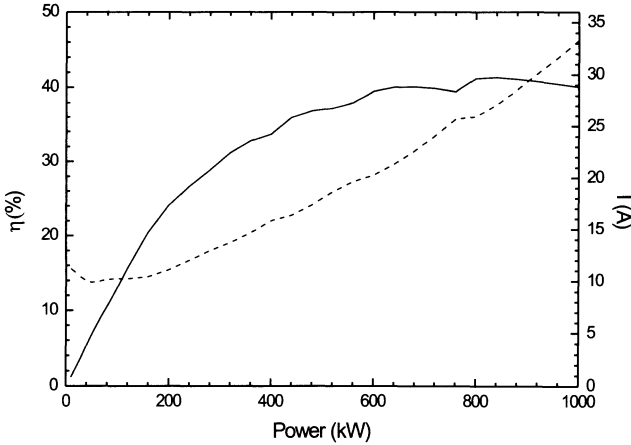
Fig. 4.3. Beam current (dashed curve) and efficiency (solid curve) as a function of output power for the $TE_{22,6}$ mode 140 GHz gyrotron ($R_0 = 15.57$ mm, $R_b = 7.93$ mm, $U_b = 75$ kV, $\alpha = 1.5$, $\theta_1/\theta_2/\theta_3 = 5/0/3°$, $L_1/L_2/L_3 = 14/16/12$ mm, $f = 140$ GHz and $Q = 1040$) [163]

Curves such as those shown in Fig. 4.3 are useful for obtaining a first estimate of the dynamical behaviour of the gyrotron. To study the dynamics of the gyrotron, we start with the energy balance equation

$$\frac{dW}{dt} = \eta(t)U(t)I(t) - \frac{\omega W}{Q}.$$

In the cold cavity approximation for the fields, the efficiency is a function of the field amplitude or, equivalently, of the output power P. As a first approximation to startup, we assume U to be constant and I to start abruptly at $t = 0$ as $I(t) = I_b$.

If the transit time t_{tr} of the electrons is smaller than the rise time t_{res} of the RF field in the cavity, the electrons will feel an approximately constant field. We can then rewrite the above equation using $P = \omega W/Q$ in the form

$$\frac{Q}{\omega}\frac{dP}{dt} = \eta(P)UI_b - P.$$

From this equation, it is obvious that if $\eta(P)$ is known, the dynamics of the system can easily be calculated. For a steady state, $P = \eta(P)UI_b$. The function $\eta(P)$ can be calculated by integrating the equation of motion numerically for various P_{out}. The steady state is stable if $dI_b/dP > 0$ and unstable if $dI_b/dP < 0$.

A gyrotron will not oscillate if the current is below a threshold value I_{start}, which depends on the beam properties, magnetic field, resonator geometry, etc. Stable operation is possible only for $I > I_{start}$ and $dP_{out}/dI_b > 0$. Otherwise, oscillation will not start at the operating point under consideration. The starting current I_{start} is the minimum current for which $dP_{out}/dt > 0$ in the limit $P_{out} \longrightarrow 0$:

$$I_{start} = \left(U\left.\frac{d\eta}{dP}\right|_{P=0}\right)^{-1}.$$

If the slope of $\eta(P)$ at $P = 0$ is negative, oscillation will not start for the operating point under consideration.

As an example, we have shown in Fig. 4.3, the beam current and efficiency versus output power. The numerical example is for a 140 GHz gyrotron considered for FZK experiment [163]. The resonator is for a TE$_{22,6}$ mode with geometry, frequency, quality factor, cold-cavity and self-consistent field profiles as shown in Fig. 4.4. The operating parameters are selected for an efficiency around 40% at 1 MW.

For the case under consideration, the starting current is slightly higher than the current corresponding to output powers between 50 kW and 200 kW, for which I(P) is less than the starting current. Stable operation would not be possible in this range. Oscillation can start at currents slightly above the starting current, but the system will soon jump to a stable steady state (having output power of about 500 kW in this example). The region of parameter

space in which the starting current exceeds the minimum current is called the region of *hard excitation*; in the region of *soft excitation*, the starting current is slightly below the current for the parameters considered. In some cases, the parameters corresponding to optimum efficiency lie in the hard excitation region, making access difficult. However, in the soft excitation region, where the starting current is smaller than the current at optimum efficiency in parameter space, the high-efficiency region is more easily accessed if the magnetic field is increased slightly. If this can be done without an overly large decrease in efficiency, it is probably desirable to do so [128]. The starting current can be calculated in linearized theory and a detailed derivation is given in the next chapter.

4.2 Self-Consistent Calculations

Up to now this formalism has not included the effect of the current term on the right hand side of (3.33), which describes the influence of the beam on the cavity field profile, including the resonant frequency (frequency pulling) and quality factor. These effects are not negligible. Calculations of the output power and efficiency for a given set of beam parameters performed using the solution of the homogeneous version of the Vlasov equation (3.33) for the field profile are known as calculations using the fixed field approximation. This is a useful first approximation, but must be extended to include the effect of the beam on the cavity field. This requires a model for the current term.

Thus one must solve the equation of motion and wave equations simultaneously to reach a self-consistent solution in a dynamic system which takes into account the effects of the beam on the cavity field profile. A self-consistent model for the gyrotron, very similar to that presented in this section [128], was first given by Bratman in 1973 [164]. The model derived here is basically that due to Fliflet et al. [150], although the algorithms used for the numerical solution of the equations are probably different. Similar and equivalent models have been reported by many other authors, for example by Charbit et al. [165]. Here, the equations are given for arbitrary harmonics. It is assumed that the RF electric field is described to sufficient accuracy by a single TE_{mp} mode, with field profile described to sufficient accuracy by the Vlasov [166] equation (3.33). The equation of motion is then as given above in (4.16). It has to be noted that this assumption neglects the distortion of the transverse structure of the RF field by the beam. It remains to determine the current term J_{mp}. The current density due to electrons in an annular beam is assumed to be given by

$$J = \sum q_i v_i \frac{\delta \left(r_i - R_e - r_L \; e^{(\Omega \tau_i + \phi_i - \phi_{0i})} \right)}{2\pi R_e} \tag{4.26}$$

where q_i is the charge of the ith electron and $\boldsymbol{v}_i$ is its velocity. The total current is given by

$$-I_0 = \int J_z dA \,. \tag{4.27}$$

Inserting (4.26) into (3.26) gives

$$J_{mp} = \frac{\mu_0}{2\pi R_e} \frac{\partial}{\partial t} \int \sum_i q_i \delta \left(r_i - R_e - r_L \, e^{i(\Omega \tau_i + \phi_i - \phi_{0i})} \right) \boldsymbol{v}_{ti} \cdot \boldsymbol{e}_{mp}^* \, dA \,. \tag{4.28}$$

Following Fliflet et al. [150], we have

$$\frac{1}{2\pi R_e} \int \delta \left(r_i - R_e - r_L \, e^{(\Omega \tau + \phi_i - \phi_0)} \right) \boldsymbol{v}_t \cdot \boldsymbol{e}_{mq}^* \, dA$$
$$= \mp C_{mq} k_{mq} J_{m\pm 1}(k_{mq} r) e^{-i(1\pm m)\theta} \boldsymbol{v}_t e^{-i(\Omega \tau + \phi_i - \phi_0)} \,. \tag{4.29}$$

Using Graf's theorem, and assuming the gyration radius r_L to be small gives for the co-rotating components (corresponding to the lower sign)

$$\left(\frac{d^2}{dz^2} + \frac{\omega_{mq}^2}{c^2} - k_{mq}^2(z) \right) V_{mq} e^{i\omega_{mq}t}$$
$$= -\mu_0 I_0 C_{mq} k_{mq} \sum \frac{J_{m-s}(k_{mq} R_e)}{2^{s-1}(s-1)!}$$
$$\times \frac{\partial}{\partial t} \left\{ \sum_i \left(\frac{u_{ti}}{u_{zi}} \right) e^{is(\Omega \tau_i * \phi_i - \phi_{0i})} \left(\frac{c k_{mq} u_{ti}}{\Omega_0} \right)^{s-1} e^{i(m-s)\theta_e} \right\} \,. \tag{4.30}$$

Introducing $P = iu_t e^{-i\Lambda}$ and selecting a single harmonic s gives

$$\left(\frac{d^2}{dz^2} + \frac{\omega_{mq}^2}{c^2} - k_{mq}^2(z) \right) V_{mq} e^{(i\omega_{mq}t)}$$
$$= -Z_0 I_0 C_{mq} k_{mq} \left[\frac{e^{im\theta_e} J_{m-s}(k_{mq} R_e)}{2^{s-1}(s-)!} \right]$$
$$\times \sum_i \left[\frac{is\omega_a P_i + \frac{\partial P_i}{\partial t}}{cu_{zi}} \right] \left[\frac{c k_{mq} P_i}{\Omega_0} \right]^{s-1} e^{is(\omega_a t_i - \theta_e)} \tag{4.31}$$

where $\Lambda = \omega_a t - \Omega \tau - \phi$ and ω_a are defined in Sect. 4.1. Here, $Z_0 = \mu_0 c \simeq 377$ Ohm is the free space impedance and for counter-rotating components, the factor $J_{m-s}(k_{mq} R_e) \exp(im\theta_e)$ should be replaced by $(-1)^s J_{m+s}(k_{mq} R_e) \exp(-im\theta_e)$, as in the previous section.

Here t_i is the time at which the ith electron passes $z = \int (\gamma_0 v_{z0}/\gamma) dt$. We wish to use the trajectories of a representative group of electrons as they move through the resonator. Since the behaviour of the system is periodic, for any electron passing through a plane $z = z_0$ outside any cycle of interest,

there is another one within some cycle an integral number of cycles sooner or later which will contribute the same amount to the sum in (4.31). Hence the summation can be taken over all the electrons passing an initial plane within one cycle. In addition, the sum must extend over the initial electron azimuth θ_e. For a single mode calculation, it suffices to average over the initial phase $[\Lambda_0 + (m/s - 1)\theta_e]$. This gives

$$
\frac{d^2 V_{mq}}{dz^2} + \left(\frac{\omega_{mq}^2}{c^2} - k_{mq}^2(z) \right) V_{mq}
$$
$$
= -Z_0 I_0 \left[\frac{C_{mq} k_{mq} G_{mq}}{(s-1)!} \right] \left(\frac{\omega_{mq}}{c u_{z0}} \right) \left(\frac{-i c k_{mq}}{2 \Omega_0} \right)^{s-1} \langle P^s \rangle . \quad (4.32)
$$

For completeness, we recall and rewrite the equation of motion (4.16) as follows:

$$
\frac{dP}{dz} + \left(\frac{i\omega}{c\beta_{z0}} \right) \left(\frac{\gamma}{\gamma_0} - \frac{\Omega_0}{\omega\gamma_0} \right) P
$$
$$
= \frac{i\tilde{\eta}}{2} \frac{\gamma}{u_{z0}} C_{mp} G_{mp} k_{mp} \frac{V_{mp}(z)}{1022 \text{ kV}} \cdot \left(\frac{c k_{mp} P^*}{2\Omega_0} \right)^{s-1} .
$$

Recall that

$$
G_{mp} = J_{m-s}(k_{mp} R_e) \quad \text{for co-rotating modes,}
$$
$$
= (-1)^s J_{m+s}(k_{mq} R_e) \quad \text{for counter-rotating modes.}
$$

For numerical calculations, the boundary condition at z_{in} is used to determine the starting value of dV/dz for the integration of (4.32) and the boundary condition at z_{out} is reformulated in the form (3.32) given in the previous chapter as

$$
|R| = \left| \frac{\frac{dV}{dz} + i k_z V}{\frac{dV}{dz} - i k_z V} \right| = \text{minimum} .
$$

When a source term is present, the eigenfrequency of a steady state solution is real, in contrast to the cold cavity case, for which the eigenfrequency has a positive imaginary part to account for the damping due to radiation out of the cavity. The normalization of the field profile is now determined by the source term and this is reflected in the fact that the coupled equations plus boundary conditions cannot be satisfied for arbitrary initial values of $V(z_{in})$. For this reason, the most efficient method of solution is to solve the coupled equations (4.16) and (4.32) simultaneously, and vary the values of ω and $|V(z_{in})|$ until $|R|$ is minimized. Note that the derivative of V at the input is given by the initial condition

$$
V'(z_{in}) = \kappa_{mp} V(z_{in}), \quad \text{where} \quad \kappa_{mp} = \sqrt{k_{mp}^2(z_{in}) - \left(\frac{\omega_{mp}^2}{c^2} \right)} .
$$

Some authors specify $V'(z_{in})$. When $V(z_{in})$ is then specified by the initial condition, this is completely equivalent. If, as is almost always the case, $|V(z_{in})| \ll V_{max}$, there is no numerical difference compared with setting $|V(z_{in})| \approx 0$.

For the numerical solution of the coupled equations (4.16) and (4.32), it is very advantageous to use the Heun predictor–corrector method [146] for the equation of motion (4.16) and the so-called *leapfrog* algorithm [147] to integrate the equation (4.32) for the field profile. This algorithm has the distinct advantage that it was not necessary to know the value of $\langle iP \rangle$ at the point $z + h$ (h is the integration step) in order to determine the field profile at $z+h$, that is, the derivatives dV/dz are evaluated at points midway between the points at which P and f are evaluated, with the result that only preceding values of $\langle P \rangle$ are used in the computation of the subsequent value of dV/dz and the integration of the coupled equations is consistent to the second order. Since one may wish to average over 30 initial gyrophases, the advantage of only having the evaluate $\langle P \rangle$ once at each step of the integration is obvious. When used in a cold cavity calculation, the *leapfrog* method gave results nearly identical to those obtained using Numerov method [123]. Most of the numerical calculations used an average over 30 electrons. This choice is a compromise between required accuracy and computer time. If significantly more than 30 electrons are used, the computer time can become prohibitive. The resonant frequency was nearly independent of the number of electrons (for 18–36 electrons, the frequency varied by at most 2 MHz), while the efficiency and output power fluctuated by about ±5%. A usable solution is usually obtained if the reflection coefficient $|R|$ is less than 0.001, even though the field profile may still contain some evidence of standing waves in the output taper.

The output power is determined by (3.31):

$$P_{out} = Re\left(\frac{1}{2\mu\omega}\right) k_{mp}^* \left| V_{mp}(z_{out}) \right|^2 .$$

If the solution is really self consistent, this will also be equal to

$$P_{out} = \eta_{el} U_0 I_0 .$$

This can be used to check the quality of the solution. The quality factor can then be found from (3.35):

$$Q P_{out} = \omega W = \left(\frac{\omega\epsilon_0}{2}\right) V_{max}^2 \int_{z_{in}}^{z_{out}} \left| \hat{f}_{mp}(z) \right|^2 dz .$$

In general, the quality factor determined in a self-consistent calculation is somewhat larger than the cold cavity Q. This effect is partially numerical. At the cavity output, the function $V(z)$ has the form

$$V(z) \simeq e^{-ik_z z} \text{ with } k_z^2 = \frac{\omega^2}{c^2} - k_{mp}^2(z_{out}) .$$

If ω is complex, then k_z is also. The sign of the imaginary part of k_z is the same as that of ω. Thus, there is a small exponential increase in the function $V_{cc} \approx \exp\left(\omega z / 2Qc\right)$ for the cold cavity field profile which is absent in the self-consistent field profile, for which ω is real. At sufficiently large values of current, another effect also called *overbunching* [164] tends to increase the quality factor. The electronic efficiency reaches a maximum somewhere before the end of the resonator, and the field strength becomes so large that the electrons gain energy from the RF field. The efficiency drops again, resulting in more energy stored in the field and less output power for a given current. This is one reason why maximum output power is achieved for other parameters than maximum efficiency. If overbunching becomes too severe, the maximum local wall losses will be too large. Obviously the gyrotron should be operated at parameters for which excess wall loading does not occur. An illustration of the self-consistent calculations for a practical FZK gyrotron operating in the TE$_{22,6}$ mode at 140 GHz [163] is shown in Figs. 4.4–4.5. Figure 4.4 shows the normalized field profiles for the resonator designed to operate in the TE$_{22,6}$ mode. Here, for the dashed curve, the beam current is 35 A and for the dotted curve, it is 60 A. It is clear from this figure that a sufficient increase in current will cause overbunching as described above, resulting in a decrease of power and efficiency. Here, the cold cavity field profile (solid curve) is also shown for comparison. The variation of power (and efficiency) with magnetic field as computed self-consistently for a typical set of operating parameters is shown in Fig. 4.5.

It is usually useful to use the cold cavity fixed field approximation to determine approximate starting values, although it turns out to be necessary to modify these at times to obtain reasonable convergence. A calculation thus requires the evaluation of the cold cavity eigenfrequency, quality factor and field profile, followed by calculations of the electron equation of motion and efficiency for various normalizations of this field profile. From these results, one selects parameter sets of interest for the full self-consistent calculation and uses the results of the cold cavity calculation as starting values for the simultaneous self-consistent solution of the equations (4.16) and (4.32). The cold cavity calculations can, therefore, give a good first overview of the desired parameter region but must be supplemented with self-consistent calculations.

Effect of Beam Velocity Spread

From the earlier studies it is observed that when velocity spread is taken into account, the initial values of u_t and u_z are not fixed, and the average in the self-consistent equations must be extended to include an average over initial values of these quantities. As a first step, one may consider a simple three point average over a triangular distribution in initial perpendicular velocity. The full width at half maximum is $2\ \Delta\beta_\perp$ and the electrons are assumed to be distributed with half at the central value $\beta_{\perp 0}$ and one quarter each at $\beta_{\perp 0} \pm \Delta\beta_\perp$. This can be considered to be a crude approximation to a
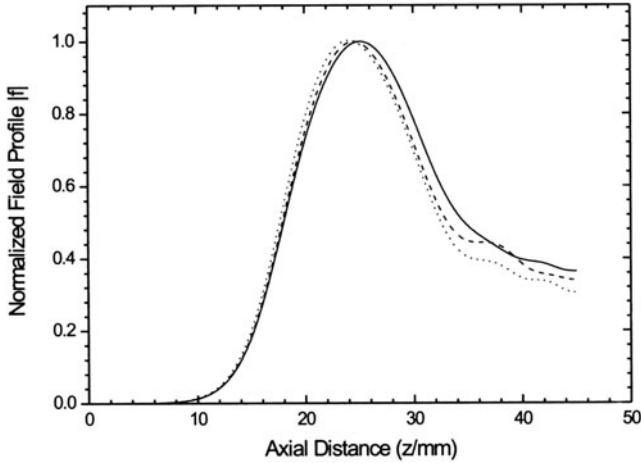
Fig. 4.4. Normalized field profile for a $TE_{22,6}$ mode 140 GHz gyrotron resonator with $R_0 = 15.57$ mm, $\theta_1/\theta_2/\theta_3 = 5/0/3°$, $L_1/L_2/L_3 = 14/16/12$ mm. Solid curve: cold cavity, $f = 140$ GHz, $Q = 1040$; Dashes: self-consistent, $f = 140.030$ GHz, $Q = 1135$, $I_b = 35$ A; Dots: self-consistent, $f = 140.082$ GHz, $Q = 1380$, $I_b = 60$ A; for the self-consistent calculations, $U_b = 78$ kV and $\alpha = 1.5$ [163]

Gaussian distribution. It has been pointed out by Ergakov and Moiseev [167] that the detailed form of the velocity distribution is less important than the size of the velocity spread. Numerous studies indicate that velocity spread can lead to a reduction of the output power and efficiency.

Beam energy spread is less important; a spread of 2% in the kinetic energy of an electron beam with 80 keV ($\Delta E_{kin} = 1.6$ keV), corresponds to a spread in γ_0 of only ± 0.003, or about 0.3%, which has no observable effect on output power and efficiency.

4.3 Dimensionless Variables

A number of different sets of dimensionless variables have been proposed and used by various workers or groups of workers. These can be very helpful in analyzing gyrotron behavior independent of nonessential parameters. The choice depends partly on the application and/or approximations used, and partly on the taste of the user.

For example, if we define $\widetilde{P}$ by

$$P = u_{t0}\widetilde{P} \tag{4.33}$$

and a detuning parameter δ as
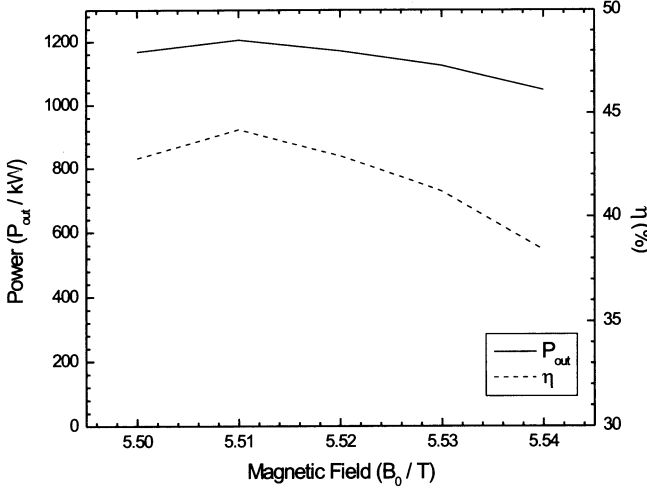
Fig. 4.5. Output power (solid curve) and efficiency (dashed curve) as a function of beam current for a TE$_{22,6}$ mode 140 GHz gyrotron ($U_b = 78$ kV, $I_b = 35$ A, $\alpha = 1.5$, $\theta_1/\theta_2/\theta_3 = 5/0/3°$, $L_1/L_2/L_3 = 14/16/12$ mm) [163]

$$\delta = 1 - \frac{s\Omega_0}{\gamma_0\omega}, \tag{4.34}$$

and

$$F_{mp} = \frac{eV_{\max}}{2m_ec^2} \frac{C_{mp}G_{mp}}{u_{t0}} \frac{ck_{mp}}{\omega} \frac{1}{(s-1)!}, \tag{4.35}$$

recall that one may write $V_{mp}(z) = V_{\max}\hat{f}_{mp}(z)$ where $\hat{f}_{mp}(z)$ is the normalized (complex) field profile, and

$$C_{mp}G_{mp} = (\mp 1)^s \frac{J_{m\pm s}(k_{mp}R_e)}{J_m(x_{mp})\sqrt{\pi(x_{mp}^2 - m^2)}}, \tag{4.36}$$

the equation of motion (4.16b) becomes

$$\frac{d\widetilde{P}}{dz} + i\frac{\omega}{v_{z0}}\frac{1}{s}\left(\frac{\gamma}{\gamma_0} - 1 + \delta\right)\widetilde{P}$$

$$= -i\frac{\omega}{v_{z0}}\frac{\gamma}{\gamma_0}F_{mp}\hat{f}_{mp}(z)\left(\frac{ick_{mp}u_{t0}\widetilde{P}^*}{2\Omega_0}\right)^{s-1}. \tag{4.37}$$

In a self-consistent formulation, the field profile satisfies

$$\frac{d^2 F_{mp}\hat{f}}{dz^2} + \left(\frac{\omega^2}{c^2} - k_{mp}^2(z)\right) F_{mp}\hat{f}_{mp}$$
$$= -\widetilde{I}_{mp}\left(\frac{-ick_{mp}u_{t0}}{2\Omega_0}\right)^{s-1}\langle\widetilde{P}^s\rangle, \qquad (4.38)$$

with

$$\widetilde{I}_{mp} = \frac{eZ_0 I_b}{2m_e c^2}\left(\frac{C_{mp}k_{mp}G_{mp}}{(s-1)!}\right)^2 \cdot \frac{1}{u_{z0}}. \qquad (4.39)$$

Here, I_b is the beam current. As usual, one imposes radiation boundary conditions at the output. If these equations are rewritten in terms of the independent variable $\widetilde{z} = \omega z/v_{z0}$, they become essentially independent of the mode, i.e.:

$$\frac{d\widetilde{P}}{d\widetilde{z}} + i\frac{1}{s}\left(\frac{\gamma}{\gamma_0} - 1 + \delta\right)\widetilde{P} = -i\frac{\gamma}{\gamma_0}F_{mp}\hat{f}_{mp}(\widetilde{z})\left(\frac{ick_{mp}u_{t0}\widetilde{P}^*}{2\Omega_0}\right)^{s-1}, (4.40)$$

$$\frac{d^2 F_{mp}\hat{f}_{mp}}{d\widetilde{z}^2} + \kappa^2(\widetilde{z})F_{mp}\hat{f}_{mp} = -\widetilde{I}_{mp}\frac{v_{z0}^2}{\omega^2}\left(\frac{-ick_{mp}u_{t0}}{2\Omega_0}\right)^{s-1}\langle\widetilde{P}^s\rangle, (4.41)$$

with $\kappa^2(\widetilde{z}) = \beta_{z0}^2\left(1 - \frac{c^2 k_{mp}^2(\widetilde{z})}{\omega^2}\right)$.

The quantity F_{mp} is related to the similar quantity used by Russian researchers by

$$F_G = \left(\frac{s\beta_{\perp 0}^2}{2}\right)^{s-2} F_{mp}. \qquad (4.42)$$

Binomial expansion of $\gamma \simeq 1 + \frac{1}{2}(\beta_z^2 + \beta_\perp^2)$ gives

$$\frac{\gamma}{\gamma_0} - 1 + \delta \simeq \frac{\beta_{\perp 0}^2}{2}\left(\left|\widetilde{P}\right|^2 - 1\right) + \delta = \frac{\beta_{\perp 0}^2}{2}\left(\left|\widetilde{P}\right|^2 - 1 + \Delta\right), \qquad (4.43)$$

and the electronic efficiency can be written as

$$\eta_{el} = \frac{u_{t0}^2\left(1 - \left\langle\left|\widetilde{P}\right|^2\right\rangle\right)}{u_{t0}^2 + u_{z0}^2}, \quad \text{or} \qquad (4.44)$$

$$\eta_{el} = \frac{\alpha^2}{1 + \alpha^2}\eta_\perp, \quad \alpha = \frac{v_{\perp 0}}{v_{z0}} \qquad \text{(this defines } \eta_\perp\text{)}. \qquad (4.45)$$

If one regards $(|\widetilde{P}|^2 - 1)$ as essential and defines a new independent variable

$$\zeta = \widetilde{z}\,\frac{\beta_{\perp 0}^2}{2} \qquad (4.46)$$

the system of equations becomes (for $s = 1$)

$$\frac{d\widetilde{P}}{d\zeta} + i\left(\left|\widetilde{P}\right|^2 - 1 + \Delta\right)\widetilde{P} = -i\left(\frac{2}{\beta_{\perp 0}^2}\right)F\hat{f}, \tag{4.47}$$

$$\frac{d^2 F\hat{f}}{d\zeta^2} + \left(\frac{2}{\beta_{\perp 0}^2}\right)^2 \kappa^2(\widetilde{z})F\hat{f} = -\widetilde{I}\frac{v_{z0}^2}{\omega^2}\left(\frac{2}{\beta_{\perp 0}^2}\right)^2 \langle\widetilde{P}\rangle. \tag{4.48}$$

After a few more minor redefinitions one obtains the system of equations given, for example by [157, 164, 168]. In particular, one must set $\frac{ck_{mp}(\zeta_m)}{\omega} \approx 1$ and $\gamma_0 \approx 1$ in the definition of $\widetilde{I}$.

In particular, one has the following dimensionless variables, namely, normalized interaction length (μ), normalized field amplitude (F), and normalized detuning (Δ):

$$\mu = \left(\frac{\pi L}{\lambda}\right)\left[\frac{\beta_{\perp 0}^2}{\beta_{z0}}\right], \quad \zeta = \left(\frac{\pi z}{\lambda}\right)\left[\frac{\beta_{\perp 0}^2}{\beta_{z0}}\right] = \frac{\widetilde{z}\beta_{\perp 0}^2}{2}, \tag{4.49a}$$

$$\Delta = \left(\frac{2}{\beta_{\perp 0}^2}\right)\left(1 - \frac{s\Omega_0}{\omega\gamma_0}\right) = \left(\frac{2}{\beta_{\perp 0}^2}\right)\delta, \tag{4.49b}$$

$$F_G = \left(\frac{2}{\beta_{\perp 0}^2}\right)\left[\frac{eV_{\max}}{2m_e c^2}\right]\left(\frac{C_{mp}G_{mp}}{u_{t0}}\right)\left(\frac{s\beta_{\perp 0}}{2}\right)^{s-1}\left(\frac{1}{s!}\right), \tag{4.49c}$$

and, for self − consistent calculations

$$I_G = \left(\frac{2}{\beta_{\perp 0}}\right)^{4-s}\left(\frac{eZ_0 I_0}{2m_e c^2}\right)\left[\beta_{z0}\left(C_{mp}G_{mp}\right)^2 s\right]\left(\frac{s}{(s-1)!}\right)^2. \tag{4.49d}$$

Here L is the effective length of the field profile, usually taken to be the length of an equivalent Gaussian field profile of the form $\exp[-(2z/L - 1)^2]$.

The relation the variables described at the beginning to those used by the IAP group [157] is given by equations (4.42), (4.46) and

$$\widetilde{I}_{mp} = \left(\frac{\beta_{\perp 0}^2}{2}\right)^3\left(\frac{ck_{mp}}{\omega}\right)\left(\frac{I_G}{\gamma_0}\right). \tag{4.50}$$

Antonsen, et al. [169] introduced another set of dimensionless variables, namely

$$\delta_A = \left(\frac{L\omega}{2v_{z0}}\delta\right), \tag{4.51a}$$

which is the transit angle given by Bratman et al.[155] and

$$\varepsilon_A = \left[\frac{eV_{\max}}{2m_e c^2}\right]\left[\frac{C_{mp}G_{mp}}{u_{t0}}\right]\left(\frac{L\omega}{2v_{z0}}\right). \tag{4.51b}$$

These approximations are adequate for beam voltages less than about 80 kV, but may not be sufficiently accurate at higher voltages. Suitable dimensionless variables for relativistic gyrotrons and other cyclotron resonance masers have been introduced by the IAP group, and the physics of such devices is
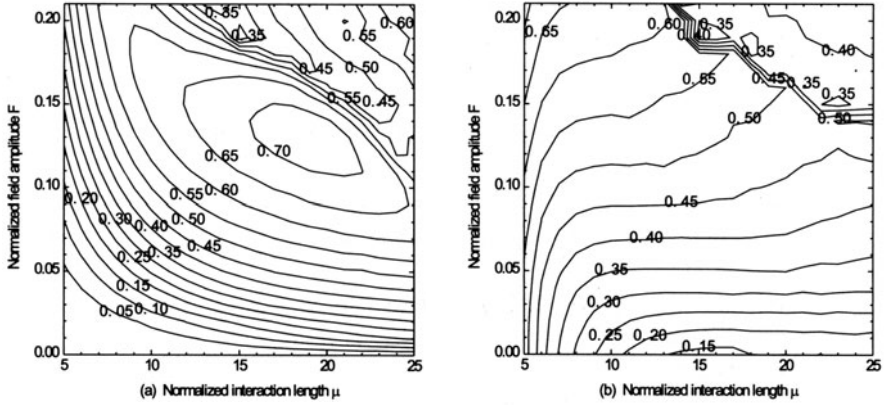
Fig. 4.6. Contours of Iso-transverse efficiency $\eta_\perp$ (**a**) and corresponding normalized iso-detuning Δ (**b**) for normalized field amplitude and interaction lengths for the fundamental cyclotron harmonic operation of the gyrotron [173]

discussed [170–172]. The results of calculations of the perpendicular efficiency for optimized for detuning parameter computed for various normalized field amplitude and interaction lengths are shown in Fig. 4.6 for fundamental operation of the gyrotron. The contours are similar for higher harmonics [173].

For cold cavity calculations, the dimensionless variables μ, Δ and F provide a compact description of the essential features of gyrotron behaviour, within the limits of the approximations made, which includes neglect of any form of velocity spread. In a self-consistent calculation, both μ and Δ will be modified from the input values by frequency pulling and distortion of the field profile. As has been pointed out by Bratman et al.[154], the value of μ at which optimum efficiency occurs is reduced to 14.5 from the Gaussian cold cavity value of 17. Even then, overbunching can occur if the beam current parameter is too large. Also, by choosing an even shorter resonator (that is, a smaller value of μ), it is possible to raise the maximum output power with only a modest sacrifice in efficiency, since the quality factor is decreased, and with it the wall loading [174]. Antonsen and Levush [169] point out that devices having a smaller value of μ have larger stable operating regimes. Such trade-offs limit the value of the popular $\mu - F$ contour plots (which do not appear at all in the IAP collected papers [155]). They are of some use for a first orientation in parameter space, but must be supplemented by self-consistent calculations over a fairly large region of the parameter space of interest, considerations of wall loading, voltage depression [175, 176] and mode competition.

4.4 Mode Competition in Gyrotron Oscillators

One of the most important problems in the design of high-power gyrotrons is to ensure that the device operates in the desired mode. For high-power, high-frequency devices the effective mode density is very high, since the spectrum is dense and the current is above threshold for many modes. One must ask the following questions: Is operation in a single mode possible? How can one ensure single mode operation at the highest possible efficiency? It turns out that if certain conditions are met, single mode operation is stable. However, for a given set of parameters, any one of several modes can be the stable operating mode, and typically only one of these has the desired high efficiency. One must then ask how to access this mode in a manner that ensures that it operates stably.

The problem of mode interaction in gyrotron oscillators was first studied around 1974 [177–179]. A more systematic review of the main effects of mode interaction was given in [86, 156, 157]. The role of these effects depends on several characteristic times that are important for the dynamics of multimode gyrotrons.

To describe mode interaction in gyrotrons, several time scales are important. First there is a pulse rise time t_{pulse}. This is the rise time for the beam parameters (typically a few hundred μs). In the case of CW (or long pulse operation), the electron beam will be neutralized as a result of collisions with residual gas molecules in the tube. This occurs on a time scale t_{neut} which is of the order of a few tens of milliseconds. The cavity reaction time is given approximately by

$$t_{res} \simeq \frac{Q}{\omega} \tag{4.52}$$

where Q is the quality factor of the resonator, or by τ_c, as defined in equation (5.45). The electron transit time is

$$t_{tr} = \frac{L}{v_{z0}} \tag{4.53}$$

where L is the length of the interaction region. The cyclotron resonance band is given by

$$\frac{\Omega_0}{\gamma_0} - \frac{\pi}{t_{tr}} < \omega < \frac{\Omega_0}{\gamma_0} + \frac{\pi}{t_{tr}}. \tag{4.54}$$

Typically

$$t_{tr} \ll t_{res} \ll t_{pulse} \ll t_{neut}. \tag{4.55}$$

When the transit time is much shorter than the cavity reaction time, one can neglect changes in the amplitudes of the various modes during the pass of a single electron through the resonator. If this is not the case, the so-called self modulation instability can occur [180]. This can occur in very short-pulse experiments (see [2] and the references therein), but is not relevant for gyrotrons developed for technological applications or fusion plasma heating.

It is also necessary to consider the beat period between two modes labeled 1 and 2 (for example), defined by the expression

$$t_{beat} = \frac{2\pi}{|\omega_1 - \omega_2|}. \tag{4.56}$$

If three modes are involved, additional periods such as

$$\frac{2\pi}{|\omega_1 + \omega_3 - 2\omega_2|}$$

must be considered (here it has been assumed that the modes numbered 1,2,3 are approximately evenly spaced, with $\omega_1 < \omega_2 < \omega_3$).

The width of the resonance curves of the cavity modes $(1/t_{res})$ is generally much smaller than the cyclotron resonance band. However, the separation between mode frequencies can be of the order of the width of the cyclotron resonance band. In this case, the phase difference between the two modes can vary significantly during the electron transit time and an electron bunch formed as a result of interaction with one mode may have different phases with respect to different modes. The dispersive properties of the beam, as an active medium which causes the modes to interact with one another, are important. For the case of two mode interaction, this can happen when $t_{beat} \geq t_{tr}$ but not when $t_{beat} \gg t_{tr}$. The effects of such dispersion will be described later. We next discuss phase beating in multimode gyrotrons. A thin annular beam of gyrating electrons excites TE_{mp} modes of cylindrical (or coaxial) cavities near cutoff. The fields of these modes rotate azimuthally (here for the jth mode) as

$$\exp[i(\omega_j t - m_j \phi)].$$

Each mode can be resonant with the electron beam at its cyclotron harmonic s_j. Hence the phase of the resonant component of this mode with respect to the gyrophase can be taken to be

$$\frac{1}{s_j}(\omega_j t - m_j \phi).$$

Thus in the equations describing mode interaction via the electron beam, one must deal with the difference in phases of the resonant components of the various modes. For two modes, this is

$$(\Delta\phi)_2 = \frac{1}{s_1}(\omega_1 t - m_1 \phi) - \frac{1}{s_2}(\omega_2 t - m_2 \phi), \tag{4.57a}$$

for three modes

$$(\Delta\phi)_3 = \frac{1}{s_1}(\omega_1 t - m_1 \phi) + \frac{1}{s_3}(\omega_3 t - m_3 \phi) - \frac{2}{s_2}(\omega_2 t - m_2 \phi), \tag{4.57b}$$

and so on. When one considers the interaction of modes with a beam of electrons having various azimuthal guiding center coordinates θ_e, one may

conclude that the evolution of amplitudes for two modes does not depend on their phases not only when the period of the resonant phase beating is much smaller than the cavity reaction time

$$|s_2\omega_1 - s_1\omega_2| \gg \frac{1}{t_{res}} = \frac{\omega}{Q} \tag{4.58}$$

but also when the azimuthal indices of the modes fulfill the condition [156, 181]

$$s_2 m_1 \neq s_1 m_2. \tag{4.59}$$

If three modes are involved, the corresponding conditions are

$$|s_2 s_3 \omega_1 + s_1 s_2 \omega_3 - 2 s_1 s_3 \omega_2| \gg \frac{\omega}{Q} \tag{4.60a}$$

and

$$s_2 s_3 m_1 + s_1 s_2 m_3 \neq 2 s_1 s_3 m_2. \tag{4.60b}$$

The starting point for a calculation of mode competition is the equation of motion for an electron in the field produced by a superposition of modes; then one must consider the power transfer from the electrons to each individual mode and determine the possible equilibrium states.

The equation of motion for an electron in an RF field produced by several modes is

$$\frac{dP}{dz} + i\frac{\omega_a}{c\beta_{z0}}\left(\frac{\gamma}{\gamma_0} - \frac{\Omega_0}{\gamma_0 \omega_a}\right) P$$
$$= -i\frac{\gamma \omega_a}{c u_{z0}} \sum_j F_j \hat{f}_j(z) e^{[i\psi_j]} \left(\frac{ick_j P^*}{2\Omega_0}\right)^{s_j - 1}. \tag{4.61}$$

Here the index j is used as an abbreviation for mp. As before $P = iu_t \exp(-i\Lambda)$ describes the transverse component of the normalized electron momentum $\boldsymbol{u} = \boldsymbol{p}/m_0 c = \gamma \boldsymbol{v}/c$, with $\Lambda = \omega_a t - \Omega \tau - \phi$ as the slowly varying part of the gyrophase; ω_a is an averaging frequency introduced by Nusinovich [156, 157] as mentioned in Sect. 4.1; s_j is the harmonic number; and $k_j = x_j/R(z)$ (x_j is the pth root of $J'_m(x_j) = 0$ for the TE_{mp} mode). The other variables are defined by (as in equation (4.35)

$$F_j = \frac{eV_{\max j}}{2m_e c^2} \frac{C_j G_j}{u_{\perp 0}} \frac{ck_j}{\omega_a} \frac{1}{(s_j - 1)!} \quad \text{and} \tag{4.62a}$$
$$\psi_j = (\omega_j - s_j \omega_a) t + (s_j \pm m_j) \theta_e. \tag{4.62b}$$

Again, θ_e is the initial azimuth of the electron in the hollow beam. In the fixed guiding center approximation, it is constant for a single electron. The factor $C_j G_j$ is given in (4.36). One can define $C_{BF} = C_j^2 k_j^2 G_j^2$ as the beam-field coupling coefficient. Note that

$$t = \int \frac{\gamma}{\gamma_0 v_{z0}} dz = \frac{1}{\omega_a} \int \frac{\gamma}{\gamma_0} d\tilde{z}. \tag{4.63}$$

In terms of dimensionless variables, one has, with $\widetilde{P} = P/u_t$, $\widetilde{z} = \omega_a z/v_{z0}$ and $\delta = 1 - \frac{\Omega_0}{\gamma_0 \omega_a}$,

$$\frac{d\widetilde{P}}{d\widetilde{z}} + i\left(\frac{\gamma}{\gamma_0} - 1 + \delta\right)\widetilde{P} = -i\frac{\gamma}{\gamma_0}\sum_j F_j \hat{f}_j(\widetilde{z})\exp[i\psi_j]. \qquad (4.64)$$

It is possible to redefine $\widetilde{P}$ with the extra phase factor $\exp[-i\psi_1]$ for $j = 1$ (usually for the so-called main mode, but the choice is in principle arbitrary) and $t = 0$. In that case, the equation of motion takes the form

$$\frac{d\widetilde{P}}{d\widetilde{z}} + i\left(\frac{\gamma}{\gamma_0} - 1 + \delta\right)\widetilde{P} = -i\frac{\gamma}{\gamma_0}\sum_j F_j \hat{f}_j(\widetilde{z})\exp[i(\psi_j - \psi_1)]. \qquad (4.65)$$

In this case,
$$\psi_j - \psi_1 = (\omega_j - \omega_1)t + (m_1 - m_j)\theta_e. \qquad (4.66)$$

One sees that only the azimuthal phase difference $(m_1 - m_j)\theta_e$ appears, and it has been shown [86] that it is sufficient to average over only the initial azimuth angle for the guiding centers. One must be sure that the number of averaging steps is not a divisor of $(m_{j1} - m_{j2})$ for any of the interesting modes.

In a self-consistent formulation, the field equations have the form (with the same assumptions as above)

$$\frac{d^2 F_j \hat{f}_j}{d\widetilde{z}^2} + \kappa_j^2(\widetilde{z})F_j \hat{f}_j = -I_{Cj}\frac{\Omega_0}{\omega_a}\langle\langle\widetilde{P}/\gamma\rangle\exp[-i(\psi_j - \psi_1)]\rangle \qquad (4.67)$$

where
$$I_{Cj} = \frac{eZ_0 I_b}{2mc^2}(C_j G_j)^2 \cdot \frac{\beta_{z0}}{\gamma_0} \qquad (4.68)$$

(the approximation $ck_j/\omega_j \simeq 1$ has been made in the right hand side of the equation for the field profile). One can also take $\omega_a = \omega_1$, at least for fixed field calculations (not self-consistent). Actually, a small correction term in the field equation should be included [182]. It amounts to replacing $\kappa_j^2(\widetilde{z})$ by $\kappa_j^2(\widetilde{z}) - I_{Cj}$ in the equations for the field profiles.

4.4.1 Energy Transfer to a Single Mode

The rate of energy transfer to the jth mode is given by

$$\frac{d\gamma_j}{dt} = -\frac{e}{m_e c^2}\boldsymbol{E}_j \cdot \frac{\boldsymbol{u}c}{\gamma} = -\frac{\widetilde{\eta}}{\gamma}\boldsymbol{E}_j \cdot \boldsymbol{u} \qquad (4.69)$$

where $\boldsymbol{E}_j$ is the RF electric field corresponding to the jth mode. Recalling that

$$u_x = -u_t \sin \Psi, \qquad u_y = u_t \cos \Psi \qquad (4.70)$$

where u_t is the component of $\boldsymbol{u}$ perpendicular to the external magnetic field; Ψ is given in equation (4.3) and that

$$E_{jx} = E_{jr} \cos \theta - E_{j\theta} \sin \theta \,, \qquad (4.71a)$$

$$E_{jy} = E_{jr} \sin \theta + E_{j\theta} \cos \theta \,, \qquad (4.71b)$$

one finds

$$\frac{d\gamma_j}{dt} = \frac{u_t}{\gamma} \frac{du_{tj}}{dt} \qquad (4.72)$$

where du_{tj}/dt is the particle acceleration due to the electric field of the jth mode. The efficiency of energy transfer to this mode is given by

$$\frac{\Delta\gamma_j}{\gamma_0 - 1} \,.$$

And the total efficiency is the sum of the efficiency for energy transfer to each mode. In practice, η_j is calculated by means of an integral over the beam-field interaction:

$$\eta_j = \mathrm{Im} \left(\int_{z_{in}}^{z_{out}} \widetilde{P}(\tilde{z}) F_j \hat{f}_j^*(\tilde{z}) \exp[-i(\psi_j - \psi_1)] d\tilde{z} \right) \frac{u_t^2}{\gamma_0(\gamma_0 - 1)} \,. \qquad (4.73)$$

4.4.2 Mode Suppression

If a mode is oscillating, it can suppress the startup of a second mode. The phenomenon was discovered by Nusinovich [86, 156] and has been studied by numerous other authors [181, 183, 184]. In many of the earlier studies it was sufficient to use the two mode formalism, since the modes of interest were the TE_{0n} and TE_{2n} modes. When one is dealing with whispering gallery modes or with high order volume modes, more modes must be taken into account. As an example, we show what happens when a single mode (here the TE_{03} mode) oscillates with the power predicted by single mode theory, and only a small amount of power is in the TE_{23} mode (or vice-versa). The cavity geometry and other parameters are similar to those discussed in [182].

In order to study this, we must consider the dynamics and time behaviour of two interacting modes. When the two modes are described by the cold cavity fixed field approximation, we have (4.69) and

$$\frac{Q_j}{\omega_j} \frac{dP_j}{dt} = \eta_j(P_1, P_2) U_b I_b - P_j \,, \qquad (4.74)$$

where $\eta_j(P_1, P_2)$ (calculated from equation (4.73)) is the efficiency for power transfer to the mode j when the power in each mode is P_1 and P_2, respectively; P_j is proportional to F_j^2 and specifies the normalization of the jth mode; U_b is the beam voltage; and I_b is the beam current.
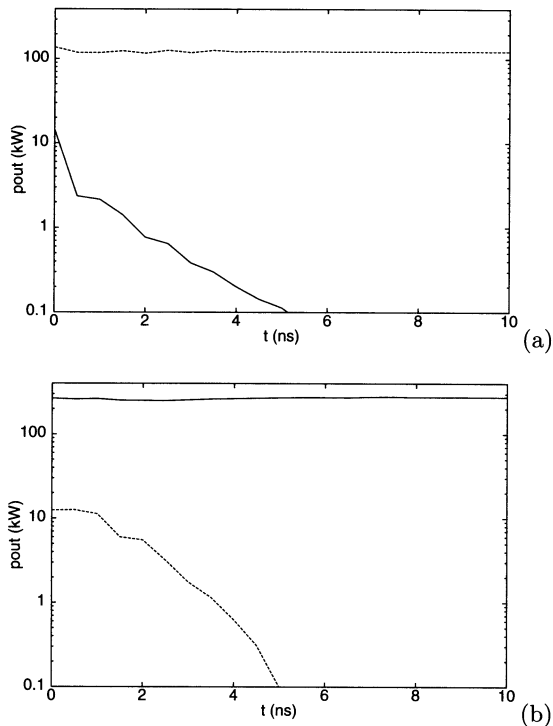
Fig. 4.7. Gyrotron dynamics for $I_b = 8\,\text{A}$, $U_b = 70\,\text{kV}$, $B = 5.42\,\text{T}$, $R_b = 1.82\,\text{mm}$, $\alpha = 1.5$. (**a**) The TE_{03} mode is present at the beginning; (**b**) The TE_{23} mode is present at the beginning

Figure 4.7 shows two cases of competition between the TE_{03} mode and the TE_{23} mode. The time dependence of P_{out} is shown for two different sets of starting amplitudes. The presence of one mode clearly suppresses the other. Generally, if a mode is oscillating, its stability against a parasitic mode can be determined by the sign of dP_{par}/dt in the presence of the mode of interest (assumed to be oscillating with a large amplitude). If dP_{par}/dt is greater than zero, the main mode is unstable; if dP_{par}/dt is less than zero, the main mode is stable. This criterion is completely equivalent to the one described by Nusinovich [156], although the proof is rather lengthy.

4.4.3 Startup

The dense mode spectrum of high order modes requires consideration of the temporal evolution of the beam parameters during the startup phase. The choice of startup scenario (the method in which the cathode and anode voltages of the gyrotron are raised from zero to their nominal values) determines the evolution of beam energy, velocity ratio and beam current during the

(initial) time changing portion of the electron beam pulse. Current neutralization during long pulse or CW operation also has an effect on the beam parameters which influences which mode oscillates in this case. This will be discussed below. Depending on the path taken, one of the possible modes will start to oscillate and will grow to a large amplitude. This mode can suppress all other competing modes even when the final beam parameters are such that another startup path would have resulted in excitation and oscillation of a different mode at higher power. Studies of the effect of startup on the behavior of cavity modes have been performed in [86, 136, 157, 181–183, 185–189], among others.

For given beam parameters, modes with a range of detunings (value of δ) are possible single mode equilibria. Which of these is reached depends on the startup scenario. If all the parameters were to instantly achieve their final values and the noise level is low, the mode with the largest linear gain (lowest starting current) grows fastest and suppresses its neighbors. However, if the system parameters attain their final values on a time scale long compared with the cavity reaction time Q/ω then the device is likely to pass through a series of "mode hoppings" as described in [181, 182].

Typically, the mode with the lowest power threshold will be excited first. As the beam parameters approach their final values, a different mode can be excited; however, its threshold must be determined in the presence of the oscillating mode and is not the one given by a single mode starting current calculation. Thus, the starting current curves (see Chap. 5) can provide useful information as to which mode is likely to be excited first, but cannot help in determining whether or not the mode remains stable when the large amplitude regime is reached. Most of the time the system passes through a sequence of stable steady states. If and when one of these becomes unstable with respect to perturbation by a parasitic mode, the system jumps to a different stable steady state. The final state is almost always dominated by a single mode. The procedure described in [181, 182] with about ten points on the voltage rise curve is usually sufficient. Results obtained with a more versatile fully time dependent code [136] are very similar to those given by [182], as shown in Fig. 4.9. Here the startup of a 140 GHz gyrotron operating in the TE_{03} mode is simulated. Parameters are the same as for the case presented in [182]: I_b=8 A, U_b=70 kV, B=5.42 T, R_e =1.82 mm, α=1.5. In both startup scenarios $\beta_\perp$ increases linearly with time (the voltage rise time is 190 μs). In one case (a) it is assumed that the accelerating voltage and the modulation anode voltage are coupled by a voltage divider, (approximating a diode–type startup), so that both beam energy and $\beta_\perp$ are proportional to the time. In case (b) a so-called triode–type startup is simulated, with the beam energy constant and only $\beta_\perp$ increases with the modulation anode voltage. These quantities are shown in Fig. 4.8. Figure 4.9 shows the output power in the various modes as a function of time. For the diode–type startup, the TE_{52} mode starts first, but is suppressed after about 122 μs by the TE_{23} mode,
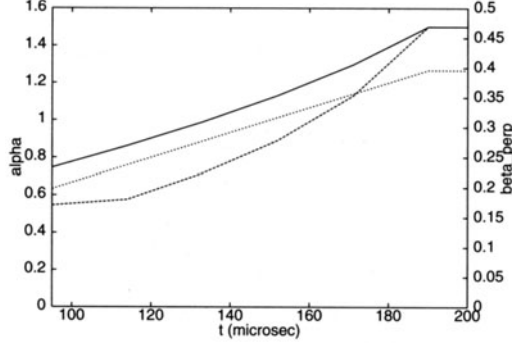
Fig. 4.8. Beam properties for two different startup scenarios. Final beam properties $U_b = 70\,\text{kV}$, $\alpha = 1.5$. $\beta_\perp$ increases linearly with time (short dashes, right axis). $\beta_\perp$ and the velocity ratio α are shown as a function of time for two startup scenarios. Solid curve: α for diode-type startup, the beam energy also increases linearly with time. Long dashes: α for triode-type startup, the beam energy is constant (70 keV)

which in turn is suppressed by the TE$_{03}$ mode (the desired mode) which achieves an output power of 278 kW. In the case of the triode–type startup, the TE$_{23}$ mode starts, and prevents the TE$_{03}$ mode from oscillating. This result is different from that given in [182] mainly because of the fact that the time-dependent code calculates the RF fields self-consistently, whereas the earlier work used the cold-cavity fixed field approximation.

4.4.4 Time Dependent Formulation

As discussed previously, most of the time the system passes through a sequence of stable steady states, and the explicit time dependence of the field amplitude does not have to be taken into account. Sometimes it is useful to consider the explicit time dependence of the field amplitude, at least under the assumption that this changes slowly compared with a gyration period. This can be applicable when the beam parameters are changing, as is the case during startup, or during beam current neutralization. In a self-consistent formulation, the field equations have the form (with the same assumptions as above)

$$\frac{\partial^2 F_j \hat{f}_j}{\partial \tilde{z}^2} + \kappa_j^2(\tilde{z}) F_j \hat{f}_j - \frac{2i\beta_{z0}^2 \omega_j}{\omega_a} \frac{\partial F_j \hat{f}_j}{\partial \tau}$$

$$= -I_{Cj} \frac{\Omega_0}{\omega_a} \langle\langle \widetilde{P}/\gamma \rangle \exp[-i(\psi_j - \psi_1)]\rangle \,, \qquad (4.75)$$

where

$$I_{Cj} = \frac{eZ_0 I_b}{2mc^2} (C_j G_j)^2 \cdot \frac{\beta_{z0}}{\gamma_0} \,,$$

and $\tau = \omega_a t$.
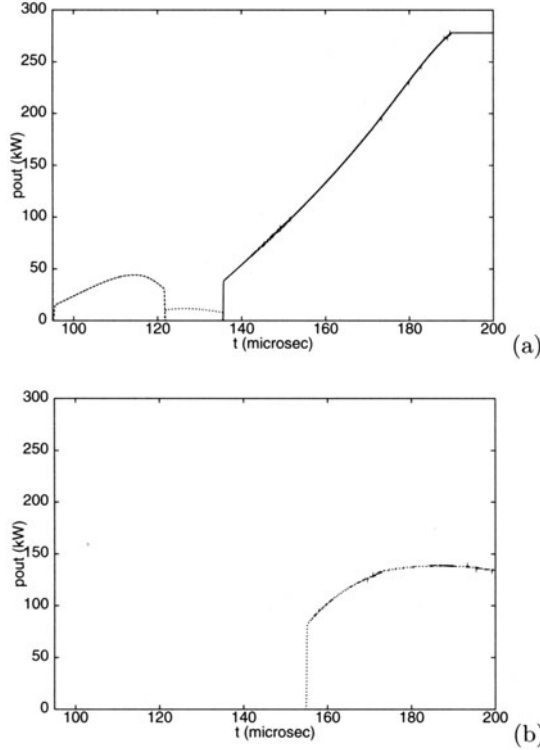
Fig. 4.9. Time dependence of output power in various modes for final beam properties $I_b = 8\,\mathrm{A}$, $U_b = 70\,\mathrm{kV}$, $B = 5.42\,\mathrm{T}$, $R_b = 1.82\,\mathrm{mm}$, $\alpha = 1.5$. Solid curve: TE_{03} mode; long dashes: TE_{52} mode; short dashes: TE_{23} mode. (**a**) Diode-type startup: the TE_{03} mode oscillates; (**b**) Triode-type startup: the TE_{23} mode oscillates; and other modes are not visible

A code to calculate the evolution of the RF field amplitudes in this approximation has been described in [136]. Equivalent equations and some applications have been presented in [190, 191], as well as in [189]. Some of the Russian work has been described in Chap. 4 of [72].

4.4.5 Current Neutralization

In long pulse or CW operation, depending on vacuum conditions in the tube, the beam space charge will, after a few tens of milliseconds, become neutralized, resulting in a change of beam energy. Since the perpendicular momentum is unaffected by voltage depression, the velocity ratio $\alpha = \beta_\perp / \beta_z$ will also be changed. The values of beam energy and velocity ratio used for startup calculations and for beam optics calculations must include the effects of voltage depression. For desired values of beam energy and velocity ratio in CW operation, it is necessary to determine the effective beam energy and

Table 4.1. Dependence of beam properties on time for two combinations of currents in the magnet coils. Accelerating voltage is 81 kV and beam current 40 A

	case 1		case 2	
t (μs)	E_k (keV)	α	E_k (keV)	α
77	65.5	1.39	64.7	1.31
88	69.5	1.44	69.8	1.35
99	73.6	1.46	73.9	1.36
110	75.6	1.46	76.0	1.36
50000	81.0	1.31	81.0	1.23

velocity ratio including voltage depression that correspond to these values. The effect on the beam parameters also influences which mode oscillates in the case of long pulse operation.

We illustrate this with some examples taken from the design of a gyrotron which is supposed to operate at power close to 1 MW at 140 GHz. The chosen operating mode is $TE_{22,8}$. Table 4.1 gives beam energy and velocity ratio as a function of time assuming that the final accelerating voltage was 81 kV and beam current 40 A, for two different assumed magnetic field profiles (cases 1 and 2) in the gun region. During startup, the accelerating voltage varied from 71 kV to 81 kV. Small differences for different values of the cavity magnetic field (which was varied in the range 5.55–5.57 T) are neglected. The beam guiding center radius is 8.1 mm. Startup is assumed to be complete after about 110 μs. The current neutralization takes place on a time scale of about 50 ms. After beam space charge neutralization the beam energy was 81 keV and the velocity ratio was 1.31, respectively 1.23.

Single mode calculations [192] indicated that at a frequency near 140 GHz, the $TE_{19,9}$ mode with counter-rotating polarization may prevent the $TE_{22,8}$ mode from oscillating at optimum parameters. To check this, calculations of startup and beam space charge neutralization were performed using the self-consistent multimode code SELFT [136]. It turned out that the $TE_{19,9}$ mode will probably not present any difficulties. However, competition with the $TE_{21,8}$ mode may prevent operation at the optimum parameters. Raising the magnetic field somewhat (and hence changing the detuning parameter $\delta = 1 - \omega_c/(\gamma\omega)$) can eliminate the problem with mode competition while affecting the output power only slightly.

Figure 4.10 shows typical results, here for B=5.56 T and the higher velocity ratio (case 1). During startup, or in short pulse operation, an output power of about 0.94 MW could be expected. For this case, the power in the $TE_{22,8}$ mode rises to 1.29 MW and there is no interference from other modes, which are not visible in the figure. If the magnetic field is lowered to 5.55 T, the $TE_{22,8}$ mode stops oscillating when the beam energy reaches 80.5 keV and the $TE_{21,8}$ mode oscillates with an output power of about 0.43 MW

Fig. 4.10. SELFT simulation results showing output power as a function of time for a $TE_{22,8}$ gyrotron considering the probable competing modes, (**a**) before and (**b**) after current neutralization. Here, $E_b = 65.5–75.6\,\text{keV}$ for (**a**) and $75.6–81\,\text{keV}$ for (**b**) and α varies accordingly, $I_b = 40\,\text{A}$ and $B = 5.56\,\text{T}$

(Fig. 4.11). With the lower value of α a higher magnetic field (5.57 T) was needed to ensure that the $TE_{22,8}$ mode continued to oscillate (with power about 1.2 MW) (Figs. 4.12 and 4.13). These results are qualitatively similar to those presented in [193] and [194].

4.4.6 Mode Competition with Different Harmonics

Second harmonic modes are difficult to excite because of mode competition between the fundamental and the second harmonic modes [195, 196] . Due to mode competition, the higher-power operation at the fundamental may suppress the second harmonic, so that higher frequencies cannot be reached. For these reasons, such a phenomenon has been intensively studied both theoretically and experimentally [86, 156, 179, 195–197]. Various approaches

Fig. 4.11. SELFT simulation results showing output power as a function of time for a $TE_{22,8}$ gyrotron considering the probable competing modes, (**a**) before and (**b**) after current neutralization. Here, $E_b = 65.5$–$75.6\,keV$ for (**a**) and 76–$81\,keV$ for (**b**) and α varies accordingly, $I_b = 40\,A$ and $B = 5.55\,T$

have been proposed to eliminate undesirable mode competition, for example specially designed cavities and careful choice of gyrotron operating conditions. In this section, we will use the formalism developed by Borie and Jödicke [183, 184, 197] to study whether two modes can oscillate simultaneously, or if the existence of one mode prevents the other from starting up because the microwave power depends strongly on the mode present.

The starting point for a calculation of mode competition is the equation of motion for an electron in the field produced by a superposition of modes, and then one must consider the power transfer from the electrons to each individual mode and determine the possible equilibrium states. As given above, this is (in unnormalized variables)
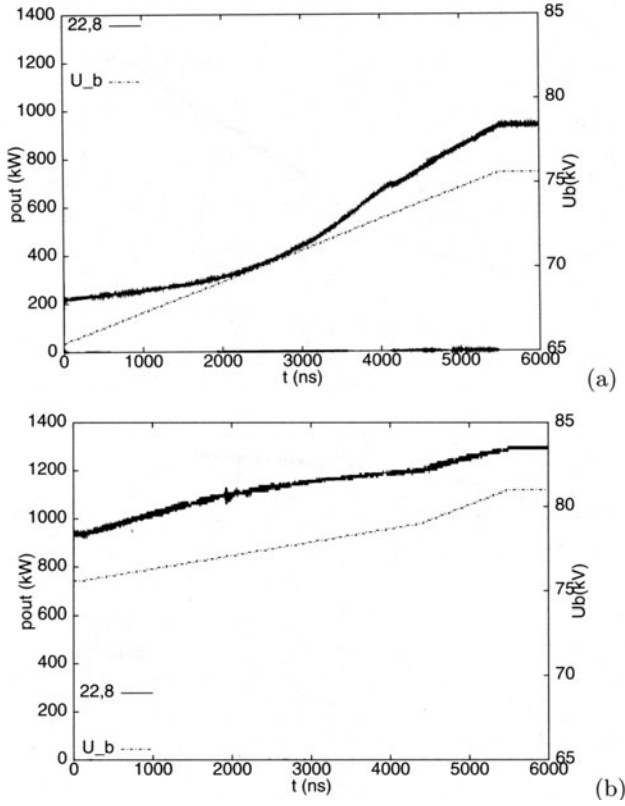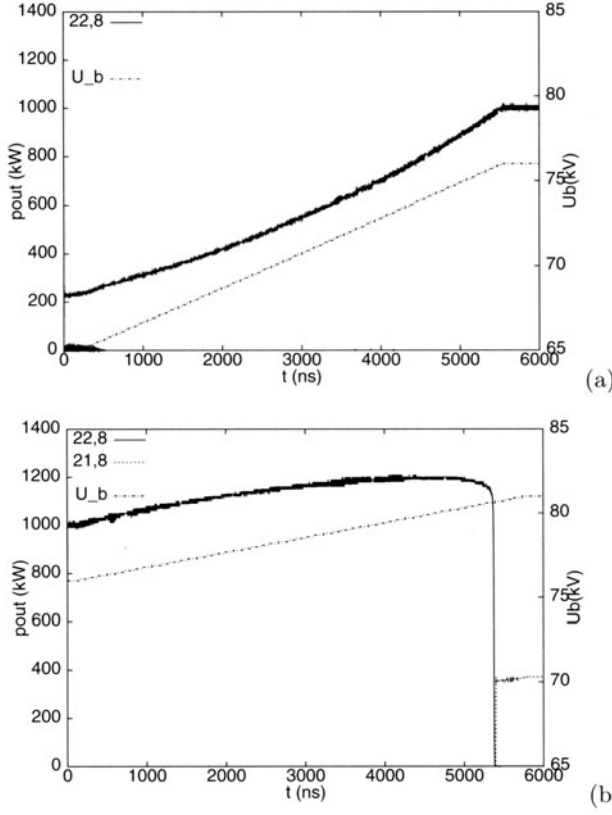
Fig. 4.12. SELFT simulation results showing output power as a function of time for a TE$_{22,8}$ gyrotron considering the probable competing modes, (**a**) before and (**b**) after current neutralization. Here, $E_b = 64.7$–76 keV for (**a**) and 76–81 keV for (**b**) and α varies accordingly, $I_b = 40$ A and $B = 5.56$ T

$$\frac{dP}{dz} + i\frac{\omega_a}{c\beta_{z0}}\left(\frac{\gamma}{\gamma_0} - \frac{\Omega_0}{\gamma_0\omega_a}\right)P = -i\frac{\gamma}{u_{z0}}\sum_j F_j \hat{f}_j(z) e^{[i\psi_j]}\left(\frac{ick_j P^*}{2\Omega_0}\right)^{s_j-1},$$

with

$$F_j = \frac{eV_{\max j}}{2m_e c^2}\frac{k_j C_j G_j}{(s_j-1)!}\frac{c}{\omega_a u_t},$$

and

$$\psi_j = (\omega_j - s_j\omega_a)\,t + (s_j \pm m_j)\,\theta_e\,.$$

For the purpose of studying mode competition between the fundamental and the second harmonic, we consider the dynamics and time behaviour of two interacting modes. The energy transfer to the jth mode is described in equations (4.72) and (4.74).
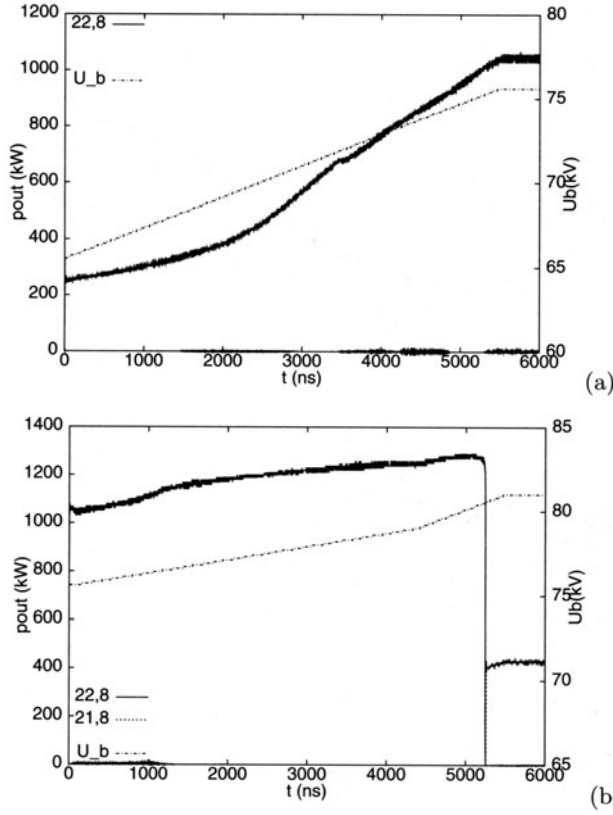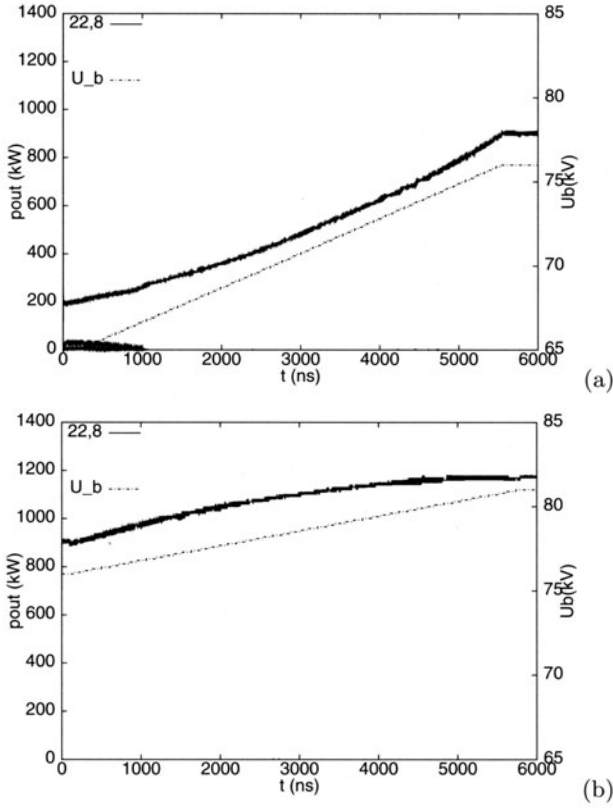
Fig. 4.13. SELFT simulation results showing output power as a function of time for a TE$_{22,8}$ gyrotron considering the probable competing modes, (**a**) before and (**b**) after current neutralization. Here, $E_b = 64.7\text{--}76$ keV for (**a**) and 76–81 keV for (**b**) and α varies accordingly, $I_b = 40$ A and $B = 5.57$ T

There is a stable two mode equilibrium if $\eta_j(P_1, P_2) = P_j/U_b I_b$ for both modes. Define $\tilde{I}_j = P_j/U_b I_b \eta_j(P_1, P_2)$; then

$$\frac{Q_j}{\omega_j} \frac{dP_j}{dt} = \eta_j(P_1, P_2) U_b(I_b - \tilde{I}_j) \ . \tag{4.76}$$

If the jth mode is arbitrarily defined to be the working mode, with $I_b = \tilde{I}_j$, it will be stable against perturbation by a parasite mode i, provided $I_b < \tilde{I}_i$, since the parasitic mode will be suppressed in such a case. The parasitic mode i could start oscillating if $I_b > \tilde{I}_i > 0$. This stability criterion is mathematically equivalent to one introduced by Nusinovich [157], but is physically more transparent. When such a situation occurs, it is necessary to calculate the full time dependence (cold-cavity, fixed-field approximation), or for the

self-consistent case, to repeat the calculation for mode j, taking into account the effect of the parasitic mode, and to iterate until $\tilde{I}_i = \tilde{I}_j = I_b$.

Numerical Example

For the numerical calculations, one must average over the initial gyrophase Λ_0 and initial phase ψ_0 (using the cold-cavity fixed-field approximation). For convenience, we can take $\omega_a = \omega_1/s_1$. It has been shown [156, 157, 177] that an average over ψ_0 is equivalent to an average over initial azimuthal θ_e, provided $s_1 m_1 \neq s_2 m_2$. In fact, only the relative initial phase $\psi_{20} - \psi_{10}$ is important. This is equal to $(\omega_2 - s_2\omega_1/s_1)\,t_0 + (s_2 \mp m_2 - s_1 \pm m_1)\,\theta_e$ with the above choice of ω_a. For rotating modes, an additional additive constant has no effect after averaging. This is not necessarily the case when one or both of the modes involved has a standing component.

The Japanese/Australian experimental results indicate that at low powers multimoding is more likely than seems to be the case at higher powers (where fundamental operation seems to dominate unless the second harmonic mode is well isolated). The full time dependent formalism can be used to calculate such operating points. i.e. equation (4.76) is solved either until a two mode equilibrium is reached or until it is clear that a single mode equilibrium is stable against perturbation by the parasite.

The example presented here is based on the Gyrotron FU 2 of the Fukui University with cavity radius 2.425 mm and length 14.5 mm [196, 198]. In the experiment, the electron beam radius was chosen to be 1.25 mm ($R_e/R_0 = 0.515$), which corresponds to the third maximum of the coupling coefficient for the TE_{26} co-rotating mode. For this beam radius, the TE_{23} mode may have a standing wave structure. Figure 4.14 shows typical results for competition between the TE_{26} mode and TE_{23} mode. The TE_{26} mode is started at the amplitude expected from a single mode calculation, and the TE_{23} mode is started with an amplitude corresponding to an output power of 1/10 of that in the TE_{26} mode. The beam parameters are assumed to be constant, and startup scenarios are not considered. Thus the physical picture is that a working mode (here TE_{26}) is established and a perturbation (here TE_{23}) is applied. For a current of 0.40 A, the TE_{26-} mode is stable and the TE_{23} mode is suppressed. At a much higher current, for example I_b=1.10 A, only the TE_{23} mode oscillates.

One found [199] that the maximum current for single mode operation of the TE_{26-} mode is about 0.48 A, and for a current above 0.54 A the output power of the competing TE_{23} mode will exceed that of the working TE_{26} mode. The experiment at Fukui University [196] on the Gyrotron FU 2 shows that, at the beam current 0.5 A, a single TE_{26} mode at the second harmonic was observed; when the current was increased to 0.80 A, the TE_{23} mode at the fundamental appeared and coexisted with the TE_{26} mode, with an output power about 1.40 times of that of the TE_{26} mode; at the higher
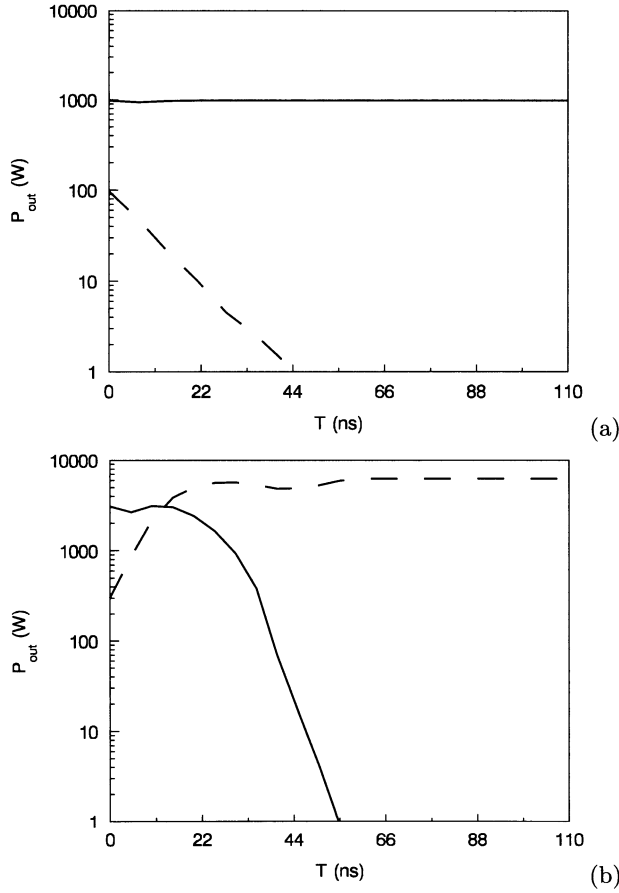
Fig. 4.14. Output power P_{out} versus time for the TE_{26-} and TE_{23} modes, where $U_b = 40\,kV$, $B = 7.31\,T$, $\alpha = 1.50$, $R_e = 1.25\,mm$. Solid curve: TE_{26} mode; dashed curve: TE_{23} mode. (**a**) beam current $I_b = 0.40\,A$, (**b**) beam current $I_b = 1.10\,A$ [199]

current 1.1 A, only the fundamental oscillated and the second harmonic is completely suppressed. One can find good qualitative agreement between our theory and the Japanese experiment.

5 Practical Considerations for Gyrotron Design

5.1 Introduction

The design of a particular gyrotron always involves tradeoffs among a number of mutually incompatible design goals and constraints (of both physical and technological nature). Design specifications and goals will become more stringent if one wishes to work at elevated frequencies, higher power levels from long-pulse to CW operation, and with higher cyclotron harmonics ($s > 1$). The general design constraints for high power gyrotrons are shown in Table 5.1.

In Table 5.1, the first four constraints are related to electron beam physics whereas the emitter radius and the corresponding current density are technological constraints. The magnetic compression has a direct relation to the emitter radius. We first discuss the physical constraints that limit the operating parameters of a gyrotron. Wall loading is a major problem to be dealt with as wall losses can make it impossible to operate the device at long pulses or CW. The voltage depression and limiting current are problems related to the beam quality which has a direct influence on the resonance condition and interaction mechanism.

In this chapter, we present some general design considerations for particular gyrotrons in terms of the main design constraints, namely, wall losses, voltage depression, and limiting current. Choice of the beam radius and the importance of Fresnel parameter are also discussed. In addition, starting current calculations and Rieke diagrams to estimate the effect of reflections are presented.

5.2 Wall Losses

The problem of the distribution of wall losses is important for long pulse to CW operation of high power gyrotrons since the problem of cooling depends on the local wall loading as well as the total losses. It is desired to keep the maximum local wall losses at a level below $2.0 \, \text{kW/cm}^2$.

The local wall losses are given by [129]

$$\frac{dP_{\text{loss}}}{dA} = -\frac{1}{2} Re \left[\boldsymbol{n} \cdot (\boldsymbol{E} \times \boldsymbol{H}^*) \right] . \tag{5.1}$$

<div align="center">Table 5.1. Gyrotron design constraints</div>

Constraint	Limit
Peak ohmic wall loading (ρ_Ω)	$< 2\,\text{kW/cm}^2$
Voltage depression ($\Delta V/V$)	< 0.1
Ratio of beam current to limiting current (I_b/I_L)	≤ 0.5
Magnetic compression ($b_{\text{comp}} = B_{\text{cav}}/B_{\text{gun}}$)	< 50
Electric field at the emitter (E_e)	$< 7\,\text{kV/mm}$
Emitter mean radius (R_e)	$< 50\,\text{mm}$
Cathode current density (j_e)	$< 4\,\text{A/cm}^2$

The skin depth is defined as

$$\delta = \left(\frac{2}{\mu_0 \omega \sigma}\right)^{\frac{1}{2}} = \left(\frac{\lambda}{\pi \mu_0 c \sigma}\right)^{\frac{1}{2}} = \left(\frac{\lambda}{\pi Z_0 \sigma}\right)^{\frac{1}{2}}, \tag{5.2}$$

where λ is the free space wavelength, μ_0 is the permittivity, σ is the electrical conductivity, and $Z_0 = \mu_0 c \simeq 377\,\Omega$. Inside the conductor, the fields depend on the coordinate ξ perpendicular to the conductor wall as $\exp[-(1-i)\xi/\delta]$. One then uses the following Maxwell's curl equation

$$\nabla \times \boldsymbol{H} = \boldsymbol{J} + i\omega\epsilon_0 \boldsymbol{E}$$

to show that

$$\frac{dP_{loss}}{dA} = \left(\frac{1}{2\sigma\delta}\right)|H_{tan}|^2 = \left(\frac{\mu_0 \omega \delta}{4}\right)|H_{tan}|^2 = \left(\frac{\omega\delta}{4\mu_0}\right)|B_{tan}|^2. \tag{5.3}$$

Here H_{tan} is the tangential component of $\boldsymbol{H}$ given by

$$\boldsymbol{H}_{tan} = \boldsymbol{n} \times \boldsymbol{H} = \hat{\phi}\left(H_r \sin\theta + H_z \cos\theta\right) - \hat{z}H_\phi \cos\theta - \hat{r}H_\phi \sin\theta.$$

Thus

$$\frac{dP_{loss}}{dA} = \left(\frac{\mu_0 \omega \delta}{4}\right)\left(\frac{|H_z|^2}{\cos^2\theta} + |H_\phi|^2\right). \tag{5.4}$$

Since we use the model for the high frequency fields described in Chap. 3 (as described in [123]), we can write for the TE modes

$$\omega\mu_0 H_z = Re \sum_p \left[-ik_{mp}^2 V_{mp}\psi_{mp}(r,z,\phi)e^{i\omega t}\right],$$

$$\omega\mu_0 H_\phi = Re \sum_j \left(\pm\frac{im}{r}\right)\left[\psi_{mp}(r,z,\phi)\frac{dV_{mp}}{dz} - \frac{rR'}{R}\frac{d\psi_{mp}}{dr}V_{mp}\right]e^{i\omega t},$$

with $\psi_{mp} = C_{mp}J_m(k_{mp}r)\exp[\mp im\phi]$. For a weakly tapered resonator ($\tan\theta_w \ll 1$), one may neglect terms involving R'/R and truncate the expansion in cylindrical eigenmodes at a single term. Using the fact that

$$C_{mp}^2 J_m^2(x_{mp}) = \frac{1}{\pi\left(x_{mp}^2 - m^2\right)},$$

we obtain

$$\frac{dP_{loss}}{dA} \simeq \left(\frac{\delta}{4\pi\mu_0\omega}\right)\left[\frac{1}{\left(x_{mp}^2 - m^2\right)}\right]\left(k_{mp}^4 |V_{mp}|^2 + \frac{m^2}{R^2}\left|\frac{dV_{mp}}{dz}\right|^2\right). \quad (5.5)$$

For weakly tapered cavities, $dA \simeq R(z)d\phi dz$ and for azimuthally symmetric ($m = 0$) or rotating modes, one may integrate over ϕ to obtain

$$\frac{dP_{loss}}{dz} = \left(\frac{\delta R}{2\mu_0\omega}\right)\left[\frac{1}{\left(x_{mp}^2 - m^2\right)}\right]\left(\frac{x_{mp}^4}{R^4}|V_{mp}|^2 + \frac{m^2}{R^2}\left|\frac{dV_{mp}}{dz}\right|^2\right). \quad (5.6)$$

The total wall losses are given by integrating over z. We have, for a weakly tapered resonator

$$\frac{d^2V_{mp}}{dz^2} \simeq \left[k_{mp}^2(z) - \frac{\omega^2}{c^2}\right]V_{mp}$$

(a more exact system is given in Chap. 3). We then have

$$\int_0^L \left|\frac{dV_{mp}}{dz}\right|^2 dz = \frac{1}{2}\left.\frac{d|V_{mp}|^2}{dz}\right|_0^L + \int_0^L \left(\frac{\omega_0^2}{c^2} - k_{mp}^2(z)\right)|V_{mp}|^2\,dz, \quad (5.7)$$

where ω_0 is the real part of ω. The surface term is usually negligible. Then we may write,

$$P_{loss} \simeq \left(\frac{\delta R}{2\mu_0\omega}\right)\left[\frac{1}{\left(x_{mp}^2 - m^2\right)}\right]$$
$$\cdot \int_0^L \left[k_{mp}^4 |V_{mp}|^2 + \frac{m^2}{R^2}\left(\frac{\omega_0^2}{c^2} - k_{mp}^2(z)\right)|V_{mp}|^2\right]dz$$
$$\simeq \left(\frac{\delta R}{2\mu_0\omega}\right)\left[\frac{1}{\left(x_{mp}^2 - m^2\right)}\right]$$
$$\cdot \left[k_{mp}^4 + \frac{m^2}{R^2}\left(\frac{\omega_0^2}{c^2} - k_{mp}^2\right)\right]dz\int_0^L |V_{mp}|^2\,dz$$
$$\simeq \left(\frac{\delta}{2\mu_0\omega R}\right)\left[\frac{x_{mp}^2}{R^2} + \frac{\omega_0^2}{c^2}\left(\frac{m^2}{x_{mp}^2 - m^2}\right)\right]\int_0^L |V_{mp}|^2\,dz. \quad (5.8)$$

The ohmic Q of the resonator is defined by

$$Q_\Omega P_{loss} = \omega W, \tag{5.9}$$

where W is the total energy stored in the resonator so that

$$W = \frac{\epsilon_0}{2} \int_0^L |V_{mp}|^2 \, dz, \quad \text{so that}$$

$$\frac{1}{Q_\Omega} = \frac{P_{loss}}{\omega W} = \left(\frac{\delta}{\epsilon_0 \mu_0 \omega_0^2 R} \right) \left[\frac{x_{mp}^2}{R^2} + \frac{\omega_0^2}{c^2} \left(\frac{m^2}{x_{mp}^2 - m^2} \right) \right]$$

$$= \left(\frac{\delta}{R} \right) \left[\frac{c^2}{\omega_0^2} \frac{x_{mp}^2}{R^2} + \left(\frac{m^2}{x_{mp}^2 - m^2} \right) \right]. \tag{5.10}$$

The first term in the square brackets is very close to unity for TE modes operating near cutoff. The second term vanishes for azimuthally symmetric modes but can be quite large for whispering gallery modes. Setting the first term equal to unity, we obtain

$$\frac{1}{Q_\Omega} \simeq \left(\frac{\delta}{R} \right) \left(\frac{x_{mp}^2}{x_{mp}^2 - m^2} \right). \tag{5.11}$$

A knowledge of the ohmic Q is useful for efficiency studies. The total efficiency is given by

$$\eta_{tot} P_{in} = P_{out}.$$

The electronic efficiency is the fraction of electron energy given to the electromagnetic field

$$\eta_{el} P_{in} = P_{out} + P_{loss}.$$

Since $P_{out} = \omega W / Q$, we have $P_{loss} = P_{out} \cdot Q/Q_\Omega$ and $\eta_{el} P_{in} = (1 + Q/Q_\Omega) P_{out}$, and we can write

$$\eta_{tot} = \frac{\eta_{el}}{1 + \frac{Q}{Q_\Omega}}. \tag{5.12}$$

For high power gyrotrons, it is desirable to keep Q/Q_Ω as small as possible. For numerical calculations, we took σ for ideal copper at room temperature (≈ 300 K). As it has already been mentioned, the general limitation set for the wall loading is 2 kW/cm^2 for CW operation of the gyrotron. The actual wall temperature is not uniform, and will depend on details of the cooling system design. Variations in σ or in δ due to effects of roughness of the cavity surface (which can lead to $\delta_{eff} \simeq 2\delta$ [200]) can be taken into account by scaling P_{loss} with the factor δ_{eff}/δ.

5.3 Voltage Depression and Limiting Current

The most important effect of space charge on the operation of a gyrotron is the degradation of beam quality [175, 176]. The potential drop across a uniform annular beam of thickness Δ at radius R_e is

$$\Delta\phi_b = \frac{IZ_0}{2\pi\beta_z}\, g\left(R_e + \frac{\Delta}{2}\right) = 60\Omega\,\frac{I}{\beta_z}\,\frac{\Delta}{2R_e}\,. \tag{5.13}$$

Here,

$$g(r) = \int_{R_e - \frac{\Delta}{2}}^{r} \frac{I(r')}{Ir'}\,dr' \quad \text{with} \tag{5.14a}$$

$$I(r) = 0\,, \quad r < R_e - \frac{\Delta}{2}\,, \tag{5.14b}$$

$$= \frac{I}{2R_e\Delta}\left[r^2 - \left(R_e - \frac{\Delta}{2}\right)^2\right]\,, \quad R_e - \frac{\Delta}{2} < r < R_e + \frac{\Delta}{2}\,, \tag{5.14c}$$

$$= I\,, \quad r > R_e + \frac{\Delta}{2}\,. \tag{5.14d}$$

Thus,

$$g\left(R_e + \frac{\Delta}{2}\right) = \frac{1}{2R_e\Delta}\left[R_e\Delta - \left(R_e - \frac{\Delta}{2}\right)^2 \ln\left(\frac{R_e + \frac{\Delta}{2}}{R_e - \frac{\Delta}{2}}\right)\right] \tag{5.15a}$$

$$\simeq \frac{\Delta}{2R_e} \quad \text{for} \quad \frac{\Delta}{2R_e} \ll 1\,. \tag{5.15b}$$

This will give rise to a spread in the initial beam energy of $e\Delta\phi_b$ or

$$\Delta\gamma_0 = \frac{\Delta\phi_b}{m_e c^2}\,. \tag{5.16}$$

In addition, the nominal beam energy is reduced by

$$\Delta U = \frac{IZ_0}{2\pi\beta_z}\ln\left(\frac{R_e - \frac{\Delta}{2}}{R_0}\right) + \Delta\phi_b \tag{5.17a}$$

$$\simeq -60\Omega\,\frac{I}{\beta_z}\ln\left(\frac{R_0}{R_e}\right)\,. \tag{5.17b}$$

This can change the resonance condition, which involves $\Omega_0/\gamma_0\omega$ and the value of $\alpha = v_\perp/v_z$ for which the mirroring of the beam can be a problem. In addition, the spread in β_z will increase, which has further deleterious effects on beam quality. Both these effects should be kept as small as possible. A change of 1 kV in beam voltage results in a change of γ_0 of 0.002. For

the calculation of the modification of beam properties, we note that the momentum component perpendicular to the magnetic field

$$\gamma\beta_\perp \simeq \gamma \, \frac{E_c}{cB_c} \, \sqrt{B/B_c} \tag{5.18}$$

is not affected by the voltage depression. Here E_c is the electric field at the cathode, B_c is the cathode magnetic field and B is the resonator magnetic field. It is clear that $\beta_z = (1 - \beta_\perp^2 - 1/\gamma^2)^{1/2}$ will be affected by the voltage depression, since γ is effectively reduced from $\gamma_0 = 1 + U/511\,\mathrm{kV}$ to

$$\gamma_{eff} = \gamma_0 - \left|\frac{e\Delta U}{mc^2}\right| = \gamma_0 - \frac{I^*}{\beta_z} \tag{5.19a}$$

$$= \gamma_0 - I^* \left[1 - \frac{\gamma_0^2 \left(1 - \beta_{z0}^2\right)}{\gamma_{eff}^2}\right] , \tag{5.19b}$$

with

$$I^* = \frac{60\Omega \, I}{511 \text{ kV}} \cdot \ln\left(\frac{R_0}{R_e}\right) , \tag{5.20}$$

and β_{z0} is the value of β_z in the absence of voltage depression. The operating parameters at the resonator are thus:

$$\gamma_{eff}, \ \beta_\perp = \frac{\gamma_0 \beta_{\perp 0}}{\gamma_{eff}}, \quad \text{and} \ \beta_z = \sqrt{1 - \beta_\perp^2 - 1/\gamma_{\text{eff}}^2} .. \tag{5.21}$$

This will also result in a reduction in total efficiency by the factor

$$\frac{\gamma_{eff} - 1}{\gamma_0 - 1} = 1 - \frac{|e\Delta U|}{511 \ kV \ (\gamma_0 - 1)} \tag{5.22}$$

unless a depressed collector is used to regain some of the beam energy. The accelerating voltage applied is not fully available to the beam due to voltage depression and one has to take this fact into account when designing the gyrotron device. On the other hand, if the gyrotron is to be designed for long pulse or CW operation, one must remember that the beam space charge will be neutralized on a time scale of 50–100 ms. Then the beam will have a higher energy, but the effective velocity ratio will be reduced.

These considerations are related to the limiting current [175, 176], since this is a natural consequence of voltage depression. The limiting current (I_L) is the current beyond which the voltage depression becomes so large that $\beta_z \longrightarrow 0$ and mirroring of the beam occurs. One therefore has to consider the value of the limiting current when designing the gyrotron. β_z is reduced to zero and becomes imaginary when $I > I_L$, where [176]

Table 5.2. Bessel zero, cavity radius, beam radius, voltage depression, limiting current and maximum power density of wall losses, assuming a beam current of 40 A, $\beta_z = 0.27$ and an output power 1 MW for candidate modes of a 140 GHz, gyrotron (TE$_{10,4}$ was chosen as the operating mode)

mode TE$_{mp}$	x_{mp}	R_0 (mm)	R_e (mm)	ΔV (kV)	I_L (A)	$x_{mp}^2 - m^2$
10, 3	20.223032	6.90	3.65	5.62	65.9	309.0
10, 4	23.760715	8.10	3.65	7.04	52.6	464.6
11, 3	21.430855	7.31	4.01	5.30	69.9	338.3
12, 3	22.629299	7.72	4.37	5.02	73.8	368.1
15, 2	22.142248	7.55	5.45	2.89	128.3	265.3
16, 2	23.264269	7.93	5.80	2.76	134.0	285.2

$$I_L = \frac{\left(\frac{511\,\text{kV}}{60\,\Omega}\right) I_{\max}^*}{\ln\left(\frac{R_0}{R_e}\right)} \quad \text{and} \tag{5.23a}$$

$$I_{\max}^* = \gamma_0 \left[1 - \left(1 - \beta_{z0}^2\right)^{1/3}\right]^{3/2} . \tag{5.23b}$$

Numerically, for $\gamma_0 \simeq 1.157$ and $\beta_{\perp 0} \simeq 0.43$, (5.23) gives $I_{\max}^* \simeq 0.004$. When $I^* > I_{\max}^*$, there is no real solution to (5.19), which determines γ_{eff}. As an example, the limiting current, voltage depression and wall loading factor $(x_{mp}^2 - m^2)$ for a typical case is shown in Table 5.2. For a Gaussian field profile, the integral in (5.8) can be evaluated analytically. In the table, the wall loading is not given because of the inadequacy of this approximation, which tends to underestimate the maximum wall loading. Realistic wall losses, including the effect of surface roughness, will be higher by a factor of approximately 2.0. However, to assess the relative wall loading for different modes, the quantity $x_{mp}^2 - m^2$ is included. Therefore, these calculations will give the designer a first estimate for the choice of operating mode. A more exact figure on wall losses must be provided by self-consistent calculations of the beam-field interaction, which take into account a realistic field profile.

Ideally in CW operation, the limiting current should be at least a factor two larger than the operating current. The fact that in long pulse operation the beam space charge is neutralized by background gas permits one to consider relaxing this constraint somewhat. The upper limit for voltage depression is roughly estimated to be around 10% of the applied accelerating voltage; above this value instabilities may occur. It was observed that the effect of voltage depression can be partly compensated by increasing the beam voltage [160]. But the price paid is a loss of efficiency in short pulse operation. Use of a depressed collector can offset this somewhat.

5.4 Choice of Beam Radius

In gyrotrons the electron beam radius R_e is usually chosen such as to maximize the coupling of the electron beam to the RF field, which is polarized either co-rotating or counter-rotating with respect to the gyrating electrons ($|J_{m\pm s}(k_{mp}R_e)|$ is maximum). Sometimes for various reasons, the beam radius has some other value, especially in a step-tunable gyrotron, since the magnetic field is varied over a wide range and the beam radius is related to the magnetic field (see Chap. 6). In such cases, the coupling of the beam to both rotating RF field components may become comparable. It was shown a long time ago by Moiseev and Nusinovich [178] that if the beam-field coupling coefficients differ by as little as 10%, the azimuthal polarization component with the strongest coupling to the beam will suppress the other. This was confirmed by Borie [128] for the case of the $TE_{15,2}$ mode at 140 GHz, and also by others.

One can summarize the influence of the beam radius on the azimuthal polarization as follows. From the beam-field coupling coefficient $C_{BF} = C_{mp}^2 k_{mp}^2 J_{m\pm s}^2(k_{mp}R_e)$, one can see that:

– when $J_{m+s}^2(k_{mp}R_e) < J_{m-s}^2(k_{mp}R_e)$, only the co-rotating wave is excited;
– when $J_{m-s}^2(k_{mp}R_e) < J_{m+s}^2(k_{mp}R_e)$, only the counter-rotating wave is excited;
– when $J_{m+s}^2(k_{mp}R_e)$ and $J_{m-s}^2(k_{mp}R_e)$ are comparable, and both nonzero, it is difficult to determine exactly how much of each rotating component is present. In this case, a so-called mixing angle Θ can be used to characterize the admixture if the RF field is a linear superposition of co-rotating and counter-rotating polarizations. The classical azimuthal standing wave is characterized by a mixing angle $\Theta = \pi/4$.

However, we note that even a small admixture of an oppositely rotating component can produce a large signal in a diagnostic such as thermopaper [201]. At any axial position, a superposition of the two rotating components, normalized to a factor which takes into account energy conservation, can be written as

$$E \propto \mathrm{Re}[\cos\Theta \exp(i\omega t - m\phi) + \sin\Theta \exp(i\omega t + m\phi)]$$

The blackening of the thermopaper is proportional to the local time averaged power:

$$S = \frac{1}{T}\int_0^T |E|^2 \, dt \propto 4\sin\Theta\cos\Theta\cos^2 m\phi + (1 - 2\sin\Theta\cos\Theta) .$$

If even 10% of the power is in the counter-rotating mode, the signal caused by the azimuthal standing wave is stronger than that due to the rotating mode by a factor of 3. The signal is still comparable when only 1% of the power is in the counter-rotating mode. Also, window reflections or reflections from

the diagnostic can introduce small contributions from the counter-rotating mode, which makes a comparison between theory and experiment difficult.

5.5 Fresnel Parameter

Russian researchers introduced a parameter called the *Fresnel parameter* (C_F) which can influence how a particular mode oscillates [139]. It is defined there as

$$C_F = \frac{L^2}{8R_0\lambda\sqrt{1 - \left(\frac{m}{x_{mp}}\right)^2}} . \tag{5.24}$$

Here L is the effective length of the interaction region. It describes the effective diffraction of a wave at the taper transitions in a resonator. For TE modes near cut-off, $(2\pi/\lambda) \simeq (x_{mp}/R_0)$. Substituting this approximation in (5.24), we obtain the following expression for the Fresnel parameter:

$$C_F \cong \frac{\pi}{4} \cdot \frac{\left(\frac{L}{\lambda}\right)^2}{\sqrt{x_{mp}^2 - m^2}} . \tag{5.25}$$

In most design studies, this modified expression (5.25) is considered as the original definition for the Fresnel parameter. However, one should not forget the relevance of the cavity radius R_0 in C_F as given in (5.24). According to Gaponov et al. [139], cavities with $R_0 \gtrsim L$, the Fresnel parameter is rather small $C_F < 1$. This gives an unfixed longitudinal and transverse structure of the RF field. But in later studies, it was never discussed except that a physical constraint of $C_F \geq 1$ is assumed for the buildup of a particular mode.

In this context, if we recall the basic formula for the cavity radius $R_0(\text{mm}) = 300x_{mp}/(2\pi f(\text{GHz}))$, it will be much larger for higher order modes for the same frequency. Therefore, according to Gaponov et al. [139], it may be interpreted that the fixation of the longitudinal and transverse structure of the RF field is difficult when $R_0 \gtrsim L$ in the case of operation with higher order modes. However, the limiting value of C_F is not yet fixed, since for many of the successfully working gyrotrons operating with very high order modes, namely, $\text{TE}_{22,6}, \text{TE}_{28,8}, \text{TE}_{31,8}, \text{TE}_{25,10}, \text{TE}_{31,17}$, its value is around 0.5–0.8 and the ratio $R_0/L \approx 1.2 - 2.0$. Other considerations appear to be more important. Although the last word on the subject has not yet been spoken, it is probable that a value $C_F > 0.5$ is desirable, but that $C_F \geq 1$ is not necessary.

5.6 Starting Current

The starting current I_{start} was defined in the previous chapter as the minimum current for which $dP/dt > 0$ in the limit $P \longrightarrow 0$:

$$I_{start} = \left(U \left. \frac{d\eta}{dP} \right|_{P=0} \right)^{-1} .$$

The starting current can be calculated in a linearized single mode theory. This has been done in a number of ways by [202–205]. Here, we sketch the derivation given in [205]; the others are similar or equivalent. For simplicity, we limit ourselves to the first harmonic.

The differential equation describing the efficiency is

$$\frac{d\eta}{dz} = \frac{1}{I_b U_c} \, Re \int \boldsymbol{E}^* \cdot \boldsymbol{J}_\omega \, dA \,, \tag{5.26}$$

where I_b is the beam current, U_c is the accelerating voltage. Here the electric field is given in chap. 3 and the current term J_ω is described in Chap. 4. Recall that in the equation of motion, the factor G_{mp} determines the beam-field coupling for the rotating field components. Then, one can write the integral appearing in (5.26) as

$$\int \boldsymbol{E}^* \cdot \boldsymbol{J}_\omega \, dA = -iI_b \, \frac{C_{mp} k_{mp} G_{mp}}{u_{z0}} \, \langle P(z) \rangle \, V^*_{mp}(z) \,, \tag{5.27}$$

where the average is carried out over the initial gyrophases Λ_0.

Recall the equation of motion (4.37) in dimensionless variables (here for s=1):

$$\frac{d\widetilde{P}}{dz} + i\frac{\omega}{v_{z0}} \left(\frac{\gamma}{\gamma_0} - 1 + \delta \right) \widetilde{P} = -i\frac{\omega}{v_{z0}} \frac{\gamma}{\gamma_0} F_{mp} \hat{f}_{mp}(z) \,.$$

To linearize the theory, let us consider the case $F \ll 1$, and write $P = P_0 + FP_1 + \cdots$. Let

$$\Delta_1(z) = \frac{\omega}{v_{z0}} \left(1 - \frac{\Omega(z)}{\omega\gamma_0} \right) .$$

To zeroth order in F, we have

$$\frac{dP_0}{dz} + i\Delta_1(z)P_0 \simeq 0 \,, \tag{5.28}$$

with the formal solution

$$P_0 = u_0 \exp \left[-i \left(\Lambda_0 + \int_0^z \Delta_1'(z')dz' \right) \right] . \tag{5.29}$$

For a weakly tapered magnetic field, one can write

$$\Delta_1(z) = \Delta_1 + \Delta_1'(z).$$

Then,

$$\int_0^z \Delta_1(z')dz' = \Delta_1 z + \int_0^z \Delta_1'(z')dz' .$$

For the moment, let us assume a constant magnetic field ($\Delta_1' \simeq 0$). The generalization to nonuniform fields is trivial, and can be easily included in the numerical calculations. It is easy to show from (4.16b) that

$$\frac{d\,|P|^2}{dz} = -2\gamma\,\frac{F}{\gamma_0}\,\mathrm{Im}(P^*\hat{f})\,. \tag{5.30}$$

Hence,

$$\frac{d\,\langle\gamma\rangle}{dz} = -\frac{F}{\gamma_0}\,\Big\langle\mathrm{Im}\left(P_0^*\hat{f} + FP_1^*\hat{f}\right)\Big\rangle\,. \tag{5.31}$$

with $P_0 = u_{t0}\,\exp[-i(\Lambda_0 + \Delta_1 z)]$. Obviously, $\langle P_0^*\hat{f}\rangle = 0$ and hence

$$\frac{d\,\langle\gamma\rangle}{dz} = -\frac{F^2}{\gamma_0}\,\Big\langle\mathrm{Im}\left(P_1^*\hat{f}\right)\Big\rangle\,. \tag{5.32}$$

P_1 is a solution of

$$\frac{dP_1}{dz} + i\Delta_1(z)P_1 + \frac{i\omega}{v_{z0}}\,\mathrm{Re}\left(P_0^*P_1\right) = i\hat{f}(z)\,, \tag{5.33}$$

with $P_1(0) = 0$. Let $P_1(z) = g(z)\exp[-i(\Lambda_0 + \Delta_1 z)]$ and substitute (5.29) into (5.33). This result is

$$\frac{dg}{dz} \simeq -\frac{i\omega}{v_{z0}}\left(\frac{u_{t0}}{\gamma_0}\right)^2\,\mathrm{Re}\,g + i\,\hat{f}\,e^{[+i(\Lambda_0 + \Delta_1 z)]}$$

$$= -\frac{i\omega}{v_{z0}}\,(\beta_{\perp 0})^2\,\mathrm{Re}\,g + i\,\tilde{f}\,. \tag{5.34}$$

This defines $\tilde{f} = \hat{f}\exp[-i(\Lambda_0 + \Delta_1 z)]$. Then

$$\frac{d\,\langle\gamma\rangle}{dz} = \frac{F^2}{\gamma_0}\,\mathrm{Im}\,\Big\langle g\tilde{f}^*\Big\rangle\,. \tag{5.35}$$

Equation (5.34) has the formal solution

$$\mathrm{Re}\,g = -\int_0^z \mathrm{Im}\,\tilde{f}(z')dz'\,,$$

$$\mathrm{Im}\,g = \int_0^z\left[\mathrm{Re}\,\tilde{f}(z') + \frac{\omega\beta_{\perp 0}^2}{v_{z0}}\cdot\left(\int_0^{z'}\mathrm{Im}\,\tilde{f}(z'')dz''\right)\right]dz'\,. \tag{5.36}$$

We can now solve for the electronic efficiency:

$$- (\gamma_0 - 1)\, \eta = \int_0^L \frac{d\,\langle\gamma\rangle}{dz}\, dz$$

$$= \frac{F^2}{\gamma_0} \left\{ \int_0^L \left\langle \operatorname{Im}\tilde{f}(z) \cdot \int_0^z \operatorname{Im}\tilde{f}(z')dz' \right\rangle dz \right.$$

$$+ \int_0^L \left\langle \operatorname{Re}\tilde{f}(z) \cdot \int_0^z \operatorname{Re}\tilde{f}(z')dz' \right\rangle dz$$

$$+ \left. \frac{\omega\beta_{\perp 0}^2}{v_{z0}} \int_0^L \left\langle \operatorname{Re}\tilde{f}(z) \cdot \int^z \left(\int^{z'} \operatorname{Im}\tilde{f}(z'')dz'' \right) dz' \right\rangle dz \right\}.$$

$$(5.37)$$

The first two terms of (5.37) combine to give

$$\frac{1}{2}\frac{F^2}{\gamma_0} \left\langle \left| \int_0^L \tilde{f}(z)dz \right|^2 \right\rangle .$$

One can show that the last term of (5.37) is equal to

$$\frac{F^2}{\gamma_0}\frac{\omega\beta_{\perp 0}^2}{2v_{z0}} \cdot \int_0^L \left[\left\langle \operatorname{Re}\tilde{f}(z) \cdot \int^z \left(\int^{z'} \operatorname{Im}\tilde{f}(z'')dz'' \right) dz' \right\rangle \right.$$

$$\left. - \left\langle \operatorname{Im}\tilde{f}(z) \int^z \left(\int^{z'} \operatorname{Re}\tilde{f}(z'')dz'' \right) dz' \right\rangle \right] dz$$

$$= \frac{F^2}{\gamma_0}\frac{\omega\beta_{\perp 0}^2}{2v_{z0}}\frac{1}{2}\frac{\partial}{\partial\Delta_1} \left\langle \left| \int_0^L \tilde{f}(z)dz \right|^2 \right\rangle .$$

Hence

$$- (\gamma_0 - 1)\, \eta = \frac{1}{2}\left(\frac{F^2}{\gamma_0} \right) \left[1 + \frac{\omega\beta_{\perp 0}^2}{2v_{z0}}\frac{\partial}{\partial\Delta_1} \right] \cdot \left\langle \left| \int_0^L \tilde{f}(z)dz \right|^2 \right\rangle .$$

Since

$$\left\langle \left| \int_0^L \tilde{f}(z)dz \right|^2 \right\rangle = \left\langle \left| \int_0^L \hat{f}(z)e^{i\Delta_1 z}dz \right|^2 \right\rangle ,$$

the average over initial gyrophase is now trivial. Next observe that

$$QP_{\text{out}} = Q\eta I_b U_c$$

$$= \frac{1}{2}\omega\epsilon_0 \int_0^L |V_{mp}(z)|^2\, dz$$

$$= \frac{1}{2}\omega\epsilon_0 F^2 \int_0^L \left| \hat{f}(z) \right|^2 dz \cdot \left[\left(\frac{2m_e c^2}{e} \right) \frac{v_{z0}}{ck_{mp}C_{mp}G_{mp}} \right]^2 . \quad (5.38)$$

The starting current is given by

$$
I_{start} \, U_c = \left(\left. \frac{d\eta}{dP_{out}} \right|_{P_{out}=0} \right)^{-1} , \tag{5.39}
$$

and for the fixed-field case considered here

$$
\frac{d\eta}{dP_{out}} = \frac{d\eta}{dF^2} \frac{1}{2} \frac{Q}{\omega \epsilon_0} \left[\left(\frac{e}{m_e c^2} \right) \frac{k_{mp} C_{mp} G_{mp}}{\beta_{z0}} \right]^2 \cdot \frac{1}{\int |\hat{f}|^2 dz} .
$$

Thus we can write the expression for the starting current (for arbitrary harmonics) as follows:

$$
\frac{-1}{I_{start}} = \left(\frac{Q Z_0 e}{8 \gamma_0 m_e c^2} \right) \left(\frac{\pi}{\lambda} \int_0^L \left| \hat{f}(z) \right|^2 dz \right)^{-1}
$$
$$
\cdot \left(\frac{k_{mp} C_{mp} G_{mp}}{\beta_{z0}(s-1)!} \right)^2 \left(\frac{c k_{mp} \gamma_0 \beta_{\perp 0}}{2 \Omega_0} \right)^{2(s-1)}
$$
$$
\cdot \left(s + \frac{1}{2} \frac{\omega \beta_{\perp 0}^2}{v_{z0}} \frac{\partial}{\partial \Delta_s} \right) \cdot \left| \int_0^L \hat{f}(z) e^{i \Delta_s z} dz \right|^2 . \tag{5.40}
$$

This is identical to the expression derived using other methods by Nusinovich and coworkers, except for the additional factor $1/\gamma_0$. Here, in the above expression (5.40),

$$
\Delta_s(z) = \frac{\omega}{v_{z0}} \left(1 - \frac{s \Omega_0(z)}{\omega \gamma_0} \right) .
$$

s is the harmonic number and $\hat{f}(z)$ is the normalized field profile. All other quantities have been defined previously. For a Gaussian field profile, $\hat{f}(z) = \exp[-(2z/L - 1)^2]$, one obtains

$$
\left| \int_0^L \hat{f}(z) e^{i \Delta_s z} dz \right|^2 \simeq \frac{L^2 \pi}{4} \exp \left[-\frac{(\Delta_s L)^2}{8} \right] . \tag{5.41}
$$

When comparing this result with a realistic field profile, the full width at half maximum of $|\hat{f}(z)|$ is useful. For the Gaussian field profile, it is $L_{FWHM} = L \cdot \sqrt{\ln 2} \simeq 0.83L$.

If the RF field is a linear superposition of co-rotating and counter-rotating components (this can occur, for instance, when the beam is not exactly centered on the resonator axis or is not perfectly homogeneous and $m \neq 0$), then the RF field has the form

$$
E_\theta = C_{mp} k_{mp} J_m'(k_{mp} r) e^{i\omega t} \hat{f}_{mp}(z) \left(V_+ e^{+im\theta} + V_- e^{-im\theta} \right) ,
$$
$$
E_r = -i C_{mp} k_{mp} (m/k_{mp} r) J_m(k_{mp} r) e^{i\omega t} \hat{f}_{mp}(z) \left(V_+ e^{+im\theta} + V_- e^{-im\theta} \right) ,
$$

with

$$
V_+ = V_{max} \sin \Theta e^{+i\chi} \text{ and } V_- = V_{max} \cos \Theta e^{-i\chi} .
$$

Here Θ is an arbitrary parameter, analogous to the mixing angle used commonly in particle physics [206]. It is well known that this linear combination is the most general one possible [207]. This choice preserves the normalization of the basis states, as it is shown in any text book on linear algebra. Also, we follow Feynman [207] in distributing the relative phase symmetrically over the components. Other conventions are possible, but the symmetric one is, according to our opinion, the most useful. For standing waves, $\Theta = \pi/4$. If the cavity is slotted, this choice gives the appropriate normal modes, as was pointed out by Petelin [202]. For a slightly elliptical or displaced beam this is unlikely to be the correct choice. The mixing angle should be a continuous function of beam eccentricity. In this case, the factor G_{mp} in (4.16) should be replaced by

$$\left[\cos\Theta e^{-i(\chi+m\theta_e)} J_{m-s}(k_{mp}R_e) + (-1)^s \sin\Theta e^{+i(\chi+m\theta_e)} J_{m+s}(k_{mp}R_e)\right] . \tag{5.42}$$

The average over θ_e is then equivalent to an average over $\chi/m + \theta_e$ and the relative phase disappears trivially. For practical calculations, it is preferable to remain with a linear superposition of two modes, rather than to try to combine (5.42) into amplitude and phase. This formulation retains more explicitly the basic linearity of Maxwell's equations and is computationally less intensive. In the linearized theory, after averaging over θ_e, one obtains the above expression (5.40) for the starting current, except that G_{mp}^2 is replaced by

$$\cos^2\Theta J_{m-s}^2(k_{mp}R_e) + \sin^2\Theta J_{m+s}^2(k_{mp}R_e) .$$

This is an obvious generalization of the formula for standing waves given by the IAP group [202].

   As a typical example, the starting currents for a $TE_{10,4}$ mode gyrotron operating at 140 GHz along with its competing modes is shown in Fig. 5.1. A Gaussian field profile was employed for these calculations, which is a common practice to initially compute the starting currents of main mode and its competitors to have a preliminary assessment. The linear theory and the extrapolation of the nonlinear theory with a fixed field profile to a very low field amplitude give very similar results for the same cold-cavity field profile. The starting current calculated with a realistic field profile differs somewhat from that calculated using a Gaussian field profile. Starting current curves calculated self-consistently, so that the electron beam influences the field profile are quite different from those calculated with a fixed field profile. This is due to the fact that the beam excites a backward wave as well as a forward wave and at higher magnetic fields, the backward wave becomes more important [128, 205]. At the highest magnetic fields, the backward wave becomes so important that the self-consistent solution becomes ill defined. Frequency pulling is also important and is never described well either by linear theory [117] or by perturbation theory [152]. Now let us discuss a few more param-
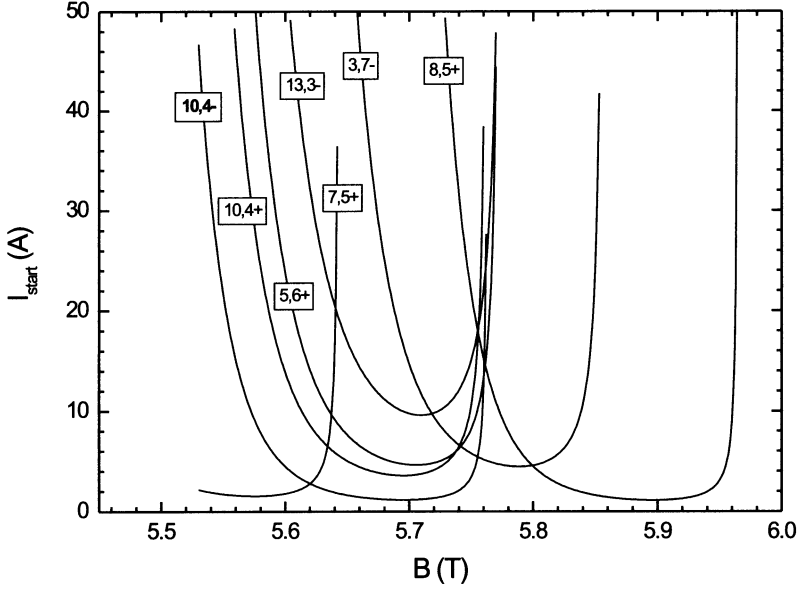
Fig. 5.1. Starting current I_{start} as a function of magnetic field B for various modes with the beam radius (R_e) optimized for the $TE_{10,4-}$ mode gyrotron at 140 GHz. Here $U_b = 75\,\text{kV}$, $\alpha = 1.4$, $R_e = 3.65\,\text{mm}$

eters, namely, equilibrium points and rise time, which are farmed a part of designers glossary in addition to the starting current.

Equilibrium Points

An equilibrium or steady state point is defined by $dP/dt = 0$. As discussed in Chap. 4,

$$P = \eta(P)UI.\tag{5.43}$$

The equilibrium point is stable if

$$\left.\frac{d\eta}{dP}\right|_{P_{eq}} < \frac{1}{UI}, \quad \text{and unstable if} \quad \left.\frac{d\eta}{dP}\right|_{P_{eq}} > \frac{1}{UI}.\tag{5.44}$$

Rise Time of the RF Field

The time required to reach steady state is given by integrating the power balance equation (see Chap. 4)

$$\tau_c = \frac{Q}{\omega}\int (\eta(P)UI - P)^{-1}\,dP.\tag{5.45}$$

The point at $P = 0$ is stable if $I < I_{start}$. If $I > I_{start}$, this point is unstable and a small (noise) power P_n causes the field to increase until a steady state is reached. For an estimate of the rise time, we assume η to vary linearly with P as $\eta \simeq P/UI_{start}$. In this case

$$\tau_c \simeq \frac{Q}{\omega} \int_{P_n}^{P} I_{start} \left[(I - I_{start}) \; P \right]^{-1} dP$$

$$\simeq \frac{Q}{\omega} \frac{I_{start}}{I - I_{start}} \; \ln \left(\frac{P}{P_n} \right) . \tag{5.46}$$

The factor $\ln(P/P_n)$ is nearly independent of the resonator and is approximately equal to 20. For a 150 GHz gyrotron, $Q/\omega = 1$ ns if $Q = 1000$ and $Q/\omega = 1/2$ ns for $Q = 500$. The rise time thus depends mainly on the factor $I_{start}/(I - I_{start})$. This can be as small as 0.05 (if I=6 A, and I_{start}=0.2 A) or greater than 10 (if I=6 A, and I_{start}=5.5 A). The result of this estimate is in fair agreement with that obtained by numerically integrating equation (5.45).

If the starting current is very low, the assumption $t_{tr} \ll t_{res}$ is no longer valid. However, in most cases the rise time of the current is much longer than the electron transit time t_{tr}. This means that the field follows the current almost instantaneously and that the rise time of the field is given by the current rise time. The electrons will still see an approximately constant field during their flight through the cavity and the above stated energy balance equation remains valid. In the case of high starting current, the rise times of the field and current can be comparable. The field cannot react fast enough to a change in the current. Although this may not be too much of a problem for CW operation, such a resonator cannot be operated in a (short) pulsed mode under these conditions.

Mode competition can have a significant effect on these considerations. Even when the mode can start and would be stable in the absence of neighbouring modes, this is no guarantee that this remains the case when other modes at nearby frequencies also have a stable operating point for the same parameters. It turns out that if certain conditions are met, single mode operation is stable. However, for a given set of parameters, any one of several modes can be the stable operating mode, and typically only one of these has the desired high efficiency. One must then ask how to access this mode in a manner that ensures that it operates stably. This question is addressed in Chap. 4.

5.7 Rieke Diagrams for Gyrotrons

A diagram giving the real and imaginary parts of the reflection coefficient R (defined in previous chapters, see (3.32)) along contours of constant frequency

and output power is known as a *Rieke diagram* [208]. It is sometimes useful to consider the dependence of the reflection coefficient R on the frequency and output power. Since the load is not always ideally matched, some power may be reflected back into the resonator and it is possible that reflections from load can change the applicable boundary condition from $R = 0$ to $R = R_1$ (for some given R_1). Useful operation is unlikely if $|R_1| > 0.3$ (corresponding to 10% of the power being reflected back into the resonator).

Rieke diagrams (or their analogs) have been successfully used (as shown in [209]) for determining whether or not a solution to the self-consistent set of equations (4.16b) and (4.32) with a given value of $R = R_1$ (usually $R = 0$) exists at all for a given set of beam parameters, magnetic field and resonator geometry. For this purpose, the system of equations was solved for a range of frequencies, the value of P_{out} was computed from

$$P_{out} = \frac{1}{2} \int dA \text{ Re } (\boldsymbol{E} \times \boldsymbol{H}^*)_z \bigg|_{z=z_{out}}$$

$$= \text{Im } \frac{1}{2\mu\omega} \, f(z_{out}) \, \frac{df^*(z_{out})}{dz} \, ,$$

and the values of the reflection coefficients were suitably interpolated to give contours of constant output power. A typical view of a Rieke diagram drawn to study the reflections on the single mode operation of a $TE_{25,6-}$ gyrotron [210] is shown in Fig. 5.3.

From this, one observes that equifrequency lines converge on an approximately circular curve which can be interpolated as a "caustic". Points on this curve correspond to small values of $|f(0)|$. They do not necessarily correspond to zero output power. In the case of hard excitation, they will generally correspond to nonzero power. There is almost always one branch of a curve corresponding to constant output power (even for rather high output power) which also lies near the "caustic". This set of curves encloses a "hole" in the $\text{Re}(R) - \text{Im}(R)$ plane. If the reflection coefficient corresponding to the load lies inside this "hole", there is no solution to the set of self-consistent equations with the given boundary conditions. Such Rieke diagrams provide a quick method for determining whether or not a solution exists for the reflection coefficient of interest, and to determine approximately the value of frequency and $f(0)$ to which this solution corresponds. A more precise solution can then be found using the usual version of the self-consistent code (see Chap. 4) which solves the same set of equations subject to the boundary condition $R = R_1$.

Further, it is important to mention that the reflection coefficients shown in Fig. 5.3 were calculated at the resonator output. This is related to the reflection coefficient at the window by
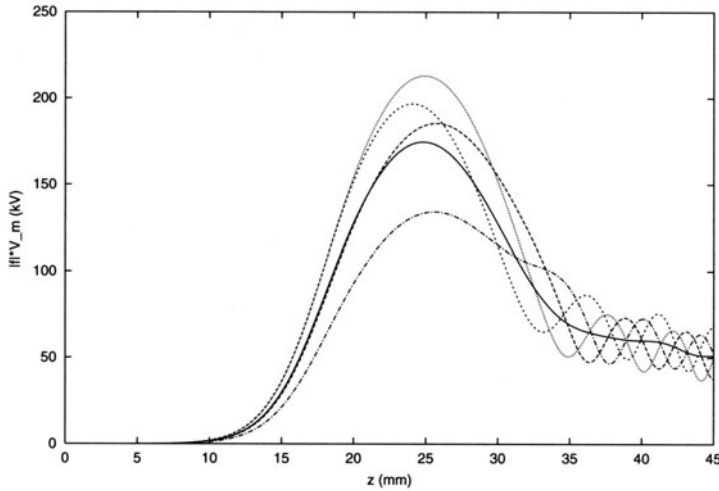
$$R_{win} = R_{res} \, e^{2i\omega L/c} \, , \tag{5.47}$$

Fig. 5.2. RF field profile for the $TE_{25,6-}$ mode for: matched load (solid curve), 6% power reflection and $\phi = 0°$ (long dashes), 6% power reflection and $\phi = 180°$ (short dashes), 6% power reflection and $\phi = 90°$ (dots), and 6% power reflection and $\phi = 270°$ (dashed-dotted) [210]

where L is the distance from the load to the input. A variation of 2π in the phase of R at the window corresponds to a segment of the Rieke diagram at the resonator. A good account of the use of these Rieke diagrams for quick estimation of the parameters for self-consistent calculations and estimating the effect of reflections from the window are given in [209–211].

In addition, the effect of wave reflections on the single-mode operation of a gyrotron can be investigated with the help of Rieke diagrams [210]. In long pulse operation, the frequency varies with time. This has an effect on the efficiency and also influences the reflection coefficient. To investigate this effect, one has to consider some effects of window reflection on single-mode operation. For this purpose, the self-consistent calculations have to be carried out taking into account the effect of the electron beam and the reflection coefficient on the frequency and RF field profile. The amplitude of the reflection coefficient due to a ceramic window is easily computed. The phase is harder to determine.

As an example, the RF-field profiles for the $TE_{25,6-}$ mode with a typical set of beam parameters and resonator geometry are shown in Fig. 5.2. In these curves, the effect of the phase of the reflection coefficient on the RF field profile is shown. The corresponding Rieke diagram is shown in Fig. 5.3. As also observed by other authors [211], there is a region where equifrequency lines converge and where two or more frequencies can be present simultaneously, for the same load characteristics. This "unstable region" occurs for $|R|$ slightly less than 0.4 and phase $\phi \approx 240°$. In most cases investigated numerically,
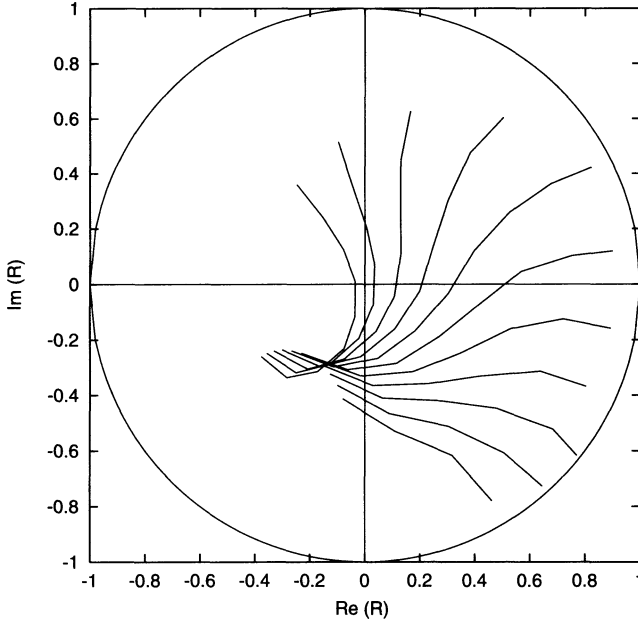
Fig. 5.3. Rieke diagram for the $TE_{25,6-}$ mode with beam energy of 78.9 keV, $I_b = 46.6$ A, $B = 6.03$ T, beam radius of 8.1 mm, and average velocity ratio $\alpha = 1.11$. The equifrequency lines cover the frequency range 151.10–151.20 GHz in steps of 10 MHz [210]

this occurred for a phase of the reflection coefficient ϕ slightly less than 270°. This may explain why the field profile is so strongly distorted in this region. For other cases, the Rieke diagram provides other information [209]. Though a quantitative fit to the data has not been performed, the use of Rieke diagrams to estimate the effect of reflection on the behavior of particular gyrotrons may qualitatively conclude the following [210]:

– Power reflection back into the gyrotron cavity frequently has a significant effect on the RF field profile. Calculations using a fixed Gaussian field profile may not be as accurate as one might wish.
– The poorly known phase of the reflection coefficient is important, even in single-mode approximation. The field profile, output power, and quality factor depend sensitively on it, even for small values of $|R|$.
– Frequency pulling depends on magnetic field, beam radius, velocity ratio, and reflection coefficient. Its magnitude typically varies from about 50 to 100 MHz.
– Long line (that is the distance from the load to input) effects [209] basically change the phase and spread out the Rieke diagram.

– Mode competition calculations including the dependence on the phase of the reflection coefficient, which will be different for each mode, will be computationally very expensive. However, not including it is unlikely to be sufficiently accurate.

6 Electron Optical and Guiding System

6.1 Introduction

Electron optical and guidance systems, namely, the magnetic coils, electron gun, and collector, are major components of a gyrotron oscillator. In gyrotrons, the source of electrons is frequently a magnetron injection gun (MIG), which produces annular electron beams having the desired beam properties. After passing through the interaction region and transferring energy to the output RF beam, the spent beam is collected at the beam dump, generally called the collector. In conventional linear beam tubes, the external magnetic field is used to focus the electron beam with required beam properties whereas in gyrotrons it is responsible for the interaction phenomenon as well as the guidance of the electron beam from the point of emission up to its collection.

A detailed discussion of the formation, focussing and collection of electron beams for microwave tubes is given by True [212]. Piosczyk has given an excellent account of the design of magnetron injection guns for gyrotron oscillators [213]. The basic theory of the design of helical beams has also been given earlier by Russian researchers [214–216]. In this chapter, our attention is focussed on the design of the magnetron injection gun, collector and magnetic coil systems for particular gyrotrons. Similar design methodology and approach are also applicable to the design of electron optical and magnetic guidance systems of other gyro–devices.

6.2 Magnetron Injection Gun

6.2.1 General Remarks

Most high power gyrotrons use magnetron injection guns (MIGs), which produce annular electron beams in which electrons execute small cyclotron orbits at a frequency required for cyclotron resonance interaction in a gyrotron. For good interaction efficiency, the perpendicular velocity component should be as large as possible. A spread in perpendicular velocity results in a spread in axial velocity, and should be kept as small as possible. The cathodes used
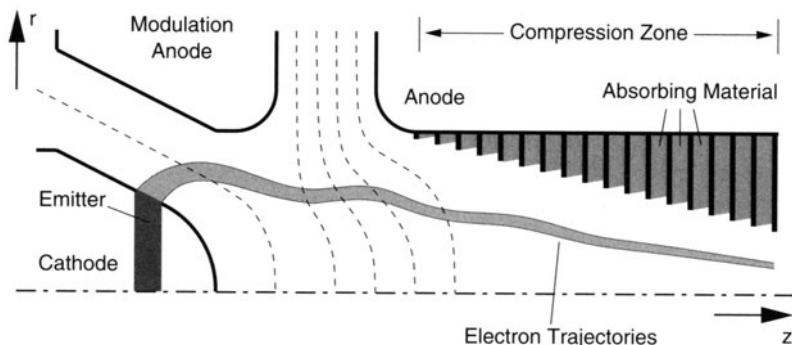
Fig. 6.1. Schematic of a Magnetron Injection Gun (MIG)

in magnetron injection guns for gyrotrons are operated under temperature-limited regime rather than in space-charge-limited to minimize the velocity spread in the beam [217].

A MIG is placed in an axially symmetric magnetic field at a magnetic field strength determined by the compression ratio. The electrons are extracted from a heatable conical emitting ring on the cathode. The beam current can be varied by adjusting the cathode temperature. The initial electron motion occurs in crossed electric and magnetic fields so that the electrons follow helical trajectories around the magnetic field lines. The anode accelerates the beam to the final beam energy. Sometimes a modulation anode is also employed (triode type MIG); this has an additional control over the electric field perpendicular to the cathode. Downstream from the gun the magnetic field increases smoothly in a magnetic compression region to the required peak value in the interaction region. The electrons emitted from the emitter surface follow the magnetic flux lines on helical orbits and drift towards the cavity region. The magnetic field compression reduces the radius (and thickness) of the beam and results in an increase of the velocity component perpendicular to the magnetic field. Since the total energy is constant, the drift velocity is correspondingly reduced. We have profited from the experience obtained in the extensive design studies of MIG's that have been presented previously, for example in [213, 218–221]. A schematic of MIG is shown in Fig. 6.1.

Electron guns are usually designed with the help of a trajectory program such as EGUN [222], BFCRAY [223, 224], DAPHNE [225] or EPOSR [226]. The design is facilitated by determining the initial design following analytical expressions of Baird and Lawson [227] (very similar expressions were derived much earlier by Russians, but this work is not readily available in the western literature), and then carrying out the design optimisation using any available trajectory program. Such a code computes a solution of Poisson's equation on a two–dimensional mesh covering the gun's cross-sectional area. The boundary of the gun is determined partly by electrodes at various potentials (Dirichlet boundaries) connected by appropriate segments with

Neumann boundary conditions. The space charge of the beam is modelled by integrating a selected number of electron trajectories from the cathode through the acceleration region of the gun and calculating the resulting space charge at each mesh point along the trajectories. The process of solving for the potentials on the mesh, then determining the electron trajectories is iterated until a self-consistent steady-state solution is obtained. This method is fairly reliable and the design of any gun is always tested and adjusted to its final form using such a code.

The codes calculate the contribution to velocity spread from beam optics and space charge. Some other sources can be estimated:

- surface roughness
- thermal spread in initial velocity
- nonuniform emission
- small departures from azimuthal symmetry
- beam instabilities.

The first two sources add about 5% to the calculated velocity spread. Some effects which can affect gun performance but are not always included, are initial velocities of the emitted electrons and irregularity of the emitter surface. The effect of surface roughness on velocity spread, and hence on beam quality, seems to be rather well described by adding its contribution quadratically to that due to beam optics (see [218, 228]). The effect of initial velocities has also been investigated by [218, 229]. Edgcombe, among others, has also demonstrated the importance of computing the space charge fields in the vicinity of the emitter surface accurately. The other sources of velocity spread require more sophisticated analysis and will not be considered here (see, for example, [230]).

Experimentally determined beam parameters are frequently in fair agreement with the results of a simulation based on ray tracing [215], but some effects are difficult to explain in the framework of such codes [230]. These include:

- The velocity spread is sometimes much larger than the calculated velocity spread.
- Large values of the velocity ratio α, when specified in the design, are frequently unattainable in practice. The limiting values correlate with the velocity spread.
- Sometimes electrons are reflected at a magnetic mirror in the region of increasing magnetic field; trapping of these particles leads to an increase of spread and decrease in the limiting value of α [219].
- Intense quasi-periodic oscillations in the frequency range 10–1000 MHz are sometimes observed at large beam currents. In such cases and for large pulse lengths a difficult-to-control growth of the emission current appears that leads ultimately to a failure of the operating regime of the gyrotron.

One knows that there are effects which may play a role in gun performance which are not modelled well by a trajectory code. For example, the enhanced velocity spread due to the non-uniform axial space charge field which arises from gyromotion of the electrons in the drift region, where the magnetic field is increasing, probably requires a fully self-consistent calculation with a large number of simulation electrons, and finer mesh spacing, than is convenient using some of the older codes. And, of course, nonstationary processes cannot be simulated at all.

6.2.2 Preliminary Design

From the resonator design calculations, one has information about the requirements concerning magnetic field and beam properties in the cavity region, cavity radius and beam radius. By making use of Baird's trade-off expressions [227] or an electrode synthesis program [214, 231, 232], one computes the gun design parameters in adiabatic approximation, taking into account the technical and physical constraints, namely, emitter radius, emitter current density, space charge ratio, cathode to anode distance, etc. Some of these relations are given below. Under adiabatic approximation, the electron motion in crossed electric and magnetic fields can be separated into a gyrating motion of the electrons (with Larmor radius r_L and cyclotron frequency ω_c) and a drift of their guiding centers. This adiabatic approximation is valid if the variations in the electric and magnetic fields are rather small at dimensions characteristic for the electron trajectories [213].

The initial design establishes the main gun parameters such as cathode radius (average), cathode–anode spacing, emitter current density, electric field at the cathode, and the cathode slant angle to the required beam properties. In a second, more important step, simulation codes are used for a final optimisation of the shape of the electrodes, as discussed above. Use of these codes permits an examination of the dependence of the beam properties on the operating parameters.

Trade-off and Initial Design Expressions

The most important parameters for the gun design are given here. Some parameters are fixed from optimization of the interaction:

– Electron energy U_b and relativistic mass factor:

$$\gamma_0 = 1 + \frac{U_b}{511\,\text{kV}} = \frac{1}{\sqrt{1 - \beta_{\perp 0}^2 - \beta_{z0}^2}}.\tag{6.1}$$

– Beam power $U_0 I_b$, where U_0 is the accelerating voltage and I_b is the total beam current.

- Voltage depression: Due to the space charge in the beam, the potential within the beam is reduced with respect to the cavity wall. In a conventional hollow cavity, the voltage depression is given by

$$\Delta U_b = U_0 - U_b = \frac{60 \Omega I_b}{\beta_{z0}} \ln \frac{R_0}{R_e} \, , \tag{6.2}$$

and in the case of a coaxial cavity having insert radius R_i, it is given by [233]

$$\Delta U_b = U_0 - U_b \simeq \frac{60 \Omega I_b}{\beta_{z0}} \ln \frac{R_0}{R_e} \frac{\ln(R_e/R_i)}{\ln(R_0/R_i)} \, , \tag{6.3}$$

where U_0 is the accelerating voltage. The cavity radius R_0 and average radius of guiding centers at interaction R_e are given by $R_0 = \frac{x_{m,q}\lambda}{2\pi}$ and $R_e = \frac{x_{m\pm1,1}R_0}{x_{m,q}} = \frac{x_{m\pm1,1}\lambda}{2\pi}$, where x_{mq} is the qth root of $J'_m(x)$ and λ is the free space wavelength. In general, the co-rotating mode (with the lower sign) is chosen, since this provides better coupling of the beam to the RF-field. Nevertheless, the voltage depression as a practical design constraint for the design of gyrotrons is discussed in detail in the previous chapter.

- Optimum cyclotron frequency:

$$\omega_c = \frac{eB_0}{m_e \gamma_0} \, . \tag{6.4}$$

- Larmor radius at interaction:

$$r_{L0} = \frac{v_{\perp 0}}{\omega_c} = 1.705 \, \text{mm} \times \frac{\gamma_0 \beta_{\perp 0}}{B(\text{T})} \, . \tag{6.5}$$

- Velocity ratio:

$$\alpha = \frac{v_{\perp 0}}{v_{z0}} \, . \tag{6.6}$$

- The radial thickness of the beam at interaction should not exceed $\lambda/8 + 2r_{L0}$.

The other parameters should be chosen to provide the above beam parameters with minimal velocity spread. These include:

- Compression ratio:

$$b = \frac{B_0}{B_c} \, . \tag{6.7}$$

- Emitter Radius: From Busch's theorem, the cathode radius is related to the beam radius (in paraxial approximation) by

$$R_c = \sqrt{b} R_e \tag{6.8}$$

and the emitter radius thickness can be estimated from

$$\Delta R_c = \sqrt{b} \Delta R_e \, . \tag{6.9}$$

Emitter Length: Simple geometry determines the emitter length l_s from total current

$$I_b = (2\pi R_c l_s) J_c \, , \tag{6.10}$$

where ϕ_c is the cathode slant angle and J_c is the cathode current density, note that (also)

$$\Delta R_c = l_s \sin \phi_c \, . \tag{6.11}$$

– Cathode electric field: A first estimate of the required cathode electric field E_c can be obtained from

$$\gamma_0 v_{\perp 0} = \sqrt{b} \gamma_c v_{\perp c} = \frac{\sqrt{b} E_c \cos \phi_c}{B_c} \, , \tag{6.12}$$

and this requires

$$E_c \cos \phi_c = \frac{B_0 \gamma_0 v_{\perp 0}}{b^{3/2}} \, . \tag{6.13}$$

– Cathode–anode spacing: The cathode–anode spacing (d) is given by

$$d = R_c \frac{r_{L0} D_F \mu}{\cos \phi_c} \, , \tag{6.14}$$

where D_F is the cathode-anode spacing factor (select $D_F \geq 2$) and μ is the Tsimring cylindricity parameter ($= 1/\sqrt{(r_{g0}/r_{L0})^2 - 1}$ and r_{g0} is the guiding center radius at the RF interaction region).

6.2.3 Codes for the Design of MIGs

The design of a gun requires the use of numerical simulation in rather complicated geometries with nonuniform magnetic fields. Analytical estimates, such as given by Baird and Lawson [227], or by electrode synthesis [214, 231, 232], are not sufficient for accurate calculation of the beam properties.

Numerical simulation of gyrotron guns requires the calculation of the electric field produced by the voltages applied to the electrodes plus the space charge produced by the beam as a result of its motion in the applied electric and magnetic fields. Most codes compute a self–consistent solution of Poisson's equation on a two dimensional mesh covering the gun's cross sectional area. The boundary of the gun is determined partly by electrodes at various potentials (Dirichlet boundaries) connected together by appropriate segments with Neumann boundary conditions. This part of the calculation is the so–called field solver.

The space charge of the beam is modelled by integrating a selected number of electron trajectories from the cathode through the acceleration region of the gun and calculating the resulting space charge at each mesh point along the trajectories. The trajectory calculation involves solving the relativistic

equation of motion for the electrons in the given electric and magnetic fields (particle pusher) and then assigning the resulting space charge and current density to the grid points. In order to solve the equation of motion, the particles must also be localized and the fields interpolated from the grid points to the particle position.

For trajectory, or ray tracing codes, the solution process of solving for the potentials on the mesh, then determining the electron trajectories is iterated until a self-consistent steady–state solution is obtained. By contrast, the particle-in-cell (PIC) method solves the field equations after every few particle pushing time steps (i.e., subcycling, see [147]). For a truly steady state situation, the final results obtained with both methods should be quite similar. Examples are: The BFCRAY code is in fact a modification of the BFCPIC code. It was modified to a ray tracing version, BFCRAY, in order to reduce the computational effort to a level suitable for gun design work, as described in [223]. An extension of the EPOSR code to a particle-in-cell version has been described in [230].

The PIC method is required to simulate the effect of reflected and trapped electrons and possible secondary emission from the cathode. Beam instabilities cannot be simulated any other way. One should keep in mind that a well–designed gun will provide a beam that is substantially free of such problems. Although MIG guns are usually operated in the temperature-limited regime, as described here, it is sometimes useful to consider space charge limited emission. The numerical modelling of space-charge-limited emission has been discussed in [314] and references therein. See also [230].

6.2.4 Design Procedure of MIGs

Before describing the design procedure for specific MIGs, we summarize the most important basic gun and beam flow types:

- Depending on the type of interaction cavity, MIGs are broadly divided into two catagories. One is an ordinary MIG which is used in most of the gyro-devices without a coaxial insert and the second one is the inverse MIG (IMIG) or coaxial MIG (CMIG) which is employed in coaxial gyrotrons and in similar devices with a coaxial insert.
- Based on the number of anodes, MIGs are of two types. One is a diode type and the second one is a triode MIG. A diode type configuration is generally preferred if one is able to achieve the desired beam quality and parameters since it involves less technical complexity (in particular, the power supply is usually simpler). A triode type configuration has an additional anode (modulation anode) to provide a better control over the beam properties (for instance, beam velocity ratio α) but obviously at the cost of an extra power supply and associated technical complexities.
- The initial velocity of the electrons as they are emitted from the cathode surface is determined to a large extent by the $\boldsymbol{E} \times \boldsymbol{B}$ drift (in the ϕ direction) at the cathode surface. This is given by

Table 6.1. Schematic of the design procedure of MIGs

Nominal beam parameters from design goals
Decision of gun type : Diode or Triode (depends on necessity and technological limits)
Initial design from trade-off expressions (or synthesis codes to give preliminary electrode shapes, etc.)
Design analysis using established computer codes (any electron trajectory code)
Diagnostics of simulation and design optimization (done iteratively to reach design goals using the design codes)
Final beam parameters to be used in interaction computation

$$\beta_\phi = \frac{E_c \cos \phi_{EB}}{cB_c}, \qquad (6.15)$$

where ϕ_{EB} is the angle between the electric field and the magnetic field at the cathode surface. $\phi_{\mathrm{EB}} = \phi_c + \phi_{\mathrm{B}}$ where ϕ_c is the tilt angle of the emitter and ϕ_{B} is the angle between the magnetic field and the z-axis at the emitter surface. In view of the gun topology, that is, ϕ_{EB}, the electron beams in MIGs are classified as follows:

1. regularly intersecting electron beams (non-laminar type) $\longrightarrow 10° < \phi_{EB} < 15°$
2. boundary beams $\longrightarrow 17° < \phi_{EB} < 22°$
3. laminar beams $\longrightarrow 25° < \phi_{EB}$.

In most of the Russian literature mentioned above, the angle ϕ_{EB} is interpreted as the angle between the magnetic field and emitter surface. The basic types of beam flow depending upon the topology of the gun is discussed in detail in these works. A matter of practical experience from these works suggest the electron flow at general design nominal conditions is of "boundary beam" type which means a flow intermediate between non-laminar and quasi-laminar type.

MIG Design Procedure

In the design of MIGs, one can get initial design parameters from trade-off expressions shown in the previous section or from any suitable electrode synthesis procedure [231, 232]. Later numerical codes as mentioned above are used to optimize the electrode shapes and other gun parameters for the desired electron optical system and beam properties. The basic steps involved in the design procedure of MIGs are shown schematically in Table 6.1.

For optimization of the gun design for a specific case and to understand various dependencies of beam properties on governing parameters (namely,
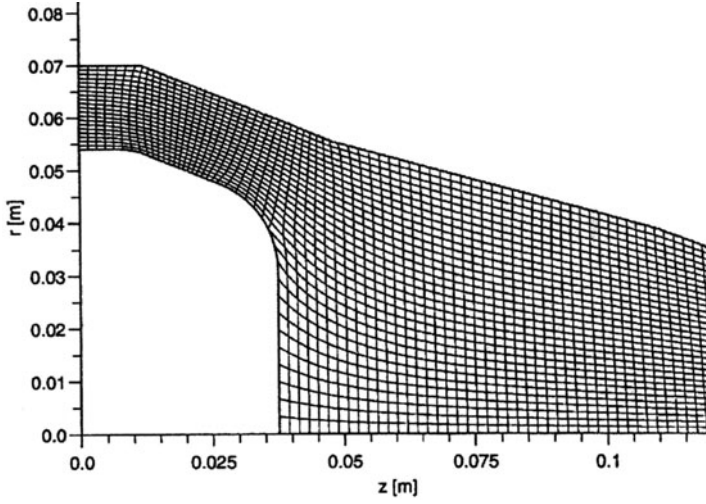
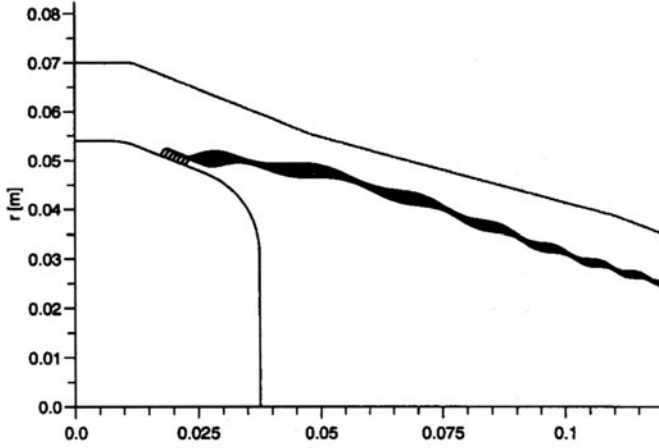**Fig. 6.2.** Section of boundary fitted grid for the 140 GHz, $TE_{28,8}$ gyrotron gun

Fig. 6.3. Typical electron trajectory plot ($U_0 = 81$ keV, $I_b = 40$ A, $B = 5.56$ T, and $b = 24$)

beam energy, current, magnetic field, gun geometry, etc.), a number of diagnostics of the simulation are possible. As an example, we show here some calculations of a typical diode gun for a $TE_{28,8}$ mode 140 GHz gyrotron [234]. Figure 6.2 shows the boundary fitted grid used for calculations with BFCRAY using a 385×65 grid. Figure 6.3 shows typical electron trajectories of such a gun.

Figures 6.4–6.7 show some typical emission plots for various beam parameters. These are plots that give the beam properties as a function of the
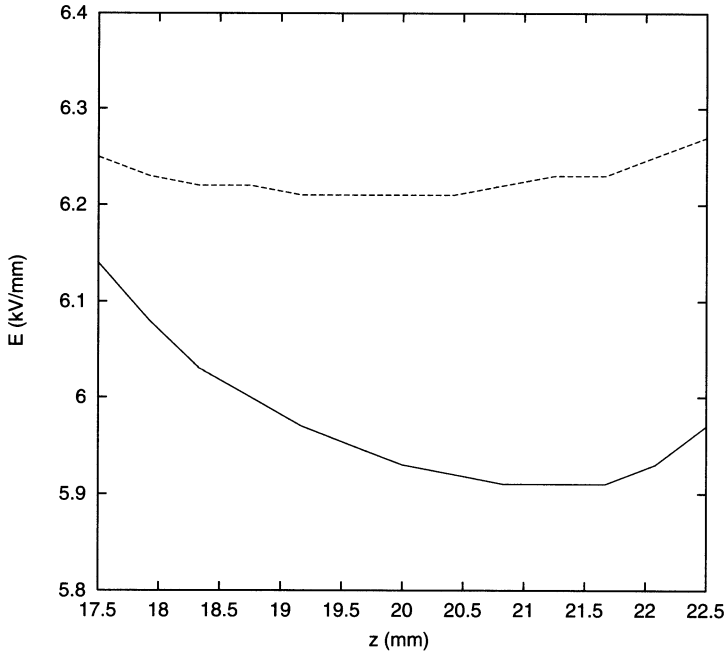
Fig. 6.4. Electric field at the emitter (for dashed line $I_b = 0\,\mathrm{A}$ and for solid line $I_b = 40\,\mathrm{A}$; $U_0 = 81\,\mathrm{kV}$)

point of emission. Such emission plots provide excellent diagnostics of the simulation for the electron optical system and its optimization. From these plots and other information, one can adjust the beam current, accelerating voltage, anode spacing, and axial alignment to obtain an optimized set of gun parameters. In addition to data for these plots, the computer codes provide all the required beam properties at the nominal operating conditions as data output for the purpose of analysis.

6.3 Beam Guidance

Most of the gyrotrons and its variants employ solenoids (either super–conducting or normal conducting coils) to provide the necessary magnetic field for beam guidance from the cathode through the interaction region up to the collector. The magnetic field lines guide the passage and exit of the electrons. A current carrying loop produces a magnetic field (Ampere's law) which forms the basis for the design of solenoids. Analytically, the magnetic field due to this current loop may well be expressed in terms of (1) Legendre polynomials, (2) complete elliptic integrals, or (3) series expansion of their
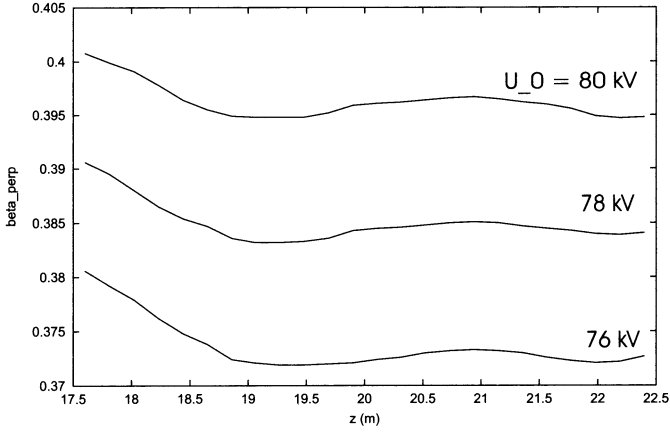
Fig. 6.5. $\beta_\perp$ as a function of point of emission for various accelerating voltages ($U_0 = 76$–$80\,\text{kV}$), $I_b = 40\,\text{A}$)
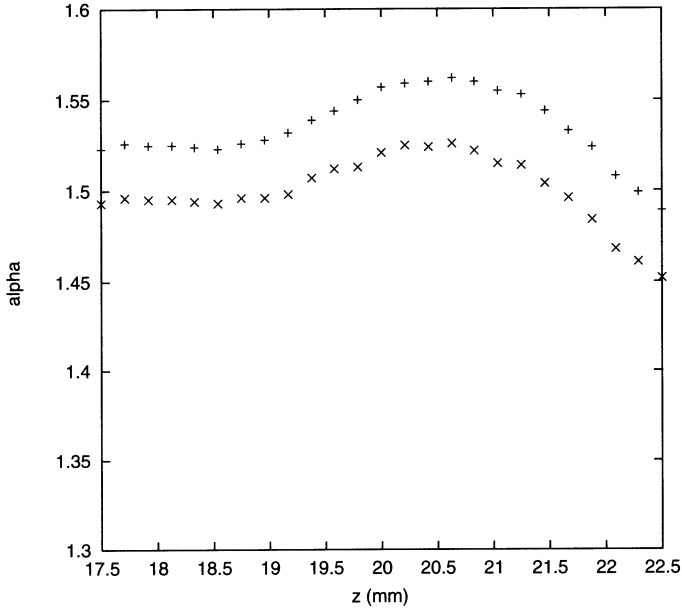

Fig. 6.6. α as a function of point of emission (+: at the start of the resonator and ×: at the middle of the resonator; $U_0 = 81\,\text{kV}$ and $I_b = 40\,\text{A}$)
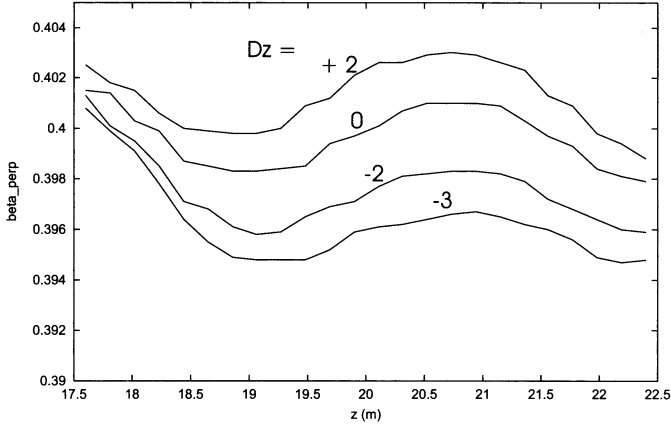
Fig. 6.7. $\beta_\perp$ as a function of point of emission for various shifts of coils relative to the emitter ($U_0 = 80\,\text{kV}$ and $I_b = 40\,\text{A}$)

on-axis values [235]. The method of Legendre polynomials give poor convergence. The other two methods can provide fairly accurate description of the on and off axis magnetic fields.

By making use of the complete elliptic integrals $K(m)$ and $E(m)$, the field due to a current loop may be expressed as follows [235]:

$$B_z(r, z) = M_1 \left[\frac{r_1^2 - r^2 - (z_1 - z)^2}{(r_1 - r)^2 + (z_1 - z)^2} \cdot E(m) + K(m) \right]$$
$$\cdot \left\{ (r_1 + r)^2 + (z_1 - z)^2 \right\}^{-1/2}, \tag{6.16}$$

$$B_r(r, z) = M_1 \left(\frac{z_1 - z}{r} \right) \left[\frac{r_1^2 + r^2 + (z_1 - z)^2}{(r_1 - r)^2 + (z_1 - z)^2} \cdot E(m) - K(m) \right]$$
$$\cdot \left\{ (r_1 + r)^2 + (z_1 - z)^2 \right\}^{-1/2}, \tag{6.17}$$

where B_z and B_r are the axial and radial components of the magnetic field respectively at (r, z) due to a coil of strength $M_1 = \mu_0 I / 2\pi$ centered at (r_1, z_1). $K(m)$ and $E(m)$ are complete elliptic integrals with argument m given by

$$m = \frac{4rr_1}{[(r_1 + r)^2 + (z_1 - z)^2]} . \tag{6.18}$$

Similarly, the off axis field components may be expressed in terms of their on–axis values as series expansion as follows [235]:

$$B_z(r, z) = B_z(0, z) - \frac{r^2}{4} B''(0, z) + \frac{r^4}{64} B_z''''(0, z) - \cdots$$

$$+ (-1)^n \frac{r^{2n}}{2^{2n}(n!)^2} B_z^{(2n)}(0, z), \qquad (6.19)$$

$$B_r(r, z) = -\frac{r}{2} B'(0, z) + \frac{r^3}{16} B_z'''(0, z) - \cdots$$

$$+ (-1)^n \frac{r^{2n-1}}{2^{2n-1}n!(n-1)!} B_z^{(2n-1)}(0, z). \qquad (6.20)$$

Here the primes denote differentiation with respect to z. The series expansion is only accurate for radii small compared to the inner radius of the coil.

By making use of one of the above two sets of analytical expressions (6.16)–(6.20), one can compute the on and off axis magnetic fields due to a current carrying loop. The actual fields are then the sum of the fields due to several such loops in a set of solenoids. The basic inputs to compute the fields are the coil geometry (width and breadth), coil location (axial and radial), coil currents and the number of turns in the coil.

Several commercially available codes (as cited in [212]) are available which could also provide the required magnetic field data to be used in the MIG design codes. However, most of the computer codes for the design of magnetron injection guns (discussed in the previous section) have incorporated internal routines for the calculation of the magnetic fields. As a typical example, the axial magnetic field due to a set of solenoids for a 140 GHz gyrotron along with gun geometry and coil positions are shown in Fig. 6.8 [236].
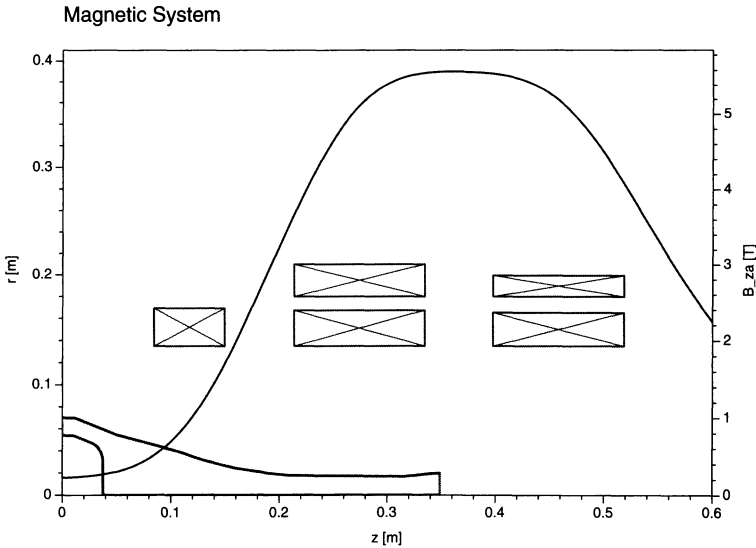

Fig. 6.8. Axial magnetic field with coils and gun geometry [236]

A knowledge of magnetic field profile from the coil design should also provide the following information, in addition to the field data:

– To estimate the location of the beam dump and size of the collector (from axial and radial flux lines). In addition, it is used for the determination of the addition of extra gun and collector coils.
– To estimate the diameter of the quasi–optical output coupler, if this is to be included.
– To calculate, roughly, the length of the tube (from a pre-determined knowledge of the positions of the emitter, cavity center region and collector position).

6.4 Beam Dump-Collecting System

6.4.1 General Remarks

In gyrotrons and similar devices, the energy of the electrons after participating in the interaction process is dissipated on the walls of the collecting surface. In most applications, the overall efficiency of gyrotrons is of paramount interest since it will considerably influence the power and cooling system requirements. To increase the efficiency, one should design and build gyrotrons with a suitable energy recovery system, namely, depressed collectors. Efforts have been made on the theoretical front [237–241] to increase the overall efficiency of gyrotrons by employing a depressed collector system as it is used in conventional microwave power sources [242–245]. Single-stage depressed collectors (SDCs) have been successfully used in gyrotrons increasing the overall efficiency to above 50% [246–248]. Although these experiments are limited to single-stage operation, they prove to be sufficient and efficient for the requirements of gyrotrons and promising in enhancing the efficiency in addition to reducing the power loading and X-ray generation at the collector surface, as well as the possibility of using less costly high voltage power supplies.

The major technological limit in the implementation of multi-stage depressed collectors (MDCs) for gyrotrons is the outer radius of the collector system and its axial extent. According to the work of Singh [237, 238], the magnetic field requirement at the collecting end must be typically between 50 to 20 Gauss. For instance, if we allow a magnetic field line of 5.4 T in the interaction region at 8 mm to fall to the desired 20 Gauss, we have to search at a radial location around 450 mm. Since the electron trajectories follow the field lines, one has to accept a very large collecting system. Therefore, we may require a collecting system with very large diameter and length for energy recovery. This problem can conveniently be alleviated by non–adiabatic magnetic decompression of the electron beam in the collector region by means of additional collector coils or other means, such as coaxially inserted soleniodal coils or by ferromagnetic insertions (see, for instance, [249, 250] and the references therein).

6.4.2 Theory of Depressed Collectors

In depressed collectors, the kinetic energy remaining in the spent beam is partially converted into electrical (potential) energy to reduce the power consumption of the high power device. To collect the spent energy on the collector walls, one has to depress the potential of the collecting surfaces with respect to the anode potential so that beam energy is recovered; this is the reason for the name depressed collectors. The figure of merit of a depressed collector is its efficiency (η_{coll}) which is defined as the ratio of the power recovered to the power fed to it (that is the power remaining after RF interaction) and is given by

$$\eta_{\text{coll}} = \frac{P_{\text{coll}}}{P_b - P_{RF}} , \tag{6.21}$$

where P_{coll} is the power recovered by the depressed collector system, P_b the total incident beam power and P_{RF} the generated RF power. Therefore, the power remaining in the spent beam after the interaction is equal to $(P_b - P_{RF})$. For a single stage depressed collector, $P_{coll} = U_{coll} \cdot I_{coll}$ where U_{coll} is the applied collector voltage and I_{coll} the collector current. Now the total efficiency of the tube with depressed collector system is given by

$$\eta_t = \frac{\varepsilon_{out}\eta_{el}}{[1 - \eta_{coll}(1 - \eta_{el})]} = \frac{P_{out}}{(P_b - P_{brec})} , \tag{6.22}$$

where $\eta_{el} = P_{RF}/P_b$ is the electronic efficiency, and $\eta_{coll} = P_{brec}/P_{bcav}$ is the efficiency of the depressed collector (as given in equation (6.21)).The RF losses inside the tube (ohmic losses and stray radiation) are described by the ratio $\varepsilon_{out} = P_{out}/P_{RF}$ where the generated RF power is P_{RF} and the RF output power is P_{out}. $P_{bcav} = (P_b - P_{RF})$ is the remaining beam power after RF interaction and $P_{brec} = (P_{bcav} - P_{bdis})$ is the part of the beam power recovered by the depressed collector and P_{bdis} is the power finally dissipated in the collector walls. The output efficiency without energy recovery and with a depressed collector is given by $\eta_{out} = \varepsilon_{out} \cdot \eta_{el}$. Typically, the internal RF losses are between 3–10% corresponding to $\varepsilon_{out} = 0.97$–0.90%. The efficiency of the depressed collector can be increased by using more collector stages. It has been estimated that the total efficiency of a high power gyrotron can be improved from around 31% to 51% with a single stage depressed collector [248]. After the first stage, the total efficiency is estimated to be increased by around 4% per additional collector stage. However, such a high efficiency ($> 55\%$) is not a necessary operational requirement in the case of high power gyrotrons. Moreover, multi-stage depressed collectors pose significant technological complexities when compared with the gain in the efficiency enhancement achieved.

A typical electrical setup employed in gyrotrons with a single-stage depressed collecting system is shown in Fig. 6.9 [248]. Here, experiments could be performed with a given set of operating parameters (namely, beam current
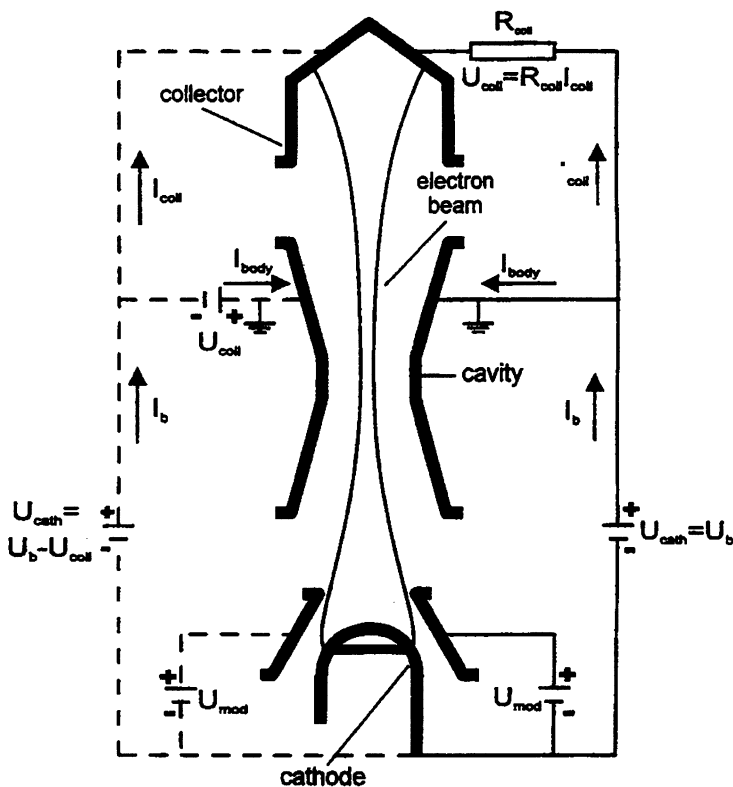
Fig. 6.9. Typical electrical setup used in the experiments for a single-stage depressed collector system for gyrotrons. The broken line on the left side indicates an equivalent arrangement with power supplies [248]

I_b, beam voltage U_b, modulation anode voltage U_{mod}, and magnetic field distribution $B(z)$) to measure the collector current I_{coll}, collector voltage U_{coll} and RF output power P_{out}. From this set up, the beam current is given by $I_b = I_{coll} + I_{body}$. Here, instead of using an additional power supply, the negative collector potential U_{coll} is obtained with a variable high voltage resistor with $R_{coll} \sim 2\,\text{k}\Omega$. I_{body} in general is very low ($\lesssim 0.1\%$ of I_b) which reduces the requirement on the body power supply. An equivalent electrical set up that is used for operation with power supplies is indicated with broken lines on the left side of the Fig. 6.9.

6.4.3 Magnetic Decompression

We have seen that in gyrotrons, the electron beam is guided by the external magnetic field. In adiabatic magnetic decompression, the magnetic field is

reduced sufficiently slowly to allow a decrease of the transverse momentum $p_\perp$ of the electrons with decreasing magnetic field according to the adiabatic approximation of motion [251]. Following Busch's theorem, the guiding centers of the electron beam trajectories, independently of the electron energy, follow a path along a constant magnetic flux surface with the enclosed flux given by

$$\phi_b(z) = \pi \int_0^{R_e(z)} B_z(z,r)r\,dr$$

$$\cong \pi R_e^2 B_{cav} \cong \text{constant (under paraxial conditions)}, \quad (6.23)$$

where $B_z(z,r)$ is the axial magnetic field. R_e and B_{cav} are beam radius and magnetic field at the position of the cavity $z = z_{cav}$. The possible deviation of the electrons transverse from the constant flux surface is given by the Larmor radius r_L (see equation(6.5)).

In the non–relativistic approximation the maximum Larmor radius of an electron with kinetic energy E_b is given by

$$r_{Lmax} \cong 0.11 \text{ mm} \times [E_b(\text{keV})]^{1/2} / B(\text{T}). \quad (6.24)$$

Typically, in a magnetic field of 0.01 T, the maximum Larmor radii are between 59 and 110 mm for electrons with energies from 30 to 100 keV (a typical energy distribution in the case of high power gyrotrons).

If the magnetic decompression is performed naturally (that is adiabatically) with the decaying stray fields of the main magnetic coils, then according to equation (6.23), the beam radius in the collector region has to be very large in order to keep the peak wall loading within the technological limits ($\lesssim 0.5$ kW/cm^2) on the collector surface. Busch's theorem determines the beam radius R_e and the radial width ΔR_e of the hollow electron beam in the collector region given by [252]

$$R_{ecoll} \cong R_e \times \sqrt{\frac{B_{cav}}{B_{zcoll}}} \quad \text{and} \quad (6.25a)$$

$$\Delta R_{ecoll} \cong \Delta R_e \times \sqrt{\frac{B_{cav}}{B_{zcoll}}}. \quad (6.25b)$$

In this case R_{ecoll} and ΔR_{ecoll} have the same dependence of the magnetic field. Typically, for a 2 MW, TE$_{31,17}$, 165 GHz coaxial cavity gyrotron with $R_e = 9.41$ mm and $B_{cav} \cong 6.6$ T, $R_{ecoll} = 480$ mm for $B_{zcoll} = 0.01$ T, and $R_{ecoll} = 680$ mm for $B_{zcoll} = 0.005$ T, respectively. A collector with such parameters is possible only for very large collector diameters exceeding the technologically feasible limits.

This problem can be conveniently solved by the non–adiabatic magnetic decompression of the hollow electron beam. One has to make a note that in adiabatic motion: the magnetic momentum is conserved; the transverse momentum $(p_\perp)$ decreases with the magnetic field as $p_\perp \propto \sqrt{B(z)}$, the Larmor

radius is small, and the radial beam width incident on the collector surface (ΔR_{ecoll}) is small. For a collector with a given radius R_{ecoll}, the power density on the walls can only be modified by varying the axial beam width of the electrons incident on the walls given by [252]

$$\Delta L_{\text{coll}} \cong \frac{\Delta R_{\text{ecoll}}}{\sin \phi_{\text{coll}}} , \qquad (6.26)$$

where ϕ_{coll} is the angle of incidence between the beam and the collector surface. Therefore, to decrease the power density on the collector surface walls, one has to increase the width of the beam incident on the collector surface.

The width of the beam can be increased by properly tapering the collector radius or by using a non-adiabatic decompression method. In this case, part of the longitudinal momentum of the electron is converted into a transverse motion resulting in an increase of the Larmor radius. This can be achieved by suitably tailoring the magnetic field lines with the help of additional coils or ferromagnetic insertions (or conventionally termed pole pieces) [237–241, 249, 250]. According to [252], the instantaneous surface power density can be decreased by non–adiabatic motion and then the radial width ΔR_{ecoll} can be increased significantly up to twice the Larmor radius since $r_L \propto 1/B$.

6.4.4 Design of Depressed Collectors for Gyrotrons

The basic steps involved in the design of an efficient depressed collector system for high power gyrotrons is shown schematically in Table 6.2. As a typical example, the design of a single–stage depressed collector system with coaxial collector coils is considered [250, 252]. In the design of a depressed collector system, one first has to prepare electron beamlets with an energy distribution representing the true energy distribution of the beam after RF interaction. The energy dispersion of the beam after RF interaction for the present case of a 2 MW coaxial gyrotron is shown in Fig. 6.10.

In general 80–200 beamlets are sufficient to represent the true energy distribution. With realistic beamlet information generated from the energy dispersion, EGUN (or any equivalent code) is run in steps from the output end of the cavity to the entrance of the collector domain. In each step the beamlet information from the preceding run is fed to the following run. Finally, by making use of the stored beamlet information at the entrance of the collector, the trajectory code is run in the collector domain with various collector shapes and collector potentials until technological constraints are fulfilled with minimized reflections and scattering problems. Figure 6.11 shows the geometry of the collector with coaxial collector coils resulting from the design presented in [250]. The electron trajectories in the collector domain are shown in Fig. 6.12. In this collector configuration, additional coils are used inside the coaxial portion of the collector domain.

Table 6.2. Schematic of the design procedure of collectors for gyrotrons

Energy dispersion from interaction computation
Preparation of realistic beamlets from energy dispersion
Decision for the number of collector stages (depends on necessity, technological limits and economics)
Decision to employ additional coils or inserts (for magnetic decompression to reduce the collector size)
Design analysis with realistic beamlet information (with available electron trajectory codes)
Design optimization (for single-stage collectors until desired wall loading) (for multi-stage collectors by changing the electrode shapes and potentials)
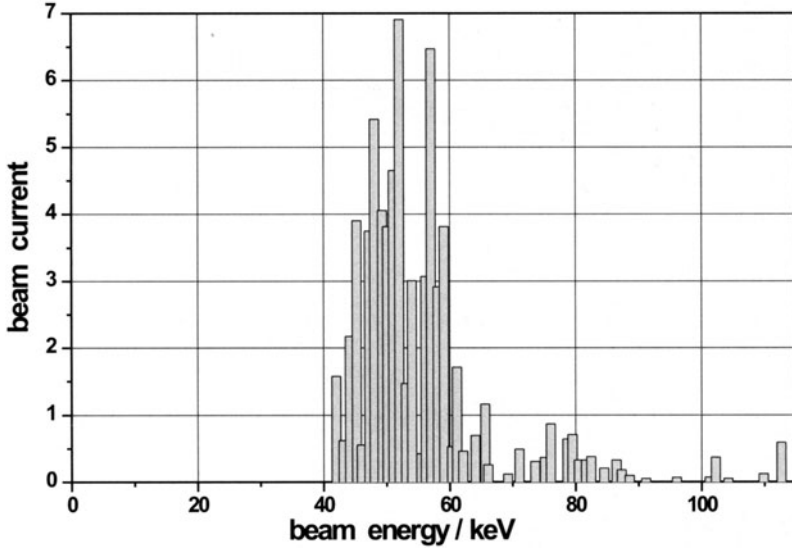
Fig. 6.10. Energy dispersion of the electron beam after RF interaction as taken for the design calculations [252]

In addition, calculations are performed to estimate the effect of secondary electrons (discussed in the next section). The calculated trajectories of the secondary electrons for the present example of single–stage depressed collector is shown in Fig. 6.13. In total 100 beamlets have been taken to simulate this process using the EGUN code. 50 beamlets for elastically scattered secondaries ($\phi_{sec} = \phi_{ins}$, $E_{sec} = E_{inc}$) and 50 beamlets for non–elastically scattered secondaries (ϕ_{sec} is aribitrary, $E_{sec} \leq E_{inc}$). Since the number of
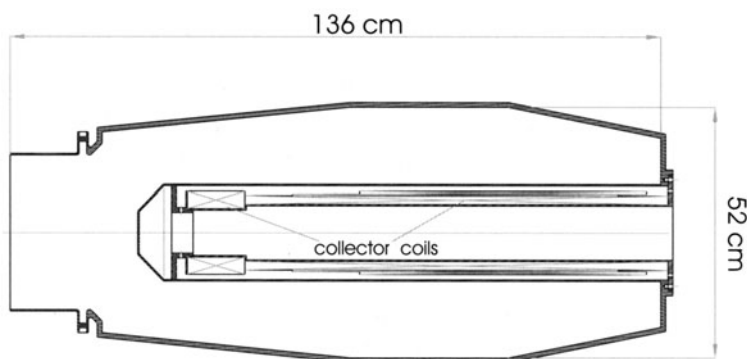
Fig. 6.11. Schematic view of the 2.2 MW single-stage depressed collector with coaxially inserted collector coils [250]
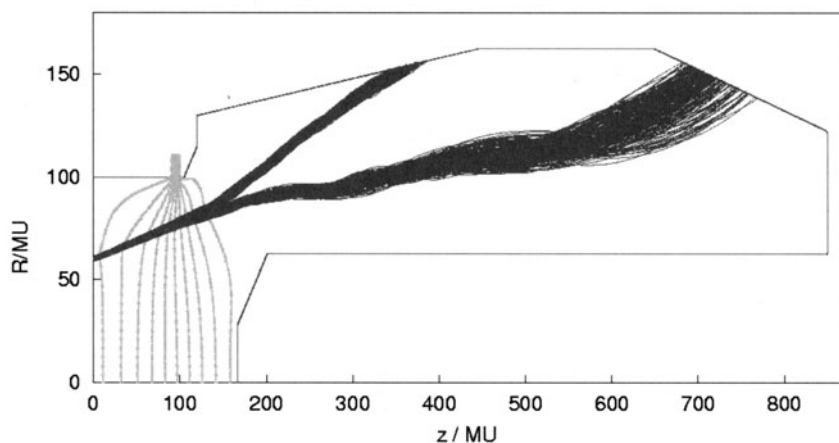

Fig. 6.12. The potential lines and electron trajectories for the top and bottom beam position [250]

secondary electrons depends on different parameters, such as material surface, energy, angle of incidence, etc., the results are of a rather qualitative nature. They allow to determine loading on the insert and collector walls due to secondary electrons and to estimate the number of backscattered electrons moving towards the interaction region. The sophisticated codes of Singh [240] could handle the effect of secondaries more accurately.

In addition, one may add additional sweeping coils to reduce the power density on the collector walls. These additional sweeping coils avoid the single spot incidence of the electron beam on the collector surface and reduce power density on the wall. The sweep frequency is limited by the skin effect in the collector walls and is given by [253]
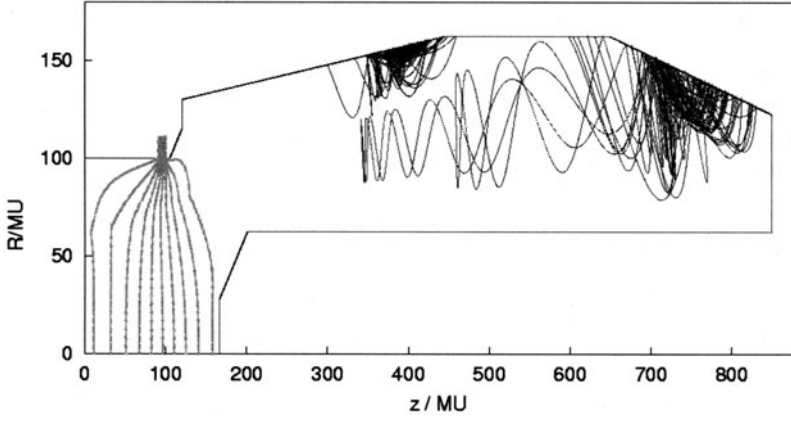
Fig. 6.13. Potential lines and trajectories of secondary electrons (both elastically and non-elastically scattered) [250] for primaries shown in Fig. 6.12

$$f_{\text{sweep}} < \frac{1}{\pi \sigma \mu_0 d_c^2} \, . \tag{6.27}$$

Here σ is the conductivity of the collector wall material and d_c its thickness. Generally, for a collector made of copper with $\sigma = 59 \text{ m}\Omega^{-1}\text{mm}^{-2}$, $d_c = 10$ mm, the sweep frequency is around 10–15 Hz because of the skin effect. However, the magnetic induction of these sweeping coils should be low, of the order around 0.01–0.05 T [253].

According to a one dimensional model for heat transport, the temperature increase ΔT of a surface exposed to the power P_{wall} is given by [184, 250, 252]

$$\Delta T \simeq 0.82 \times P_{wall} \times \sqrt{\frac{2\tau}{c\lambda\rho}} \tag{6.28a}$$

$$= 0.32 \times P_{wall} \ (\text{W/cm}^2) \times \sqrt{\tau(\text{sec})} \quad \text{for copper} \, . \tag{6.28b}$$

Here, P_{wall} is the surface power loading, τ is the time of exposure with P_{wall}, λ is the heat conduction coefficient, and ρ is the specific heat capacity. From this model[184], the characteristic length of heat diffusion in copper is $\delta_{1/e} \simeq 15 \times \sqrt{\tau(\text{sec})}$. From equation (6.28a), the amplitude of temperature oscillations ΔT_{max} due to beam sweeping decreases as the square root of f_{sweep} as

$$\Delta T_{\text{max}} \propto \sqrt{\frac{1}{f_{\text{sweep}}}} \, . \tag{6.29}$$

6.4.5 Some General Remarks

The basic steps that have to be dealt in the design of depressed collectors, particularly of multi–stage type, are (i) sorting of electrons according to their energies, and (ii) avoiding a flow of secondary and reflected electrons. Let us now discuss these problems individually.

Sorting of Electrons

After the RF interaction the electron beam has a wide energy dispersion. In efficient gyrotrons the energy distribution covers typically an energy range of about 35–140% of the incident electron beam energy. For an efficient depressed collector system, it is necessary to spatially separate the trajectories of electrons with different energies. Since in gyrotron devices the magnetic field distribution has a strong influence on the electron motion, the sorting of the electrons according to their energies always requires a careful shaping of the magnetic field lines in the collector domain. In conventional TWTs [242–244], multi–stage systems with more than 5 stages have been used with high efficiency. Compared to the TWTs, the high energy dispersion due to the efficient beam-RF interaction makes the sorting of the electrons much more difficult in the case of gyrotrons. So far, single–stage depressed collectors have been used in gyrotrons when a depressed collector was used at all. However, a further improvement of the collector and total efficiency could be achieved with multi–stage depression provided one can handle the technological problems such as complex shapes of tilted electrodes, ceramics, mechanical fabrication, and brazing cycles of such parts, etc. In some conventional microwave tubes, a magnetic refocusing system is employed in the collector region to sort out the electrons and to improve the efficiency of such a system.

Secondary and Reflected Electrons

When electrons hit a surface, secondary electrons are emitted with a certain probability depending on the surface material and on the energy and angle of the incident electrons. The secondary electrons can be divided mainly into two population types, namely the "true" secondaries with an energy of about $E_{\text{true}} \leq 50\,\text{eV}$ and the so–called "backscattered" electrons with an energy close to the energy of the primary electrons [254]. The "true" secondaries leave the surface isotropically, the "backscattered" electrons are reflected quasi–elastically at the surface. The secondary electron emission coefficient defined as the ratio of the secondary to the primary electrons depends on the material properties and on the energy of the primaries [245].

   These secondary electrons may create a serious problem mainly in multi-stage depressed collectors and they may reduce the overall efficiency of the collecting system. A flow of the secondaries between the electrodes of the

depressed collector has to be reduced as much as possible. The best way to deal with such secondaries is (a) to take care of the proper material selection for the collectors (low secondary emission coefficient), and (b) choice of electrode shapes and the potential distribution so that the emitted secondaries will always face a negative potential well. Depending on the retarding potential of the collector electrodes and the energy distribution of the beam, part of the electrons may be reflected towards the cavity and may become trapped between the collector and the negative gun potential [248]. These electrons which are traveling through the cavity may influence the RF generation. Therefore, according to the experimental results obtained in [248], its value should not exceed a few percent ($< 5\%$) of the beam current. For a given energy distribution, these reflected electrons have an influence on the choice of the retarding potential values of the electrodes. An easy way to avoid this is to simply limit the retarding potential to a value where this does not occur (typically $eU_{\text{dep}} < E_{\text{kin}-\text{min}}$).

7 Output Taper and Quasi-optical Launcher

7.1 General Remarks

In gyrotrons, the output system consists of an output taper which connects the interaction region with the main waveguide system, a quasi-optical mode converter (in the case of the radial output coupling) and the RF vacuum window. In the case of the axial extraction of power, the window is fixed at an appropriate axial location in the main waveguide after the taper section. In the case of the radial extraction of power, the regular waveguide section after the taper is transformed into a quasi-optical mode converter to convert the RF power in the waveguide modes to a Gaussian beam followed by an appropriate mirror system for beam focussing and necessary phase corrections. In this case, a radially located RF window is used to extract output power. The high ohmic attenuation and low power handling capability of standard metallic waveguides supporting the fundamental mode are prohibitive for the transmission and output section of gyrotrons and their variants in the systems. Thus, in order to design low attenuation high power waveguides, oversized or overmoded structures are preferred. Electron cyclotron emission (ECE) and microwave reflectometry plasma diagnostics also employ such low loss oversized transmission lines.

High power millimeter wave sources such as gyro-devices operate in higher order modes of circular waveguides. For interfaces of these devices to high power microwave transmission lines operating with waves with simple field structures, for feeding of gyro– and Cherenkov amplifiers as well as for low power ("cold-test") measurements of electrodynamic circuits of such high power tubes, mode converters for high order modes are required. The appropriate mode conversion and transmission technology is mostly determined by the output mode and power of the source and by its frequency. In high power mm-wave systems, long distance transmission from the source to the load with very low ohmic attenuation and high mode purity can be accomplished by the following methods:

1. Closed, highly overmoded smooth-wall circular waveguides propagating a TE_{0n} mode (preferably TE_{01}).
2. Closed, highly oversized, circumferentially corrugated or dielectrically coated smooth walled circular HE_{11} mode waveguides.

3. Open, quasi-optical (q.o.) transmission of a Gaussian beam (TEM$_{00}$ mode) using focusing metallic mirrors as phase-correcting elements.

The first method is adapted for high power mm-wave systems employing TE$_{0n}$ mode gyrotrons with output power up to 200 kW and external waveguide mode converters or external quasi-optical mode transducing antenna radiators to produce a pencil beam with well defined direction and polarization. Such waveguides are employed in ECRH installations and in technological gyrotron systems for materials processing. The second and third methods are appropriate for ECRH complexes composed of 500 kW (or higher) gyrotron oscillators, for example TE$_{mn}$ mode gyrotrons with built in quasi-optical mode converter which directly converts the complicated cavity interaction mode into a linearly polarized free space Gaussian beam.

This chapter mainly deals with the output taper and quasi-optical mode converter for gyrotrons and similar technical devices. Such design studies of output systems are extensively given in the literature (for example see [255, 256] and the references therein). We have outlined only the salient features to keep the topic sufficiently brief and necessary references are given wherever required.

7.2 Output Taper

Tapers are required to transform from the standard size waveguide outputs to the oversized waveguide components and to transform to dimensions required for optimum component design. In gyrotrons, cross-section tapers, in general of cylindrical type, are employed between the output section of the cavity to the main waveguide section. Cross-section tapers should not generate spurious modes above a certain acceptable level. Basic types of cross-section tapers are shown in Fig. 7.1.

One can design either straight tapers with constant taper angle and abrupt discontinuities at each end, or variable tapers in which the taper angle is varied continuously along the length of the taper [255–260]. Very low unintentional mode conversion from the propagating mode to unwanted parasitic modes is obtained by employing relatively short nonlinear tapers with a gradual change of the cone angle. The synthesis of non-linear taper contours for highly overmoded transmission systems has been studied by several workers; a comprehensive summary can be found in [255, 258, 259]. The properties of several gyrotron uptapers and tapers developed for ECRH transmission lines are listed in [257] and [255] together with experimental values obtained by measurements using wavenumber spectrometers. The main difficulties in the design of gyrotron output tapers in comparison with highly oversized waveguide tapers for ECRH transmission systems are as follows [258]:
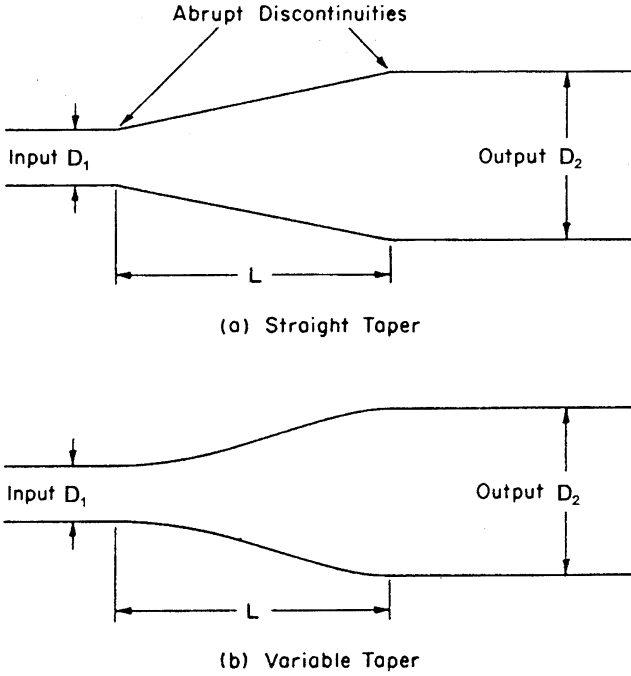
Fig. 7.1a,b. Different types of waveguide tapers [256]

- At the taper input, the working mode is very close to cut off. Input reflections as well as forward and backward scattered waves have to be considered.
- In the case of conventional gyrotrons with axial output coupling, where the output waveguide serves as the electron beam dump, the ratio of the collector to the cavity output radii is very large so that many parasitic modes may be strongly excited.
- Higher order working modes tend to couple to higher and lower undesired neighbouring modes with $\Delta m = 0$. TE_{mn} modes with $n > 0$ couple not only to TE_{mq} modes but also excite TM_{mq} modes.

7.2.1 Methods of Taper Analysis and Synthesis

The presence of a taper in a waveguide introduces unwanted parasitic modes. Gyrotron output tapers should act as a near perfect match at the input port with suppressed spurious modes at the output port with a taper length as short as possible. Conical tapers with constant cone angle introduce a higher degree of parasitic modes which is not desirable. Tapers with gradual

change in the cone angle cause considerably less power conversion to spurious modes. Since all gyrotron output tapers are cylindrically symmetric, their performance does not depend on the sense of the rotation of the mode. The principle methods employed for the analysis and synthesis of gyrotron output tapers are given in detail in [255] and the references therein. Here, we discuss them briefly.

Taper Analysis using Generalized Telegraphist's Equation

In this method, the following basic set of equations describing the propagation and coupling of different modes in nonuniform transmission lines are integrated and solved for the coupling coefficients:

$$\frac{d}{dz} \begin{bmatrix} V_1 \\ V_2 \\ \vdots \\ I_1 \\ I_2 \\ \vdots \end{bmatrix} = \begin{bmatrix} C_{11} & C_{12} & \cdots & -j\beta_1 Z_1 & 0 & \cdots \\ C_{21} & C_{22} & \cdots & 0 & -j\beta_2 Z_2 & \cdots \\ \vdots & & & \vdots & & \\ -\frac{j\beta_1}{Z_1} & 0 & \cdots & -C_{11} & -C_{21} & \cdots \\ 0 & -\frac{j\beta_2}{Z_2} & \cdots & -C_{12} & -C_{22} & \cdots \\ \vdots & & & \vdots & & \end{bmatrix} \cdot \begin{bmatrix} V_1 \\ V_2 \\ \vdots \\ I_1 \\ I_2 \\ \vdots \end{bmatrix} . \quad (7.1)$$

Here, V_i and I_i are complex amplitudes of the transverse electric and magnetic field vectors, Z_i the characteristic impedance, and β_i the phase constant of the particular ith mode. The coupling coefficients are given by

$$C_{mnq} = \int \int_{(S)} e_{mn} \frac{de_{mq}}{dz} dS , \quad (7.2)$$

where S is the cross section of the waveguide and e_{ij} is the eigenvector of a mode with transverse electric field $E_{ij} = e_{ij}V$ [259]. The values of the coupling matrix elements $j\beta_i/Z_i$ and C_{ij} depend on the contour of the gyrotron taper and on the frequency.

The complex field amplitudes are related to the forward and backward wave amplitudes by the square root of the characteristic impedance of the particular mode as given by:

$$V_i = (A_i + B_i) \sqrt{Z_i} ,$$
$$I_i = \frac{(A_i + B_i)}{\sqrt{Z_i}} . \quad (7.3)$$

The generalized telegraphist's equations are usually preferred for the taper analysis of gyrotrons.

Modular Analysis Concept – Scattering Matrix Method

In this method, the taper section is discretized into a number of small steps as shown in Fig. 7.2. Each module consists of an abrupt junction of two uniform
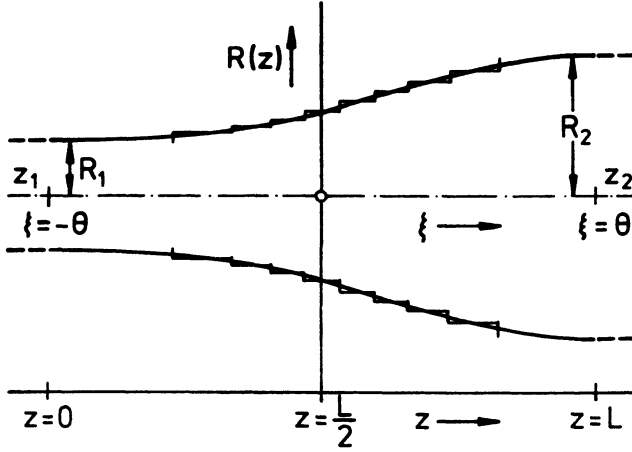
Fig. 7.2. Longitudinal cross section of circular waveguide taper and approximation of its contour by waveguide steps and uniform waveguide sections [255]

cylindrical waveguides separated by a small step. If the taper is fed by a TE_{mn} mode (with $m \neq 0$), the complete set of eigenfunctions is represented by forward and backward travelling TE_{mq} and TM_{mr} modes which are excited at each step discontinuity. If the tapers are fed by axisymmetric TE_{0n} modes, no coupling to TM modes occurs [260]. By applying the boundary conditions for the tangential electric and magnetic fields at the step boundaries, an infinite system of linear coupled equations (including evanescent modes) is obtained for unknown expansion coefficients in matrix form. Since their dimensions are infinite, they are truncated for numerical analysis using matrix manipulations, and the scattering matrix of the each modular waveguide step is obtained in the following form:

$$\begin{bmatrix} [B_1] \\ [B_2] \end{bmatrix} = \begin{bmatrix} [S_{11}] & [S_{12}] \\ [S_{21}] & [S_{22}] \end{bmatrix} \begin{bmatrix} [A_1] \\ [A_2] \end{bmatrix} . \tag{7.4}$$

Now the scattering matrix of the complete taper can be determined by cascading all the modules for the individual steps in a modular fashion. The previous telegraphist's method and this method yield very similar results with similar computational time.

Taper Synthesis

In this procedure, the coupled wave equations for cylindrical modes consisting of main and parasitic modes with complex forward amplitudes are solved and the magnitude of the unwanted mode amplitude, which is an integral of the

mode conversion distribution function, is calculated. Then the taper contour is calculated by numerical integration of the coupling distribution function by any suitable method suggested in [255]. The taper syntheses employed a near-optimum mode conversion distribution including reconversion and reflection [255]. Further, the quality of the taper synthesis should be checked by taper analysis.

If the transition between two oversized waveguides of different diameters is gradual and reflections are very low, then waves propagating in the backward direction can be neglected and the coupled wave equations for the forward propagating cylindrical modes can be written as:

$$\frac{d}{dz}\begin{bmatrix} A_{mn} \\ A_{mq} \end{bmatrix} = \begin{bmatrix} j\beta_{mn} & \kappa_{mnq} \\ \kappa_{mqn} & j\beta_{mq} \end{bmatrix}\begin{bmatrix} A_{mn} \\ A_{mq} \end{bmatrix}. \tag{7.5}$$

Here, A_{mn} and A_{mq} are complex forward wave amplitudes, β_{mn} and β_{mq} are the corresponding phase constants of the working and parasitic modes respectively, and κ_{mnq} denote the amplitude coupling coefficients. The magnitude of the unwanted mode amplitude is calculated from:

$$|A_{mq}| = W(\eta) = \int_{-\theta}^{\theta} CK(\xi)\, e^{-(j\eta\xi)}d\xi. \tag{7.6}$$

Here, $CK(\xi)$ is the mode conversion distribution function defined as

$$CK(\xi) = \frac{\eta\kappa_{mqn}}{\beta_{mn} - \beta_{mq}} = \frac{2k_0 R}{x_{mq}^2 - x_{mn}^2}\, C_0 R' \tag{7.7}$$

and

$$\kappa_{mnq} = C_0\,\frac{R'}{R}\,; \quad R' = \frac{dR}{dz}\,; \quad J'_m(x_{mn}) = 0\,; \quad \text{and} \quad \eta = \frac{f_0}{f} > 1 \tag{7.8}$$

where f is the operational frequency and f_0 is the upper limit of the desired frequency band. Here,

$$k_0 = 2\pi f_0 \sqrt{\mu\epsilon}\,, \tag{7.9}$$

$$\xi(z) = \int_0^z \frac{x_{mq}^2 - x_{mn}^2}{2k_0 R^2(z')}\, dz' - \theta\,, \quad \text{with} \tag{7.10}$$

$$2\theta = \int_0^L \frac{x_{mq}^2 - x_{mn}^2}{2k_0 R^2(z')}\, dz'. \tag{7.11}$$

In the above expressions, $\xi(z)$ is a measure for the accumulated phase with $\xi(z) = -\theta$ and $\xi(L) = \theta$. Since 2θ increases with increasing frequencies, a taper should always be designed for the highest frequency of the band so that its performance is better at lower frequencies. The coupling distribution function $CK(\xi)$ has to be chosen such that, for a minimum value of θ (shorter taper), the spurious mode amplitude $W(\eta)$ remains below the given limit W_{max} with the following equations satisfied:

$$CK(-\theta) = CK(\theta) = 0\,, \tag{7.12}$$

$$\int_{-\theta}^{\theta} CK(\xi)d\xi = C = C_0 \ln\left(\frac{R_2}{R_1}\right)\,. \tag{7.13}$$

From equation (7.12), it is understood that the coupling at the taper input $(\xi = -\theta)$ and taper output $(\xi = \theta)$ vanishes. The nonlinear taper contour is calculated by numerical integration from:

$$\ln\left(\frac{R(\xi)}{R_1}\right) = \ln\left(\frac{R_2}{R_1}\right)\int_{-\theta}^{\xi} K(\xi')d\xi'\,, \quad \text{and} \tag{7.14}$$

$$z(\xi) = \left(\frac{2k_0}{x_{mq}^2 - x_{mn}^2}\right)\int_{-\theta}^{\xi} R^2(\xi')d\xi'\,. \tag{7.15}$$

There are several approaches for the representation of $K(\xi)$ in the above expressions to compute the taper contour. The main methods are (i) Fourier series representation, (ii) Dolph–Chebychev distribution, (iii) modified Dolph–Chebychev distribution, (iv) three mode coupling distribution, and (v) near optimum mode-conversion distribution including reconversion and input reflection. These are discussed in detail in [255]. However, all are equivalent approaches for the synthesis of taper contours.

In actual gyrotron taper design, the synthesized contours were subsequently analyzed by numerically solving the generalized telegraphist's equations. The input contours of the gyrotron taper are matched to the flare angle of the resonator output. The spurious mode levels predicted by the synthesis and analysis codes were always in good agreement. The high power experimental results are slightly higher, but this is not surprising since insulation gaps and the gyrotron RF output window are additional sources of unwanted parasitic modes. The taper analysis of a 140 GHz, $TE_{10,4}$ mode gyrotron is presented as an example. The calculated levels of undesired modes at the output of the taper indicate that they are very low and the mode purity of the main mode is 99%. The excitation of the parasitic modes $TM_{10,3}$ and $TM_{10,4}$ together with the $TE_{10,4}$ transmission loss along a $TE_{10,4}$ gyrotron taper and the optimum taper contour are plotted in Fig. 7.3. It is evident that the effect of reconversion into the operating $TE_{10,4}$ mode is quite important.

Conversion of the operating gyrotron mode to the unwanted parasitic modes at discontinuities of cavity input and output taper sections can be reduced considerably by introducing smooth transition regions between the individual parts of the open resonators. The cavity and adjacent tapered output waveguide should be optimized as a single unit [258].

7.3 Quasi-optical Mode Converter

For gyrotrons with radial output coupling, an output coupler that separates the spent electron beam from the outgoing RF power is required. In addition,
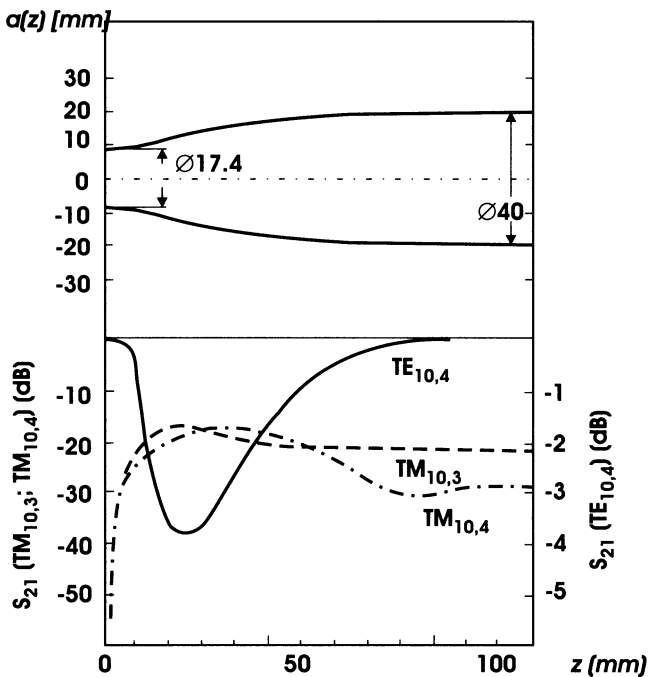
Fig. 7.3. Optimum contour of a 17.4–40.0 mm $TE_{10,4}$ uptaper together with the excitation of the $TM_{10,3}$ and $TM_{10,4}$ modes and the $TE_{10,4}$ transmission loss along the taper [255]

such a coupler allows to increase the electron beam interception area of the collector. It is the short wavelength, high output power and the rotating asymmetric high order cavity mode of such tubes which have led to the need for novel mode conversion concepts. The down conversion of these high order cavity modes with complicated field structure by using conventional waveguide mode transducers with highly oversized waveguide diameter is practically impossible due to the extreme mode competition involved.

The higher the operating mode is, the more it is appropriate to employ an asymptotic procedure for its description, namely the method of geometrical optics (g.o.) (see e.g. [255, 261]). In the framework of this method the initial mode is represented as a system of rays successively reflected from the waveguide walls (Brillouin–Keller concept). To directly convert the complicated field structure of rotating high order asymmetric gyrotron cavity modes into a linearly polarized Gaussian beam, i.e. to modify the configuration of rays, one can use quasi-optical (q.o.) devices, a proper combination of a specific mode converting waveguide slot radiator (launcher) together with a few curved mirrors [262, 263], often called a Vlasov converter. This method is universal, but diffraction effects limit its efficiency to approximately 80%,

which cannot be accepted for high power gyrotrons. This section summarizes
the principles and advantages of q.o. mode converters and discusses the de-
sign of improved launchers and beam shaping reflectors with higher efficiency.
Different output coupling schemes for gyrotrons are schematically shown in
Fig. 3.1 (see Chap. 3). The q.o. mode converter is a part of the internal elec-
trodynamic system of the gyrotron like the cavity and the uptaper (Fig. 3.1b
in Chap. 3). Radial output coupling of the RF power into the fundamental
Gaussian (TEM$_{00}$) free space mode has three significant advantages for high
power operation:

-   The linearly polarized TEM$_{00}$ mode is directly usable for low-loss trans-
    mission as well as for effective antenna feeding and no further mode con-
    verters are needed. Therefore, q.o. mode converters are also used for rela-
    tively modestly overmoded systems when a very compact mode conversion
    to the TEM$_{00}$ mode is required [264, 265].
-   The converter separates the electron beam from the RF-wave path
    (Fig. 3.1b), so that the electron collector is no longer part of the output
    waveguide as in the case of a tube with an axial output (Fig. 3.1a). Hence,
    the collector can be designed especially for handling the high electron-
    beam power. In addition, energy recovery with a depressed collector is
    much easier.
-   The harmful effects of RF power reflected from the output window are ex-
    pected to be significantly reduced especially if the window disk is slightly
    tilted.

7.3.1 Basic Principle of Quasi-optical Mode Converters

The principal schemes of q.o. mode converters for (i) rotating asymmetric
modes and (ii) for circular symmetric modes are shown in Fig. 7.4. TE- and
TM-modes in a circular waveguide can be decomposed into a series of plane
waves, each propagating at the Brillouin angle θ_B relative to the waveguide
axis:

$$\theta_B = \sin^{-1}\left(\frac{x_{mn}}{k_0 a}\right) \tag{7.16}$$

where x_{mn} is the Bessel root, k_0 is the free space wavenumber, and a is the
radius of the launcher waveguide.

The requirement of a zero azimuthal electric field at the waveguide wall
defines their relative phases. In the geometrical optics (g.o.) limit a plane
wavefront is represented by a single ray. Its transverse location is defined by
the requirement that at a particular point of interest the ray direction must
coincide with the direction of the Poynting vector of the original TE– or TM–
mode field distribution. If the point of interest is located at the waveguide
wall the ray has the distance:

$$R_c = \left(\frac{m}{x_{mn}}\right) a \tag{7.17}$$

(1) quasi-optical antenna (launcher)
(2) quasi-parabolic reflector

a)   b)

rotating TE$_{mn}$-or TM$_{mn}$ -modes   symmetric TE$_{0n}$ - or TM$_{0n}$ -modes

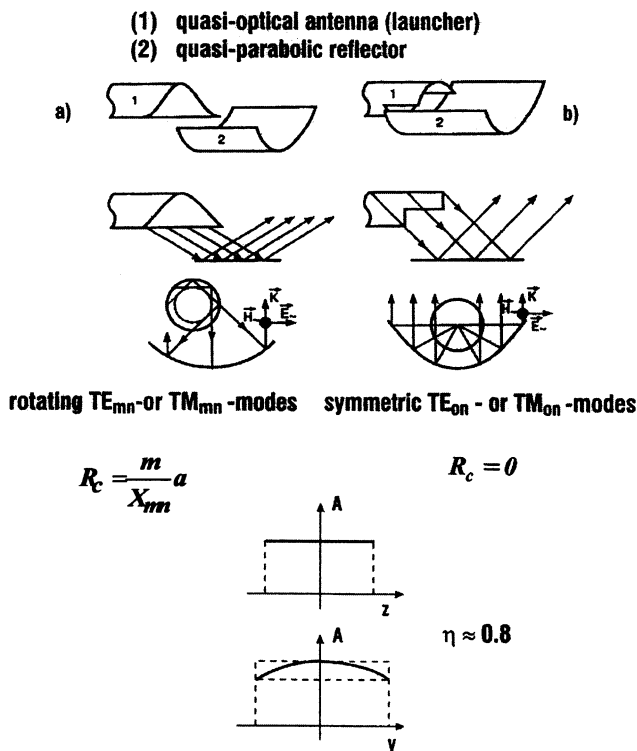$$R_c = \frac{m}{X_{mn}} a \qquad\qquad R_c = 0$$

$$\eta \approx 0.8$$

Fig. 7.4. Principal schemes of quasi-optical mode converters and amplitude distribution at the launcher. The electric field orientation shown in (**b**) applies only for TE$_{0n}$ modes [256]

from the waveguide axis. Hence if all plane waves are represented by g.o. rays they form a caustic at the radius R_c (Fig. 7.4). In an unperturbed circular waveguide the density of the rays along the caustic is uniform [261].

The distance that a ray has propagated in the axial direction between two subsequent reflections from the waveguide wall is

$$L_B = 2a \left[1 - \left(\frac{m}{x_{mn}} \right)^2 \right]^{1/2} \cot \theta_B . \tag{7.18}$$

In the transverse direction a section of angle:

$$\Delta\varphi = 2\theta = 2 \cos^{-1} \left(\frac{m}{x_{mn}} \right) \tag{7.19}$$

reflects all rays exactly once.

Accordingly, for modes with $m \neq 0$ the reflection points of each of the rays are placed on the waveguide surface in a helical line with the angle of inclination [255]

$$\psi = \tan^{-1}\left(\frac{\theta \tan \theta_B}{\sin \theta}\right) \tag{7.20}$$

and the distance (pitch) that a ray has propagated in the axial direction when it has completed a full turn is [255]

$$H = 2\pi a \cot \psi$$

$$= 2\pi a^2 \left(\frac{\beta}{x_{mn}}\right) \frac{\sqrt{1 - \left(\frac{m}{x_{mn}}\right)^2}}{\cos^{-1}\left(\frac{m}{x_{mn}}\right)}$$

$$= L_c = \text{launcher cut length} \tag{7.21}$$

which is the launcher cut length. Hence waveguide sections (wound parallelograms: "G region") with the length L_c and the transverse width defined by $a\Delta\varphi$ reflect each ray once. Back scattering effects due to diffraction of the incident high-order mode by the helical and straight edges of the launcher have been estimated by using the method of equivalent currents [266]. For $\theta_B < 70°$ the total reflected power is lower than - 30 dB. The helical-cut launcher radiates the RF power via its straight cut onto the first phase correcting mirror of quasi-parabolic shape (Fig. 7.5). The power reflected from the first mirror propagates as an astigmatic beam onto a series of two elliptical or hyperbolical reflectors where the astigmatism is removed and the output beam transverse dimensions are matched to the window size [255, 267]. In the recent works of Neilson [268], a surface integral analysis of quasi-optical launchers considering edge diffraction losses with the magnetic field integral equation (MFIE) approach is given.

7.3.2 Improved Quasi-optical Mode Converters

The wave beam produced by the conventional launcher differs significantly from a Gaussian beam, i.e., an eigenwave of the mirror transmission line, due to the fact that the field amplitude on the wall is constant. The coefficients of excitation of the Gaussian beam are about 0.8 (power) and depend slightly on the wave indices [263]. This cannot be accepted for high power gyrotrons owing to the harmful diffracted radiation (stray radiation) in the tube. The following requirements for the q.o. mode converter should be satisfied:

– low diffraction losses inside the tube (less than 3%)
– matching of the output wave beam to the HE_{11} waveguide mode or the fundamental Gaussian beam with efficiencies higher than 97%.
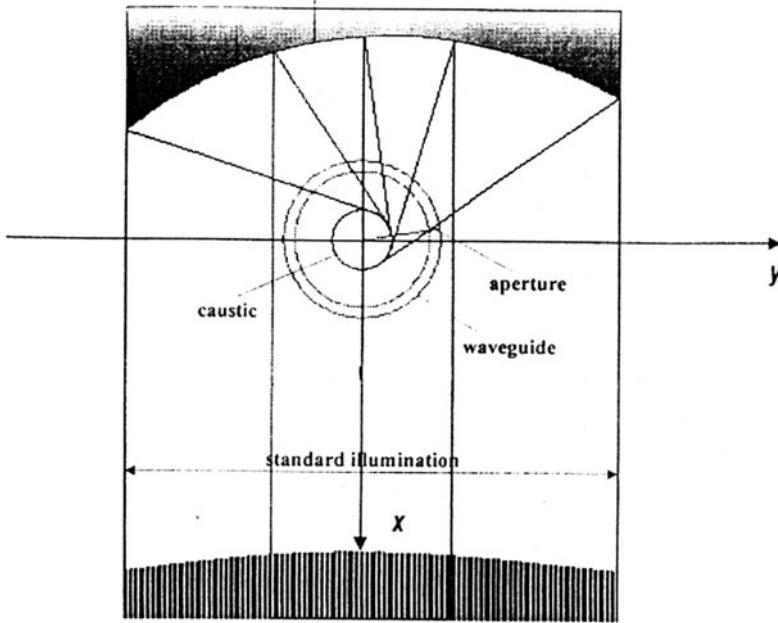
Fig. 7.5. Cross section of the launcher and the standard quasi-parabolic mirror. Care is taken here that the central ray is reflected onto the gyrotron axis, avoiding a transverse offset of the following two mirrors [256]

At the aperture of conventional Vlasov launchers there exists an approximately uniform field distribution in the axial and azimuthal directions (Figs. 7.4 and 7.5), leading to the high diffraction losses. There are two general methods to reduce the diffraction losses and produce a pencil like wave beam:

1. Employing tailored aperture distributions at the radiating launcher such that the sidelobes are reduced (see [255] and references therein), which means preshaping of the wave beam before its launching. The shaped beam has weaker fields at the cut edges (low diffraction) and a nearly Gaussian angular spectrum.
2. Synthesis of mode converting, phase correcting mirrors with complicated surface contours [269–272]. This method allows one to synthesize a desired field structure of paraxial wavebeams.

Preshaping of the wave beam before launching and mode converting phase correcting mirrors are described in the following parts of this section.

Beam Shaping by a Flared Launcher Cut

To tailor the aperture field distribution and to reduce the side lobes caused by the straight launcher cut, flared radiation cuts (visors or wings) have been used. In the case of transformation of a whispering gallery mode (WGM) with a single radial field maximum (e.g. $TE_{15,1}$) into a Gaussian beam one achieves a theoretical efficiency of 98% whereas the efficiency for the transformation of the $TE_{15,2}$ mode [274] or the $TE_{12,2}$ mode [275] is only 92–93%. In the case of higher order volume modes such as $TE_{15,4}$, this method gives a rather poor efficiency of only 87% [276].

Beam Shaping by Mode Converting Feed Waveguide

To achieve a sidelobe-free fundamental Gaussian beam as the output mode, the launcher must have feed waveguide deformations such that the incident rotating TE mode is converted to a mode mixture generating a Gaussian beam distribution [276–279]. A Gaussian aperture field distribution can be well approximated by a raised-cosine field distribution which can be obtained by means of a superposition of nine specific waveguide modes with matched amplitudes and relative phases given by [280]:

$$f(\varphi, z) = \left(1 + \frac{1}{2} e^{j(2\pi/L)z} + \frac{1}{2} e^{-j(2\pi/L)z}\right)$$
$$\cdot \left(1 + \frac{1}{2} e^{j(\pi/\theta)\varphi} + \frac{1}{2} e^{-j(\pi/\theta)\varphi}\right). \tag{7.22}$$

The interference of the nine waveguide modes creates an RF-field bunching in the axial and azimuthal directions. Requirements for this bunching are:

1. *longitudinal bunching*: the modes must have equal caustic radii and an interference length close to the launcher cut length L_c,
2. *azimuthal bunching*: the modes must have equal caustic radii and similar Bessel zeros.

This leads to the following mode selection rules:

$$\Delta\beta = \pm\frac{2\pi}{L_c} \text{ and } \Delta m = \pm\frac{\pi}{\theta}. \tag{7.23}$$

For the example of the $TE_{22,6}$ mode, we have $\Delta\beta = \beta_{mv} - \beta_{m\pm1,v}$ and $\theta \approx \pi/3$ which means $\Delta m = \pm3$. Power conservation requires that the relative power of the corresponding modes $TE_{22,6}, TE_{23,6}, TE_{21,6}, TE_{25,5},$ $TE_{19,7}, TE_{26,5}, TE_{24,5}, TE_{20,7}$ and $TE_{18,7}$ must be 0.44, 0.11, 0.11, 0.11, 0.11, 0.03, 0.03, 0.03 and 0.03, respectively.

These wall distortions (scattering surface) transform the input eigenwave to an eigenwave of the weakly perturbed transmission line. By means of this

principle each required amplitude distribution can be approximated. Numerical optimization calculations include many more than nine coupled modes. The helical converter ("dimpled-wall converter") is described by the following wall perturbation:

$$a(\varphi, z) = a_0 \left[1 + \varepsilon_1 \cos(\Delta\beta_1 z - l_1\varphi) + \varepsilon_2 \cos(\Delta\beta_2 z - l_2\varphi) \right] \qquad (7.24)$$

where

$$\Delta\beta_1 = \pm(\beta_1 - \beta_2), \quad l_1 = \pm(m_1 - m_2) = \pm 1,$$
$$\Delta\beta_2 = \pm(\beta_1 - \beta_3), \quad l_2 = \pm(m_1 - m_3) = \pm 3,$$

and β_1 is the propagation constant of the operating mode and β_2 and β_3 the propagation constants of modes which fulfill the requirement of (7.23).

The required minimal launcher length is

$$L_{min} = \frac{\pi}{2 \left| 2\beta_{mv} - \beta_{m+1,v} - \beta_{m-1,v} \right|} . \qquad (7.25)$$

The result of the numerical calculation for the first dimpled-wall q.o. mode converter which was used in a Russian 0.5 MW, 110 GHz, TE$_{15,4}$ gyrotron [276] is shown in Fig. 7.6. The corresponding geometrical structure of the space-periodic launcher in shown in Fig. 7.7. A shallow linear uptaper of the mean launcher radius a_0 reduces the danger of spurious gyrotron oscillations in the launcher [281, 282] due to an unintentional cavity introduced by the dimples.

This class of improved mode converters even can be employed in stepwise tunable multifrequency gyrotrons where specific series of cavity modes are utilized at their corresponding magnetic fields [44, 280]. A double beam q.o. output utilizing a two-cut launcher can be achieved with dimple type feed waveguides employing an $l_1 = 2$ perturbation for longitudinal bunching instead of $l_1 = 1$ [280, 304].

In the framework of geometrical optics the performance of the dimpled-wall launcher can be explained in the following way. Among the rays composing the initial mode let us define one to be the leader and find the points of its reflections from the waveguide wall. Then we deform the inner waveguide surface to make it focus near the reflection points of the leader ray and defocus at the remaining area. Then, when successively reflected from the walls, the rays will converge to the leader and finally, will compose an eigenmode of an open mirror waveguide with the transverse distribution of the RF field depending on the mirror profile.

Mode Converting Phase Correcting Mirrors

In cases where a simple Vlasov launcher or only a weakly beam preshaping launcher is used in connection with a large quasi-parabolic reflector, special
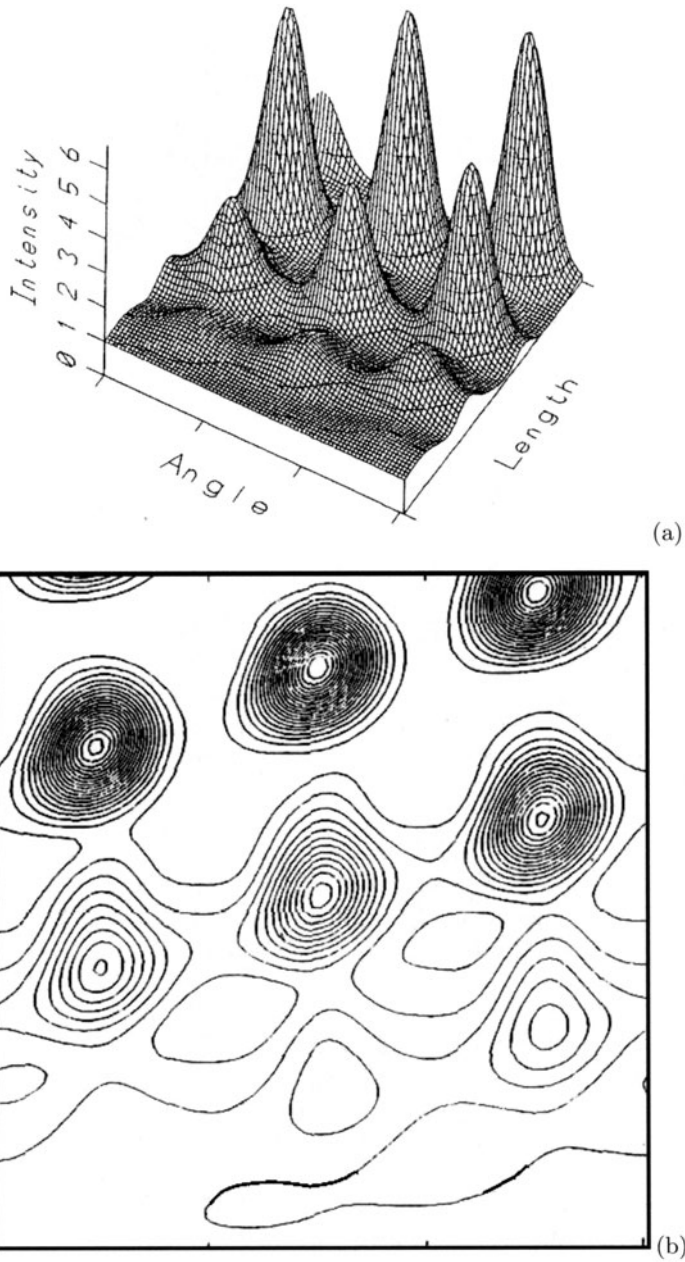
Fig. 7.6. Numerical calculation of the q.o. launcher used in a 0.5 MW, 110 GHz gyrotron to convert the $TE_{15,4}$ cavity mode. The distribution of wave-field intensity on the waveguide wall is shown. Here, (**a**) 3D plots, and (**b**) intensity contour map [276]
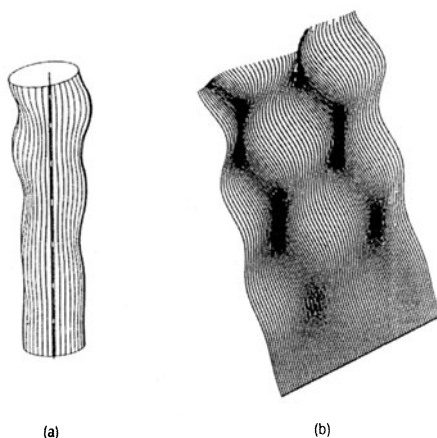
(a)   (b)

Fig. 7.7. (a) Space-periodic q.o. mode launcher of Fig. 7.6 and **(b)** its unfolded structure [276]

non-quadratic phase correcting mirrors allow one to generate any desired amplitude and phase distribution of the wave beam. The amplitude distribution may be Gaussian [283, 284] but can also be flat or even ring-shaped in order to optimize the power distribution for a given vacuum window geometry and material [285]. Advanced iterative computer algorithms have been developed to provide the optimized shapes of the mirrors [269–273] which are manufactured on numerically controlled milling machines. Fig. 7.8 shows as an example the shaped mirrors inside the GYCOM 170 GHz, ITER gyrotron [283]. The computer codes are also used for the phase retrieval from amplitude measurements, thus allowing detailed mode diagnostics and reconstruction of the overall fields [269–272, 286–290]. The knowledge of phase and amplitude at any point of the longitudinal axis of the beam makes a calculation of the field pattern at all other points possible. Finally, the example of an optimized quasi-optical launcher system for a megawatt, 140 GHz, $TE_{22,8}$ mode multifrequency gyrotron [273] is mentioned to see the effect of the optimization of the mirror profile on the radiation pattern at the window plane. This system consists of a classical Vlasov launcher, a non-quadratic elliptical mirror and two phase correcting mirrors. Figure 7.9 shows the radiation pattern at the window plane before and after optimization and applying the phase corrections to the mirrors. In this case, the mode purity of the Gaussian beam at the window plane is around 99% after optimization. Thus, the advanced computer codes will enable one to design much improved and excellent launcher and mirror systems with reduced losses.
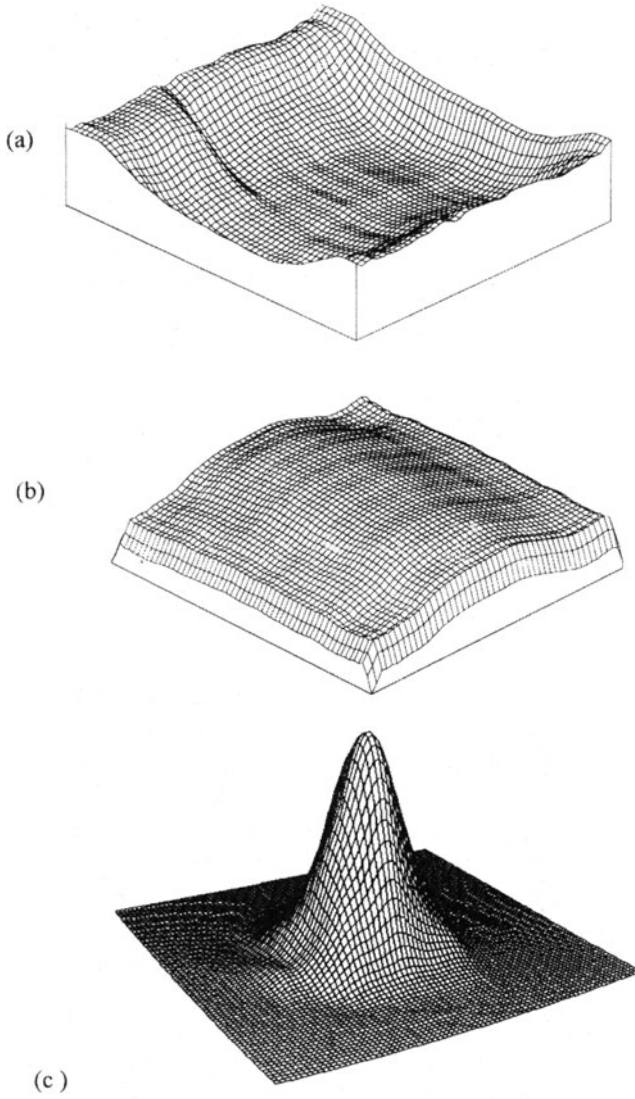
Fig. 7.8. Typical surfaces (**a,b**) of shaped mirrors inside the GYCOM 170 GHz ITER gyrotron (mirror no. 1: $120 \times 135 \times 1.44$ mm, mirror no. 2: $90 \times 93 \times 1.93$ mm). (**c**) Field intensity of the output beam at the gyrotron window [283]
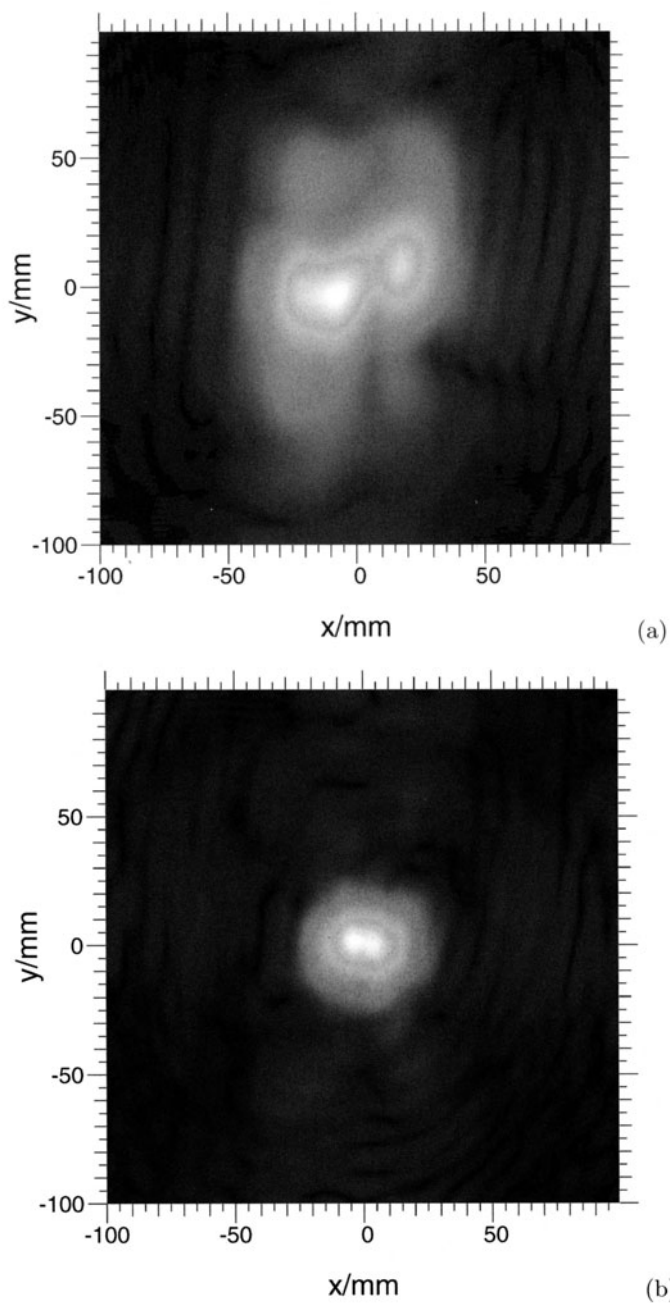
Fig. 7.9. Radiation pattern at the window plane (**a**) before and (**b**) after optimizing the mirror system of a 140 GHz, $TE_{22,8}$ mode multifrequency gyrotron [273]

7.4 Concluding Remarks

Practically all passive components for conversion and transmission of high power mm-waves have reached a high grade of development. Mode conversion processes in smooth wall and corrugated wall waveguides as well as on phase-modifying (non-quadratic) reflector surfaces are well understood, and high efficiency performance is usually obtained. The quality of q.o. mode converters reached now, allows the building of high power mm-wave gyrotrons with high purity of the Gaussian output beam. Transmission systems employing waveguides and mirror lines show high reliability and efficiency, and devices for polarization control, power measurement, mode analysis and pulse compression are available. A challenge for the future is the development of wideband, tunable gyrotron sources for high power mm-waves. Although the transmission lines themselves are broadband, this requires the design of multifrequency q.o. mode converters and appropriate matching optics as well as corresponding polarizing and measuring devices.

To satisfy the continuing need for increased power, the exploration of power combination techniques and generally the potential for simplification of high power microwave and mm-wave mode conversion and transmission systems will be of growing interest.

8 RF Window

8.1 General Remarks

An important component of the output system of gyrotrons is the RF window. It serves as a barrier between the vacuum side of the gyrotron and the output transmission line. It should withstand high power, mechanical and thermal stresses, be leak tight ($\approx 10^{-10}$ Torr) and be lossless. The basic problems to be addressed for high power RF windows are power handling capability, selection of window material, thermal and mechanical stresses and their management, window flashing/arcing, and puncturing/physical damage. Therefore, care must be taken in selecting a proper window material with low loss tangent ($\tan \delta$), high thermal conductivity, suitable mechanical strength, and perfect design to minimize power reflections and absorption for better transmission.

Gyrotrons with an output power of over 1 MW per unit are under development for use in ECRH systems. Therefore, overmoded high power dielectric vacuum windows are required for various high power microwave tubes (gyrotrons, power klystrons, etc.). In fusion plasma heating, vacuum barrier windows also serve as a primary tritium containment boundary of the plasma torus. This application is technically more demanding because a torus window must withstand a static 0.2 MPa pressure during off-normal events (safety requirement). It should use a fusion reactor compatible cooling liquid and, in addition, its mechanical and mm-wave performance should not be severely degraded by modest neutron and γ irradiation, i.e., it must also be resistant to radiation damage. An extensive survey and design studies of the RF windows for gyrotrons are given in the literature (for example see [2, 253, 291–294]). In this chapter, high power RF windows mainly for gyrotrons, but also suitable for their amplifier variants and similar applications, is presented. Most of the practical and technical requirements for the design and development of such vacuum barrier windows are discussed. Disc type windows, broadband Brewster windows and application of the latest synthetic diamond windows are described.

8.2 Practical Aspects of High Power Windows

The most important aspect of high power mm-wave window development is the dielectric characteristics of the window material i.e., loss tangent $\tan\delta$ and permittivity ϵ'_r because they affect both the power absorption and transmission [291]. The thickness d of a window disc is determined such that the power reflection is minimized. It is evident that a temperature dependence of ϵ'_r complicates the choice of d and that once d is fixed, maximum transmission occurs at a series of frequencies f_i (multi-passband window). An appropriately small partial reflection can enlarge the power capability of dielectric RF windows compared to the conventional resonant matched windows in which the RF field represents a superposition of counter-propagating waves. It is obvious that the RF load on the dielectric would decrease if the wave could only propagate in one direction. A pair of symmetrically located inductive irises on both sides of the window disk in a tubular waveguide [295] or symmetric gratings in quasi-optical arrangements [296, 297] can be used to set up a standing wave in the regions between them and each of the disk surfaces. This results in forcing a lower impedance at the disk surfaces that exactly matches the characteristic impedance inside the dielectrics, thereby causing a pure travelling wave condition inside the window disk. Therefore such windows with matched anti-mirror reflection are called travelling wave windows.

Depending on various cooling schemes, four general classes of high power long pulse capable windows have been suggested and experimentally investigated (see Fig. 8.1) for gyrotrons and similar applications for transmission of high power microwave and millimetric waves. These are, (i) distributed, (ii) liquid-edge-cooled single disc, (iii) gas-surface-cooled single disc, and (iv) liquid-surface-cooled double disc. A variety of low loss tangent dielectric materials (beryllia, boron nitride, silicon nitride, sapphire, Au–doped silicon, and synthetic diamond) have currently been used for high power RF windows. The distributed window consists of a planar slotted structure of alternating thin bars of dielectric material between microchannel cooled metal ribs. The main disadvantages are the complicated and expensive mechanical structure (with a large number of window elements), high losses, arcing problems even in an evacuated waveguide, and its limitation to only one direction of polarization. Cryogenically edge cooled single disc windows are an attractive option. For a number of materials, including sapphire, it is found that the thermal conductivity increases and the loss tangent decreases as the temperature is reduced. Operating points are usually found between liquid Helium (LHe) and liquid Nitrigen (LN2) temperatures, depending on the material. The advantages of this type of windows are that they are low loss and generally not polarization dependent. Disadvantages are that they are large, the operating point is subject to thermal runaway and they must be prevented by a cold trap from cryo-pumping of dust in the antenna waveguide. Liquid surface cooled double disc windows have the disadvantages that two discs are required per
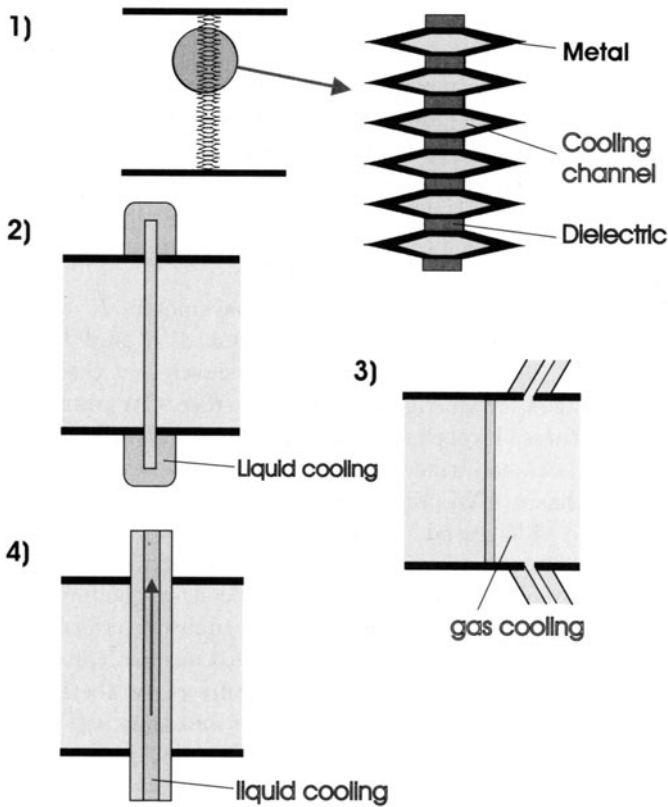
Fig. 8.1. General classes of high power, long pulse capable RF windows for gyrotrons [291]

barrier, and the losses in the cooling liquid also have to be considered. Single disc microwave plasma assisted chemical vapor deposition (MPACVD) diamond windows have proved to be an excellent choice as potential windows for high power gyrotrons whereas application of Brewster windows is an excellent solution for the broad band transmission of high power mm-waves [292, 298].

Several methods exist for increasing the power capability of the window without fundamentally altering the design [291]. One such method is the optimization of the beam profile. Flat non-Gaussian mm-wave beam profiles increase the power handling capability by as much as 50%, and annular profiles by as much as 100%. The disadvantage of these methods is that they require the use of waveguide mode converters or mode-converting (non-quadratic profiled) mirrors. Alternatively, high aspect ratio elliptical (or rectangular) windows can be used to reduce the thermal path length in one dimension. However, unless the transmission remains in an elliptical (or rectangular)

waveguide, rather long mode converters or profile-transforming mirrors are required.

In order to define the appropriate concepts for the development of high average power microwave windows one has to compare the thermophysical, mechanical and dielectrical parameters of possible window materials related to the load-failure resistance R' and the power-transmission capacity P_T at different temperatures [291]. The features of beryllia, boron nitride, silicon nitride (Kyocera SN–287), sapphire, Au–doped silicon, and CVD diamond at room temperature are summarized in Table 8.1.

For a 1 MW, CW mm-wave window the parameters R' and P_T should exceed 250 and 100, respectively. The comparison of R' and P_T for the four materials BeO, BN, Si_3N_4 and sapphire clearly shows that there is no chance to use these dielectrics for an edge-cooled, single-disc, CW, mm-wave window at room temperatures. Experiments at CPI in the USA and at NIFS and JAERI in Japan have confirmed that even a double disk FC75-face-cooled sapphire window has a CW power limit around 0.3–0.4 MW. Nevertheless these materials are widely used at lower frequencies and for pulsed operation. The mechanical features and the required cooling auxiliaries make sapphire cryo-windows very complicated. Au–doped silicon at cooling temperatures somewhat lower than $0°C$ could avoid a thermal runaway and transmit 1 MW, CW but this material is too brittle and tends to mechanical cracking [256]. However, recent developments in the manufacture of synthetic diamonds in a controlled fashion with the required diameter and thickness and improved brazing and mounting techniques have allowed the use of single disc, water-edge-cooled CVD diamond windows for use in high power windows. They provide technically a practical solution for the transmission of CW mm-waves at power levels in excess of 1 MW [292, 293]. Diamond windows for gyrotrons are also discussed in this chapter.

Another practical aspect of high power windows is the resistance to mechanical stresses since the disc thickness is smaller for large bandwidth windows and is limited by mechanical stability. The pressure gradient Δp between the two sides of the window causes a deflection w of the disc given by [253, 299]

$$w = \left(\frac{\alpha_1 R_{win}^4}{d^3}\right) \cdot \left(\frac{\Delta p}{E}\right) \tag{8.1}$$

where $\alpha_1 = 1/6$ for a clamped disc at the circumference and is equal to $2/3$ for a freely supported disc, R_{win} is the window radius, and E is the modulus of elasticity. Here, the Poisson number is taken as $1/3$. The tensile stresses occurred are expressed as [253, 300]

$$\sigma = \frac{\alpha_2 \Delta p R_{win}^2}{d^2} \tag{8.2}$$

where $\alpha_2 = 2$ for a clamped disc and $\alpha_2 = 5$ for a freely supported disc, respectively. In the selection process of the suitable window material, one has

Table 8.1. Thermophysical, mechanical, and dielectrical parameters of window materials related to thermal load-failure resistance and power transmission capacity of edge-cooled windows at room temperature. Here, pc = polycrystalline and sc = single crystal

Material	BeO (pc)	BN (CVD) (pc)	Si_3N_4 composite (SN-287) (pc)	Sapphire (Al_2O_3) (sc)	Si (Au-doped) (sc)	Diamond (PACVD) (pc)
Thermal Conductivity κ (W/mK)	260	55	59	40	150	1900
Ultimate Bending Strength σ_B (MPa)	140	80	800	410	1000	500
Poissons Number ν	0.3	0.25	0.28	0.22	0.1	0.1
Density ρ (g/cm^3)	2.85	2.3	3.4	4.0	2.3	3.52
Specific Heat Capacity c_p (J/g K)	1.05	0.8	0.6	0.8	0.7	0.52
Young's Modulus E (GPa)	345	70	320	385	190	1050
Therm. Expans. Coefficient $\alpha(10^{-6}/K)$	7.2	3	2.4	5.5	2.5	1.0
Permittivity (145 GHz) ε_r'	6.7	4.7	7.84	9.4	11.7	5.67
Loss Tangent (145 GHz) $\tan\delta \times 10^{-5}$	70	115	30	20	0.35	2
Metallizing/Brazing	o.k.	o.k.	o.k.	o.k.	o.k.	o.k.
Bakeout ($^\circ$ C)			550	550	550	550
Possible Size $\oslash$ mm	150	145	300	270	127	120
Cost	medium	medium	high	high	low	very high
Failure Resistance (R')	10.3	15.7	44.5	6.0	284	858
RF-Power Capacity (P_T)	0.09	0.05	0.36	0.09	106	118
Radiation Sensitivity	no	no	no	no	no	no

$$R' = k\sigma_B(1-\nu)/E\alpha$$
$$P_T = R'\rho c_p/[(1+\varepsilon_r')\tan\delta]$$

to ensure that the mechanical stresses including those due to dielectric losses should not exceed the prescribed critical values of the material chosen [253].

8.3 Theory of Disc Type Windows

The basic theory of disc type waveguide windows for gyrotrons based on the scattering matrix formulation is presented in the literature [253, 294]. It offers a simple description of the incident, transmitted and reflected waves. Here, we give the basic formalism for disc type windows. Figure 8.2 shows a typical single disc waveguide window with its equivalent two-port scattering matrix network representation depicting the incident and reflected waves a_i and b_i $(i = 1, 2)$ respectively.
The incident and reflected waves at the window plane are represented by a set of equations in matrix form as

$$[S] = \begin{bmatrix} S_{11} & S_{12} \\ S_{21} & S_{22} \end{bmatrix} = \begin{bmatrix} \dfrac{b_1}{a_1}\Big|_{a_2=0} & \dfrac{b_1}{a_2}\Big|_{a_1=0} \\ \dfrac{b_2}{a_1}\Big|_{a_2=0} & \dfrac{b_2}{a_2}\Big|_{a_1=0} \end{bmatrix}. \tag{8.3}$$

The reflection (R), transmission(T), and absorption (A) coefficients in terms of the scattering matrix parameters are given as

$$R = |S_{11}|^2 = \frac{P_{1,refl}}{P_{1,in}}\Big|_{P_{2,in}=0} = \frac{|b_1|^2}{|a_1|^2}\Big|_{P_{2,in}=0}, \tag{8.4a}$$

$$T = |S_{21}|^2 = \frac{P_{2,trans}}{P_{1,in}}\Big|_{P_{2,in}=0} = \frac{|b_2|^2}{|a_1|^2}\Big|_{P_{2,in}=0}, \tag{8.4b}$$

$$A = 1 - |S_{11}|^2 - |S_{21}|^2 = \frac{P_{abs}}{P_{1,in}}\Big|_{P_{2,in}=0} = \frac{P_{1,in} - P_{1,refl} - P_{2,trans}}{P_{1,in}}\Big|_{P_{2,in}=0} \tag{8.4c}$$
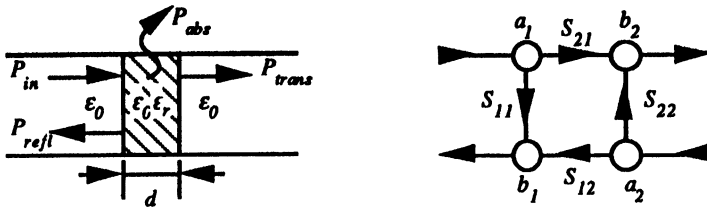

Fig. 8.2. Schematic of a single disc waveguide window and its equivalent two-port network

In the case of a single disc window, the scattering matrix $[S]$ is

$$[S] = \frac{1}{(1 - \rho_{mn}^2 e^{-2\gamma_{mn}d})} \begin{bmatrix} \gamma_{mn}\left(1 - e^{-2\gamma_{mn}d}\right) & \left(1 - \gamma_{mn}^2\right)e^{-\gamma_{mn}d} \\ \left(1 - \gamma_{mn}^2\right)e^{-\gamma_{mn}d} & \gamma_{mn}\left(1 - e^{-2\gamma_{mn}d}\right) \end{bmatrix}, \quad (8.5)$$

where

$$\gamma_{mn} = \alpha_{mn} + j\beta_{mn} = \sqrt{k_{cmn}^2 - \varepsilon_r k_0^2}, \quad k_{cmn} = \frac{x_{mn}}{R_{win}} \quad \text{and} \quad k_0 = \frac{2\pi f}{c_0}. \quad (8.6)$$

Here, x_{mn} is the Bessel zero of the mode and R_{win} the aperture of the window disc. The complex permittivity of the disc is $\varepsilon_r = \varepsilon_r'(1 - j\tan\delta)$. γ_{mn}, α_{mn} and β_{mn} are the propagation, attenuation, and phase constants, respectively, of the disc loaded waveguide and are given by

$$\alpha_{mn} = \frac{k_0^2 \varepsilon_r' \tan\delta}{2\sqrt{\varepsilon_r' - \left(\frac{k_{cmn}}{k_0}\right)}}, \quad (8.7a)$$

$$\beta_{mn} = \sqrt{k_0^2 \varepsilon_r' - k_{cmn}^2} \cdot \sqrt{\frac{1}{2} + \frac{1}{2}\sqrt{\left(\frac{\varepsilon_r' \tan\delta}{\varepsilon_r' - \left(\frac{k_{cmn}}{k_0}\right)^2}\right)^2 + 1}}. \quad (8.7b)$$

The complex reflection coefficient due to the wave impedance discontinuity at the single dielectric transition plane ρ_{mn} is given by

$$\rho_{mn} = \frac{\sqrt{1 - \left(\frac{k_{cmn}}{k_0}\right)^2} - \sqrt{\varepsilon_r - \left(\frac{k_{cmn}}{k_0}\right)^2}}{\sqrt{1 - \left(\frac{k_{cmn}}{k_0}\right)^2} + \sqrt{\varepsilon_r - \left(\frac{k_{cmn}}{k_0}\right)^2}} \quad \text{for a TE mode,} \quad (8.8a)$$

$$= \frac{\sqrt{\varepsilon_r - \left(\frac{k_{cmn}}{k_0}\right)^2} - \varepsilon_r\sqrt{1 - \left(\frac{k_{cmn}}{k_0}\right)^2}}{\sqrt{\varepsilon_r - \left(\frac{k_{cmn}}{k_0}\right)^2} + \varepsilon_r\sqrt{1 - \left(\frac{k_{cmn}}{k_0}\right)^2}} \quad \text{for a TM mode,} \quad (8.8b)$$

$$= \frac{1 - \sqrt{\varepsilon_r}}{1 + \sqrt{\varepsilon_r}} \quad \text{for a TEM mode if } k_{cmn} \ll k_0. \quad (8.8c)$$

Now, by making use of (8.5) through (8.8) in (8.4), we obtain the following expressions for reflection, transmission and absorption coefficients for a single disc window:
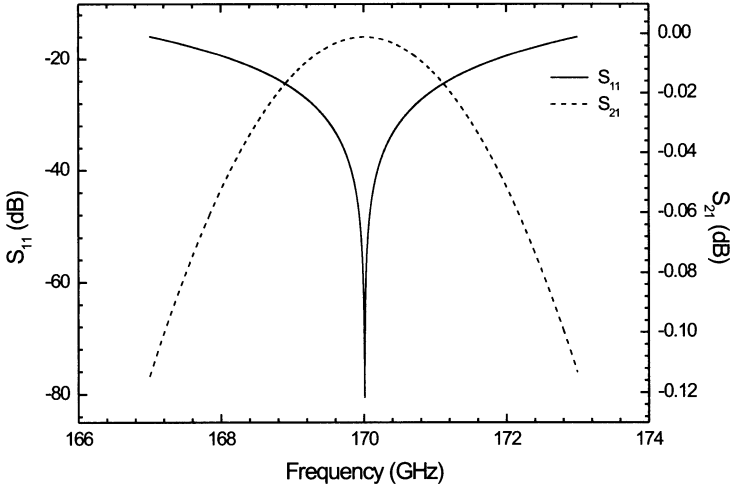
Fig. 8.3. Reflection (S_{11}) and transmission (S_{21}) as a function of frequency for a single disc diamond window

$$R = \frac{R_0 \left(1 - 2T_0 \cos(2\beta_{cmn}d) + T_0^2\right)}{1 - 2R_0T_0 \cos(2\beta_{cmn}d - 2\phi) + R_0^2T_0^2} \,, \tag{8.9a}$$

$$T = \frac{T_0 \left(1 - 2R_0 \cos(2\phi) + R_0^2\right)}{1 - 2R_0T_0 \cos(2\beta_{cmn}d - 2\phi) + R_0^2T_0^2} \,, \tag{8.9b}$$

$$A = \frac{\zeta_1 \cdot \zeta_2}{1 - 2R_0T_0 \cos(2\beta_{cmn}d - 2\phi) + R_0^2T_0^2} \quad \text{where} \tag{8.9c}$$

$$\zeta_1 = \left(1 - R_0 - T_0 - R_0T_0^2 - R_0^2T_0 - 2R_0T_0\right) \,, \tag{8.9d}$$

$$\zeta_2 = 2R_0T_0 \left\{\cos(2\beta_{cmn}d - 2\phi) - \cos(2\beta_{cmn}d) - \cos(2\phi)\right\} \,, \tag{8.9e}$$

$$R_0 = |\rho_{mn}|^2 \,, \quad \phi = \arg \rho_{mn}, \quad \text{and} \quad T_0 = e^{-2\alpha_{mn}d} \,. \tag{8.9f}$$

As an example, the S parameters of a single disc diamond window (with $\varepsilon_r = 5.67$, $\tan \delta = 2.0 \times 10^{-5}$) for operation at 170 GHz with a Gaussian output beam is shown in Fig. 8.3. Here, the radius of the window aperture is taken as 50 mm and the thickness of the window is 1.11 mm.

If there are n cascaded dielectric layers, then by cascading the individual scattering matrices in order, we get the total scattering matrix of such system given by

$$[S_{tot}] = [S_A] \cdot [S_B] \cdot [S_C] \cdots\cdots\cdots [S_n] \,. \tag{8.10}$$

Similarly, one can also write the transmission matrix $[T]$ for such waveguide windows; this can be expressed in terms of the corresponding scattering matrix elements and vice versa [294].

8.4 Broadband Output Windows

For a broadband operation of the window suitable for multifrequency or step-tunable operation of the gyrotron, one needs a very wideband window, for example, with a workable range from 105–170 GHz. Window reflections cause a major problem to design such windows. One possibility to remove window reflections, at least for a set of discrete frequencies, is given by mounting a window plate of specially chosen thickness perpendicular to the mm-wave output beam. To make sure that the part of the power reflected by the first material discontinuity (vacuum to material), interferes destructively with parts reflected out of the window plate (multiple reflections), the plate's thickness has to be a multiple N of the wavelength $\lambda_n/2$ in the material given by

$$d_N = \frac{\lambda_n}{2} \cdot N \Longrightarrow d_N = \frac{c_0}{2 f_0 \sqrt{\varepsilon_r'}} \cdot N \,, \tag{8.11}$$

$$f_n = f_0 + n \cdot \Delta f, \quad \Delta f = \frac{f_0}{N} \,,$$

$$n = -0, \pm 1, \cdots\cdots, \pm N \,. \tag{8.12}$$

Since the window in this case provides a resonant thickness for the mm-wave beam, the amount of power oscillating between the two surfaces leads to an increase of the absorption coefficient, which results in the following expression for the absorbed power [44]

$$A_M \approx \frac{\pi f d \tan \delta (1 + \varepsilon_r')}{c_0} \,. \tag{8.13}$$

However this method is not very suitable for multifrequency and high power operation since the reflections and power absorption are larger. An elegant method to realize a gyrotron output window with very large bandwidth is given by using a Brewster window (see Fig. 8.4) [291, 292, 298].

If the angle between the normal to the window plate and the propagation constant of the mm-wave beam is chosen according to the equation (8.14), it can be shown that the reflections vanish, independent of the frequency, for parallel polarization; the Brewster angle θ_B is given by

$$r_{\parallel} = 0 \Longleftrightarrow \theta_i = \theta_B = \tan^{-1}\left(\sqrt{\varepsilon_r'}\right) \,. \tag{8.14}$$
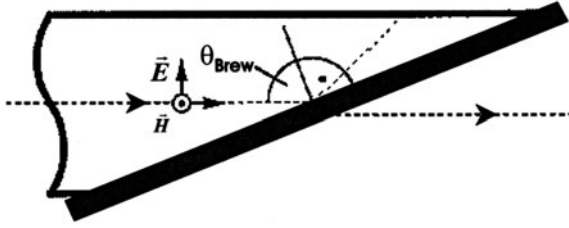
Fig. 8.4. Schematic of a Brewster window [291]

Due to the parallel boundary conditions of the window plate, there are further frequency dependent angles where the reflections vanish independent of the polarization. Similar to the case of a perpendicular incident beam, the reflections can vanish if the phase displacement of the first reflection and the ray scattered out of the material is a multiple of $(2n + 1) \cdot \pi$. The reflection derived from this is given by

$$\sin \theta_i = \sqrt{\varepsilon_r' \left[1 - \left(N \cdot \frac{\lambda_n/2}{d} \right)^2 \right]};$$

$$int \left[\frac{d}{\lambda_n/2} \right] > N > int \left[\frac{d}{\lambda_n/2} \sqrt{\frac{\varepsilon_r' - 1}{\varepsilon_r'}} \right]. \qquad (8.15)$$

If it is intended to remove reflections of both the perpendicular and the parallel polarization for at least one frequency, one has to choose the thickness of the Brewster window according to the following equation:

$$d_N = N \cdot \lambda_n \sqrt{\frac{\varepsilon_r' + 1}{\varepsilon_r'}} \implies d_N = N \cdot \frac{c_0}{f} \cdot \frac{\sqrt{\varepsilon_r' + 1}}{\varepsilon_r'}. \qquad (8.16)$$

For a plate mounted at the Brewster angle, each ray passes the window material only once, which results in the following absorbed power:

$$A_B \approx \frac{2 \pi f \sqrt{\varepsilon_r'} \tan \delta}{c_0} \cdot \frac{d}{\sin \theta_B}. \qquad (8.17)$$

The reflection (S_{11}) contours of a diamond Brewster window designed for operation at 170 GHz is shown in Fig. 8.5. Here, the window thickness (d) is 1.11 mm, $\varepsilon_r = 5.67$, and $\tan \delta = 2.0 \times 10^{-5}$.

It is observed that compared to the amount of power absorbed in the multi bandpass window, for the same thickness of the window, the Brewster window provides a lower absorption, particularly for high permittivities [44].
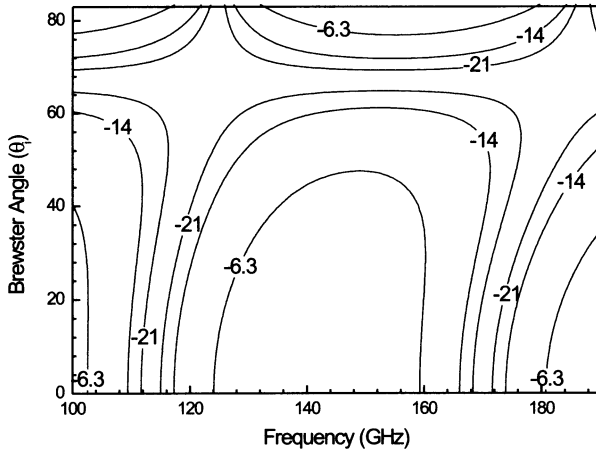
Fig. 8.5. Contours of reflection coefficient (S_{11}) as a function of frequency and Brewster angle for a CVD diamond Brewster window

8.5 Diamond Windows for Gyrotrons

The development of high power mm-wave windows has been hampered by the lack of a suitable dielectric material which does not suffer from thermal runaway. As a potential new material for simple water-edge-cooled single disc windows, MPACVD diamond is extremely attractive due to its good mechanical properties, modest dielectric constant, small loss tangent, excellent thermal conductivity and insensitivity to nuclear radiation [298]. Current MPACVD capabilities [292] have allowed for tests with optical– and radio-frequency (RF)-grade diamond discs (DIAFILM) of up to 119 mm diameter and 2.23 mm thickness (see the "Star-of-FZK", 434 carats MPACVD diamond window in Fig. 8.7).

Dielectric and Thermal Properties

The characterization of dielectric properties in the mm-wave range showed that in the center of optical-grade material the dielectric loss tangent at room temperature can be very low ($\tan \delta = 5 \times 10^{-6}$) whereas RF-grade material discs have a center value of $\tan \delta = 1 - 2 \times 10^{-5}$ at 145 GHz. The frequency dependence was measured to be proportional to f^{-x} with $x = 0.6$ to 0.8 which favours higher frequencies. The temperature dependence of the center loss tangent of two discs is shown in Fig. 8.6. A steady weak increase from 1.8×10^{-5} at 300 K to 5×10^{-5} at 750 K is observed.

For various qualities of MPACVD-diamond discs with the center values of $\tan \delta$ ranging from 5×10^{-6} up to 6×10^{-4} the dielectric permittivity at room
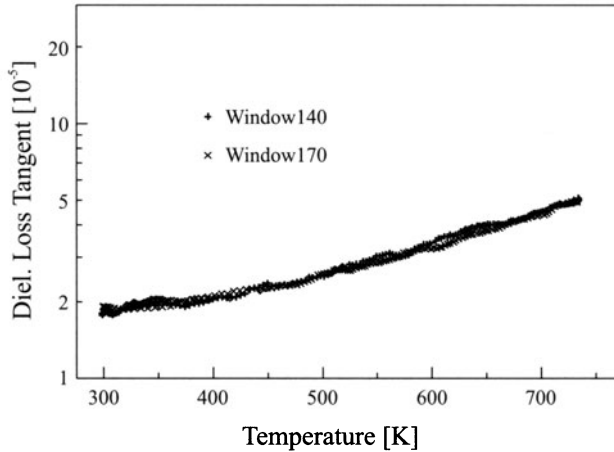
Fig. 8.6. Dielectric loss tangent determined at 145 GHz for two gyrotron window discs of MPACVD diamond [292]

temperature was always measured to be $\epsilon'_r = 5.67 \pm 0.01$. At temperatures higher than 400 K a small increase has been observed.

Due to the typical columnar growth texture of polycrystalline CVD-diamond layers with rough surface and grain size

$$d_G(z) \approx 0.15z$$

where z is the thickness of the layer, the thermal conductivity increases with increasing thickness. Finite Element (FE) thermal calculations using the measured dielectric parameters and a $1/T$ relationship to predict the fall in thermal conductivity show that MPACVD-diamond windows are capable of transmitting high mm-wave power [292]. Thermal finite element computations performed at FZK shows that for a power of 1 MW at 140 GHz (in a Gaussian mode), an upper value of the loss tangent of 4×10^{-5}, a cooling rim of 5 mm and for a heat transfer coefficient of 12 kW/m$^2 \cdot$ K to the cooling water at 20° C, the temperature increase of the window in the center and at the edge is 61° C and 51° C, respectively. The absorbed power is 705 W. These simulations show that steady state conditions in the window are generally achieved in less than 5 sec and that the transmission capability is even above 2 MW, CW. Due to temperature insensitivity of ε'_r, $\tan \delta$, and α' (thermal expansion coefficient), there is practically no change of the electrical thickness of the disc during the tube operation.

Mechanical Properties and Mounting

The ultimate bending strength σ_B measured on the growth side in ball-on-ring experiments for discs cut out of window grade MPACVD material
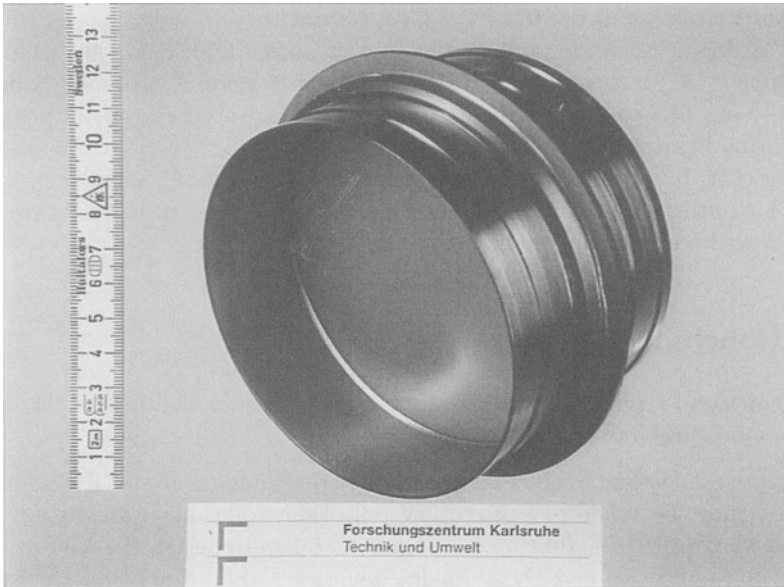
Fig. 8.7. "Star-of-FZK" window mounting with two Inconel cuffs and Molybdenum strengthening rings [292]

(thickness $d = 0.9 - 1.5$ mm) revealed no changes ($\sigma_B \approx 380 - 415$ MPa for the case that the growth side is under tension) at neutron fluences up to 10^{21} n/m^2. But the colour of the discs changed to dark grey and after brazing to green [292].

First metallization/bonding techniques for MPACVD-diamond discs have been developed in a collaboration of FZK Karlsruhe with DeBeers [292]. The elastic properties of a ductile Al–based braze joined by solid-phase diffusion bonding to the diamond disc are used to reduce the thermal stresses as much as possible. The disadvantage of this technique is the relatively low allowed maximum bakeout temperature of the window unit of 450°C (guaranteed by DeBeers). Several test windows were thermally cycled as if they would be installed as a window on a gyrotron. No diffusion degradation of the brazing has been observed. Figure 8.7 shows a photograph of the "Star-of-FZK" window mounting. In the mean time, other bonding techniques have been developed.

Existing brazing techniques for CVD-diamond discs are [301]:

1. Al-braze: 600°–650°C / DeBeers–UKAEA, Culham
   This technique is uncritical for graphitization of diamond surfaces but allows only reduced bake-out temperatures for the gyrotron (450°–500°C) and is problematic with respect to Al-corrosion in the cooling water.

  2. Au-(Cu)-braze: 900°–1000°C / CPI, Palo Alto
     This braze is resistant to corrosion and allows high bake-out tempera-
     tures (550°) but is problematic with respect to graphitization of diamond
     surfaces (depending on vacuum conditions and Oxygen partial pressure
     during brazing).
  3. Ag-(Cu)-braze: 750°–850°C / Thales Electron Devices, Vélizy
     This optimum brazing technique employs a corrosion resistant braze and
     allows high bake-out temperatures.

8.6 Concluding Remarks

In the design of gyrotron windows, one may encounter and has to take care
of the following problems [245, 302]:

– Electrical Design Problems: In the electrical design of the RF window,
   care must be taken to achieve low reflections, optimal transmission and
   low absorption. In addition, care must be taken to design the window free
   of unwanted trapped ghost modes generated and trapped in the mode
   converters, transition regions and ceramic surfaces. Such trapped mode
   resonances may cause a higher local field and heat the ceramic material
   of the window. Even though such trapped mode resonance problems are
   less prominent in the case of gyrotron windows, a proper investigation
   may give a fair idea of their existence and suppression and/or removal.
– Electrical Breakdown Problems: This is a general problem of most high
   power microwave tubes of both conventional and fast-wave type. It is a
   phenomenon related to the window material, its surface field strength and
   electrical characteristics. Accumulation of RF losses in the ceramic ma-
   terial causes an increase in the surface electric field strength and thereby
   leads to electric breakdown. Proper evacuation of the transmission line
   could avert such breakdown situations. However, care should be taken
   by arc detection and other electrical means to avoid breakdowns causing
   physical damage to the windows.

Although multipactoring and localized heating of the dielectric surface not a
significant pronounced problem for high power gyrotron windows, it should
also be kept in mind when selecting the window material. Other thermome-
chanical factors to be considered for window design have been discussed in
the previous sections.

Advances in chemical-vapour-deposition (CVD) production of free-stand-
ing synthetic diamond discs have enabled the (still ongoing) development of
vacuum barrier windows with CW power capability in the MW range. Large
area free standing polycrystalline diamond discs with diameter and thickness
up to 119 mm and 2.23 mm, respectively, have been manufactured at De-
Beers Industrial Diamond Division (UK) Ltd. by microwave plasma assisted
chemical vapor depostion (MPACVD) with good reproducibility in thickness

and dielectric properties. Due to low mm-wave losses ($\tan \delta = 2 - 3 \times 10^{-5}$), outstanding thermal conductivity (≈ 1900 W/mK), good ultimate bending strength (> 400 MPa) and radiation insensitivity up to a neutron fluence of 10^{20} n/m^2 (10^{-5} dpa), water-edge-cooled MPACVD-diamond windows promise to provide a practical technical solution for the transmission of CW millimeter waves at power levels in excess of 1 MW.

9 Examples

9.1 General Remarks

This chapter is mainly devoted to the design examples of some typical gyrotrons. It may be of interest for the relevant designers and researchers if they are introduced to such design exercises. Here, major emphasis is given to the design start up, that is, feasibility, mode selection and interaction computation. Keeping in mind the physical and technological constraints and needs of the particular gyrotrons, the initial design and its conceptualization have to be carried out. After this feasibility study is done, the design of the other modules, mainly, MIG, electron beam guidance, type of mode converters depending upon the requirement, have to be performed as described in earlier chapters. It is well known that the conception of a particular gyrotron is design critical. In addition, based on the application, needs, availability of materials, fabrication techniques and components, the design selection varies. The technological, physical and economic limits also have to be taken into account. The performance figures (mainly, power, efficiency, internal losses, etc.) will depend on these design procedures. Therefore, the designer is well advised to keep the pricing, performance and requirements as the basic guide lines for the design work.

As a general guideline, one should prepare comparison tables with beam radius, wall radius, voltage depression, limiting current and wall loss factors, as well as the computed beam-field coupling coefficient C_{BF} for all the candidate modes in order to select a proper operating mode since these constitute the major physical constraints in the selection. The rules and governing equations to estimate these limiting factors are essentially the same for the second harmonic case as for first harmonic operation. These aspects are discussed in detail in Chap. 5 and there is no need to repeat them here. Then one should carry out calculations of I_{start} to choose a particular operation mode. This is a general practice of the mode selection process.

Following this, the equations of motion for the electrons are solved to compute the output power and interaction efficiency in cold cavity and self consistent approximations for various parameters until an acceptable cavity design compatible with the design goals such as efficiency, Q, wall losses, output power etc., is obtained. The procedure is discussed in detail in Chap. 4.

As usual, in addition to the starting currents, one has to estimate the wall losses, voltage depression, and limiting currents.

As a first example we started with the feasibility of operating a conventional gyrotron at 140 GHz at powers well above 1 MW. Several conventional gyrotrons have been successfully developed at this frequency and their power levels are given in a periodical review [2]. This is a generic example of such devices. The second example is a successfully developed megawatt coaxial cavity gyrotron at 165 GHz. The third example is a rather recent study on multi-frequency gyrotrons. Finally, we show some design examples of gyrotrons under second harmonic operation. The design studies of different varieties of gyrotrons typically for different applications are presented to enable the readers to get familiarized with such problems. However there is a long way to go from basic conceptualization to a final design and its translation to an actual working device.

9.2 A Very High-Power, 140 GHz Conventional Gyrotron

This is an example to see the feasibility of the operation of a particular gyrotron of conventional type (that is hollow cavity type) [193]. Here a study of the feasibility of CW operation of a 140 GHz conventional cavity gyrotron at high power levels operating in the $TE_{31,8}$ mode is presented. The design parameters and goals are shown in Table 9.1. The required high power dictates the choice of a very high order mode, such as $TE_{31,8}$ or $TE_{25,10}$. Gyrotrons have been successfully operated in these modes at 170 GHz [194, 303].

The given frequency corresponds to a wavelength of 2.14 mm. For operation in the $TE_{m,p}$ mode, the cavity radius is related to λ by $R_0 = \frac{x_{m,p}\lambda}{2\pi}$ where x_{mp} is the pth root of $J'_m(x)$. For operation at the first harmonic ($s = 1$) the optimum beam radius is given by $R_e = \frac{x_{m\pm1,1}R_0}{x_{m,p}} = \frac{x_{m\pm1,1}\lambda}{2\pi}$. In general, the co-rotating mode (with the lower sign) is chosen, since this provides better coupling of the beam to the RF-field. In the mode selection procedure, the cavity radius, beam radius, wall loading and limiting current for a number of

Table 9.1. Design parameters and goals of a $TE_{31,8}$, 140 GHz, 1.5–2.0 MW, CW gyrotron

Output power	$\approx$ 1.5–2.0 MW
Efficiency	$\approx$ 30%
Beam current	60–70 A
Accelerating voltage	80–90 kV
Beam velocity ratio	1.2–1.4
Magnetic field	$\approx$ 5.6–5.7 T
Diffraction Q	$\approx$ 1000

candidate modes having a Bessel zero between 62 and 65, and radial index 4-10, were inspected carefully and the $TE_{31,8}$ mode was chosen as the operating mode as it satisfied most of the technological constraints (see [193]).

If the beam current is 70 A, the voltage depression ranges from 11 kV for modes with radial index 10 to 4 kV for modes with radial index 4. It is clear that if modes with radial index larger than 8 are selected, the current should be limited to 60 A, in order to keep the ratio I/I_L less than 2/3. The wall losses may become uncomfortably high for modes with radial index less than 6, since they are likely to be higher than the values given here. The optimum magnetic field for a detuning of 0.039 is 5.66 T. It is difficult to manufacture an emitter ring if the cathode radius is significantly larger than 50 mm. The beam radius is related to the cathode radius by $R_e = R_c/\sqrt{b}$ where b is the magnetic compression ratio. It is usually taken to be less than 30. However, it should be larger than about 20 to obtain a sufficiently large velocity ratio. This means that the beam radius should not be too large, which indicates selection of a mode with higher radial index. Putting these considerations together leads to the conclusion that the $TE_{31,8}$ mode is a very good candidate.

Since it is a conventional gyrotron, the interaction cavity has the usual three section structure, with an input taper and a uniform middle section followed by an output uptaper, as discussed in Sect. 3.2. As described in Chap. 4, the cavity design is carried out by computing the interaction efficiency in cold cavity and self consistent approximations for various parameters until an acceptable cavity design compatible with the design goals such as efficiency, Q, wall losses, output power etc., is obtained. The preliminary design has a cavity mid-section length of 14 mm. The lengths of the tapered sections were fixed at $L_1 = L_3 = 16$ mm, $\theta_1 = 2.5°$, $\theta_2 = 0.0°$, and $\theta_3 = 3.5°$. Roundings of length 5 mm were included at each transition. For the $TE_{31,8}$ mode, the cavity radius is 21.75 mm. The cold-cavity resonant frequency and quality factor are 140.083 GHz and 851, respectively.

Figure 9.1 shows Q times the coupling coefficient value (in arbitrary units) as a function of frequency in the frequency range 137–143 GHz taking the main mode to be $TE_{31,8}$. From this figure, we see that the main mode is fairly well separated from major competing modes ($TE_{32,8}$ and $TE_{30,8}$). The results of a preliminary design and self consistent computations are given in Figs. 9.2–9.3. It is known that in long pulse or CW operation, the beam space charge is neutralized after a few hundred milliseconds, resulting in a change of operating point compared with short pulse operation. In particular, the beam energy is higher and the velocity ratio is correspondingly lower, since $\gamma\beta_\perp$ is invariant. For example, if the final operating point corresponds to a beam energy of 90 keV, current 65 A, and velocity ratio 1.20, the beam energy and velocity ratio during startup will be 81.3 keV and 1.39, respectively.

Figure 9.2 shows the output power as a function of magnetic field for the $TE_{31,8}$ mode, for beam parameters corresponding to CW operation at
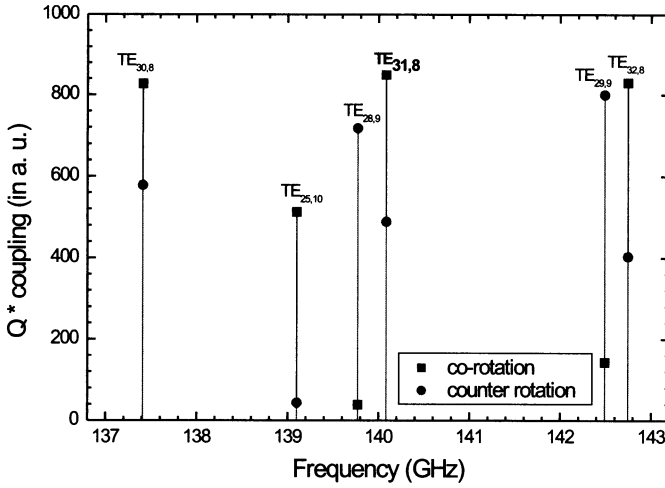
Fig. 9.1. Q times coupling coefficient (in arbitrary units) versus frequency for various competing modes. Here the main mode is taken to be $TE_{31,8}$ [193]
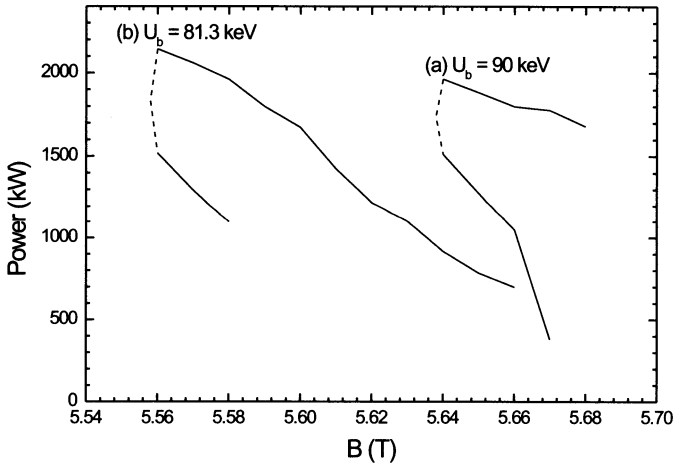

Fig. 9.2. Power as a function of magnetic field for the $TE_{31,8}$ mode. Here the beam current is taken to be 65 A. The two sets of curves correspond to (**a**) $U_b = 90$l,keV, $\alpha = 1.20$ (after space charge neutralization) and (**b**) $U_b = 81.3$ keV, $\alpha = 1.39$ (before space charge neutralization) [193]

a current of 65 A and accelerating voltage of 90 kV. This gives information regarding selection of a proper operating point for further computation. The voltage depression shifts the curves significantly. The curves overlap completely when the detuning δ (see equation(4.34) is taken as the independent variable. One can see that a magnetic field of 5.66 T lies well within the
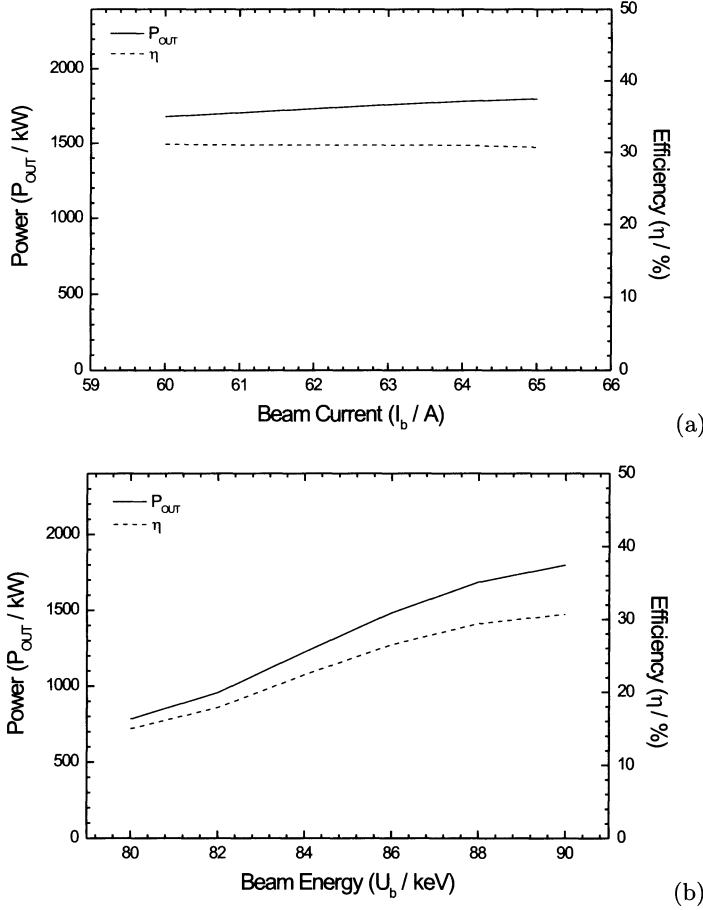
Fig. 9.3. Power and efficiency as a function of (**a**) beam current and (**b**) beam energy for the $TE_{31,8}$ mode. Here the non varying parameters are: $U_b = 90\,keV$, $I_b = 65\,A$, $B = 5.66\,T$ and $\alpha = 1.2$ [193]

region of soft excitation during startup, where the beam energy is around 81 keV.

Figure 9.3 shows the output power and efficiency as function of (a) beam current and (b) beam energy for the $TE_{31,8}$ mode. The nonvarying parameters are: beam energy=90 keV, current=65 A, average velocity ratio=1.2 and magnetic induction B=5.66 T. These would correspond to CW operation. Higher power (2 MW) and efficiency ($> 33\%$) were calculated for slightly lower values of the magnetic field, but the mode may not be accessible for these parameters. The calculated maximum wall loading for ideal hot copper is slightly under 2 kW/cm^2. The quality factor calculated self-consistently
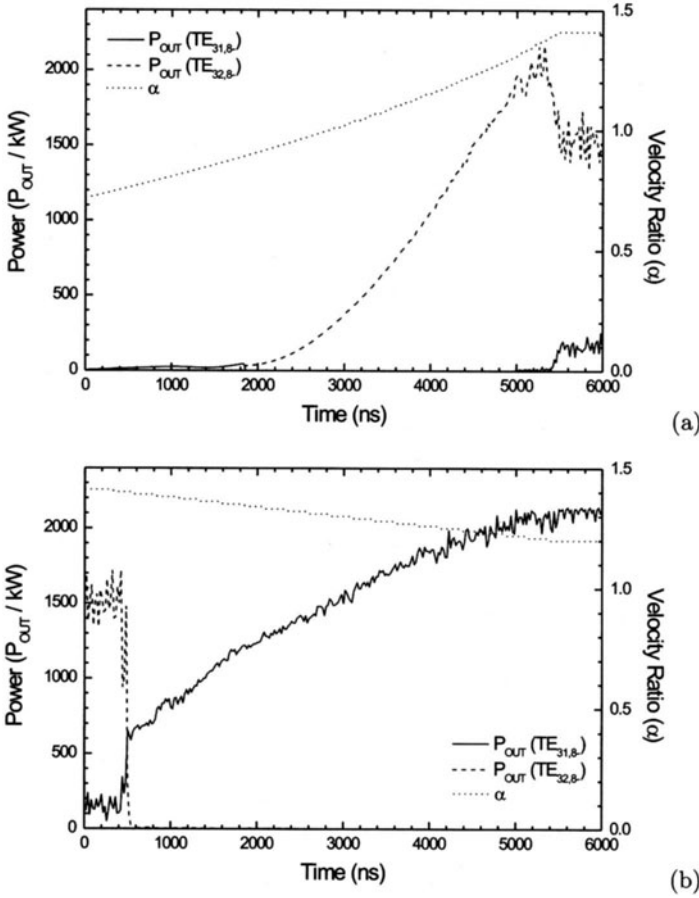
Fig. 9.4. SELFT simulation results for a $TE_{31,8}$ gyrotron considering the probable competing modes, (**a**) before and (**b**) after current neutralization. Here, $U_b = 45$–80.5 keV for (**a**) and 80.5–90 keV for (**b**) and α varies accordingly, $I_b = 70\,A$ and B$=5.66$ T [193]

for these parameters is somewhat higher (around 1200) than the cold cavity value. Wall loading may limit the obtainable CW output power to 1.5 MW.

Figure 9.4 show the results of a simulation with SELFT [136] for the $TE_{31,8}$ mode along with probable competing modes, before and after current neutralization. In these calculations, the beam energy is increased from 45 keV to 80.5 keV over a fictitious startup time of 5000 ns (typical voltage rise times are around 100 μs) and the velocity ratio varies accordingly (from 0.7 to 1.4). The beam current and magnetic field are held constant. Then the beam energy is increased to 90 keV while the velocity ratio drops to 1.20, again over a time interval of 5000 ns, although the real time scale over which

space charge neutralization occurs is about 100 ms. For this case (I_b= 70 A) the TE$_{31,8}$ mode oscillates at high power after space charge neutralization. However, at this high current, the voltage depression is large and the TE$_{31,8}$ mode does not give high power until after space charge neutralization has taken place. These results indicate that stable operation of a gyrotron in the TE$_{31,8}$ mode at 140 GHz at power levels up to 2 MW should be possible. If the current is too high, stable operation at high efficiency may not be possible except in CW. The wall losses may still be too high at 2 MW for CW operation, but CW operation at 1.5 MW (with beam energy up to 85 keV and current around 65 A) should be feasible.

9.3 A 165 GHz Coaxial Gyrotron

Coaxial cavity gyrotrons have been successfully designed and developed at FZK [2] and elsewhere [13, 132]. Here we discuss a coaxial cavity gyrotron designed to operate at 165 GHz in the TE$_{31,17}$ mode [304]. It is equipped with a quasi-optical output system consisting of a Vlasov type launcher with a single cut and two mirrors, one with quasi-elliptic and another with a non-quadratic phase correcting surface. A maximum output power of 1.7 MW has been achieved. The efficiency increases to 41% in operation with a single–stage depressed collector system. The nominal operating parameters of this coaxial gyrotron are shown in Table 9.2.

The geometrical dimensions of the TE$_{31,17}$ cavity with coaxial insert are shown in Fig. 9.5. Because of the uncertainty of the maximum safely achievable magnetic field, the cavity was designed with a relatively high quality factor $Q_D \cong 3080$ for operation at a low voltage ($U_c = 74\ kV$) and a correspondingly low velocity ratio. The relative coupling normalized to unity for the main mode along with other competing modes for an electron beam radius $R_e = 9.41$ mm is shown in Fig. 9.6. Experimentally, the TE$_{31,17}$ mode has been found to oscillate with a frequency of 165 GHz and in good agreement with the design. A wide single-mode operating range has been observed for a given magnetic field and magnetic compression ratio (shown in Fig. 9.7). Also, self-consistent and time dependent multimode calculations were carried out

Table 9.2. Design parameters and goals of a TE$_{31,17}$, 165 GHz, coaxial gyrotron

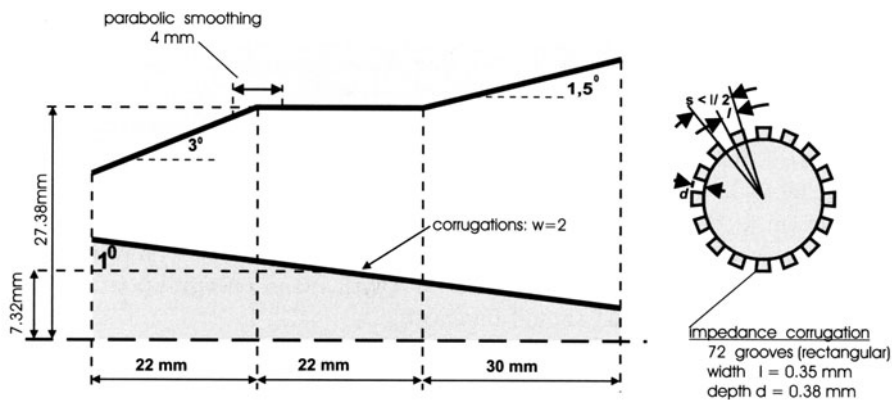|	
Output power	≈ 1.5 MW
Efficiency	$> 35\%$
Beam current	50 A
Accelerating voltage	90 kV
Magnetic field	≈ 6.63 T
Peak wall loading (ideal copper):	
Outer wall	1.04 kW/cm^2
Coaxial insert	0.15 kW/cm^2

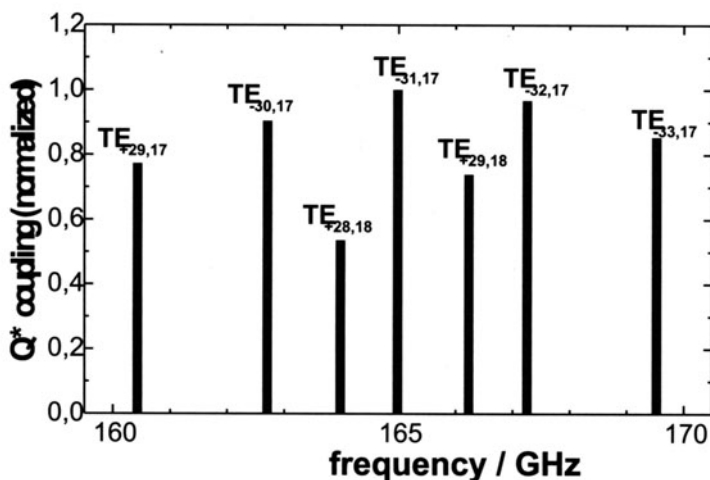**Fig. 9.5.** Geometry of the 165 GHz, $TE_{31,17}$ coaxial cavity [304]

Fig. 9.6. Relative values of Q times coupling for the nominal and possible competing mode, normalized to unity for the design mode [304]

using the operating parameters as input. Figure 9.8 shows the measured and self-consistently computed RF output power as a function of beam current. Here, the cathode voltage has been adjusted to give maximum output power. Figure 9.9 shows the simulated and measured values of RF output power as a function of cathode voltage. The six neighbouring modes shown in Fig. 9.6 have been considered as possible competitors in the calculations. The RF losses inside the tube are estimated to be around 12% and are taken into account for computational purpose. For the electron velocity ratio (α), the values calculated by the trajectory codes EGUN and EPOSR have been taken into account. A velocity spread of $\beta_{\perp rms} = 6\%$ has been assumed. Within
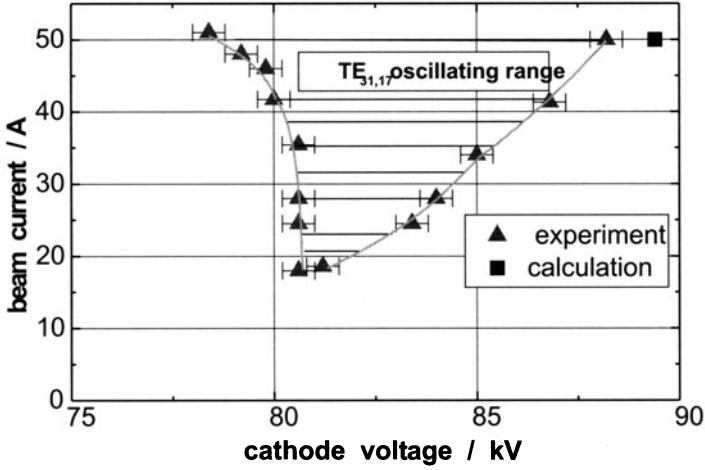
Fig. 9.7. Single-mode operating range for $B = 6.55$ T and $R_e = 9.41$ mm [304]
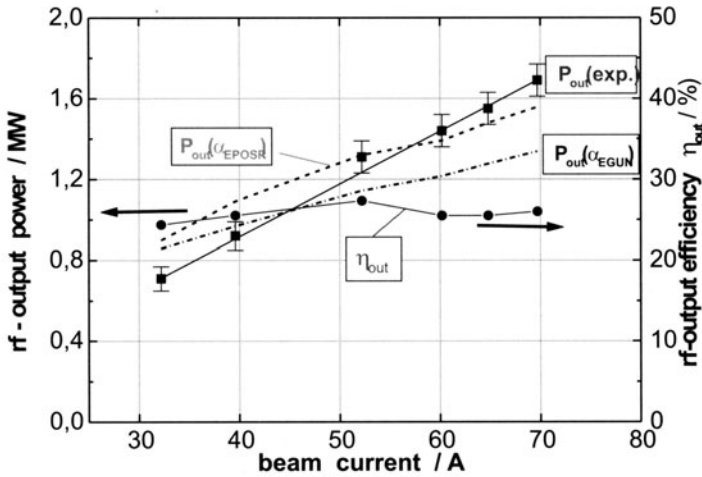
Fig. 9.8. Measured and computed RF-output power and efficiency as a function of beam current. Here, $B = 6.65$ T, $R_e = 9.45$ mm. Calculations were performed with α taken from EGUN and EPOSR and with velocity spread $\Delta\beta_{\perp rms} = 6\%$ [304]

the uncertainty of the electron beam parameters, the agreement between the experimental and numerical results is fairly good. Under the nominal operating parameters and without the depressed collector system, the tube operates with an efficiency around 30%. With a single-stage depressed collector system, the efficiency increased to 41% at an output power around 1.2 MW. This demonstrates a successfully designed and developed high power coaxial gyrotron. After modification of gun and cavity ($Q_D = 2000$), a record out-
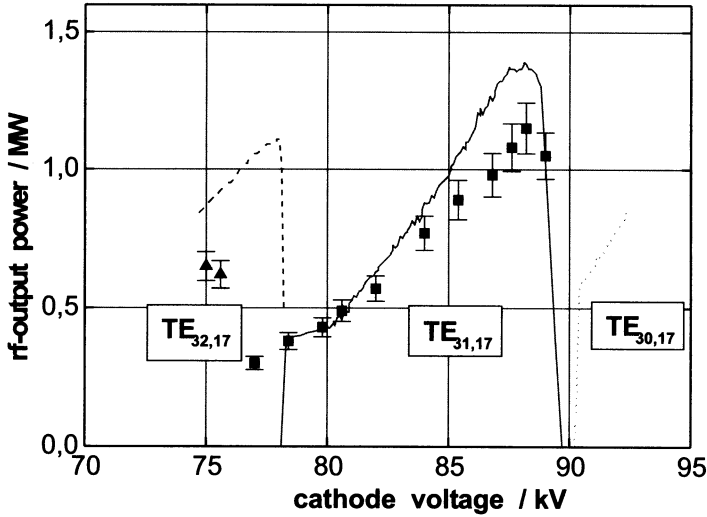
Fig. 9.9. SELFT simulation results for a $TE_{31,17}$ gyrotron considering the probable competing modes. Here, $I_b = 50\,A$, $\alpha = 0.9\text{--}1.1$ and the cathode voltage $U_c = 75\text{--}87\,kV$ with velocity spread $\Delta\beta_{\perp rms} = 6\%$ [304]

put power of 2.2 MW has been obtained. The efficiency increased to 49% in operation with a single-stage depressed collector (at 1.5 MW).

9.4 Multifrequency Gyrotron

Frequency tunable gyrotrons are of interest for controlling instabilities in magnetically confined fusion plasmas [22]. For devices such as ASDEX-Upgrade, there is interest in a step-tunable gyrotron operating at frequencies between about 105 GHz and 140 GHz. In this example, the possibility of mul-tifrequency operation of a 140 GHz gyrotron, which is designed to operate in the $TE_{22,8}$ mode at 140 GHz and the $TE_{19,6}$ mode at 111 GHz or the $TE_{17,6}$ mode at 105 GHz [305] is presented. A similar tube has been successfully tested at IAP [306].

The beam radius for a gyrotron operating in the $TE_{22,n}$ mode at 140 GHz is about 8.0 mm. The cavity radius for the $TE_{22,8}$ mode is 17.96 mm. The optimum beam radius for the other candidate modes is slightly larger than 8 mm and can be adjusted by appropriate setting of the coil currents in the magnet system. Figure 9.10 shows the beam radius as a function of fre-quency, for $TE_{m,p}$ modes, assuming that the $TE_{22,8}$ mode has a frequency of 140.0 GHz, and a beam radius of 7.95 mm. Here, the candidate mode in the vicinity of 105 GHz is the $TE_{17,6}$ mode at a frequency of 105 GHz and an optimum beam radius of 8.2 mm.
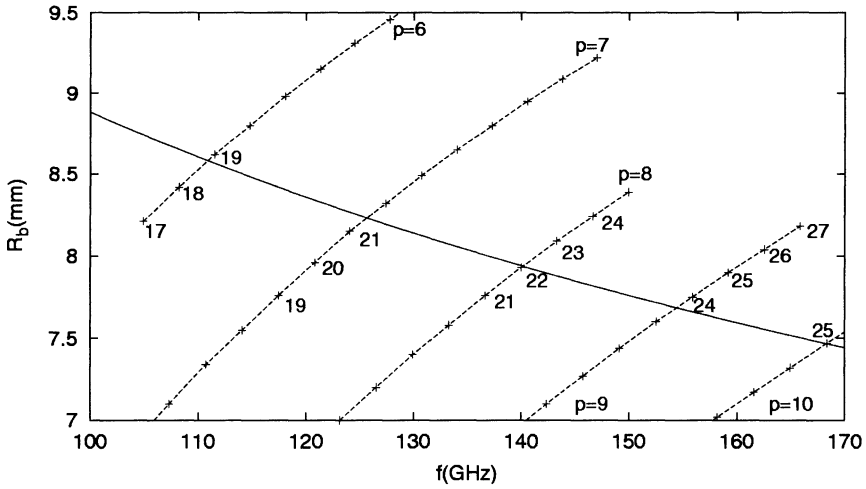
Fig. 9.10. Beam radius as a function of frequency, for $TE_{m,p}$ modes, assuming that the $TE_{22,8}$ mode has a frequency of 140.0 GHz, and a radius of 7.95 mm. Also shown is the curve $R_b = R_{b0}(140.0/f)^{1/3}$ for diode-type MIGs

It is planned to use the same gun and magnet system as in previous experiments that have been performed on a tube designed to operate at 140 GHz in the $TE_{22,6}$ mode [44, 298]. The magnet system and gun [307] used for this tube provide the possibility to vary the magnetic compression and velocity ratio independent of one another, which seems to be advantageous for varying the frequency over such a wide range. The beam properties were calculated for various accelerating voltages, beam currents and magnetic field profiles (set of coil currents) using the program ESRAY [236], which uses boundary fitted coordinates and optimized numerical algorithms.

The resonator design calculations used these computed beam properties to compute the output power and efficiency. This was done separately for each mode. Calculations of output power and efficiency for some of these modes were performed for the beam properties calculated. The results indicate that for an accelerating voltage of 81 kV and beam current of 40 A, an output power (in long pulse operation) of well over 1 MW in the $TE_{22,8}$ mode and around 1 MW in the $TE_{18,6}$, $TE_{19,6}$, $TE_{19,7}$, $TE_{20,7}$ $TE_{21,7}$, $TE_{21,8}$, $TE_{23,8}$, $TE_{24,8}$, $TE_{24,9}$, $TE_{25,9}$, $TE_{26,9}$ and $TE_{27,9}$ modes can be reached. Mode competition was studied and should not be more of a problem than is the case with other, similar, gyrotrons. The results of some typical SELFT simulations for the $TE_{22,8}$ mode are shown in Chap. 4 (see Figs. 4.10–4.13).

Efficient operation for such a large number of modes requires the use of a broadband window. A CVD diamond Brewster window is well suited for this purpose (but is expensive). The average value of the loss tangent of a disc with 120 mm diameter and 1.92 mm thickness is $3.6 \cdot 10^{-5}$. The measured
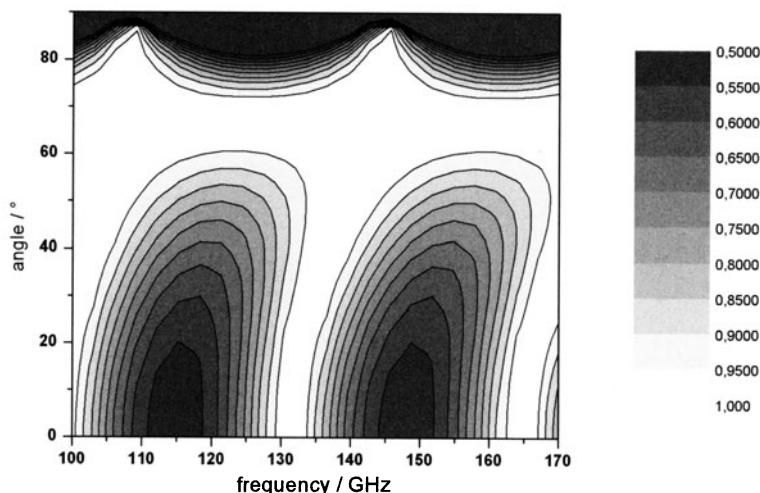
Fig. 9.11. Transmisson of a CVD diamond Brewster window (thickness $= 1.92\,\mathrm{mm}$)

values for the entire disc range from $\tan\delta = 2\cdot10^{-5}$ to $8\cdot10^{-5}$. Figure 9.11 shows the calculated transmission as a function of frequency and angle.

The quasi-optical mode converter consists of a dimpled-wall antenna and a beam forming mirror system optimized for nine modes from $\mathrm{TE}_{17,6}$ to $\mathrm{TE}_{23,8}$. For these modes the dimpled-wall antenna shows a well focussed beam with low diffraction of the radiation pattern compared to a so-called Vlasov antenna. The radiation patterns for the $\mathrm{TE}_{22,8}$ mode with (a) an advanced Denisov launcher and (b) a conventional Vlasov launcher are shown in Figs. 9.12 and 9.13 respectively.

The first mirror is large and quasi-elliptical. The second and third mirrors are phase correcting mirrors with a nonquadratic shape of the surface. These two mirrors were also optimized for broadband operation of the nine design modes.

For cold tests, a quasi-optical design is used for a high-order mode generator [308]. A Gaussian-like beam is coupled via two cylindrical lenses and a quasi-parabolic caustic mirror into a perforated gyrotron-like coaxial resonator. The caustic mirror is shaped in such a way that all waves are tangent to the so-called caustic of the mode. Since the eigenvalues of an overmoded resonator are very close to each other, an inner rod is used to improve the mode selection. Since all the modes of interest for this gyrotron have a similar structure, with their caustic radius being approximately one half of the cavity radius, only one resonator and a set of lenses is required. A minor readjustment of the quasi-optical components is sufficient for excitation of different modes. Three dual-mode horns and a set of inner conductors have been made to cover the full frequency range.
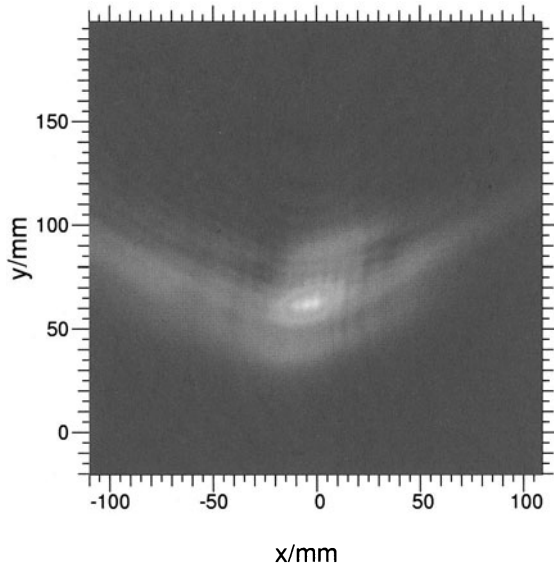
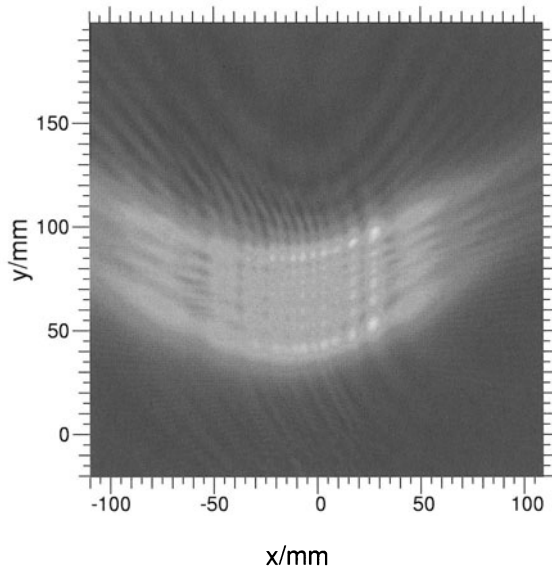**Fig. 9.12.** Radiation pattern of the $TE_{22,8}$ mode using a dimpled-wall antenna (Denisov launcher)

Fig. 9.13. Radiation pattern of the $TE_{22,8}$ mode using a slightly tapered antenna with a helical cut (Vlasov launcher)

9.5 Second Harmonic Gyrotrons

Gyrotron operation at the second harmonic of the electron cyclotron frequency has the advantage over conventional operation at the fundamental in that to obtain radiation at a given frequency only half the magnetic field is required. Or, expressing this another way, given a particular magnetic field strength one can obtain gyrotron output at twice the frequency. A number of near-millimeter wave gyrotrons have been developed by using the second harmonic of the cyclotron frequency. Recently, the low-cw power, tunable gyrotron at the University of Sydney has attained 330 GHz at the fundamental and 516 GHz at the second harmonic [309] , and the Gyrotron FU IVA, the latest gyrotron of Fuikui University, has achieved 889 GHz at the second harmonic [310].

However, the second harmonic modes are difficult to excite because of mode competition between fundamental and the second harmonic modes [195, 196, 309, 311]. Due to mode competition, higher-power operation at the fundamental may suppress the second harmonic, so that higher frequencies cannot be reached. For these reasons, such a phenomenon has been intensively studied both theoretically and experimentally [86, 156, 179, 195–197]. Various approaches have been proposed to eliminate undesirable mode competition, for example specially designed cavities and careful choice of gyrotron operating conditions [198]. We have discussed mode competetion between different harmonics, starting current calculations, and (single-mode) self-consistent computations in the previous chapters.

As far as the mode selection procedures are concerned, the same rules as discussed above and in Chap. 5 apply to the design of second harmonic gyrotrons. Voltage depression, limiting current and wall losses play the same significant role in determining the operating mode of interest. In addition, one has to consider mode competition between the fundamental and second harmonic modes. The frequency spacing between modes increases as the cavity radius is decreased. Thus, to improve operation at the second harmonic, a smaller cavity radius should be chosen in order to keep the modes farther apart and reduce competition between the fundamental and second harmonic. Another factor to consider is the fact that the starting current for excitation of a mode is inversely proportional to a factor proportional to the beam-field coupling coefficient, which was given in Chap. 4 as

$$C_{BF} = C_{mp}^2 k_{mp}^2 G_{mp}^2$$

The use of this is illustrated in the next example.

A 24 GHz Gyrotron for Materials Processing

Here we present the example of a proposed, 24 GHz, 25–50 kW technology gyrotron (for materials processing) operating at the second harmonic [312].
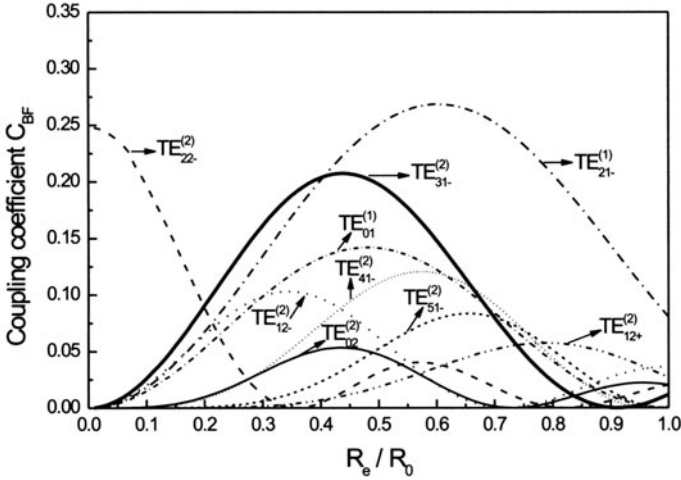
Fig. 9.14. Beam-field coupling coefficient C_{BF} as a function of normalized beam radius R_e/R_0 for some important candidate modes of a 24 GHz, TE$_{31}$ mode second harmonic gyrotron, where the superscript (1) and (2) denote the fundamental and second harmonic, and the sign $-$ and $+$ in the subscript denote co-rotating and counter-rotating modes, respectively [312]

First, the beam-field coupling coefficients as a function of normalized beam radius R_e/R_0 for some important competing modes near the TE$_{31}$ mode [312] is shown in Fig. 9.14. Here, for the main mode, $R_e/R_0 = 0.44$, and the beam-field coupling coefficient is moderately large when compared with some of the first and second harmonic competing modes. This will give a first estimate of the mode competition for mode selection. One obtains a better estimation by computing the starting currents, since this provides an estimate of the segregation of the different modes in the magnetic field domain.

The starting current can be calculated in a linearized single mode theory, as shown in Chap. 5. The starting current as a function of magnetic field is computed for the second harmonic main mode TE$_{31}$, and other first and second harmonic competing modes for the above 24 GHz industrial gyrotron is shown in Fig. 9.15. These plots are useful to estimate the stability against mode competition by examining the starting currents for various competing modes. From the initial mode selection procedures, TE$_{31}$ was chosen as the operating mode, because it is very well isolated from possible competing modes.

As a possible resonator, a standard three section cavity with rounded transitions was considered. The input and output taper angles are, for the most part, fixed at 2.5° and 3.0°, respectively. The length of the mid section is varied. Table 9.3 shows the resonant frequency and quality factor for various lengths of the cavity mid-section. The lengths of the tapered sections are fixed at $L_1 = L_3 = 50$ mm, $\theta_1 = 2.5°$, $\theta_2 = 0.0°$, and $\theta_3 = 3.5°$. Roundings of
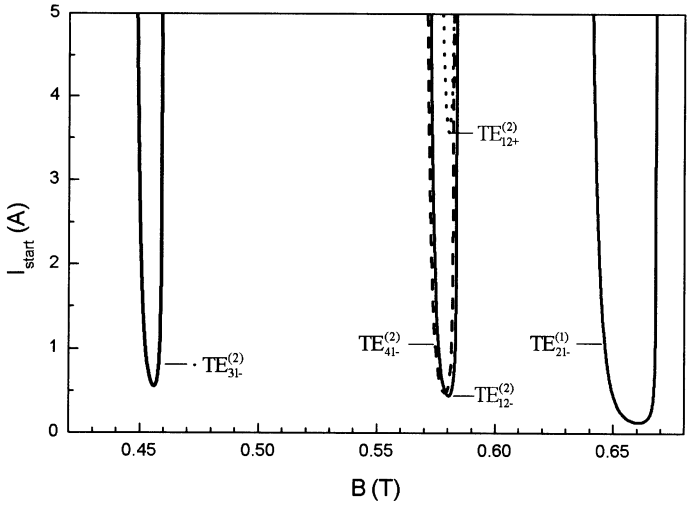
Fig. 9.15. Starting current I_{start} as a function of magnetic field B for various modes with beam radius R_e optimized for the TE$_{31}$ mode, where $U_b = 35\,\text{kV}$, $\alpha = 1.50$, and $R_e = 3.64\,\text{mm}$ [312]

Table 9.3. Frequency and quality factor as a function of resonator length

L_2	f (GHz)	Q_D
65	24.201	560
70	24.192	670
75	24.184	801
80	24.178	948
85	24.172	1113
90	24.168	1209

length 15 mm are included at each transition. For the TE$_{31}$ mode, the cavity radius was 8.31 mm If L_1 is decreased to 25 mm, to reduce the probability of beam interception at the end of the compression region, the calculated frequency and quality factor are unchanged.

A plot of the field profile along with cavity geometry is shown in Fig. 9.16 for L_2=80 mm. In Fig. 9.17, the output power and efficiency as a function of beam current for $L_2 = 80$ mm, $\alpha = 1.65$ and $L_2 = 85$ mm, $\alpha = 1.50$, respectively, is shown. For a beam current I_b=2.5–5.5 A, one can obtain an output power 26.3–63.5 kW and an efficiency of 30.1-34.1% with $L_2 = 80$ mm, $\alpha = 1.65$; and output power 23.2–54.0 kW and efficiency 26.5–31.4% with $L_2 = 85$ mm, $\alpha = 1.50$. However, this exercise remained only a paper study. No tube was ever built or operated. Tubes in this frequency range which are operational are discussed by Bogdashov et al. [313].
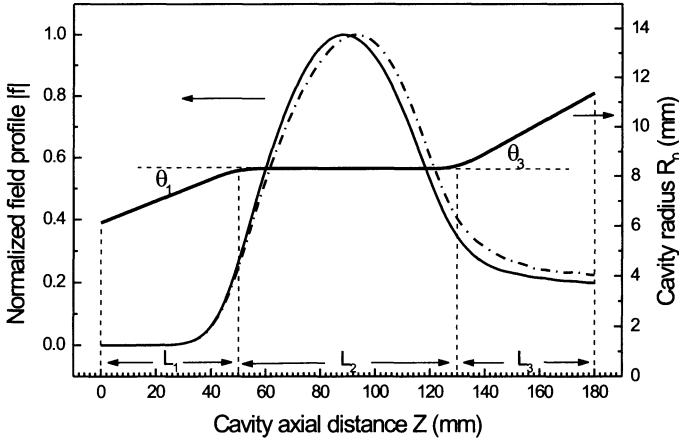
Fig. 9.16. Normalized field profile $|f|$ as a function of z (Solid: cold cavity, dash dot: self consistent) for a 24 GHz gyrotron using the TE_{31} mode with $L_2 = 80$ mm and other parameters as in Table 9.3. For the self-consistent field profile, beam voltage $U_b = 35$ kV, beam current $I_b = 4$ A, velocity ratio $\alpha = 1.5$, resonator magnetic field $B = 0.45$ T, and beam radius $R_e = 3.64$ mm [312]
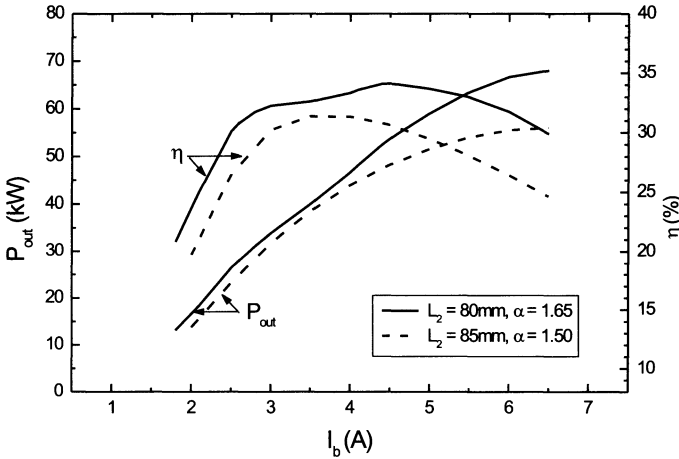

Fig. 9.17. Output power P_{out} and efficiency η as a function of beam current with $U_b = 35$ kV and $B = 0.449$ T, for $L_2 = 80$ mm, $\alpha = 1.65$ (solid line) and $L_2 = 85$ mm, $\alpha = 1.50$ (dashed line), respectively [312]

A 384 GHz FU Gyrotron

We now present some numerical results of self-consistent calculations of one of the FU gyrotrons operating at 384 GHz in the TE_{26} mode [199]. The resonator geometry chosen ($L_1 = 4.5$ mm, $L_2 = 14.5$ mm, $L3 = 2.5$ mm; $\theta_1 = 2.227°$, $\theta_2 = 0°$, $\theta_3 = 32.211°$; $R_0 = 2.425$ mm) corresponds to the Gyrotron FU 2 [198]. The field profile along with cavity geometry are shown in Fig. 9.18. For the cold cavity field (CCF), the frequency is $f = 384.047$ GHz, and the quality factor Q_D is 33697; for self-consistent field (SCF), $f=384.049$ GHz, and $Q_D =33252$. In this case, the profile of SCF is very close to that of CCF due to the very large value of Q.

The dependence of output power and efficiency on the beam current is shown in Fig. 9.19 for the magnetic field $B = 7.31$ T. In the calculation, the Ohmic loss has been taken into account. From the figures one can see that the power increases with current, but the efficiency has an optimum value. When the current is small, the RF field excited is weak, and the efficiency of beam-wave interaction is low. If the current is too large, the RF field excited is too strong. This will lead to "over bunching" of the electrons, and the efficiency is reduced. Here, the starting current is about 0.19 A for $B = 7.31$ T, and 0.10 A for $B = 7.35$ T. A comparison with the results of a calculation with CCF is also shown. In this case, the output power and efficiency from SCF is slightly higher than that from CCF, but this is not always the case.
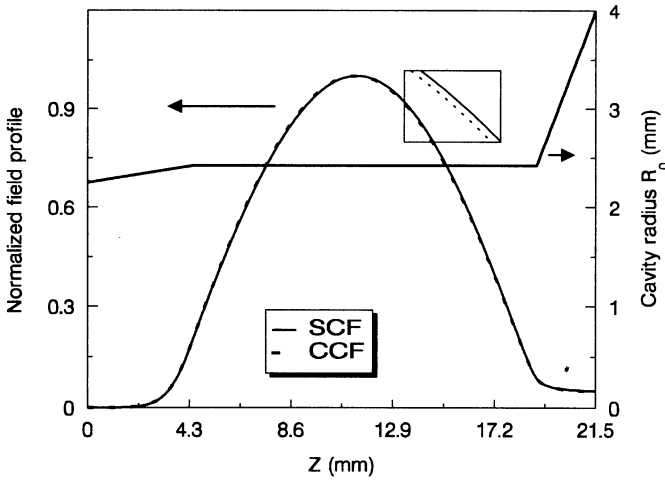

Fig. 9.18. Normalized field profile $|f|$ as a function of cavity axial position z. Solid curve: self-consistent field (SCF) with $U_b = 40$ kV, $B = 7.31$ T, $\alpha = 1.50$, $I_b = 0.50$ A, and $R_b = 1.25$ mm; Dotted curve: cold cavity field (CCF). The cavity shape is also shown. Note that for these parameters there is almost no difference in the field profiles [199]
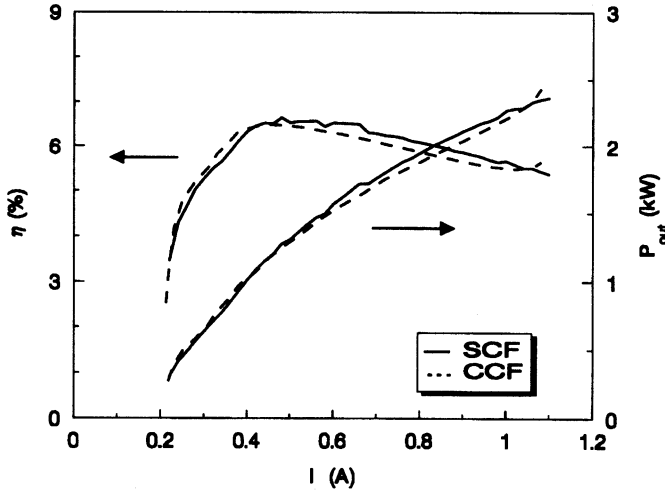
Fig. 9.19. Efficiency η and output power P_{out} versus beam current for the TE$_{26}$ modes, with $U_b = 40\,\text{kV}$, $B = 7.31\,\text{T}$, $\alpha = 1.50$, and $R_b = 1.25\,\text{mm}$. Solid curve: self-consistent calculation; Dashed curve: cold cavity, fixed field (CCF) approximation [199]

9.6 Concluding Remarks

This chapter introduced some typical design examples. For the design of low and medium power (powers less than 10–200 kW) gyrotrons, a conventional type of interaction cavity structure is suitable as it poses fewer technical complexities. Even for powers up to 1 MW under CW operation, a conventional hollow cylindrical cavity will serve well as interaction structure with a high order operating mode. But for ultra high power gyrotrons where the power levels exceed 1.5 MW under CW operation, the ultimate choice will be a coaxial cavity gyrotron. A diode type MIG is a popular choice if it is able to provide the required beam parameters since it has fewer technical requirements and complexities. However, a triode type MIG has some advantages as compared with the diode configuration in providing an electron beam with the required quality. In case of axial extraction of the output power, external mode converters or suitable transmission lines have to be added for the beam transportation. In case of radial extraction of the output beam, a Vlasov type launcher with suitable mirror system is a popular and cost effective choice for low and medium power operation. However, since the diffraction losses are high with classical Vlasov type launchers, it is usually better to employ advanced dimpled launchers of the Denisov type with appropriate optimized mirror system for high power gyrotrons as it reduces the losses considerably. The other components (such as the window and its ma-

terial, collecting system, beam guidance, additional gun-collector coils, etc.) also play an important role in the selection procedure. Second harmonic operation is also an excellent option, particularly for low power gyrotrons if one can live with moderate efficiencies without depressed collectors. Therefore, the design involves a crucial trade-off between physical, technical and economical constraints.

10 Applications

10.1 Introduction

The possible applications of high power microwaves span a wide range of technologies. Long pulse and high power gyrotron oscillators have successfully been used for various electron cyclotron wave applications in magnetically confined for thermonuclear fusion energy research. They are also used to generate ECR plasmas for the production of multi charged ions and soft X-rays. In high frequency, high magnetic field EPR spectroscopy, gyrotrons serve as sub-millimetric wave sources. Sub-millimetric wave gyrotrons are also used for plasma diagnostics and are proposed for use in catheters for irradiation of living bodies. Medium power CW gyrotrons are used in several technological and industrial applications such as sintering of advanced ceramics and other types of material processing. Gyroklystron amplifiers are being used in novel mm-wave radar systems and are under development for RF-drivers of future multi–TeV linear colliders. Gyro-twystrons and gyro-TWTs are other members of the gyro-amplifier family which are under development for the latter applications [5].

The book of Gaponov–Grekhov and Granatstein [4] gives a comprehensive review of various applications of high power microwave and millimetric waves. In this chapter, we present some of the major applications of gyro-devices other than plasma heating application. Of great interest are ECR sources of multiply charged ions and soft X-rays, in which ECR breakdown and plasma heating with powerful microwaves are used to produce intense ion beams with the maximum possible degree of ionization and intense, incoherent soft X-ray radiation. The EC heating of electrons in a magnetic mirror trap provides the possibility of achieving electron distribution functions with a high share of fast particles, which efficiently provide multiply charged heavy ions and soft X-rays. It is evident that an increase of the EC frequency applied in the source must lead to an increase of plasma density and consequently, to an improvement of the source parameters. There are now several projects for the development of ECR sources of multiply charged ions and soft X-rays with the use of gyrotron oscillators (or shorter: gyrotrons) as mm-wave generators in the frequency range of 30 to 80 GHz [315, 316].

The availability of millimeter and and sub-millimeter wave gyrotrons with output power larger than 100 W allows high resolution ESR experiments on

samples having short relaxation constants. Tatsukawa et al. [317] presented the first application of a step-wise frequency tunable gyrotron for ESR.

In materials processing, microwaves are used to heat food, textiles, wood products, polymers, minerals, structural and functional ceramics, composites, multilayer structures and chemicals. Low pressure and low temperature plasma processing in electrodeless ECR microwave discharges in waveguide and cavity applicators for etching and thin film deposition is widely used by industries. The application of gyrotron radiation for processing of advanced materials such as nanocrystalline alumina and improved piezoceramics will be presented as an outstanding example.

The development of high power microwave sources has opened up a number of possible applications for advanced radars. There are two ways in which the new generation of sources enhances capability, first they extend to new regimes of peak power (for example, relativistic backward wave oscillators: > 0.5 GW), and second, they extend high power capability to new frequency regimes. Particularly in the mm-wave band, the recent development of gyrotrons, gyroklystrons, gyrotwystrons, and gyro-travelling-wave amplifiers can enhance the average radiation power by several orders of magnitude. The experimental state-of-the-art of gyrotron oscillators and gyro-amplifiers are periodically given elsewhere [2]. In the radar applications we have discussed three new radar configurations made possible by these high power microwave sources. They are: monitoring of the atmosphere, space debris radar and very high power nanosecond radar.

The cost of a future linear electron–positron collider with center of mass energy in the TeV range will depend both on the number of microwave amplifiers required to drive the collider and on the cost of each amplifier. In the past, the microwave amplifier of choice for driving the highest energy linear electron accelerators has been the klystron. In considering microwave amplifier requirements for future supercolliders there has been a widespread perception that higher frequency and higher peak power will be required. Because of inherent limitations when simultaneously handling high power and high frequencies in klystron circuits, other types of amplifiers such as relativistic gyroklystrons have been explored. A performance comparison between conventional high power microwave amplifiers (klystron) with new generation gyro-klystron amplifiers for next generation accelerator applications has been presented elsewhere [5]. These klystron development programs will likely result in producing microwave amplifiers that are suitable for linear colliders in the energy range up to 1 TeV. However, for multi-TeV colliders gyroklystrons are needed.

Some interesting futuristic applications of high power microwaves are as follows [5]:

1. Generation of a gas discharge in the freely localized intersection region of two powerful nanosecond microwave beams in the upper atmosphere and stratosphere (artificially ionized layer: AIL) which may be used for:
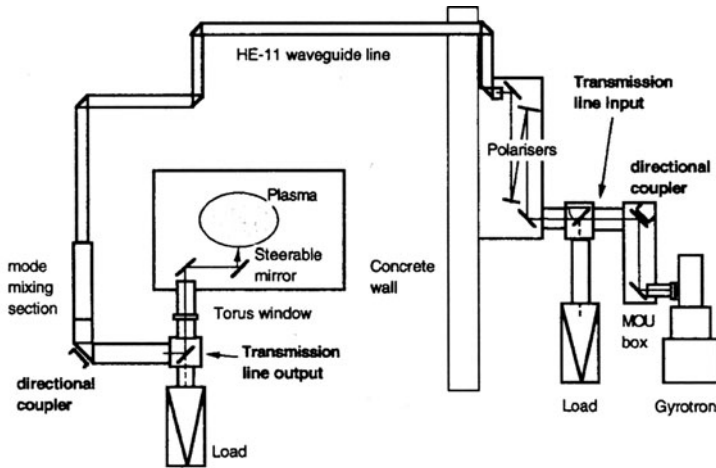
Fig. 10.1. Transmission line schematic from a gyrotron to the ASDEX toka-mak [319]

- Creation of reflecting mirrors for long-distance radio- and television communications (as an alternative to satellite communications).
- Removal of chlorine fluorocarbons from the atmosphere.
- Restoration of ozone composition in the region of local ozone "holes", with insignificant production of harmful nitrogen oxides.
2. Space propulsion and power beaming to spacecraft and space platforms using microwave and millimeter wave systems.

10.2 ECRH Applications

Resonant absorption of radio frequency electromagnetic waves is a well known method of plasma heating. It is broadly classified into three types depending on the type of resonance and species (that is electrons or ions). The first type is *ion cyclotron resonance heating* (ICRH) with a frequency range 30–120 MHz depending on the magnetic field and species. The second catagory is *lower hybrid heating* (LHH) which utilizes the frequency range 1–8 GHz. Finally, the third type is *electron cyclotron resonance heating* (ECRH) which requires sources in the range 100–200 GHz. The physics of radio frequency heating is well described elsewhere [318] and will not be discussed here. A typical transmission line from a gyrotron to a tokamak is shown in Fig. 10.1.

At present, gyrotron oscillators are mainly used as high power mm-wave sources for ECRH applications and for plasma diagnostics of magnetically confined plasmas in controlled thermonuclear fusion research. Long pulse gyrotrons utilizing open ended cylindrical resonators which generate output

powers of 100–500 kW per unit, at frequencies between 28–170 GHz have been used very successfully for plasma formation, ECRH, and local current density profile control by non-inductive electron cyclotron current drive (ECCD) in tokamaks and stellarators. Gyrotron complexes with total power of up to 4.5 MW have been installed. As experimental devices become larger and operate at higher magnetic fields ($B_0 \leq 6\ T$) and higher plasma densities ($n_{e0} = (1-2) \times 10^{20}/m^3$) in steady state, present and forthcoming ECRH systems require gyrotron output powers of at least 1 MW, continuous wave (CW) at frequencies ranging from 100–170 GHz. Since efficient ECRH, ECCD and collective Thomson scattering need axisymmetric, narrow, pencil-like mm-wave beams with well defined polarization, single mode emission is necessary in order to generate a TEM_{00} Gaussian beam mode at the plasma torus launching antenna. Single mode mm-wave gyrotron oscillators capable of high average power, 05–1.0 MW per tube, in long pulse or CW operation, are currently under development in several scientific and industrial laboratories [2]. At power levels of around 1 MW, the coaxial cavity gyrotron can probably operate at frequencies greater than 300 GHz. This means that the gyrotron oscillator is the dominant mm-wave source for high power ECRH and ECCD. Even in the case of local non-inductive current drive for suppression of plasma instabilities in ITER, the gyrotron is a good option, since ultra broadband Brewster windows and special fast tunable magnet systems allow frequency step tuning in the seconds time scale in the full D–band (110–170 GHz) [45]. Diagnostic gyrotrons deliver $P_{out} = 40\ kW$ with $\tau = 40$ μs at frequencies up to 650 GHz ($\eta \geq 4\%$).

10.3 ECR Discharges for Generation of Multiply Charged Ions and Soft X-Rays

In recent years interest in investigating microwave discharges in a magnetic field under conditions of electron cyclotron resonance (ECR) has increased. This is related not only to fusion plasma heating and low pressure and low temperature plasma processing but also to the possibility of using ECR discharges in heavy ion gases as a source of multiply charged ions (MCI) for cyclotron accelerators and materials processing such as synthesis of unique semiconductor materials (ion implantation). Such ECR discharges are also being examined as a possible high intensity source of incoherent soft X-ray radiation for dry etching lithography.

In the past, there were a few tens of ECR ion sources in the world, which work in the frequency range of 2.45 to 10.0 GHz. An increase of the EC frequency employed in the source will lead to an increase of plasma density in the discharge and consequently, to an improvement of the source characteristics, particularly higher ion currents. The current of ions with charge Z is proportional to the squared frequency and the average ion charge also grows with frequency: $\langle Z \rangle \approx \ln f^{3.5}$. There are now several projects for
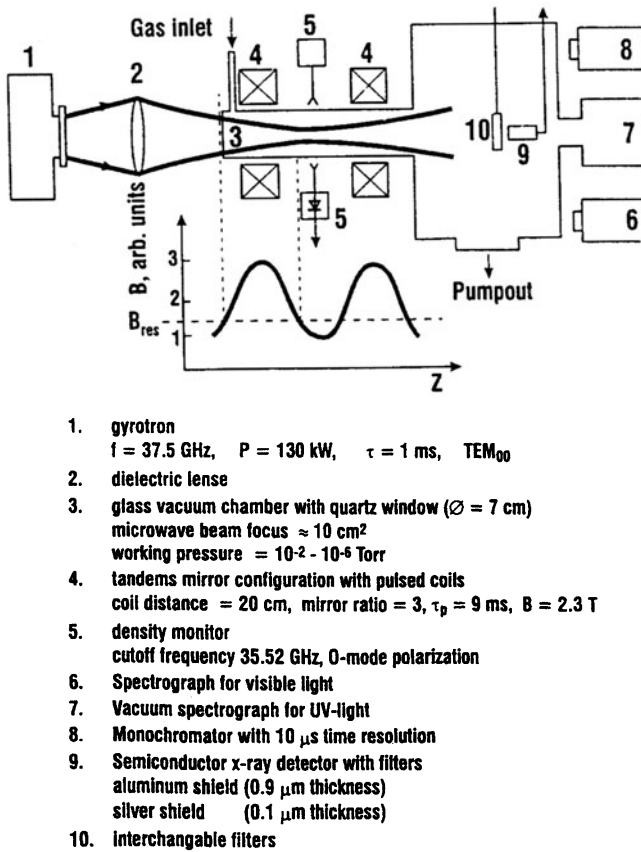
1. **gyrotron**
   $f = 37.5\,GHz$, $P = 130\,kW$, $\tau = 1\,ms$, TEM_{00}
2. **dielectric lense**
3. **glass vacuum chamber with quartz window ($\varnothing = 7\,cm$)**
   microwave beam focus $\approx 10\,cm^2$
   working pressure $= 10^{-2} - 10^{-6}\,Torr$
4. **tandems mirror configuration with pulsed coils**
   coil distance $= 20\,cm$, mirror ratio $= 3$, $\tau_p = 9\,ms$, $B = 2.3\,T$
5. **density monitor**
   cutoff frequency 35.52 GHz, O-mode polarization
6. **Spectrograph for visible light**
7. **Vacuum spectrograph for UV-light**
8. **Monochromator with 10 μs time resolution**
9. **Semiconductor x-ray detector with filters**
   aluminum shield (0.9 μm thickness)
   silver shield   (0.1 μm thickness)
10. **Interchangable filters**

Fig. 10.2. Experimental setup for ECR discharges [315]

the development of ECR sources of multiply charged ions and soft X-rays with the use of gyrotrons as microwave generators in the frequency range of 30 to 80 GHz. The experiments of Golubev et al. [315] have been performed in a magnetic trap with mirror configuration according to the arrangement shown in Fig. 10.2.

Multiply Charged Argon Ion Source

At an argon gas pressure of $P = 10^{-4}$ Torr multiply charged argon ions ranging from Ar^{2+} up to Ar^{18+} were produced with a maximum of the generation rate at Ar^{14+}, which is the present world record. In traditional ECR sources, the maximum production rate is for Ar^{10+}.

a) **Microwave pulse;**

b)
  1) O^+ **ion emission,**
     wavelength 3749.5 Å;
  2) O^{2+} **emission, 3754.7 Å;**

c) **total plasma emission in**
   the visible region;

d) **x-ray emission**
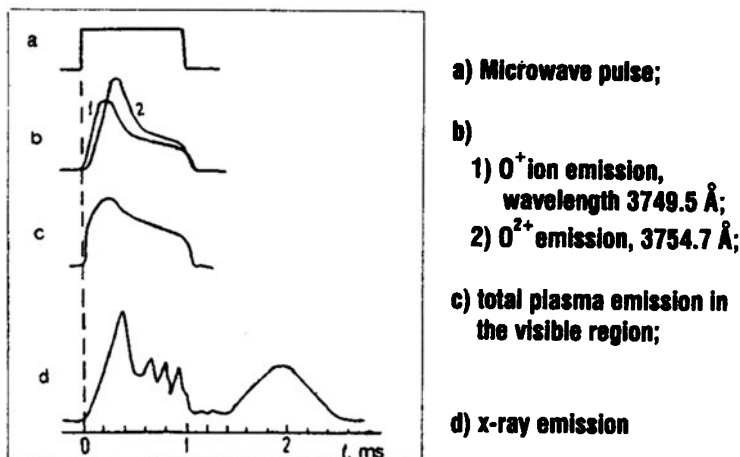
Fig. 10.3. Experimental oscillograms of ECR discharge soft X-ray source [315]

Soft X-Ray Source

The working gas pressure (air or oxygen) was $P = (3-6) \cdot 10^{-4}$ Torr. Typical oscillograms of various diagnostic signals are displayed in Fig. 10.3. Measurements by means of X-ray meters showed that the main contribution is connected with ion lines in about the 9 nm wavelength band (FWHM = 4 nm). Approximating the total power of the ECR discharge X-rays from the results of measurements, it was found that the amount of X-ray power in the region around 9 nm is in the order of 7 kW, and correspondingly, conversion efficiency is around 5%.

10.4 High Frequency Broadband ESR Spectroscopy

The investigation of electron spin resonance (ESR) is based on measurements of resonances that occur at fixed radiation energies hf corresponding to the energy differences between different spin states caused by the Zeeman interaction, the electronic quadrupole interaction and other types of interactions. Such experiments provide direct access to the values of the g–factor, the fine structure constants, etc.. Studies of ESR at high frequencies and high power offer several advantages. High frequency ESR allows high resolution measurements, so that very small differences in the g–factor, large fine structure constants, and nonlinear magnetic field interaction terms can be experimentally determined. High power pulses allow the investigation of the RF-field dependence of resonance absorption in samples having short relaxation times.
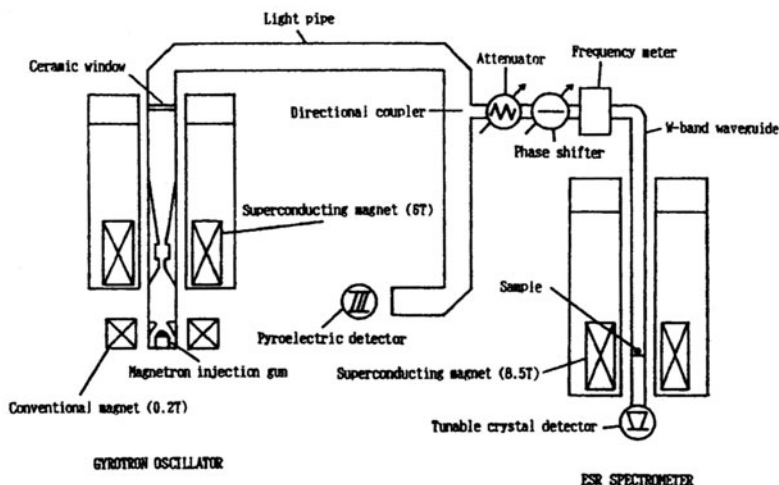
Fig. 10.4. Block diagram of an ESR spectrometer using a gyrotron as radiation source [317]

Tatsukawa et al. [317] presented the first application of a gyrotron to ESR and demonstrated the higher sensitivity that can be obtained by using a step-wise frequency tunable gyrotron which covers a broad frequency range in the millimeter and submillimeter wavelength region. The experimental setup is shown in Fig. 10.4. The gyrotron FU–I used in these experiments had in the frequency range $f = 65$–135 GHz, an output power of approximately $P_{out} = 100W$ and a pulse repetition frequency of PRF $= 3$ Hz.

In this experiment, two kinds of DPPH (1–diphenyl–2–picrylhydrazyl) samples (DPPH–A is a single crystal and DPPH–B a polycrystalline powder) are attached to a mica plate and put into the waveguide of the ESR detection system. Figure 10.5 shows the observed ESR spectra in the W–band measurements (a) for DPPH–A and (b) for DPPH–B. The observed linewidth of the resonance spectrum for DPPH–A is $2.0 \cdot 10^{-4}$T which agrees with results measured using a standard X–band ESR spectrometer. This measurement confirms that the frequency stability is better than $1 \cdot 10^{-4}$. The linewidth of DPPH–B is $3 \cdot 10^{-3}$T which is much broader than the single crystal result. However, this value can be explained by the anisotropic g–value (g–tensor) effect of the polycrystalline sample. Operating at the second harmonic of the electron cyclotron frequency enables the gyrotron to act as a medium power step tunable, mm– and sub-mm wave source in the frequency range up to 889 GHz ($TE_{8,6}$, second harmonic). Pulsed power magnetic fields up to 30 T have been generated in synchronized phase with the pulsed gyrotron operation [320]. Gyrotron based ESR spectrometers are also being used to study dynamic nuclear polarization, a technique that can result in significant enhancements of nuclear magnetic resonance (NMR) signals [321]
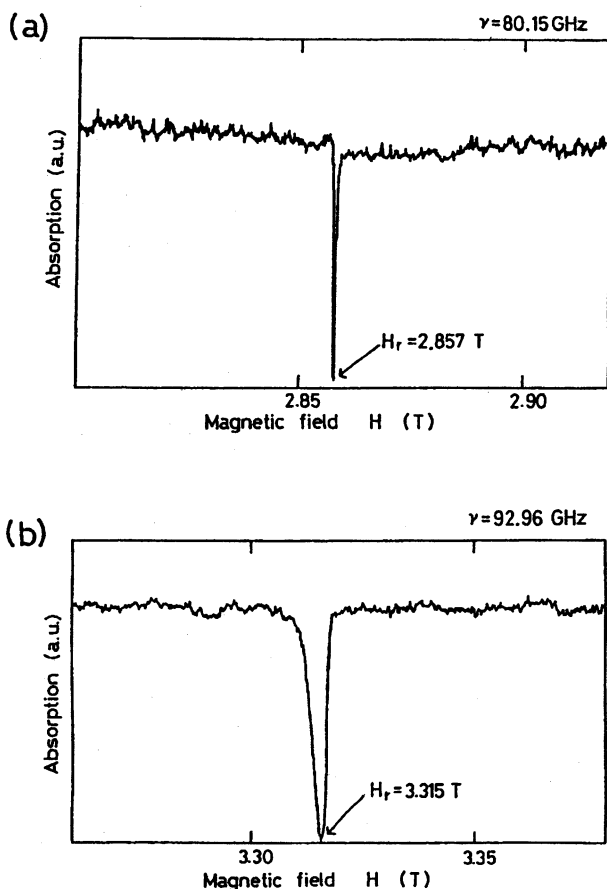
Fig. 10.5. ESR spectra of DPPH as a function of magnetic field: (**a**) for a single crystalline sample at $f = 80.15\,\mathrm{GHz}$ and (**b**) for polycrystalline powder at $f = 92.95\,\mathrm{GHz}$ [317]

and they could also be employed favorably in electron nuclear double reso-
nance experiments. 197 GHz ESR corresponds to 300 MHz NMR. For some
ESR applications, phased packets of short pulses (ns time-scale) are required;
these may be generated by future second harmonic gyroklystron amplifiers
or FEMs.

10.5 Processing of Advanced Ceramics

In recent years, there has been increasing interest in microwave processing of
materials such as ceramic sintering, joining of ceramics and metals, etc.. Vol-
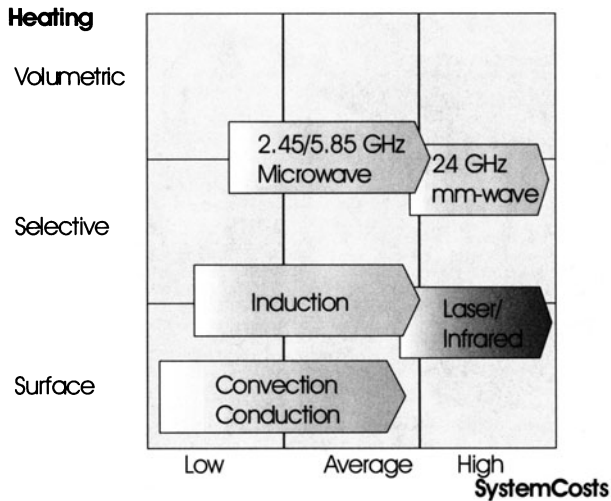
Fig. 10.6. Cost comparison of commonly used heating technologies [322]

umetric heating resulting from the absorption of microwave energy within the bulk of materials leads to savings in energy and processing time that are significant for practically all applications based on heating of materials. In fact, owing to intimate linkage in the sequence "processing conditions – microstructure of materials – final properties of materials", the fast, inertialess and easily controllable procedure of microwave heating offers unique capabilities for producing materials with new favourable properties.

Figure 10.6 gives an overview of the technical and applied heating processes compared in terms of specific physical heating properties and their estimated range of system costs [322]. Although the systems cost increase, one has to choose microwave or millimetric wave heating techniques if one prefers to have a high qualitative and selective volumetric heating of the materials.

The property to heat volumetrically and selectively is unique for microwaves and millimetric waves. However, the following factors impede the exploitation of the traditional industrial microwave techniques at frequencies of 0.915 and 2.45 GHz for practical implementation of most high temperature processes:

- Rather low absorption of decimeter wavelength radiation in most of advanced ceramic materials, especially those based on pure oxides and nitrides.
- Non-uniform distribution of the electromagnetic field within an applicator. A highly uniform distribution required for processing of large size specimens is hardly achievable at these frequencies even in multimode resonators.

Fig. 10.7. Gyrotron Oscillator Technology System (GOTS) for high temperature processing of materials ($P = 15\,\mathrm{kW}$, $f = 30\,\mathrm{GHz}$, CW) at FZK

These problems can be solved by increasing the frequency f. As a rule, the microwave absorption in dielectrics increases with f. In addition, the spatial non-uniformity of the field distribution is diminished with increasing ratio L/λ_0 (L is the furnace dimension and λ_0 the free space wavelength). Thus, mm-wave power sources initially developed for plasma heating applications found their way to the processing of new materials that are not feasible at lower frequency (f). High-temperature materials processing research at frequencies as high as 28–83 GHz is carried out in laboratories in the USA, Germany, Japan and Russia [4]. The commercially available gyrotrons for this purpose are described in periodic state-of-the-art reviews [2].

10.5.1 Experimental Setup

At the Forschungszentrum Karlsruhe a Russian compact gyrotron oscillator technological system (GOTS) developed at the Institute of Applied Physics in Nizhny Novgorod has been installed and improved. The system comprises the following parts (as shown in Fig. 10.7): gyrotron, oil cooled electromagnet system, quasi-optical and mode converting transmission line, microwave furnace (applicator), temperature data acquisition and PC-based control systems.

The gyrotron is operated in the CW regime with smoothly controlled output power up to 15 kW at a frequency of 30 GHz. The efficiency of the gyrotron working in the TE_{02} cavity mode at the second harmonic of the

cyclotron resonance is about 25% in a rather broad range of the energizing parameters (beam voltage $\leq$ 25 kV and beam current $\leq$ 2 A). Since the frequency of radiation generated by the gyrotron is related to the magnitude of the static magnetic cavity field by the equation B (T)$\approx 0.0375f$ (GHz)$/n$, where n is the number of the harmonic, the operation at $n = 2$ implies a nearly four fold decrease in power consumed by the main solenoid. In fact, for a gyrotron operating at a frequency of 30 GHz, this leads to a decrease in power consumption of the magnet from about 50 kW for $n = 1$ to 13 kW for $n = 2$, and this is a major contribution to the overall efficiency of the GOTS. The radiation generated by the gyrotron passes through the output window and a mode converting quasi-optical transmission line (mode converting output horn and two specially designed metal mirrors) to the microwave furnace. The overall transmission efficiency is over 90 %. By using a quasi-optical transmission line it is possible to reduce the influence of the radiation reflected back from the furnace on the operation of the gyrotron to an admissible level.

A high ratio $L/\lambda_0 (\approx 50)$ of the applicator and operation of an appropriate wavebeam scatterer are an essential prerequisite for homogeneous heating of materials. Having been fed into the kiln (diameter 50 cm, height 60 cm), the radiation fills rather uniformly the whole volume of the furnace, due to numerous reflections of the electromagnetic waves from its walls and superposition of their fields. The furnace applicator represents a highly oversized untuned cavity. The furnace is vacuum proofed and allows to process materials within a pressure range of $10^{-3} - 2$ bar. The microwave input window has a diameter of 80 mm and consists of an edge cooled boron nitride disk. The numerous inlets for the thermocouple signal measurements as well as a port for a pyrometer probe and a dilatometer are placed at the large diameter flange of the furnace and provide a broad capability for sample temperature monitoring.

Precise knowledge of the electromagnetic field distribution inside an empty or loaded furnace is a significant question for optimizing geometries and material processing parameters. In general the stationary electromagnetic field energy deposited inside the material processed in the furnace, is of special interest. Interference effects can lead to spatial variations of the stationary energy distribution of the electromagnetic field. The knowledge of these hotter and colder domains is very important for controlled processing of dielectric materials. These were the motivations for developing a simulation code solving Maxwell's equations by using an optical approach for tracing wavefronts in order to build up the resulting stationary field distribution. The MiRa/THESIS3D-Code package for applicator design and modelling of mm-wave materials processing also contains a numerical code solving the nonlinear heat transfer problem for a self-consistent simulation of the sintering process [323].

10.5.2 Experimental Results

Up to now, the GOTS has been used mainly for ceramic sintering and joining of ceramic parts. The large penetration depth of microwaves compared to that of thermal radiation used in conventional heating systems, permits a homogeneous volumetric heating of the samples. That is one of the most advantageous features of microwave sintering and leads to considerably reduced processing times. Due to microwave induced diffusion processes sintering temperatures are significantly lower. Al_2O_3 for example has been sintered to more than 98% theoretical density (TD) already at 1450°C and PZT piezoceramics were densified at 950°C compared to conventional sintering temperatures of 1625°C for Al_2O_3 and about 1200°C for PZT, respectively. Undesired evaporation of PbO during the PZT sintering process is notably reduced leading to improved piezoelectric properties. The microstructure of ceramics is controllable by the variation of the processing time. At short processing times the grain growth is very small so that even nanocrystalline powders can be sintered without losing a final nanoscale fine structure. A few examples of the advantages of mm-wave sintering of nanocrystalline cermics and piezoarrays are shown here.

Figure 10.8 shows SEM micrographs of mm–sintered nanocrystalline cermics (namely, Al_2O_3, TiO_2, ZrO_2) [58]. These nano powders are produced by a wire blasting technique with particle sizes in the range of 25–40 nm. All powders show a rather broad grain size distribution from 2 nm to more than 100 nm with a maximum around 25 nm. It could be demonstrated that the mm-wave sintering technique leads to a better densification of these nanostructured oxide greens without the occurrence of significant grain growth which is a problem in conventional sintering of such specimens. Reasonable densities of about 94% TD and average grain sizes of about 100–150 nm have been obtained (see Fig. 10.8). Here, the gyrotron was switched off immediately after reaching the sintering temperature. No holding time was needed.

Another example is the sintering of lead–zirconate–titanate (PZT) arrays [58]. Lead oxide (PbO) has a high vapor pressure and tends to evaporate during the sintering process. Shortening of process temperature and hold time will mitigate this problem. Initial experiments suggest that by using mm-waves, the sintering temperature of the conventional process can be reduced from 1200° C to 1100° C and the dwelling time from 60 min to only 10 min, in order to get similar densities. This leads to a reduction of PbO losses and significantly influences the grain growth during the sintering process. A comparison of the morphologies of conventionally and mm-wave sintered PZT piezoarrays are shown in Fig. 10.9. Figure 10.9a shows a micrograph of such a PZT piezoarray. As can be seen from Figs. 10.9b and c, using millimeter waves, the average grain size clearly lies in the submicrometer range compared to an average grain size of more than 1 μm after conventional sintering.

Advantages of ultrafine microstructures for synthesis, processing and property modifications of advanced ceramic materials have long been sus-
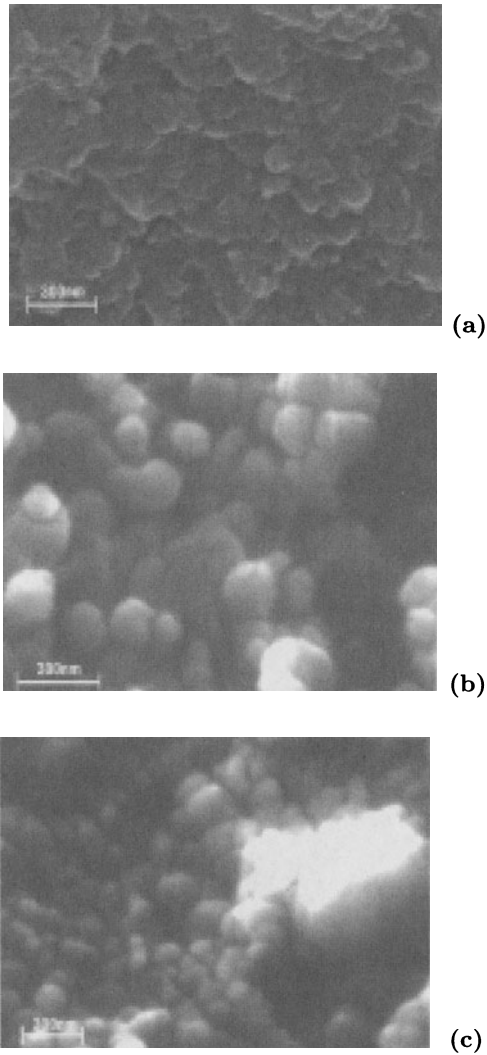
(a)

(b)

(c)

Fig. 10.8. SEM micrographs of mm-wave sintered nanocrystalline ceramics. Here, **(a)** Al_2O_3: sintering temperature $= 1150°C$, heating rate $= 30°/\text{min}$, $\rho_{green} = 2.70\,\text{g/cm}^3$ (74% TD), $\rho_{sintered} = 3.70\,\text{g/cm}^3$ (93% TD); **(b)** TiO_2: sintering temperature $= 950°C$, heating rate $= 50°/\text{min}$, $\rho_{green} = 3.35\,\text{g/cm}^3$ (85% TD), $\rho_{sintered} = 4.57\,\text{g/cm}^3$ (93% TD); **(c)** ZrO_2: sintering temperature $= 1150°C$, heating rate $= 50°/\text{min}$, $\rho_{green} = 4.8\,\text{g/cm}^3$ (82% TD), $\rho_{sintered} = 5.5\,\text{g/cm}^3$ (94.5% TD) [58]

pected. Properties of nanostructured materials are directly related to their unusual microstructure that features extremely small grains and a large fraction of highly disordered interfaces. Research is not only motivated by basic
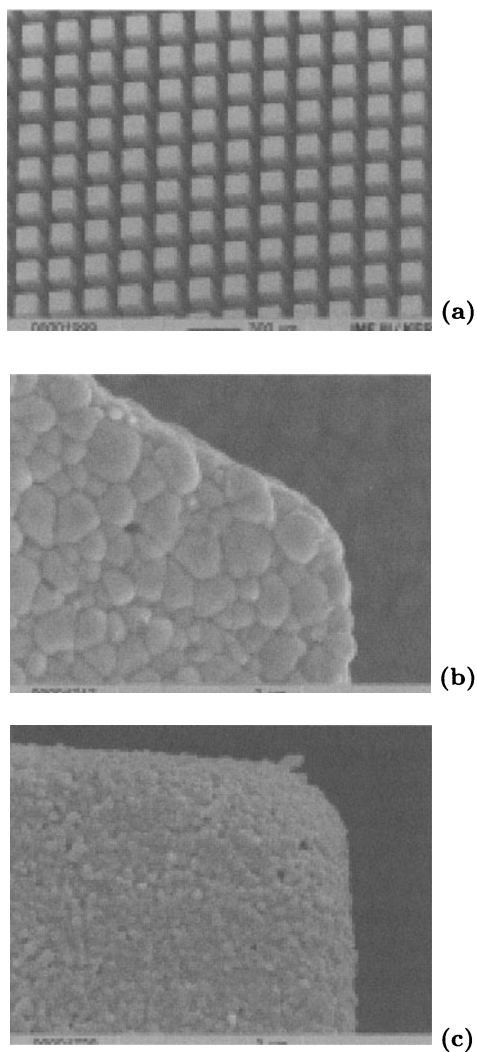
Fig. 10.9. Comparison of morphologies of conventionally and mm-wave sintered PZT piezoarrays. Here, (**a**) part of a PZT piezoarray, (**b**) conventionally sintered 1200°, 60 min, and (**c**) mm-wave sintered 1100°, 10 min [58]

science aspects but also by the expectation that novel properties will lead to new technological applications. For example sintering and creep behaviour are significantly changed by the reduction of the particle size to the nanometer range. The equations for densification rate $d\rho/dt$ and strain rate $d\varepsilon/dt$ show a strong dependence on the grain size d, that is, $(1/d)^q$, with q in the

Table 10.1. α-Al_2O_3 densities after sintering with different techniques

Sintering parameters		green density in g/cm^3 (% TD)		
temperature °C	heating rates °C/min	2.5 (68)	2.7 (74)	2.9 (79)
1300	2	3.32 (83)	3.16 (79)	3.66 (92)
1300	5	3.22 (81)	3.62 (91)	3.76 (94)
1300	10	3.29 (82)	3.60 (90)	3.73 (93)
1300	fast firing	–	3.56 (89)	3.67 (92)
1150	30 (with mm-waves)	3.57 (89)	3.70 (93)	–

range of 2 to 4. Thus it becomes possible to tailor the mechanical properties by controlled grain growth.

The phase transformation and densification behaviour under high power mm-wave radiation of the 30 GHz gyrotron and during fast conventional sintering of nanocrystalline $\gamma - Al_2O_3$ powder have been investigated and compared [324]. The powder used for compacts was synthesized from aluminum metal by using the exploding wire technique in an oxidizing atmosphere. The particle size distribution of this powder has a maximum at about 20 nm. A magnetic pulse technique was used for the compression of samples up to 80% of the TD. Both mm-wave sintering and fast firing in a conventional electrical resistance furnace permit the densification and a complete phase transformation into $\alpha - Al_2O_3$ already at a temperature of approximately 1150°C. The average grain size of the sintered ceramic is in the range of 50 to 100 nm. With mm-waves densification starts at about 50°C lower temperatures compared to conventional techniques and higher final densities were obtained even at 150°C lower temperatures (see Table 10.1).

Figure 10.10 shows typical kinetic curves of densification during sintering experiments with linear heating up to 1300°C. During conventional sintering the linear shrinkage was optically measured. It has been used, together with the green density, to deduce the density as a function of temperature. These data are shown in Fig. 10.10 together with the densities of several mm-wave sintered samples of similar green density dependent on final sintering temperatures. This explains the more pronounced scattering of mm-wave data than of conventional sintering data. Millimeter-wave sintering of samples with green densities of 2.5g/cm^3 leads to a final density of 3.57g/cm^3 already at 1150°C, while the maximum density with conventional sintering techniques to 1300°C was 3.32g/cm^3. For samples with green densities of 2.7g/cm^3 the obtained final densities were 3.7g/cm^3 and 3.62g/cm^3 for mm-wave and conventional sintering, respectively.

Sintering with mm-wave irradiation leads to an enhancement of the densification process, as can be seen from Fig. 10.10. With mm-waves the "active"
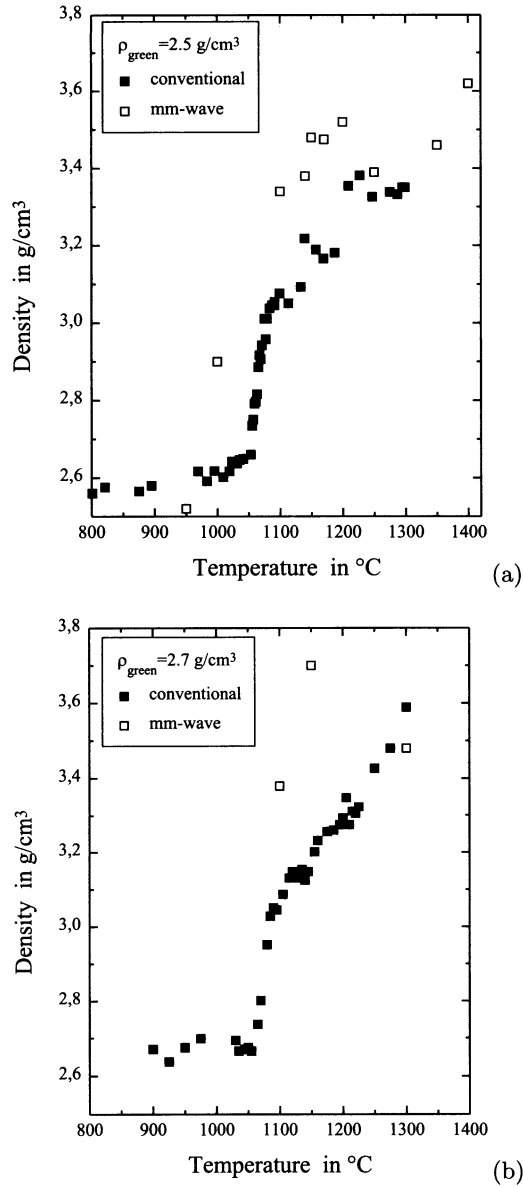
Fig. 10.10. Comparison of linear conventional heating and mm-heating of alumina samples with green densities of (a) 2.5 and (b) $2.7\,\mathrm{g/cm^3}$, respectively [5]

stage of sintering starts at temperatures approximately 50°C lower than for conventional sintering. An increase of the sintering temperature $>$ 1200° C gives no essential increase of final densities but a distinct increase of grain

size to average values of about 200 nm at 1400°C. In the initial stage of sintering at 1100°C small grain growth to an average size of about 50 nm and the beginning of the phase transformation to $\alpha - \text{Al}_2\text{O}_3$ can be observed. At 1150°C the phase transformation is completed. It is accompanied by further grain growth to values close to 100 nm and a neck linking of the grains. If one compares the microstructure of conventionally fast fired samples with mm-wave sintered samples, no specific difference can be seen. Coarsening of grains is slightly more pronounced in the fast-fired sample compared with the mm-wave sintered one. But there is a clear difference in the final density which is about 7 % higher for the mm-wave sintered sample already at 100° C lower temperatures.

10.6 Millimeter-Wavelength Radar

The development of novel high power microwave sources allows a number of new applications to radar [4]. The maximal range R_{max} of radar systems in given by the radar equation

$$R_{\max}^4 = \frac{P_\tau A^2 \sigma}{4\pi \lambda_0^2 P_{\min}} , \tag{10.1}$$

where P_τ is the maximum pulse power, τ is pulse duration, A the effective area of the antenna, σ the radar cross-section (RCS) of the target and $P_{\min} = kT/\tau$ the minimum detectable power of the system. The temperature is assumed to be 300 K, so kT is about $4 \cdot 10^{-21}$ W/Hz (see Table 10.2). Thus, reduction of the wavelength λ_0 results in a larger R_{max} and leads to improved angular resolution. The recent development of gyrotrons and gyroklystrons can enhance the average radiated power in the mm-wave regime by several orders of magnitude. Suitable frequencies for mm-wavelength radar systems are 35 GHz (8.6 mm), 94 GHz (3.2 mm) and 140 GHz (2.1 mm) due to the existence of absorption minima of the atmosphere at these frequencies ("mm-wave windows" of the atmosphere).

Most of the novel high power microwave sources are free running oscillators. For at least two reasons, however, amplifiers are preferable for radar applications. First, for coherent combining of the power of a number of different microwave sources into a conventional or phased array antenna, there is no choice but to use amplifiers, or at last phase controlled (locked) oscillators. The use of an amplifier also makes the processing of the returned signal easier. However, it is also possible to use free running oscillators for many applications. For instance, if the radar signal is purely sinusoidal with randomly varying phase from pulse to pulse, one can sample the phase of each transmitted signal and correct the returned signal for the transmitted phase, the classic coherent-on-receive method for signal processing. Here we discuss three new radar configurations made possible by new high power gyrotrons,

Table 10.2. Schematic analysis of the Radar Equation

Maximum Range	$R_{\mathrm{max}}^4 = K_{\mathrm{trsm}} K_{\mathrm{eds}} K_{\mathrm{rcv}}$
$K_{\mathrm{trsm}} = \frac{P_\tau}{kT\Delta f}$	P_τ transmitted power
	$kT = 4 \cdot 10^{-21}$ W/Hz
	Δf frequency band
	optimum filtration:
	$\tau\Delta f \sim 1$
	$K_{trsm} = \frac{P_\tau \tau}{kT}$
$K_{\mathrm{eds}} = \frac{\sigma A^2}{4\pi\lambda^2}$	σ target cross section
	$A = \frac{\pi}{4}\Phi_a^2$ antenna area
$K_{\mathrm{rcv}} = \frac{1}{F_n\left(\frac{S_0}{N_0}\right)L_s}$	$\frac{S_0}{N_0} = \left(\frac{signal}{noise}\right)_{\min}$
	F_n noise factor
	L_s losses

gyroklystrons and relativistic backward wave oscillators (BWOs), namely active meteorology (monitoring of the atmosphere), monitoring of space debris and high power nanosecond radar.

10.6.1 Active Millimeter Wave Meteorology-Cloud Radar

High power mm-wave sources open the possibility of a variety of active measurements of the atmosphere. At a frequency of 94 GHz the loss for very humid conditions at sea level is about 1 dB/km. By increasing the average power from 4 W to 4 kW, the additional propagation distance is increased by 15 km (30 km round trip). Millimeter waves have the advantage that they propagate well through particulates, but scatter off them strongly enough to give easily detectable signals. The radar cross-section σ of aerosols is proportional to D^6/λ_0^4 where typically $D = 10$–40 mm. Thus a mm-wave radar could resolve multiple cloud layers (structure and extension) and could give information about their humidity, dynamics and turbulence. Water clouds, on the other hand, are optically thick for laser radiation.

One of the most promising applications of fixed-frequency gyrotrons as atmospheric sensors is cloud radar which has potential applications both as ground and air based systems for fundamental study of cloud dynamics. Space based 94 GHz radar could give real time worldwide maps of the altitude, thickness and flow fields of clouds. Several properties of clouds give rise to radar returns:

– clear air turbulence (scatters preferentially low frequency radiation ≤ 10 GHz)
– raindrops, ice crystals, snow flakes
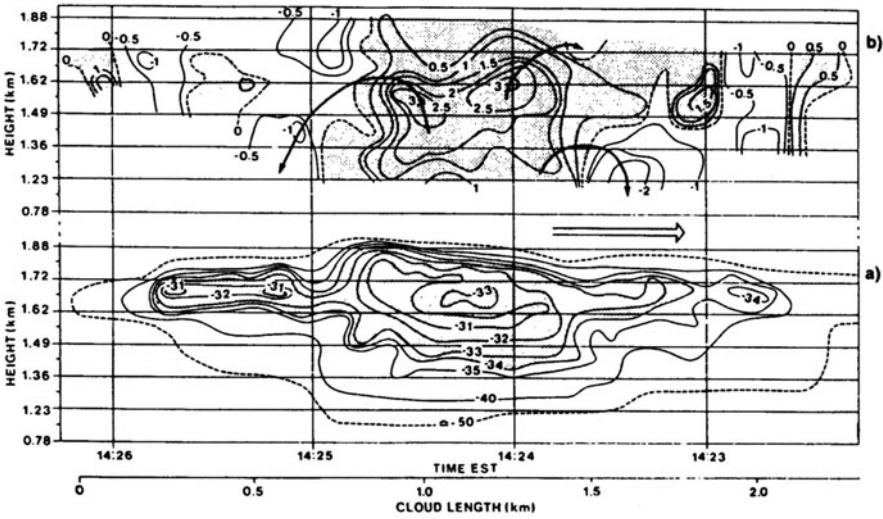
Fig. 10.11. (a) Reflectivity and (b) Doppler velocity of a small cumulus cloud [325]

– aerosols (which define the cloud, $\leq 100\,\text{aerosols/cm}^3$).

We have:

– Rayleigh regime of RCS: $D < \lambda_0/4$

$$\sigma = \frac{\pi^2 \left|K^2\right| D^6}{\lambda_0^4}\,. \tag{10.2}$$

– $K = (m^2 - 1)/(m^2 + 2)$ with m = index of refraction. For water at mm-wavelengths: $|K|^2 \approx 0.8$.
– Radar reflectance: $\eta = n\sigma$ (cross-section per unit volume) where n = density of droplets per unit volume.
– Radar range equation: $P_r = \frac{P_\tau h A \eta}{4\pi R^2}$ where h is the range resolution distance and P_r the received power.

Fig. 10.11 shows a 94 GHz radar image of a cloud taken from L'Hermitte [325]. An Extended Interaction Oscillator (EIO) with 1 kW pulse power and 4 W average power (PRF = 10 kHz) was used as the mm-wave source. With a range of 2 km, a resolution distance $h = 60$ m and an effective aperture of $4 \cdot 10^3$ cm^2 the received power was 10^{-13} W. Since L'Hermitte's receiver had an actual noise of about $5 \cdot 10^{-13}$ W, he had to integrate for 3s ($3 \cdot 10^4$ pulses).

A 4 kW average power system using a gyrotron would overcome an additional 30 dB of atmospheric absorption (compared to L'Hermitte) and allow observation much lower in the thunderstorm. A 3–dimensional image of the cloud could be formed and the range cell could be reduced to 10 m (10 MHz–BW). The greater range would also permit one to image clouds that are not directly overhead.

10.6.2 Space Debris Monitoring Radar

Manmade space debris is becoming a problem for spacecraft and space stations. A centimetre size particle, such as a bolt, colliding with a spacecraft would almost certainly have catastrophic results. So it is necessary to detect the debris, to track it and to examine its parameters. Spacecrafts and space stations must be hardened to survive collisions with debris under the size of 1 cm and will have to be maneuverable enough to avoid the large pieces. To avoid the Rayleigh case, when the effective RCS proves to be less than the physical one, the operating frequency could be in the mm-wave band. On the other hand, from the atmospheric absorption viewpoint, among the mm-wavelengths the most reliable are those close to 8 mm (35 GHz). To detect a 1 cm object at a range of 1000 km (altitude = 700 km, proposed for the "Freedom" Space station) both very high power and antenna gain are needed. If we assume that the minimum SNR necessary for reliable detection is 10 dB, that F_n is 10 dB and L_s is 15 dB, and the bandwidth is 10 kHz (100 ms pulse and 15 km range resolution), the radar equation (10.1) forces one into a very difficult region of parameter space:

$$P_\tau G^2 = 2 \cdot 10^{22} W \,. \tag{10.3}$$

Let us consider a tracking antenna with a diameter of 20 m. At a frequency of 35 GHz, its gain $G = \pi^2 D^2/\lambda^2$ is about 3×10^7. Thus, the required radiated power to detect the centimeter size piece of space debris is about 20 MW. This is larger than the power of any single 35 GHz microwave tube with 100 μs pulse length.

Since 35 GHz gyro-klystrons with an output power of 700 kW have been developed by Russian industry (see [2]), these sources can be coherently combined and fed into a large phased-array antenna. Since the motivation for an amplifier is coherent power combining and not simpler data processing, an amplifier is the only choice for the system. It would take about 30 such gyroklystrons to provide enough power for the system. A single gyroklystron, or possibly gyrotron, would provide enough power to detect a piece of debris with a RCS of about 30 cm². With a combination of mechanical and electronic steering, the radar could both scan and revisit targets.

10.6.3 High Power Nanosecond Radar

In conventional radars, range resolution is obtained with the use of a long pulse chirped in frequency and then compressed by the receiver, for instance, with the use of a matched filter. In almost every case, while the range resolution is $c/\Delta f$, there are temporal sidelobes that mix up the signals from nearby range cells. This problem can be especially serious if one is attempting to resolve a low-cross-section target in close proximity to a high-cross-section target, such as a buoy near a ship. Furthermore, pulsed Doppler radars typically have a problem with blind speed when trying to resolve the velocity

Table 10.3. Parameters of high power nanosecond radar system [4]

Microwave Generator	
Frequency	10 GHz
Radiated Pulse Power	0.35 GW
Pulse Duration	7 ns
Repetition Rate	150 Hz
Amplitude Instability	1%
Frequency Instability	0.1%
Resource	10^7 pulses
Antenna	
Radiation Reception Beam Width	3.5°
Receiver	
Frequency Band	210 MHz
Noise Factor	7 dB
A numerical signal processing sub-system is used to perform the moving target indication (MTI)	

of a target. Finally, for a low peak power system, with a not too large ratio of interpulse separation to pulse time, the dead time can also become an operating constraint.

One possible way to get around some of these difficulties is to use a very short pulse high power radar without pulse compression using a relativistic BWO. The features of such a system, developed at the IAP and for LHCE in Russia are summarized in Table 10.3.

The radar target was a small aircraft, which had a total RCS of about a square meter. The range from the target to the radar device was 50 km. The typical received radar signals are shown in Fig. 10.12 after the signals were processed so as to reduce the stationary clutter by 28 dB.

This nanosecond radar system has demonstrated:

- Long target detection range: A helicopter of $2\,m^2$ RCS was reliably tracked up to 105 km over a wood covered terrain (theoretical range = 150 km).
- High range resolution (important for target identification): Sample reflectors as well as details of the helicopter and boats have been seen separately, if distanced by more than 1 m.
- Effective moving target indication (MTI) performance: MTI algorithms provide up to 30 dB suppression of echoes from immovable targets and 10–20 dB suppression of echoes from the wind surged vegetation.

(a)

(b)

(c)

(d)
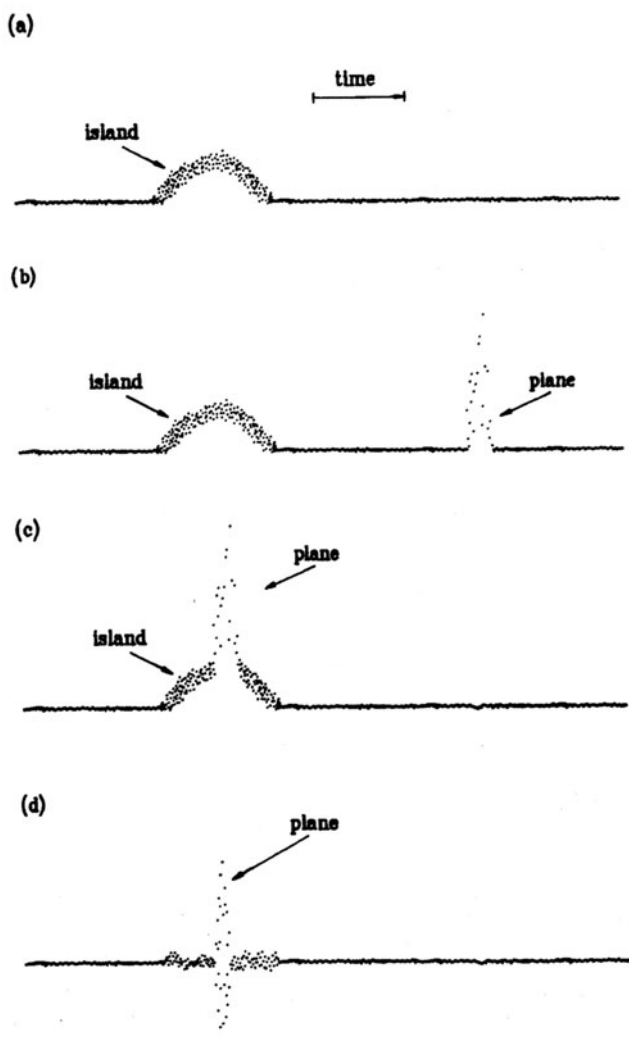
Fig. 10.12a–d. Radar return signals showing a moving airplane and a stationary island. In (**d**) the moving target indication (MTI) system was employed [4]

10.7 RF-Drivers for TeV Linear Colliders

For several decades, the microwave amplifiers of choice for driving very high energy linear electron and positron accelerators have been the multi-cavity klystrons [4]. An example of advanced present day capability is the klystron amplifier used to drive the Stanford Linear Collider (SLC) (Fig. 10.13).
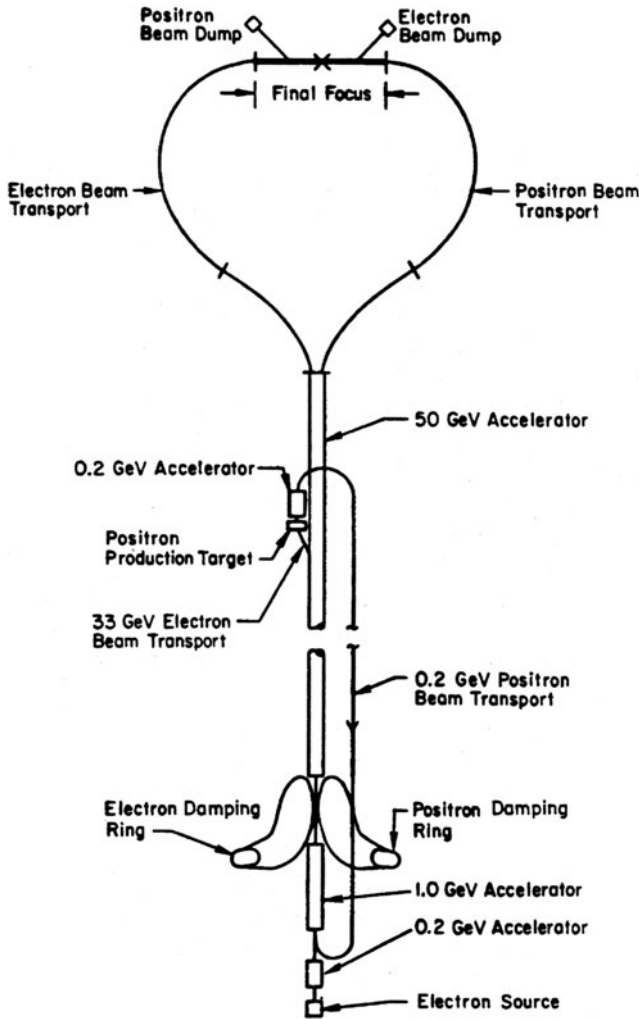
Fig. 10.13. Schematic diagram of the Stanford Linear Collider (SLC) [4]

The SLC klystrons operate in the S–band at 2.865 GHz producing output pulses with peak power $P_\tau = 65$ MW with $\tau = 3.5$ ms pulse duration and 45 % efficiency. The voltage of the modulator powering the tubes is 350 kV and the microwave output pulse is compressed by a factor of three before being applied to the accelerator cavities. Hundreds of SLC klystrons are used so that phase coherence is a parameter of great importance. In considering microwave amplifier requirements for the next generation of linear colliders, which should be shorter than 10 km, it became clear that higher frequency and higher peak power (high accelerating gradient) will be needed while the modulator voltage should not be increased too much and efficiency should be

at least 50 %. The feasibility of future electron-positron colliders operating at energies $\geq$ 1 TeV will depend on both operating efficiency and the cost of the microwave amplifiers that can be developed to drive the collider. To zeroth order, the required number of amplifiers depends inversely on the figure of merit parameter $A = P_\tau \tau / \lambda_0^2$. Thus, one goal of amplifier research is to maximize A while keeping other parameters within bounds so as not to excessively increase the cost of either the individual amplifier system nor the collider structure (for instance, amplifier voltage $V \leq$ 500 kV, wavelength $\lambda_0 \geq$ 1 cm).

The 2.865 GHz klystron amplifiers that drive the 100–GeV SLC have $A = 2.1 \times 10^4$ Ws/m^2. This value of A has been surpassed by about a factor of 5 by new 11 to 14 GHz klystrons. X–band klystron development programs are underway at the Stanford Linear Accelerator Center (SLAC) in the US and at the KEK Accelerator Laboratory in Japan. A 14 GHz klystron development program is completed at the Budker Institute for Nuclear Physics (BINP) in Russia with the aim of achieving output power near 100 MW in 1 μs pulses. These klystron development programs will probably result in producing amplifiers that are suitable for linear colliders in the energy range up to $\geq$ 1 TeV. For multi–TeV linear colliders that might be developed at some time farther into the future, RF frequency $\geq$ 17 GHz has been identified as a likely requirement. For such colliders, klystrons may no longer be an appropriate amplifier choice because of inherent limitations when simultaneously handling high power and high frequencies in klystron circuits (cavity gaps are much smaller than the wavelength and drift tubes between cavities are cut off to the fundamental mode).

Because of these limitations gyroklystrons have been explored for application to advanced colliders. Gyro-amplifiers have demonstrated values of $A = 11 \times 10^4$ Ws/m^2, which compares favourably with the best values of A achieved by klystrons. Peak powers in excess of 30 MW with pulse durations of 0.8 μs have been achieved at 19.76 GHz in the TE$_{02}$ mode via a two cavity second harmonic gyroklystron with a first harmonic drive cavity. The peak efficiency and gain were 28 % and 27 dB, respectively. At present, there is ongoing research on a new three cavity second harmonic coaxial gyroklystron, driven by a 500 kV, 720 A beam, which is predicted to have an output power of 100 MW at 17.136 GHz with an electronic efficiency in excess of 40%. With the use of a depressed collector achievable overall amplifier efficiency, which is of very great importance in the collider application, could be in the range of 50–65 %. A state-of-the-art comparison of klystrons and gyroklystrons for supercolliders is given in reference [2].

References

1. Bradford L. Smith and Michel–Henri Carpentier, Eds.: *The microwave engineering handbook.* Chapman & Hall, London, New York (1993)
2. Thumm, M. : *State-of-the-art of high power gyro-devices and free electron masers update 2002.* FZK internal report, (2003)
3. Gaponov, A.V., Petelin, M.I. and Yulpatov, V.K. : *The induced radiation of excited classical oscillators and its use in high frequency electronics.* Izv. VUZ Radiofiz. **10**, 1414 (also in Radiophys. Quantum Electr., **10**, 794) (1967)
4. Gaponov–Grekhov, A.V., Granatstein, V.L. : *Application of high-power microwaves.* Artech House, Boston, London (1994)
5. Thumm, M. : *Applications of high-power microwave devices.* In "Generation and Application of High Power Microwaves," Ed. R.A. Cairns and A.D.R. Phelps, Institute of Physics Publishing, Bristol and Philadelphia, 305(1997).
6. Thumm M. : *Novel applications of millimeter and submillimeter wave gyrodevices.* Int. J. Infrared and Millimeter Waves, **22**, 377(2001)
7. Flyagin, V.A., Gaponov, A.V., Petelin, M.I., Yulpatov, V.K. : *The gyrotron.* IEEE Trans. Microwave Theory and Techniques, **25**, 514(1977)
8. Andronov, A.A., Flyagin, V.A., et al. : *The gyrotron: high power sources of millimetre and submillimetre waves.* Infrared Physics, **18**, 385(1978)
9. Petelin, M.I. : *Physics of advanced gyrotrons.* Plasma Phys. and Contr. Nucl. Fusion, **35**, Supplement B, 343(1993)
10. Flyagin, V.A., Goldenberg, A.L., Nusinovich, G.S. : *Powerful gyrotrons.* In "Infrared and Millimeter Waves," vol. **11**, Ed. K.J. Button, Academic Press, New York, 179(1984)
11. Flyagin, V.A., Nusinovich, G.S.: *Gyrotron oscillators.* Proceedings of the Institute of Electrical and Electronics Engineers, **76**, 644 (1988) and *Powerful gyrotrons for thermonuclear research* in "Infrared and Millimeter Waves," vol. **13**, Ed. K.J. Button, Academic Press, New York, 1(1985)
12. Felch, K., Huey, H., Jory, H.: *Gyrotrons for ECH application.* J. Fusion Energy, **9**, 59(1990)
13. Goldenberg, A.L., Denisov, G.G., et al. : *Cyclotron resonance masers: state of the art.* Radiophys. and Quantum Electronics, **39**, 423(1996)
14. Gold, S.H., Nusinovich, G.S.: *Review of high-power microwave source research.* Rev. Sci. Instru., **68**, 3945(1997)
15. Granatstein, V.L., Levush, B., Danly, B.G., Parker, R.K.: *A quarter century of gyrotron research and development.* IEEE Trans. Plasma Science, **25**, 1322(1997)
16. Petelin, M.I., 1999, *One century of cyclotron radiation.* IEEE Trans. Plasma Science, **27**, 294(1999)

17. Felch, K.L., Danly, B.G., et al.: *Characteristics and applications of fast-wave gyrodevices.* Proc. IEEE, **87**, 752(1999)
18. Luce, T.C.: *Applications of high-power millimeter waves in fusion energy research.* IEEE Trans. Plasma Science, **30**, 734(2002)
19. Imai, T., Kobayashi, N., et al.: *ITER R&D: auxiliary systems: electron cyclotron heating and current drive system.* Fusion Engineering and Design, **55**, 281(2001)
20. Zohm, H., Gantenbein, G., et al.: *Experiments on neoclassical tearing mode stabilization by ECCD in ASDEX Upgrade.* Nuclear Fusion, **39**, 577(1999)
21. Gantenbein, G., Zohm, et al.: *Complete suppression of neoclassical tearing modes with current drive at the electron–cyclotron–resonance frequency in AS-DEX Upgrade tokamak.* Phys. Rev. Lett., **85**, 1242(2000)
22. Zohm, H., Gantenbein, G., et al.: *The physics of neoclassical tearing modes and their stabilization by ECCD in ASDEX Upgrade.* Nuclear Fusion, **41**, 197(2001)
23. Zohm, H., Gantenbein, G., et al.: *Neoclassical tearing modes and their stabilization by electron cyclotron current drive in ASDEX Upgrade.* Physics of Plasmas, **8**, 2009(2001)
24. Erckmann, V., Kasparek, W., et al.: *Electron cyclotron resonance heating transmission line and launching system for the Wendelstein VII–AS stellarator.* Fusion Technology, **17**, 76(1990)
25. Erckmann, V., Dammertz, G., et al.: *ECRH and ECCD with high power gyrotrons at the stellarators W7–AS and W7–X.* IEEE Trans. Plasma Science, **27**, 538(1999)
26. Kasparek, W., Erckmann, V., et al.: *ECRH and ECCD for the stellarator W7–X.* Proc. 4th Int. Workshop on Strong Microwaves in Plasmas, Nizhny Novgorod, Russia (1999)
27. Erckmann, V., Laqua, H.P., et al.: *Electron cyclotron resonance heating and EC–current drive experiments at W7–AS, status at W7–X.* Fusion Engineering and Design, **53**, 365(2001)
28. Ohkubo, K., Kubo, S., et al.: *Electron cyclotron plasma production and heating on LHD: system and its application.* Proc. 4th Int. Workshop on Strong Microwaves in Plasmas, Nizhny Novgorod, Russia (1999)
29. Idei, H., Kubo, S., et al.: *Electron cyclotron heating scenario and experimental results in LHD.* Fusion Engineering and Design, **53**, 329(2001)
30. Thumm, M.: *Progress in the development of high-power millimeter and submillimeter wave gyrotrons and of free electron masers.* Archiv für Elektrotechnik, **77**, 51(1994)
31. Thumm, M.: *Advanced electron cyclotron heating systems for next step fusion experiments.* Fusion Engineering and Design, **30**, 139(1995)
32. Thumm, M.: *Recent development of high power gyrotrons and windows for EC wave applications.* Proc. 12th Topical Conf. on Radio Frequency Power in Plasmas, Savannah, Georgia, USA, AIP Conference Proceedings, **403**, 183(1997) Thumm, M.: *Present developments and status of electron sources for high power gyrotron tubes and free electron masers.* Applied Surface Science, **111**, 106(1997)
33. Thumm, M.: *State-of-the-art and recent developments of high-power gyrotron oscillators.* Proc. Radio Frequency Workshop (RF 98), High Energy Density Microwaves, Pajaro Dunes, California, USA, AIP Conference Proceedings, **474**, 146(1998)

34. Thumm, M., Kasparek, W.: *Recent advanced technology in electron cyclotron heating systems*. Fusion Engineering and Design, **26**, 291(1995)
   Thumm, M.: *High power mode conversion for linearly polarized* HE_{11} *hybrid mode output*. Int. J. Electronics, **61**, 1135(1986)

35. Henle, W., Jacobs, A., et al.: *Conceptual study of multi–megawatt millimeter wave transmission and antenna systems for electron cyclotron wave applications in NET/ITER*. Fusion Technology 1990, Eds. B.E. Keen, M. Huguet, R. Hemsworth. Elsevier Science Publishers B.V., 238(1991)

36. Alberti, S., Tran, M.Q., et al.: *Experimental measurements on a 100 GHz frequency tunable quasi-optical gyrotron*. Phys. Fluids, **B2**, 1654(1990)

37. Hogge, J.P., Tran, T.M., Paris, P.J., Tran, M.Q.: *Operation of a quasi-optical gyrotron with a gaussian output coupler*. Phys. Plasmas, **3**, 3492(1996)

38. Kreischer, K.E. Temkin, R.J.: *Single-mode operation of a high-power, step-tunable gyrotron*. Phys. Rev. Lett., **59**, 547(1987)

39. Kurbatov, V.I., Malygin, S.A., Vasilyev, E.G.: *Commercial gyrotrons for thermonuclear investigations*. Proc. Int. Workshop on Strong Microwaves in Plasmas, Suzdal, Inst. of Applied Physics, Nizhny Novgorod, Russia(1990)

40. Bogdanov, S.D., Kurbatov, V.I., et al.: *Industrial gyrotrons development in Salut*. Proc. 2nd Int. Workshop on Strong Microwaves in Plasmas, Moscow – Nizhny Novgorod (1993)
   Zapevalov, V.E., Malygin, S.A., Pavelyev, V.G., Tsimring, Sh.E.: *Coupled resonator gyrotrons with mode conversion*. Radiophys. Quantum Electron., **27**, 846 (1984)

41. Braz, O., Dammertz, G., Kuntze, M., Thumm, M.: *D–band frequency step-tuning of a 1 MW gyrotron using a Brewster output window*. Int. J. Infrared and Millimeter Waves, **18**, 1465 (1997)

42. Braz, O., Dammertz, G., et al.: *Frequency step-tuned operation of a 1 MW, D-band gyrotron using a Brewster output window*. Proc. 8th ITG–Conference on Displays and Vacuum Electronics, Garmisch–Partenkirchen, ITG–Fachbericht **150**, 299(1998)

43. Thumm, M., Borie, E., et al.: *1.6 MW frequency step-tunable D–band gyrotron*. Proc. 4th Int. Workshop on Strong Microwaves in Plasmas, Nizhny Novgorod, Russia (1999)
   Dammertz, G., Dumbrajs, O., et al.: *Frequency-step-tunable high-power gyrotrons for plasma physics applications*. J. Comm. Tech. and Electronics, **45**, S60(2000)
   Dumbrajs, O., Nusinovich, G.S.: *Theory of a frequency-step-tunable gyrotron for optimum plasma ECRH*. IEEE Trans. Plasma Science, **20**, 452(1992)

44. Thumm, M., Arnold, A., et al.: *Frequency step-tunable (114–170 GHz) megawatt gyrotrons for plasma physics applications*. Fusion Engineering and Design, **53**, 407(2001)

45. Koppenburg, K., Dammertz, G., Kuntze, M., Piosczyk, B., Thumm, M.: *Fast frequency-step-tunable high-power gyrotron with hybrid-magnet-system*. IEEE Trans. Electron Devices, **48**, 101(2001)

46. Zapevalov, V.E., Bogdashov, A.A., et al.: *Optimization of the frequency step tunable 105–170 GHz 1 MW gyrotron prototype*. Proc. 27th Int. Conf. on Infrared and Millimeter Waves, San Diego, USA, 1(2002)

47. Golubev, S.V., Razin, S.V., et al.: *Sources of soft X-rays and multicharged ions based on ECR discharge in heavy gases sustained by high-power gyrotron*

radiation. Proc. 4th Int. Workshop on Strong Microwaves in Plasmas, Nizhny Novgorod, Russia (1999)

48. Golubev, S.V., Luchin, V.I., et al.: *Mirror-trapped plasma heated by powerful millimeter wave radiation as an ECR source of soft X-rays.* Proc. 4th Int. Workshop on Strong Microwaves in Plasmas, Nizhny Novgorod, Russia (2000)

49. Flyagin, V.A., Kuftin, A.N., et al.: *Gyrotrons for electron cyclotron heating and active plasma diagnostics.* Proc. Joint IAEA Techn. Committee Meeting on ECE and ECRH (EC-7 Joint Workshop), Hefei, P.R. China, 355(1989)

50. Flyagin, V.A., Luchinin, A.G., Nusinovich, G.S.: *Submillimeter-wave gyrotrons: theory and experiment.* Int. J. Infrared and Millimeter Waves, **4**, 629(1983)

51. Idehara, T., Tatsukawa, T., et al.: *Development and applications of submillimeter wave gyrotrons.* Proc. 3rd Int. Workshop on Strong Microwaves in Plasmas, Nizhny Novgorod, Russia, **2**, 634(1997)

52. Ogawa, I., Iwata, M., et al.: *Plasma scattering measurement using a submillimeter wave gyrotron (Gyrotron FUII) as a power source.* Fusion Engineering and Design, **34–35**, 455(1997)

53. Shimizu, Y., Ichikawa, K., et al.: *Submillimetre wave gyrotron (Gyrotron FU IV) for plasma diagnostics.* Fusion Engineering and Design, **34-35**, 459(1997)

54. Idehara, T., Ogawa, I., et al.: *Development and applications of submillimeter wave gyrotrons (FU Series).* Proc. 9th Int. Conf. Displays and Vacuum Electronics, Garmisch-Partenkirchen, ITG–Fachbericht **165**, 177(2001)

55. Bykov, Y., Goldenberg, A.F.L., Flyagin, V.A.: *The possibilities of material processing by intense millimeter-wave radiation.* Mat. Res. Soc. Symp. Proc., **169**, 41(1991)

56. Sklyarevich, V., Detkov, A., Shevelev, M., Decker, R. : *Interaction between gyrotron radiation and powder materials.* Mat. Res. Soc. Symp. Proc., **269**, 163(1992)

57. Link, G., Feher, L., et al.: *Sintering of ceramics using gyrotron radiation.* Proc. 8th ITG–Conference on Displays and Vacuum Electronics, Garmisch–Partenkirchen, ITG–Fachbericht **150**, 375(1998)

58. Link, G., Feher, L., Thumm, M., Ritzhaupt–Kleissl, H.–J., Böhme, R., Weisenburger, A.: *Sintering of advanced ceramics using a 30 GHz, 10 kW, CW industrial gyrotron.* IEEE Trans. on Plasma Science, **27**, 547(1999)

59. Kikunaga, T., Asano, H., Yasojima, Y., Sato, F., Tsukamoto, T.: *A 28 GHz gyrotron with a permanent magnet system.* Int. J. Electronics, **79**, 655(1995)

60. Bykov, Yu., Glyavin, M., et al.: *Development and experimental investigation of high power technological gyrotrons.* Conf. Digest 24th Int. Conf. on Infrared and Millimeter Waves, Monterey, California, USA, TU–A7(1999)

61. Kuftin, A.N., Flyagin, V.A., et al.: *5.8–62 GHz CW gyrotrons with warm and permanent magnets for technological application.* Proc. 4th Int. Workshop on Strong Microwaves in Plasmas, Nizhny Novgorod, Russia (1999)

62. Kuftin, A.N., Flyagin, V.A., Lygin, V.K., Malygin, O.V., Zapevalov, V.E., Zavolsky, N.A.: *Technological gyrotrons with permanent magnet system.* Proc. Int. University Conf. on Electronics and Radiophysics of Ultra-High Frequencies (UHF–99), St. Petersburg, Russia, 126(1999)

63. Kuftin, A.N., Flyagin, V.A., Lygin, V.K., Malygin, O.V., Zapevalov, V.E., Zavolsky, N.A.: *Technological gyrotrons with permanent magnet system.* Conf. Digest 25th Int. Conf. on Infrared and Millimeter Waves, Beijing, P.R. China, 267(2000)

64. Granatstein, V.L., Lawson, W., Latham, P.E.: *Feasibility of 30 GHz gyroklystron amplifiers for driving linear supercolliders.* Conf. Digest, 13th Int. Conf. on Infrared and Millimeter Waves, Honolulu, Hawaii, Proc. SPIE 1039, 230(1998)

65. Granatstein, V.L., Nusinovich, G.S. : *On the optimal choice of microwave systems for driving TeV linear colliders.* Proc. 2nd Int. Workshop on Strong Microwaves in Plasmas, Moscow – Nizhny Novgorod – Moscow (1993)

66. Granatstein, V.L., Lawson, W.: *Gyro-amplifiers as candidate RF drivers for TeV linear colliders.* IEEE Trans. on Plasma Science, **24**, 648(1996)

67. Manheimer, W.M., Mesyats, G.A., Petelin, M.I.: *Super-high-power microwave radars.* Proc. 2nd Int. Workshop on Strong Microwaves in Plasmas, Moscow – Nizhny Novgorod – Moscow (1993)

68. Manheimer, W.M.: *On the possibility of high power gyrotrons for super range resolution radar and atmospheric sensing.* Int. J. Electronics, **72**, 1165(1992)

69. Clunie, D., Mesyats, G., et al.: *The design, construction and testing of an experimental high power, short-pulse radar.* Proc. 3rd Int. Workshop on Strong Microwaves in Plasmas, Nizhny Novgorod, Russia (1996)

70. Danly, B.G., et al.: *WARLOC: A high-power millimeter-wave radar.* Proc. 27th Int. Conf. on Infrared and Millimeter Waves, San Diego, USA, 233(2002).

71. Bratman, V.L., Denisov, G.G., Ginzburg, N.S., and Petelin, M.I.: *FEL's with Bragg reflection resonators. Cyclotron autoresonance masers versus ubitrons.* IEEE Journal Quantum Electronics, **19**, 282(1983)

72. Edgcombe, C.J., Ed.: *Gyrotron Oscillators – Their Principles and Practice.* Taylor & Francis, London (1993)

73. Marshall, T.C.: *Free electron lasers.* Macmillan, New York (1985)

74. Sprangle, P., Coffey, T.: *New high power coherent radiation sources.* Infrared and Millimeter Waves, Vol. **13**, Ed. K. J. Button, Academic Press, New York, 19(1985)

75. Stone, R.R., Jong, R.A., et al.: *An FEL-based microwave system for fusion.* J. Fusion Energy, **9**, 77(1990)

76. Freund, H.P., Antonsen, T.M., Jr.: *Principles of free–electron lasers.* Chapman & Hall, London, 2nd edition (1996)

77. Freund, H.P., Neil, G.R.: *Free–electron lasers: Vacuum electronic generators of coherent radiation.* Proc. IEEE, **87**, 782(1999)

78. Hirshfield, J.L., Granatstein, V.L.: *Electron cyclotron maser – an historical survey.* IEEE Trans. Microwave Theory Tech., **25**, 522(1977)

79. Twiss, R.Q.: *Radiation transfer and the possibility of negative absorption in radio astronomy.* Aust. J. Phys., **11**, 564(1958)
   Twiss, R.Q., Roberts, J.A.: *Electromagnetic radiation from electrons rotating in an ionized medium under the action of a uniform magnetic field.* Aust. J. Phys., **11**, 424(1958)

80. Schneider, J.: *Stimulated emission of radiation by relativistic electrons in a magnetic field.* Phys. Rev. Lett., **2**, 504(1959)

81. Gapanov, A.V.: *Interaction between electron fluxes and electromagnetic waves and waveguides.* Izv. VUZ Radiofiz., **2**, 450(1959)
   Gapanov, A.V.: *Addendum.* Izv. VUZ Radiofiz., **2**, 836(1959)

82. Kleinwächter, H.: *Zur Wanderfeldröhre (in German).* Elektrotechnik, **4**, 245(1950)

83. Hirshfield, J.L., Wachtel, J.M.: *Electron cyclotron maser.* Phys. Rev. Lett., **12**, 533(1964)

84. Granatstein, V.L., Alexeff, I., Eds.: *High-power microwave sources.* Artech House, Boston, London (1987)

85. Benford, J. Swegle, J.: *High-power microwave sources.* Artech House, Boston, London (1992)

86. Nusinovich, G.S.: *Review of the theory of mode interaction in gyrodevices.* IEEE Trans. on Plasma Science, **27**, 313(1999)

87. Pendergast, K.D., Danly, B.G., Menninger, W.L., Temkin, R.J.: *A long-pulse CARM oscillator experiment.* Int. J. Electronics, **72**, 983(1992)

88. Galuzo, S.Yu., Kanavets, V.I., Slepkov, A.I., Pletyushkin, V.A.: *Relativistic cyclotron accelerator exploiting the anomalous Doppler effect.* Sov. Phys. Tech. Phys., **27**, 1030(1982)

89. Didenko, A.N., Borisov, A.R., Fomenko, G.P., Shlapakovskii, A.S., Shtein, Yu.G.: *Cyclotron maser using the anomalous Doppler effect.* Sov. Phys. Tech. Lett., **9**, 572(1983)

90. Ogura, K., Amin, M.R., et al.: *Experimental demonstration of a high-power slow-wave electron cyclotron maser based on a combined resonance of Cherenkov and anomalous Doppler interactions.* Phys. Rev. Lett. E, **53**, 2726(1996)

91. Guo, H., Chen, L., Keren, H., Hirshfield, J.L., Park, S.Y., Chu, K.R.: *Measurements of gain for slow cyclotron waves on an annular electron beam.* Phys. Rev. Lett., **49**, 730(1982)

92. Granatstein, V.L., Read, M.E., Barnett, L.R.: *Measured performance of gyrotron oscillators and amplifiers, in Infrared and Millimeter Waves.* Vol. **5**, Ed. K.J. Button, Academic Press, New York, 267(1982)

93. Chu, K.R.: *Overview of research on the gyrotron traveling-wave amplifier.* IEEE Trans. Plasma Science, **30**, 903(2002)

94. Denisov, G.G., Bratman, V.L., Phelps, A.D.R., Samsonov, S.V.: *Gyro-TWT with a helical operating waveguide: new possibilities to enhance efficiency and frequency bandwidth.* IEEE Trans. Plasma Science, **26**, 508(1998)

95. Guo, H., Chen, S.H., et al.: *A high performance, frequency doubling, inverted gyrotwystron.* Conf. Digest 22nd Int. Conf. on Infrared and Millimeter Waves, Wintergreen, Virginia, USA, 285(1997)

96. Ganguly, A.K., Ahn, S., Park, S.Y.: *Three dimensional nonlinear theory of the gyropeniotron amplifier.* Int. J. Electronics, **65**, 597(1988)

97. Nezhevenko, O.A.: *Gyrocons and magnicons: Microwave generators with circular deflection of the electron beam.* IEEE Trans. Plasma Science, **5**, 756(1994)

98. Hirshfield, J.L., LaPointe, M.A., Yoder, R.B., Ganguly, A.K., Wang, Ch., Hafizi, B.: *High-power microwave production by gyroharmonic conversion and co-generation.* Proc. 3rd Int. Workshop on Strong Microwaves in Plasmas, Nizhny Novgorod, Vol. **2**, 730(1997)

99. Hirshfield, J.L., LaPointe, M.A., Wang, C., Ganguly, A.K.: *20 GHz high-power gyroharmonic co-generation.* Proc. 4th Int. Workshop on Strong Microwaves in Plasmas, Nizhny Novgorod, Ed. A.G. Litvak, Inst. of Applied Physics, Russian Academy of Sciences, Nizhny Novgorod, 2000, Vol. **2**, 728(1999)

100. Phillips, R.M.: *The ubitron, a high-power traveling-wave tube based on a periodic beam interaction in unloaded waveguide.* IRE Trans. Electron. Dev., **7**, 231(1960)
    History of the ubitron. Nucl. Instr. Meth., A272, 1(1988)
    and private communication (1998)

101. Drori, R., Jerby, E.: *Free–electron–laser–type interaction at 1 meter wavelength range*. Nucl. Instr. Meth., A393, 284(1997)

102. Verhoeven, A.G.A., Bongers, W.A., et al: *The 1 MW, 200 GHz FOM–Fusion–FEM*. Conf. Digest 17th Int. Conf. on Infrared and Millimeter Waves, Pasadena (Los Angeles), Proc. SPIE 1929, 126(1992)

103. Urbanus, W.H., Best, R.W.B., et al.: *Design of the 1 MW, 200 GHz, FOM fusion FEM*. Nucl. Instr. Meth., A 331, 235(1993)

104. Verhoeven, A.G.A., Bongers, W.A., et al: *A broad-tuneable free electron maser for ECW applications*. Proc. 9th Joint Workshop on Electron Cyclotron Emission and Electron Cyclotron Heating, Borrego Springs, California, 309(1995)

105. Verhoeven, A.G.A., Bongers, W.A., et al: *First high power experiments with the Dutch free electron maser*. Physics of Plasmas, **5**, 2029(1998)

106. Verhoeven, A.G.A., Bongers, W.A., et al.: *First microwave generation in the FOM free electron maser*. Plasma Phys. and Contr. Fusion, **40**, Suppl. 8A, 139(1998)

107. Verhoeven, A.G.A., Bongers, W.A., et al: *First generation of mm-waves in the dutch free-electron maser*. Conf. Digest 23rd Int. Conf. on Infrared and Millimeter Waves, Colchester, UK, 21(1998)

108. Urbanus, W.H., Bongers, W.A., et al: *High-power electrostatic free–electron maser as a future source for fusion plamsa heating: Experiments in the short-pulse regime*. Phys. Rev. E, **59**, 6058(1999)

109. Verhoeven, A.G.A., Bogers, W.A., et al.: *First mm-wave generation in the FOM free electron maser*. IEEE Trans. Plasma Science, **27**, 1084(1999)

110. Urbanus, W.H., Bratman, V.L., et al.: *A high power, tunable free elctron maser for fusion*. Fusion Engineering and Design, **53**, 423(2001)

111. Freund, H.P., Granatstein, V.L.: *Long wavelength free electron laser*. Nucl. Instr. Meth., A358, 551(1994); Nucl. Instr. Meth., A375, 665(1996); Nucl. Instr. Meth., A393, 9(1997); Nucl. Instr. Meth., A407, 30(1998); Nucl. Instr. Meth., A429, 33(1999); and private communication

112. Shaw, A., Al–Shamma, A., Stuart, R.A., Balfour, C., Lucas, J.: *First results of a CW industrial FEM*. Nucl. Instr. Meth., A357, 245(1996)

113. Dylla, H.F.: *An overview of the user program for the Jefferson Lab free electron laser*. Proc. SPIE, Vol. 3618, 388(1999)
     Benson, S.V.: *What have we learned from the kilowatt IR–FEL at Jefferson lab ?*. Nucl. Instr. Meth., **A483**, 1(2002)

114. Lindsay, P.A., Jones, R.M., Lumsden, R.J.: *Some observations on gyrotron interaction models*. Int. J. Electronics, **57**, 915(1984)

115. Akhiezer, A.I., Berestetskii, V.B.: *Quantum Electrodynamics (English translation)*. Section 12.5, Wiley Interscience, New York (1965)

116. Gapanov, A.V., Goldenberg, A.L., Grigoryev, D.P., Pankratova, T.B., Petelin, M.I., Flaygin, V.A.: *Experimental study of centimeter band gyrotrons*. Radio Phys. Quantum Electron., **18**, 280(1975)

117. Kreischer, K.E., Schutkeker, J.B., Danley, B.G., Mulligan, W.J., Temkin, R.J.: *High effeciency operation of a 140 GHz pulsed gyrotron*. Int. J. Electronics, **57**, 835(1984)

118. Kreischer, K.E., Danley, B.G., Woskoboinikov, P., Mulligan, W.J., Temkin, R.J.: , 1984, *Frequency pulling and bandwidth measurements of a 140 GHz pulsed gyrotron*. Int. J. Electronics, **57**, 851(1984)

119. Carmel, Y., Chu, K.R., Dialetis, D., Fliflet, A., Read, M.E., Kim, K.J., Arfin, B., Granatstein, V.L.: *Mode competition, suppression, and efficiency enhancement in overmoded gyrotron oscillators*. Int. J. Infrared and Millimeter Waves, **3**, 645(1982)

120. Felch, K., Bier, R., Craig, L.J., Huey, H., Ives, L., Jory, H., Lopez, N., Spang, S.: *CW operation of a 140 GHz gyrotron*. Int. J. Electronics, **61**, 701(1986)

121. Bernstein, I.B., Divringi, L.K., Smith, T.M.: *Theory of irregular waveguides and open resonators*. Int. J. Infrared and Millimeter Waves, **3**, 57(1983)

122. Luginsland, J.: *Zur Berechnung inhomogener rotationssymmetrischer Gyrotronenresonatoren*. Ph.D. Thesis, University of Aachen, Germany (1985)

123. Borie, E., Dumbrajs, O.: *Calculation of eigenmodes of tapered gyrotron resonators*. Int. J. Electronics, **60**, 143(1986)

124. Fliflet, A.W., Read, M.E.: *Use of weakly irregular waveguide theory to calculate eigenfrequencies, Q–values and RF field functions for gyrotron oscillators*. Int. J. Electronics, **51**, 475(1981)

125. Kuraev. A.A.: *Theory and optimization of high frequency electronic devices*. Minsk: Izd. Nauka i Tekhnika (in Russian) (1979)

126. Derfler, H., Grant, T.J., Stone, D.S.: *Loaded Qs and field profiles of tapered axisymmetric gyrotron cavities*. IEEE Trans. Electron Devices, **29**, 1917(1982)

127. Xu, Cheng–he, Zhou, Le–zhu: *Microwave open resonators in gyrotrons*. Int. J. Infrared and Millimeter Waves, **10**, 311(1983)

128. Borie, E.: *Computation of radio-frequency behaviour*. In "Gyrotron Oscillators – Their Principles and Practice," Ed. C. J. Edgcombe, Ch. 3, Taylor & Francis, London (1993)
    Borie, E.: *Review of gyrotron theory*. Internal report KfK 4898, FZK, Karlsruhe, Germany (1991)

129. Jackson, J.D.: *Classical Electrodynamics*. John Wiley & sons, Inc., New York (1962)

130. Schied, F.: *Theory and problems of numerical analysis*. Mc Graw Hill, New York (1968)

131. Vlasov, S.N., Zagryadskaya, L.I., Orlova, I.M.: *Open coaxial resonators for gyrotrons*. Radio Eng. Electron. Phys., **21**, 96(1976)

132. Gaponov, A.V., Flyagin, V.A., Goldenberg, A.L., Nusinovich, G.S., Tsimring, Sh.E., Usov, V.G., Vlasov, S.N.: *Powerful millimeter-wave gyrotrons*. Int. J. Electronics, **51**, 277(1981)

133. Nusinovich, G.S., Read, M.E., Dumbrajs, O., Kreischer, K.E.: *Theory of gyrotrons with coaxial resonators*. IEEE Trans. Electron Devices, **41**, 433(1994)

134. Iatrou, C.T., Kern, S., Pavelyev, A.B.: *Coaxial cavities with corrugated inner conductor for gyrotrons*. IEEE Trans. MTT., **44**, 56(1996)

135. Iatrou, C.T.: *Mode selection properties of coaxial gyrotron resonators*. IEEE Trans. Plasma Science, **24**, 596(1996)

136. Kern, S.: *Numerische Simulation der Gyrotron–Wechselwirkung in koaxialen Resonatoren*. Ph.D. Thesis, Universität Karlsruhe (TH), Karlsruhe, Germany (1996)

137. Pavelyev, V.G., Tsimring, S.E. : *Inventors Certificate No. 661664*. Byull. Izobret., **17**, 240(1979)

138. Kim, K.J., Read, M.E., et al.: *Design considerations for a megawatt CW gyrotron*. Int. J. Electronics, **51**, 427(1981)

139. Gapanov, A.V., Flaygin, V.A., Gol'denberg, A.L., Nusinovich, G.S., Tsimring, S.E., Usov, V.G., Vlasov, S.N.: *Powerful millimeter-wave gyrotrons*. Int. J. Electronics, **51**, 277(1981)

140. Garin, G., Mourier, G., Teyssier, L.: *Symmetric and non-symmetric modes in high power generators for electron cyclotron resonance heating*. 14th European Conference on Controlled Fusion and Plasma Heating, Madrid, 962 (1987)

141. Dumbrajs, O., Borie, E.: *A complex cavity with mode conversion for gyrotrons*. Int. J. Electronics, **65**, 285(1988)
Borie, E., B. Jödicke, B., Wenzelburger, H., Dumbrajs, O.: *Resonator Design Studies for a 150 GHz gyrotron at KfK*. Int. J. Electronics, **64**, 107(1988)

142. Fliflet, A.W., Lee, R.C., Read, M.E.: *Self-consistent field model for the complex cavity gyrotron*. Int. J. electronics, **65**, 273(1988)

143. Pavelyev, V.G., Tsimring, S.E., Zapevalov, V.E.: *Complex cavities with mode conversion in gyrotrons*. Int. J. Electronics, **63**, 379(1987)

144. Nielson, J.M., Latham, P.E., Caplan, M., Lawson, W.G.: *Determination of the resonant frequencies in a complex cavity using the scattering matrix formalism*. IEEE Trans. Microwave Theory and Tech., **37**, 1165(1989)

145. James, F., and Roos, M.: *MINUIT long writeup*. CERN program library, Programs D506, D516 (1974)

146. Press, W.H., Flannery, B.P., Teukolsky, S.A., Vetterling, W.T.: *Numerical Recipes – The art of scientific computing (FORTRAN version)*. Cambridge University Press, Cambridge (1989)

147. Hockney, R.W., Eastwood, J.W.: *Computer simulation using particles*. McGraw–Hill, New York (1981)

148. Rapoport, G.N., Nemark, A.K., Zhurakhovskij, V.A.: *Interaction of helical electron beams with the intense electromagnetic fields of cavities operating at harmonics of the cyclotron frequency*. Radiotechnika i Elektronika, **12**, 633(1967)

149. Ganguly, A.K., Ahn, S.: *Self-consistent large signal theory of the gyrotron travelling wave amplifier*. Int. J. Electronics, **53**, 641(1982)

150. Fliflet, A.W., Read, M.E., Chu, K.R., Seeley, R.: *A self-consistent field theory for gyrotron oscillators: application to a low Q gyromonotron*. Int. J. Electronics, **53**, 505(1982)

151. Mourier, G.: *Gyrotron tubes – a theoretical study*. Archiv f. Elektronik und Übertragungstechnik, **34**, 473(1980)

152. Borie, E.: *Self-consistent code for a 150 GHz gyrotron*. Int. J. Infrared and Millimeter Waves, **7**, 1863 (1986)

153. Borie, E., Dumbrajs, O., Jödicke, B.: *Parameter studies for a 150 GHz gyrotron operating in the TE_{03} mode*. Int. J. Electronics, **61**, 735(1986)

154. Bratman, V.I., Petelin, M.I.: *Optimizing the parameters of high power gyromonotrons with RF field of nonfixed nature*. Radio Phys. Quantum Electron., **18**, 1136(1975)

155. Bratman, V.L., Moiseev, M.A., Petelin, M.I.: *Theory of gyrotrons with low–Q electromagnetic systems*. From "Gyrotrons: collected papers," USSR Academy of Sciences, Institute of Applied Physics, 104, Gorki (1981)

156. Nusinovich, G.S.: *Mode interaction in gyrotrons*. Int. J. Electron., **51**, 457(1981)

157. Nusinovich, G.S.: *Theory of mode interaction in the gyrotron*. KfK Report 4111, FZK, Karlsruhe, Germany (1986)

158. Abramowitz, M., Stegun, I.A.: *Handbook of mathematical functions*. Dover Publications, New York (1970)

159. Gantenbein, G., Borie, E.: *Gyrotron with a tapered external magnetic field*. Int. J. Infrared and Millimeter Waves, **11**, 837(1990)

160. Borie, E., Gantenbein, G.: *Self consistent theory for gyrotrons including effect of voltage depression*. Int. J. Infrared and Millimeter Waves, **12**, 65(1991)

161. Kleva, R.G., Antonsen, T.M., Levush, B.: *The effect of the time dependent self consistent electristatic field in gyrotron operation*. Phys. Fluids, **31**, 195(1988)

162. Latham, P.E.: *AC space-charge effects in gyroklystron amplifiers*. IEEE Trans. Plasma Science, **18**, 273(1990)

163. Gantenbein, G., Borie, E., Dumbrajs, O., Thumm, M.: *Design of a high order volume mode cavity for a 1 MW/140 GHz gyrotron*. Int. J. Electronics, **78**, 771(1995)

164. Bratman, V.L., Moiseev, M.A., Petelin, M.I., Erm, R.E.: *Theory of the gyrotrons with a non-fixed structure of the high frequency field*. Radio Phys. Quant. Electron., **16**, 474(1973)

165. Charbit, P., Herscivici, A., Mourier, G.: *A partly self consistent theory of the gyrotron*. Int. J. Electronics, **51**, 303(1981)

166. Vlasov, S.N., Zhislin, G.M., Orlova, I.M., Petelin, M.I., Rogacheva, G.G.: *Irregular waveguides as open resonators*. Rad. Phys. Quant. Electron., **12**, 972(1969)

167. Ergakov, V.S., Moiseev, M.A.: *Influence of electron velocity scatter on the starting current and efficiency of a gyrotron*. In "Gyrotrons: collected papers", USSR Academy of Sciences, Institute of Applied Physics, Gorki (1981)

168. Danly, B.G., Temkin, R.J.: *Generalized nonlinear harmonic gyrotron theory*. Phys. Fluids, **29**, 561(1986)

169. Antonsen, T.M., Levush, B.: *Mode competition in gyrotrons and free electron lasers*. 14th Int. Conf. Infrared and Millimeter Waves, Würzburg, Germany (1989)

170. Bratman, V.L., Ginzburg, N.S., Nusinovich, G.S., Petelin, M.I., Strelkov, P.S.: *Relativistic gyrotrons and cyclotron autoresonance masers*. Int. J. Electronics, **51**, 541(1981)

171. Petelin, M.I.: *On the theory of ultrarelativistic cyclotron self-resonance masers*. Radio Phys. Quantum Electron., **17**, 686(1974)

172. Fliflet, A.W.: *Linear and nonlinear theory of the Doppler shifted cyclotron resonance maser based on TE and TM waveguide modes*. Int. J. Electronics, **61**, 1049(1986)

173. Iatrou, C.T.: *Operating-mode selection and design of gyrotron oscillators*. FZK Internal report, FZK, Karlsruhe, Germany (1996)

174. Bykov, Yu.V., Gol'denberg, A.L.: *Influence of resonator profile on the maximum power of a cyclotron resonance maser*. Radio Phys. Quantum Electron., **18**, 791(1975)

175. Drobot, A.T., Kim, K.: *Space charge effects on the equilibrium of guided electron flow with gyromotion*. Int. J. Electronics, **51**, 351(1981)

176. Ganguly, A.K., Chu, K.R.: *Limiting current in gyrotrons*. Int. J. Infrared and Millimeter Waves, **5**, 103(1984)

177. Zarnitsina, I.G., Nusinovich, G.S.: *Stability of single mode self-excited oscillations in a gyromonotron*. Radiophys. Quantum Electron., **17**, 1418(1974)

178. Moiseev, M.A., Nusinovich, G.S.: *Concerning the theory of multimode oscillation in a gyromonotron*. Radiophys. Quantum Electron., **17**, 1305(1977)

179. Zarnitsina, I.G., Nusinovich, G.S.: *Competition between modes resonant with different harmonics of the cyclotron frequency in gyromonotrons*. Rad. Phys. Quantum Electron, **20**, 461(1977)

180. Ginzburg, N.S., Nusinovich, G.S., Zavolsky, N.A.: *Theory of nonstationary processes in gyrotrons with low Q resonators*. Int. J. Electron., **61**, 881(1986)

181. Dialetis, D., Chu, K.R.: *Mode competition and stability analysis of the gyrotron oscillator*. In "Infrared and Millimeter Waves," vol. **7**, Ed. K. J. Button, New York, Academic Press (1983)

182. Borie, E., Gantenbein, G., et al.: *Mode Competition Using TE_{03} Gyrotron Cavities*. Int. J. Electronics, **72**, 687(1992)

183. Borie, E., Jödicke, B.: *Startup and Mode Competition in a 150 GHz Gyrotron*. Int. J. of Infrared and Millimeter Waves, **8**, 207(1987)

184. Jödicke, B.: *Zur Modenrangigkeit von Hochleistungsgyrotrons mit Rotationssymmetrischen Arbeitsmoden*. Scientific Report KfK 4603, FZK, Karlsruhe, Germany (1989)

185. Levush, B., Antonsen, T.M.: *Mode competition and control in high-power gyrotron oscillators*. IEEE Trans. Plasma Science, **18**, 260(1990)

186. Kreischer, K.E., Temkin, R.J., Fetterman, H.R., Mulligan, W.J.: *Multimode oscillation and mode competition in high frequency gyrotrons*. IEEE Trans. Microwave Theory Tech., **32**, 481(1984)

187. Whaley, D.R., Tran, M.Q., Tran, T.M., Antonsen, T.M.: *Mode competition and startup in cylindrical cavity gyrotrons using high-order operating modes*. IEEE Trans. Plasma Science, **22**, 850(1994)

188. Fliflet, A.W., Lee, R.C., Gold, S.H., Manheimer, W.M., Ott, E.: *Time-dependent multimode simulation of gyrotron oscillators*. Phys. Rev., **A43**, 6166(1991)

189. Cai, S.Y., Antonsen, T.M., Saraph, G., Levush, B.: *Multifrequency theory high-power gyrotron oscillators*. Int. J. Electronics, **72**, 759(1992)

190. Zapevalov, V.E., Nusinovich, G.S.: *Multimoding in Cyclotron Resonance Masers*. Rad. Quantum Electron., **27**, 117(1984)

191. Zapevalov, V.E., Nusinovich, G.S.: *Multimoding in Cyclotron Resonance Masers*. Rad. Quantum Electron., **32**, 269(1989)

192. Zapevalov, V.E., et al.: *Problems of mode interaction and selection for high power gyrotrons*. 25th Int. Conf. Infrared and Millimeter Waves, Conf. Digest, P76 (2001)

193. Kartikeyan, M.V., Borie, E., Thumm, M.: *Possible operation of a 1.5-2 MW, CW conventional cavity gyrotron at 140 GHz*. IEEE Trans. Plasma Science, **28**, 645(2000)

194. Myasnikov, V.E., Usachev, S.V., et al.: *Long pulse operation of a 170 GHz/1 MW gyrotron for ITER*. 23rd Int. Conf. Infrared and Millimeter Waves, Conf. Digest p24(1998)

195. Brand, G.F., Idehara, T., Tatsukawa, T., Ogawa, I.: *Mode competition in a high harmonic gyrotron*. Int. J. Electronics, **72**, 745(1992)

196. Idehara, T., Tatsukawa, T., et al.: *Competition between fundamental and second-harmonic operations in a submillimeter wave gyrotron*. Appl. Phys. Lett., **58**, 1594(1991)

197. Borie, E.: *Study for second harmonic gyrotrons in the submillimeter region*. Int. J. of Infrared and Millimeter Waves, **15**, 311(1994)

198. Idehara, T., Tatsukawa, T., et al.: *Development of a second cyclotron harmonic gyrotron operating at submillimeter wavelengths*. Phys. Fluids B, **4**, 267(1992)

199. Liu, P.-K., Borie, E.: *Mode competition and self-consistent simulation of a second harmonic gyrotron oscillator.* Int. J. of Infrared and Millimeter Waves, **21**, 855(2000)

200. Nusinovich, G.S., Pankratova, T.B.: *Submillimeter band gyrotron theory.* In "Gyrotrons: collected papers", USSR Academy of Sciences, Institute of Applied Physics, Gorki(1981).

201. Jödicke, B., Möbius, A., Stickel, H.: *Thermopaper Mode Diagnostics for Gyrotrons.* Kernforschungszentrum Karlsruhe (KfK) Internal Report, unpublished (1987) .

202. Petelin, M.I.: *Self-excitation of oscillations in a gyrotron.* In "Gyrotrons: collected papers," USSR Academy of Sciences, Institute of Applied Physics, Gorki(1981)

203. Kreishcer, K., Temkin, R.J.: *Linear theory of an electron cyclotron maser operating at the fundamental.* Int. J. Infrared and Millimeter Waves, **1**, 195(1980)

204. Nusinovich, G.S.: *Linear theory of a gyrotron with weakly tapered magnetic field.* Int. J. Electronics, **64**, 127(1988)

205. Borie, E., Jödicke, B.: *Comments on the linear theory of the gyrotron.* IEEE Trans. Plasma Science, **16**, 116(1988)

206. Halzen, F., Martin, A.D.: *Quarks and Leptons, an introductory course in modern particle physics.* Chap. 12 and 13, John Wiley & sons, New York (1984)

207. Feynman, R.P., Leighton, R.B., Sands, M.: *The Feynman Lectures in Physics, vol. III – Quantum Mechanics.* Ch. 10, Addison Wesley, Reading MA (1965)

208. Frieser, A.: *Mikrowellentechnik.* Akademie–Verlag, Berlin (1965)

209. Borie, E., Jödicke, B.: *Rieke diagrams for gyrotrons.* Int. J. Infrared and Millimeter Waves, **11**, 243(1990)

210. Borie, E.: *Effect of reflection on gyrotron operation.* IEEE Trans. Microwave Theory and Techniques, **49**, 1342(2001)

211. Muggli, P., Tran, M.Q., et al.: *Effect of power reflection on the operation of a low–Q 8 GHz gyrotron.* IEEE Trans. Plasma Science, **38**, 1345(1990)

212. True, R.: *Electron beam formation, focusing, and collection in microwave tubes.* In "Handbook of Microwave Technology," Ed. T. Koryu Ishii, Ch. 14, **1**, Academic Press, New York (1995)

213. Piosczyk, B.: *Electron guns for gyrotron applications.* In "Gyrotron Oscillators – Their Principles and Practice," Ed. C. J. Edgcombe, Ch. 5, Taylor & Francis, London, (1993)

214. Manuilov, V.N., Tsimring, S.E.: *Synthesis of axially symmetric systems for shaping helical electron beams.* Radio Engineering and Electronic Physics, **24**, 111(1979)

215. Kuftin, A.N., Lygin, V.K., Tsimring, S.E., Zapevalov, V.E.: *Numerical Simulation and Experimental Study of magnetron injection guns for powerful short wave gyrotrons.* Int. J. Electronics, **72**, 1145(1992)

216. Kuftin, A.N., Lygin, V.K., Manuilov, V.N., Raisky, B.V., Solujanova, E.A., Tsimring, S.E.: *Theory of helical electron beams in gyrotrons.* Int. J. Infrared and Millimeter Waves, **14**, 783(1993)

217. Gilmour Jr., A.S.: *Microwave Tubes.* Artech House: Dedham MA (1986)

218. Edgcombe, C.J.: *Sources of velocity spread in electron beams from magnetron injection guns.* Int. J. Infrared and Millimeter Waves, **16**, 83(1995)

219. Tsmiring, S.E., Zapevalov, V.E.: *Experimental study of intense helical electron beams with trapped electrons.* Int. J. Electronics, **81**, 199(1996)

220. Tsimring, S.E.: *Limiting current of helical electron beams in gyrotrons*. Int. J. Infrared and Millimeter Waves, **14**, 817 (1993)

221. Tsimring, S.E.: *Limiting current of helical electron beams in gyrotrons*. Journal of Communications Technology and Electronics, **40**, 40(1995)

222. Hermannsfeldt, W.B.: *Numerical design of electron guns and space charge limited transport systems*. Nuclear Instruments and Methods, **187**, 245(1981)

223. Borie, E., Grüber, C., Westermann, T.: *Calculation of MIG guns for gyrotrons using the BFCPIC code*. Int. J. Electronics, **78**, 789(1995)

224. Westermann, T.: *Numerical modelling of the stationary Maxwell–Lorentz system in technical devices*, International Journal of Numerical Modelling: Electronic Networks, Devices and Fields, **7**, 43(1994)

225. Tran, T.M., Whaley, D.R., Merazzi, S., Gruber, R.: *DAPHNE, a 2D axisymmetric electron gun simulation code*. 6th EPS-APS Int. Conf. on Physics Computing, Lugano, Switzerland (1994)

226. Lygin, V.K., Manuilov, V.N., Tsimring, S.E.: *On methods of integral equations and auxiliary sources in the trajectory analysis of intense electron beams* (in Russian). Elektonika SVCh., **401**, 36(1987)

227. Baird, J.M., Lawson, W.: *Magnetron injection gun (MIG) design for gyrotron applications*. Int. J. Electronics, **61**, 969(1986)

228. Manuilov, V.N., Tsimring, S.E.: *Theory of Generation of relativistic helical electron beams*. Sov. Phys. Tech. Phys., **26**, 1470(1981)

229. Borie, E., Horcher, U.: *Effect of Surface Roughness on the Velocity Spread in Electron Guns for Gyrotrons*. Int. J. Infrared and Millimeter Waves, **18**, 577(1997)

230. Raiskii, B.V., Tsimring, S.E.: *Numerical Simulation Models of Nonstationary Processes of Intense Helical Electron Beams of Gyrotrons*. IEEE Trans. Plasma Science, **24**, 992(1996)

231. C. J. Edgcombe, C.J.: *Developments in the design of electrodes for magnetron injection sources*. Int. J. Electronics, **64**, 49(1988)

232. C. J. Edgcombe, C.J.: *Synthesis of Electrodes for relativistic Electron Streams*. Int. J. Infrared and Millimeter Waves, **16**, 1491(1995)

233. Correa, R.A., Barrosso, J.J.: *Space charge effects of gyrotron electron beams in coaxial cavities*. Int. J. Electronics, **74**, 131(1993)

234. Borie, E.: *Calculations of a diode gun for the* $TE_{28,8}$ *gyrotron with BFCRAY*. Private communication (1999)

235. Vaughan, J.R.M.: *Representation of axisymmetric magnetic fields in computer programs*. IEEE Trans. Electron Devices, **19**, 144(1972)

236. Illy, S.: *ESRAY–A computer code for the analysis of axysymmetric electron guns*. Private communication (2002)

237. Singh, A., Hazel, G., Granatstein, V.L., Saraph, G.: *Magnetic field profiles in depressed collector region for small-orbit gyrotrons with axial or redially extracted spent beam*. Int. J. Electronics, **72**, 1153(1992)

238. Singh, A., Destler, W.W., Granatstein, V.L., Hix, W.R.: *Enhancement of overall efficiency of large-orbit gyrotrons*. Int. J. Electronics, **72**, 827(1992)

239. Read, M.E., Lawson, W.G., Dudas, A.J., Singh, A.: *Depressed collectors for high power gyrotrons*. IEEE Trans. Electron Devices, **37**, 1579(1990)

240. Singh, A., Rajapatirana, S., et al.: *Design of a multistage depressed collector system for 1 MW, CW gyrotrons–Part I: Trajectory control of primary and secondary electrons in a two–stage depressed collector*. IEEE Trans. Plasma Science, **27**, 490(1999)

241. Ives, R.L., Singh, A., et al.: *Design of a multistage depressed collector system for 1 MW, CW gyrotrons–Part II: System consideration*. IEEE Trans. Plasma Science, **27**, 503(1999)

242. Koshmal, H.G.: *Modern multi–stage depressed collectors – A review*. Proc. IEEE, **70**, 1325(1982)

243. Ramnis, P., Peet, S., Force, D.A.: *A re-examination of spent beam refocussing for high-efficiency helix TWTs and small MDCs*. IEEE Trans. Electron Devices, **35**, 539(1988)

244. Gilmour Jr., A.S.: *Principles of traveling wave tubes*. Artech House: Boston(1994)

245. Smith, M.J., Phillips, G.: *Power klystrons today*. RSP:Taunton, Sommerset(1994)

246. Sakamoto, K., Tsuneoka, M., et al.: *Major improvement of gyrotron efficiency with beam energy recovery*. Phys. Rev. Lett., **73**, 3532(1994)

247. Hargreaves, T.A., Fliflet, A.W., Fischer, R.P., Barsanti, M.L.: *Depressed collector performance on the NRL quasi-optical gyrotron*. Conf. Digest, 15th Int. Conf. on Infradred and Millimeter Waves, Orlando, USA, 330(1990)

248. Piosczyk, B., Iatrou, C.T., Dammertz, G., Thumm, M.: *Single–stage depressed collectors for gyrotrons*. IEEE Trans. Plasma Science, **24**, 579(1996)

249. Ling, G., Piosczyk, B., Thumm, M.K.: *A new approach for a multistage depressed collector for gyrotrons*. IEEE Trans. Plasma Science, **28**, 606(2000)

250. Piosczyk, B.: *A 2.2 MW, CW collector for a coaxial cavity gyrotron*. Conf. Digest, 26th Int. Conf. on Infrared and Millimeter Waves, Toulouse, France (2001)

251. Leontovitch, M.A.(Edited): *Review of Plasma Physics, vol. 1*. Consultants Bureau: New York (1965)

252. Piosczyk, B.: *A single stage–stage depressed collector for a 2 MW, CW coaxial cavity gyrotron*. Private communication (2002)

253. Dammertz, G.: *Beam tunnel, resonator, collector and RF window*. In "Gyrotron Oscillators – Their Principles and Practice," Ed. C. J. Edgcombe, Ch. 6, Taylor & Francis, London, (1993)

254. Goldstein, J.I., Newbury, D.E., et al.: *Scanning electron microscopy and X-ray microanalysis*. Plenum : New York (1984)

255. Mobius, A., Thumm, M.: *Gyrotron output launchers and output tapers*. In "Gyrotron Oscillators – Their Principles and Practice," Ed. C. J. Edgcombe, Ch. 7, Taylor & Francis, London, (1993)

256. Thumm, M.K., Kasparek, W.: *Passive high-power microwave components*. IEEE Trans. Plasma Science, **30**, 755(2002)

257. Thumm, M., Erckmann, V., et al.: *very high power mm-wave components in oversized waveguides*. Microwave Journal, **29**, 103(1986)

258. Katsenelenbaum, B.Z., Mercader Del Rio, L., Pereyaslavets, M., Sorolla Ayza, M., Thumm, M.: *Theory of non-uniform waveguides: the cross-section method*. IEE Electromagnetics Waves Series: London, **44** (1998)

259. Sporleder, F., Unger, H.–G.: *Waveguide tapers, transitions and couplers*. IEE: London (1979)

260. Unger, H.–G.: *Circular waveguide taper of improved design*. Bell System Tech. J., **37**, 899(1957)

261. Weinstein, L.A.: *Open waveguides and resonators*. Boulder, CO: Golem (1969)

262. Vlasov, S.N., Orlova, I.M.: *Quasioptical transformer which transforms the waves in a waveguide having a circular cross-section into a highly-directional wave beam.* Radio. Phys. Quantum Electron., **17**, 115(1974)

263. Vlasov, S.N., Zagryadskaya, L.I., Petelin, M.I.: *Transformation of a whispering gallerey mode, propagating in a circular waveguide into beam of waves.* Radio Eng. Electron. Physics, **20**, 14(1975)

264. Thumm, M.: *High power microwave transmission systems, external mode converters and antenna technology.* In "Gyrotron Oscillators – Their Principles and Practice," Ed. C. J. Edgcombe, Ch. 13, Taylor & Francis, London, (1993)

265. Kuzikov, S.V., Petelin, M.I.: *Conversion of paraxial waveguide mode to Gaussian beam.* Proc. Int. Workshop Strong Microwaves in Plasma, Nizhny Novgorod, Russia (1996)

266. Wien, A., Thumm, M.: *Numerical analysis of quasioptical mode converters. Part 1: Backscattering analysis of shaped–end radiators.* Int. J. Electronics, **86**, 739(1999)

267. Vlasov, S.N., Shapiro, M.A.: *Bievolvent mirror for transfer of caustic surfaces.* Sov. Tech. Phys. Lett., **15**, 374(1989)

268. Neilson, J.M., Bunger, R.: *Surface integral equation analysis of quasi-optical launchers.* IEEE Trans. Plasma Science, **30**, 794(2002)

269. Bogdashov, A.A., Chirkov, A.V., et al.: *Mirror synthesis for quasi-optical mode converters.* Int. J. Infrared Millimeter Waves, **16**, 735(1995)

270. Hirata, Y., Mitsunaka, Y., Hayashi, K., Itoh, Y.: *Wave-beam shaping using multiple phase-correction mirrors.* IEEE Trans. Microwave Theory and Techniques, **45**, 72(1997)

271. Michel, G., Sanchez, E.: "*Investigations on transmission lines with non-quadratic mirrors.* Proc. 10th Joint Workshop on Electron Cyclotron Emission and Electron Cyclotron Heating, Ameland, The Netherlands, 1997, Ed. T. Donne and A.G.A. Verhoeven, World Scientific, Singapore, 589 (1997)

272. Denison, D.R., Chu, T.S., Shapiro, M.A., Temkin, R.J.: *Gyrotron internal mode converter reflector shaping from measured field intensity.* IEEE Trans. on Plasma Science, **27**, 512(1999)

273. Drumm, O.: *Numerische optimierung eines quasi-optischen wellentypwandlers für ein frequenzdurchstimmbares gyrotron.* Ph.D. Thesis, University of Karlsruhe, Germany (2002)

274. Vlasov, S.N., Shapiro, M.A., Sheinina, E.V.: *Wave beam shaping on diffraction of a whispering gallery wave at a convex cylindrical surface.* Radio Phys. Quantum Electronics, **31**, 1070(1988)

275. Iima, M., Sato, M., et al.: *Measurement of radiation field from an improved efficiency quasi-optical converter for whispering-gallery mode.* Conf. Digest, 14th Int. Conf. on Infrared and Millimeter Waves, Würzburg, Proc. SPIE 1240, 405(1989)

276. Denisov, G.G., Kuftin, A.N., Malygin, V.I., Venediktov, N.P., Vinogradov, D.V., Zapevalov, V.E.: *110 GHz gyrotron with built-in high efficiency converter.* Int. J. Electronics, **72**, 1079(1992)

277. Denisov, G.G., Petelin, M.I., Vinogradov, D.V.: *Converter of high-mode of a circular waveguide into the main mode of a mirror line.* WO90/0780 H01P1/16, PCT Gazette, **16**, 47(1990)

278. Denisov, G.G., Petelin, M.I., Vinogradov, D.V.: *Effective conversion of high waveguide modes to eigenmodes of open mirror lines.* Proc. 10th Summer-Seminar on Wave Diffraction and Propagation, Moscow, SRIRP, 96(1993)

279. Pretterebner, J., Möbius, A., Thumm, M.: *Improvement of quasi-optical mode converters by launching an appropriate mixture of modes.* Conf. Digest 17th Int. Conf. on Infrared and Millimeter Waves, Pasadena, SPIE 1929, 40(1992)

280. Thumm, M.: *Modes and mode conversion in microwave devices.* In "Generation and application of high power microwaves", Ed. R.A. Cairns and A.D.R. Phelps, IOP, Bristol, 121(1997)

281. Alberti, S., Arnold, A., et al.: *European high-power CW gyrotron development for ECRH systems.* Fusion Eng. and Design, **53**, 387(2001)

282. Dammertz, G., Alberti, S., et al.: *Development of a 140 GHz, 1 MW, continuous wave gyrotron for the W7-X stellarator.* Frequenz, **55**, 270(2001)

283. Denisov, G.G.: *Development of 1 MW output power level gyrotrons for fusion systems.* Proc. Int. Workshop on Strong Microwaves in Plasmas, Nizhny Novgorod, 1999, Ed. A.G. Litvak, Russian Academy of Sciences, **2**, 967(2000)

284. Piosczyk, B., Braz, O., et al.: *Coaxial cavity gyrotron with dual RF beam output.* IEEE Trans. Plasma Science, **26**, 393(1998)

285. Mjasnikov, V.E., Agapova, M.V., et al.: *Megawatt power level long-pulses 110 GHz and 140 GHz gyrotrons.* Proc. Int. Workshop on Strong Microwaves in Plasmas, Nizhny Novgorod, 1996, Ed. A.G. Litvak, Russian Academy of Sciences, **2**, 577(1997)

286. Chirkov, A.V., Denisov, G.G., Aleksandrov, N.L.: *3D wavebeam field reconstruction from intensity measurements in a few cross sections.* Optics Communications, **115**, 449(1995)

287. Empacher, L., Gantenbein, G., Kasparek, W., Erckmann, V., Laqua, H.: *Matching of a non-gaussian gyrotron beam to a transmission line using thermographic measurements.* Proc. of the 21st Int. Conference on Infrared and Millimeter Waves, Berlin (1996)

288. Aleksandrov, N.L., Chirkov, A.V., Denisov, G.G., Kuzikov, S.V.: *Mode content analysis from intensity measurements in a few cross sections of oversized waveguides.* Int. J. Infrared Millimeter Waves, **18**, 1323(1997)

289. Chirkov, A.V., Denisov, G.G.: *Methods of wavebeam phase front reconstruction using intensity measurements.* Int. J. Infrared and Millimeter Waves, **21**, 83(2000)

290. Michel, G., Thumm, M.: *Spectral domain techniques for field pattern analysis and synthesis.* Surv. Math. Ind., **8**, 259(1999)

291. Thumm, M.: *Development of output windows for high-power long-pulse gyrotrons and EC wave applications.* Int. J. Infrared and Millimeter Waves, **19**, 3(1998)

292. Thumm, M.: *MPACVD-diamond windows for high power and long pulse millimeter wave transmission.* Diamond and Related Materails, **10**, 1692(2001)

293. Heidinger, R., Dammertz, G., Meier, A., Thumm, M.K.: *CVD diamond windows studied with low- and high-power millimeter waves.* IEEE Trans. Plasma Science, **30**, 800(2002)

294. Nickel, H.-U.: *Hochfrequenztechnische Aspekte zur Entwicklung rückwirkungsarmer Ausgangsfenster für Millimeterwellen- gyrotrons hoher Leistung.* Ph.D. Thesis, University of Karlsruhe, Germany(1995)

295. Fowkes, W.R., Callin, R.S., Jongewaard, E.N., Sprehn, D.W., Tantawi, S.G., Vlieks, A.E.: *Recent advances in high power RF windows at X-band.* Proc. Radio Frequency Workshop (RF 98), High Energy Density Microwaves, Pajaro Dunes, California, USA, AIP Conference Proceedings, **474**, 289(1998)

296. Petelin, M.I., Caryotakis, G., Tolkachev, A.A., Kuzikov, S.V., Postoenko, G.K., Tai, M.L., Yunakovsky, A.D.: *Quasi-optical components for MMW fed radars and particle accelerator*. Proc. Radio Frequency Workshop (RF 98), High Energy Density Microwaves, Pajaro Dunes, California, USA, AIP Conference Proceedings, **474**, 304(1998)

297. Smirnova, E.I.: *Travelling wave window with matching gratings*. Int. J. Infrared and Millimeter Waves, **22**, 835(2001)

298. Dammertz, G., Braz, O., et al.: *Recent Results of the 1 MW, 140 GHz, $TE_{22,6}-$ Mode Gyrotron*. IEEE Trans. Plasma Science, **27**, 330(1999)

299. Reckling, K.–A.: *Plastizitätstheorie und ihre Anwendung auf Festigkeitsproblems*. Spinger: Berlin (1967)

300. Ross, T.F.: *Advanced applied stress analysis*. Ellis Horwood: Chichester (1987)

301. Thumm, M.: *Progress in gyrotron development*. Fusion Engineering and Design (2003)

302. http://www.inp.nsk.su/~ dolgash/window.html

303. Sakamoto, K., Kasugai, A., et al.: *Development of a 170 GHz/500 kW gyrotron*. Int. J. Infrared and Millimeter Waves, **18**, 1637(1997)

304. Piosczyk, B., Braz, O., et al.: *165 GHz, 1.5 MW coaxial cavity gyrotron with depressed collector*. IEEE Trans. Plasma Science, **27**, 484(1999)

305. Borie, E., Drumm, O., et al.: *Possibilities for multifrequency operation of a gyrotron at FZK*. IEEE Trans. Plasma Science, **30**, 828(2002)

306. Kuftin, A.N., et al., *Test results of the prototype for frequency step-tunable 105–170 GHz 1 MW gyrotron*. 12th Joint Workshop on ECE and ECRH, Aix–en–Provence, France(2002)

307. Lygin, V.K., Piosczyk, B., et al.: *A diode electron gun for a 1 MW 140 GHz gyrotron*. Int. J. Electronics, **82**, 193(1997)

308. Alexandrov, N.L., et al.: *Selective excitation of high-order modes in circular waveguides*. Int. J. of Infrared and Millimeter Waves, **13**, 1369(1992)

309. Brand, G.F., Fekete, P.W., Hong, K., Moore, K.J., Idehara, T.: *Operation of a tunable gyrotron at the second harmonic of the electron cyclotron frequency*. Int. J. Electronics, **68**, 1099(1990)

310. Idehara, T., Ogawa, I., et al.: *Development of frequency tunable, medium power gyrotrons (Gyrotron FU Series) as submillimeter wave radiation sources*. IEEE Trans. Plasma Science, **27**, 340(1999)

311. Idehara, T., Tatsukawa, T., et al.: *High-frequency, step-tunable, cyclotron harmonic gyrotron*. Phys. Fluids B, **3**, 1766(1991)

312. Liu, P.–K., Borie, E., Kartikeyan, M.V.: *Design of a 24 GHz, 25–50 kW technology gyrotron operating at the second harmonic*. Int. J. Infrared and Millimeter Waves, **21**, 1917(2000)

313. Bogdashov, A., Bratman, V., et al.: *The powerful microwave sources for materials processing*. Proc. of the 2nd Int. Workshop on Far Infrared Technologies 2002, Fukui University, Japan, 59(2002)

314. Borie, E., Illy, S., Westermann, T.: *Use of the BFCPIC and BFCRAY codes to Describe Space Charge Limited Emission in electron guns for gyrotrons*. Int. J. Infrared and Millimeter Waves, **18**, 1 (1997)

315. Golubev, S.V., Platanov, Yu.Ya., Razin, S.V., Zorin, V.G.: *Soft X-ray emission from millimeter-wave electron cyclotron resonance discharge*. J. X-ray Science and Technology, **6**, 244(1996)

316. Golubev, S.V., Razin, S.V., Zorin, V.G.: *Ion charge state distribution in plasma of electron cyclotron resonance discharge sustained by powerful millimeter wave radiation.* Rev. Sci. Intr., **69**, 634(1998)

317. Tatsukawa, T., Maeda, T., et al.: *ESR spectroscopy with a wide frequency range using a gyrotron as a radiation power source.* Int. J. Infrared and Millimeter Waves, **16**, 293(1995)

318. Wesson, J.A., Lashmore–Davies, C.N.: *Tokamaks* (in Chapter–5) 2nd Edition. Clarendon Press, Oxford (1997)

319. Leuterer, F., Beckmann, M., et al.: *The ECRH system of ASDEX upgrade.* Fusion Engineering and Design, **56–57**, 615(2001)

320. Mitsudo, S., Aripin, T., et al.: *High power, frequency tunable, submillimeter wave ESR device using a gyrotron as a radiation source.* Int. J. Infrared and Millimeter Waves, **21**, 661(2000)

321. Gerfen, G.J., Becerra, L.R., et al.: *High frequency (140 GHz) dynamic nuclear polarization: polarization transfer to a solute in frozen aqueous solution.* J. Chem. Phys., **102**, 9494(1995)

322. Feher, L., Thumm, M.: *System design development for microwave and millimeter-wave materials processing.* Intense Microwave Pulses IX, Proc. SPIE, **4720**, 75(2002)

323. Feher, L., Link, G., Thumm, M.: *The MiRa / THESIS3D – code package for resonator design and modelling of millimeter-wave material processing.* Springer Meeting on Materials Research Society, Microwave Processing of Materilas V, San Francisco, Symposium Proc. **430**, 363(1996)

324. Link, G., Ivanov, V., et al.: *A comparison of mm-wave sintering and fast conventional sintering of nanocrystalline* Al_2O_3. Springer Meeting on Materilas Research Society, Microwave Processing of Materilas V, San Francisco, Symposium Proc. **430**, 157(1996)

325. L'Hermitte, R. in J. Atmospheric and Oceanic Tech., **4**, 36 (1987) and in IEEE Trans. Geoscience and Remote Sensing, **26**, 207(1988)

Index